UCRL-LR-150541

Reflectance, Optical Properties, and Stability of Molybdenum/Strontium and Molybdenum/Yttrium Multilayer Mirrors

B. Kjornrattanawanich

Ph.D. Dissertation

U.S. Department of Energy

Lawrence
Livermore
National
Laboratory

September 1, 2002

DISCLAIMER

This work was performed under the auspices of the U. S. Department of Energy by the University of California, Lawrence Livermore National Laboratory under Contract No. W-7405-Eng-48.

Reflectance, Optical Properties, and Stability of Molybdenum/Strontium and Molybdenum/Yttrium Multilayer Mirrors

By

BENJAWAN KJORNRATTANAWANICH
B. S. (Chiang Mai University, Thailand) 1996
M.S. (University of California, Davis) 1997

DISSERTATION

Submitted in partial satisfaction of the requirements for the degree of

DOCTOR OF PHILOSOPHY

in

Applied Science

in the

OFFICE OF GRADUATE STUDIES

of the

UNIVERSITY OF CALIFORNIA

DAVIS

Approved:

Professor Richard R. Freeman

Professor Subhash H. Risbud

Dr. James A. Folta

Committee in Charge

2002

Benjawan Kjornrattanawanich
September 2002
Applied Science

Reflectance, Optical Properties, and Stability of Molybdenum/Strontium and Molybdenum/Yttrium Multilayer Mirrors

Abstract

The motivation of this work is to develop high reflectance normal-incidence multilayer mirrors in the 8-12 nm wavelength region for applications in astronomy and extreme ultraviolet lithography. To achieve this goal, Mo/Sr and Mo/Y multilayers were studied. These multilayers were deposited with a UHV magnetron sputtering system and their reflectances were measured with synchrotron radiation. High normal-incidence reflectances of 23% at 8.8 nm, 40.8% at 9.4 nm, and 48.3% at 10.5 nm were achieved. However, the reflectance of Mo/Sr multilayers decreased rapidly after exposure to air. Attempts to use thin layers of carbon to passivate the surface of Mo/Sr multilayers were unsuccessful.

Experimental results on the refractive index $\tilde{n} = 1 - \delta + i\beta$ of yttrium and molybdenum in the 50-1300 eV energy region are reported in this work. This is the first time ever that values on the refractive index of yttrium are measured in this energy range. The absorption part β was determined through transmittance measurements. The dispersive part δ was calculated by means of the Kramers-Kronig formalism. The newly determined values of the refractive index of molybdenum are in excellent agreement with the published data. Those of yttrium are more accurate and contain fine structures around the yttrium *M*-absorption edges where Mo/Y multilayers operate. These improved sets of optical data lead to better design and modeling of the optical properties of Mo/Y multilayers.

The reflectance quality of Mo/Y multilayers is dependent on their optical and structural properties. To correlate these properties with the multilayer reflectance, x-ray diffraction, Rutherford backscattering spectrometry, and transmission electron miscroscopy were used to

analyze samples. Normal-incidence reflectances of 32.6% at 9.27 nm, 38.4% at 9.48 nm, and 29.6% at 9.46 nm were obtained from three representative Mo/Y multilayers which had about 0%, 25%, and 39% atomic oxygen assimilated in their yttrium layers, respectively. Based on the optical properties, multilayers with higher oxygen content should have higher absorption. However, the 25%-oxygen multilayer had less interface roughness and thus had higher reflectance than the 0%-oxygen sample. The 39%-oxygen multilayer had the highest absorption and roughness, thus had the lowest reflectance among three samples. The optical and structural properties of the multilayers are competing in the reflectance results.

Mo/Y (39% oxygen) multilayers terminated with molybdenum, yttrium (39% oxygen), and palladium were studied. These samples all experienced significant reflectance drop in the first three months after deposition due to surface contamination or oxidation. The reflectance peaks were shifted toward shorter wavelengths because of interface contraction. The molybdenum- and palladium-capped samples exhibited the best performance with 4% relative loss in reflectance after one year. The yttrium-capped sample performed poorer, most likely due to the presence of high oxygen. The molybdenum-capped samples were further studied regarding their thermal stability. Period expansion of up to 2% relative to its initial value was observed from samples annealed at 480° C for one hour. Though the annealed samples had smoother and sharper interfaces than the as-deposited ones, their reflectances were decreased after annealing. A maximum of 9% relative drop in reflectance was observed from the sample annealed at 380° C for 24 hours. Therefore Mo/Y multilayers are proved to have relatively good thermal stability.

The performance of a Mo/Y (25% oxygen) multilayer-coated diffraction grating was investigated. The grating substrate was a replica of a holographic ion-etched blazed grating with 2400 grooves/mm. The measured peak efficiency in the third order was 2.7% at 8.79 nm. This is the highest normal-incidence grating efficiency ever obtained to date in this wavelength region.

Acknowledgements

First and foremost, I would like to thank my graduate advisor Prof. Richard Freeman for providing guidance and support throughout my graduate study and directing me to work with the most excellent research group at LLNL.

I would like to especially thank Claude Montcalm, my principle research advisor. I have learned so much from Claude about multilayers and magnetron sputtering deposition. I have benefited tremendously from his originally designed and built NRC deposition system and from his writing the proposal for the NASA funding. I have really appreciated him spending so many nights doing experiments with me at the ALS without tiring.

I would like to thank Saša Bajt and Regina Soufli for each lending me their expertise, their distinctive outlook on interpretation and communication of results, and their support of my research leading to this dissertation and several publications. I am truly indebted to Regina Soufli for kindly reviewing my dissertation and being the best-ever editor. I would like to also thank Jim Folta for taking good care of me throughout my years at LLNL.

Special thanks are due to Eric Gullikson for being an all around good guy at the ALS beamline and for his assistance in many of my measurements especially the grating studies. I would also like to thank Eric, Eberhard Spiller, Chris Walton, and Daniel Stearns for many enlightening discussions of my experimental data. I would like to thank John Seely for the grating efficiency calculations, Sherry Baker for the AFM measurements, Juergen Plitzko and Jennifer Harper for the TEM measurements and some discussion of the results, Cheng Saw for meaningful large-angle XRD measurements,

Rick Gross for explaining about TEM sample preparation, and Dino Ciarlo for providing the silicon nitride membranes.

I would like to thank the faculty at DAS (UC Davis) and EECS (UC Berkeley) for the graduate classes they taught me. I am grateful to Prof. Denise Krol, Prof. Richard Freeman, Prof. André Knoesen, Prof. Xiangdong Zhu, Eberhard Spiller, Jim Folta, and Claude Montcalm for sitting in my qualifying exam committee. I would like to thank Prof. Richard Freeman, Prof. Subhash Risbud, and Jim Folta for their efforts in reviewing this dissertation.

I am also thankful to Jay Ayers, Rick Levesque, Fred Grabner, George Wells, Steve Liapis, and Cindy Larson at LLNL; Donna Hamamoto, Gary Giangrasso, Cheryl Hauck, Steve Klingler, Charles Knopf at the ALS; Jim Bowers, Farhad Salmassi, and Drew Kemp at the CXRO, for their assistance during my work.

This section is to thank my graduate fellows John Adams, Raj Patel, Solomon Obolu, Shri Gopalakrishna, Anthony Troha, Liquin Song, and Helena Feng for their companionship and support through difficult times at DAS. I also like to thank my friends Karen Scott, Yashesh Shroff, Igor Jovanovic, and Jonathan Foster at UCB for all the good times and memories. Thanks are due to my roommates Rebecca Darlington and Zoe Hoel, and my Thai friends for their wonderful friendship.

Finally, I would like to thank my parents Olang Sae-Lao and Phenchom Bunrit, my sisters Jeera and Benjamas Sae-Lao, my husband Yutdhasak Kjornrattanawanich, my lovely sons Pat and Paul Kjornrattanawanich, and all my relatives back home in Thailand for their unconditional love, support, and everything. I could not have done this without you.

TABLE OF CONTENTS

List of Figures

List of Tables

Chapter 1

Introduction

1.1 Extreme Ultraviolet and Soft X-Ray Radiation

The terms used to describe electromagnetic radiation in the order from low to high energies are radio waves, microwaves, infrared radiation, visible light, ultraviolet rays, x-rays, and gamma rays. The so-called extreme ultraviolet (EUV) and soft x-ray radiation are portions of the electromagnetic spectrum in between ultraviolet and x-rays: EUV extends approximately from 30 to 250 eV and soft x-ray radiation extends approximately from 250 eV to several keV.[1] These two energy regions coincide with a large number of atomic resonances, resulting in high absorption in all materials. At lower energies e.g. in the visible and ultraviolet, and at higher energies e.g. in the hard x-ray region, many materials are transparent. This is how to distinguish the EUV/soft x-ray region from their neighboring spectral regions. Due to the highly absorptive nature of matter and a lack of source in the EUV/soft x-ray region, the optical properties of materials in this energy range had not been much explored experimentally until the1980s.

The advent of laser plasma sources and synchrotron radiation has relieved one of the difficulties since intense EUV/soft x-ray beams have been made available for use and studies. As is well known, EUV/soft x-ray radiation can be produced with two processes.[2] One is by emission from an atom or ion when an electron loses energy in the form of x-

rays when transferring from one atomic level to a lower level, which gives a discrete line spectrum. Examples are emission induced by electron bombardment of a low *Z* target and emission from plasma formed by a low Z material. The second type of process is acceleration of charged particles, typically electrons, which gives a continuous spectrum. Examples are emission from electrons decelerated by bombarding a high *Z* target and emission from relativistic electrons constrained to travel in curved trajectories using magnetic fields inside a synchrotron ring.

In order to consider specific designs for x-ray optics, one should understand first how EUV/soft x-ray radiation interacts with matter. There are three processes happening which are: elastic scattering, inelastic scattering, and absorption via the photoelectric effect.[2] Briefly, elastic scattering is caused by two processes: Thomson scattering from single atomic electrons that may be considered as free in the low energy limit, and Rayleigh (or coherent) scattering which occurs from strongly bound electrons. The scattered and incident beams have a definite phase relationship and Bragg interference diffraction can occur. Inelastic (incoherent or Compton) scattering occurs from loosely bound electrons and involves the transfer of a small fraction of energy of an incident photon. The scattered and incident beams do not have a well-established phase relationship. Absorption through photoelectric effect occurs when the x-ray photon transfers all its energy to an inner atomic electron, thereby releasing it from the atom (ionization). Any one of these interactions results in strong absorption in most materials as mentioned previously. The propagation of EUV/soft x-ray radiation is commonly expressed in terms of complex refractive index $\tilde{n} = 1 - \delta + i\beta$, which includes an imaginary part β to describe the absorption. In most cases, the decrement of dispersion δ

is also a small and positive number. The nearness of the real part of the refractive index to unity combined with the high absorption of the EUV/soft x-rays indicate that refractive lenses of the same type as those used to focus visible light would have incredibly long focal lengths and they would absorb essentially all of the incident radiation in the EUV/soft x-ray range. Advances in grazing-incidence reflective optics and more recently in normal-incidence multilayer mirrors have enabled focusing of the EUV/soft x-ray beams. At extremely low incidence angles, nearly parallel to the optics surface,[†] substantial reflectance can be obtained with conventional mirrors although image aberrations and instrumental costs remain important issues in utilizing glancing incidence optics.[3,4] Imaging with the glancing incidence technique was originally introduced by Kirkpatrick and Baez, where a combination of two spherical mirrors, focusing in the vertical and horizontal directions respectively, was used to focus x-rays.[5] The use of glancing incidence optics in the design of synchrotron radiation beamlines has been described in detail elsewhere.[6,7] The benefits of the use of normal-incidence optics are relatively high reflectance with smaller optics sizes, larger collection area, and less aberrations.

The first attempts to fabricate multilayers were by Koeppe[8] and Deubner[9] who deposited Cd/Ag and Au/Ag multilayers by means of electroplating technique. They observed x-ray diffraction that corresponds to the lattice spacings but not diffraction corresponding to the layer structures of these multilayers. The first multilayer diffraction was demonstrated by DuMond and Youtz from Cu/Au multilayers deposited using the thermal evaporation technique.[10] The Cu/Au multilayers were not stable because of

[†] Beam coming at a smaller angle than the critical angle for total reflection.

diffusion between these two materials. The observed changes in the diffraction intensity with time by DuMond and Youtz lead to a new research studies of diffusion using multilayers. In 1972, the idea of using multilayers as EUV/soft x-ray reflectors was first proposed by Spiller.[11] He demonstrated theoretically that sufficiently high normal-incidence reflectance can be achieved with multilayers due to constructive interference among multiple reflections. Haelbich and Kunz[12] were the first to experimentally prove Spiller's idea and they obtained about 2.7% and 1.2% reflectances from C/Au and C/Cu multilayers, respectively. At that time, it was very difficult to achieve high reflectance multilayers due to lack of precise control of the individual layer thicknesses. In 1978, Barbee and Keith introduced a sputtering technique for the fabrication of multilayers.[13] Considerable advancements in the field of EUV/soft x-ray multilayer optics have continued from there on.

1.2 Multilayer Applications

There are many challenging applications of multilayer optics particularly for astronomy and extreme ultraviolet lithography (EUVL). Early cosmic studies in the EUV/soft x-ray range had been limited to glancing-incidence optics. A list of past, ongoing, and future astrophysics missions by wavelength region, excluding those missions for solar and planetary physics, is shown in Fig. 1.1. The Chandra X-ray Observatory, for example, used a high-resolution grazing incidence x-ray telescope comprised of iridium-coated mirrors for astrophysical observations in the 0.09 to 10.0 keV energy range. The full-sky survey of the spectrum from 7 to 76 nm by the Extreme-Ultraviolet Explorer (EUVE) was recently accomplished by three Wolter-Schwarzschild grazing-incidence telescopes.[14]Again, issues with small collection angles and

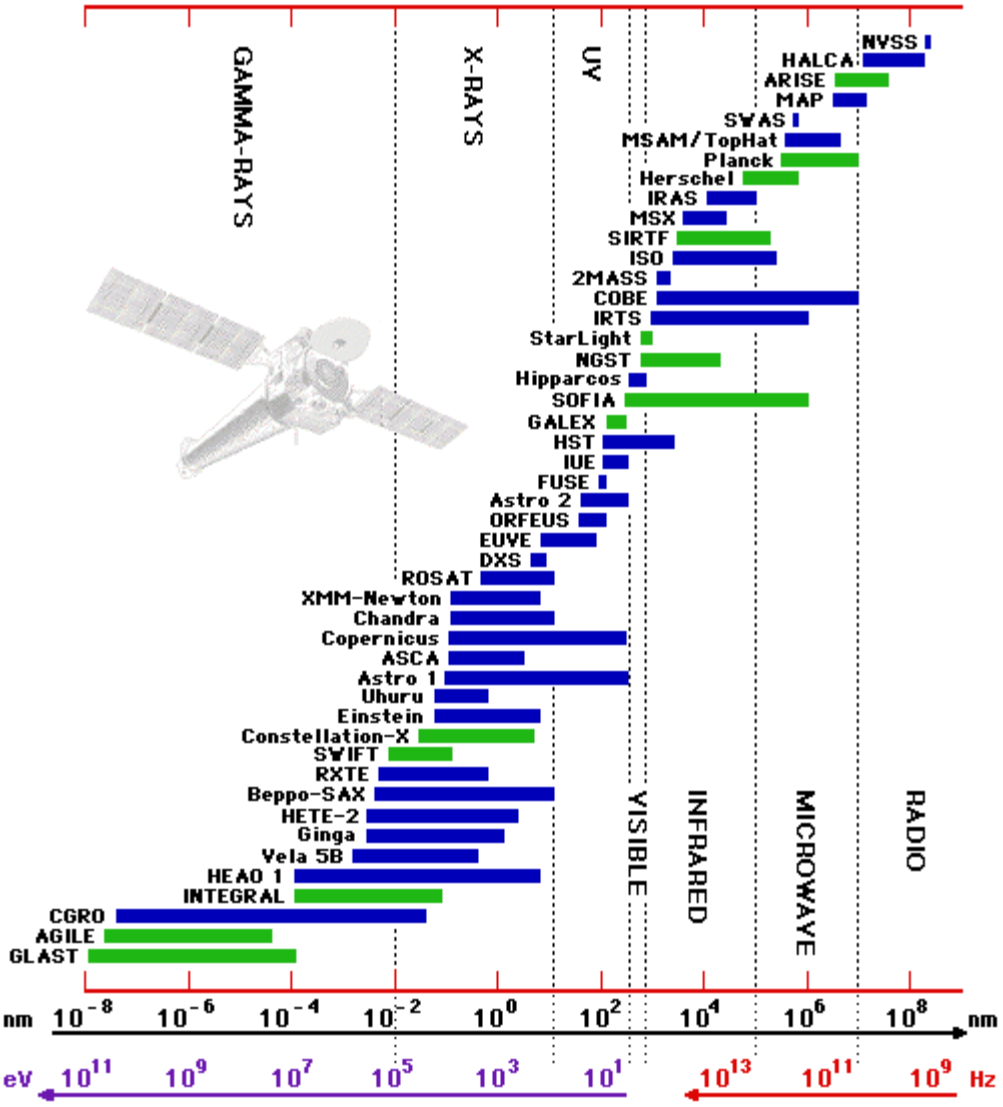

Figure 1.1. A list of past and ongoing missions (blue) and future missions (green) by wavelength region. Courtesy of the NASA Goddard Space Flight Center. Details about each mission are available at http://nssdc.gsfc.nasa.gov/astro/astrolist.html.

insufficiently narrow spectral bandpass have always been encountered with such optics. With the emergence of normal-incidence multilayer coatings, large collection angles and narrow spectral bandpass optics have become available. Much progress has been made, especially in the field of solar physics using multilayer-coated telescopes. The rocket-

launched Cassegrain telescope[15] is coated with Mo/Si coatings to record emissions at 17.3 nm. The Extreme ultraviolet Imaging Telescope (EIT) of the Solar and Heliospheric Observatory[16] and the Transition Region and Coronal Explorer[17] (TRACE) telescope are

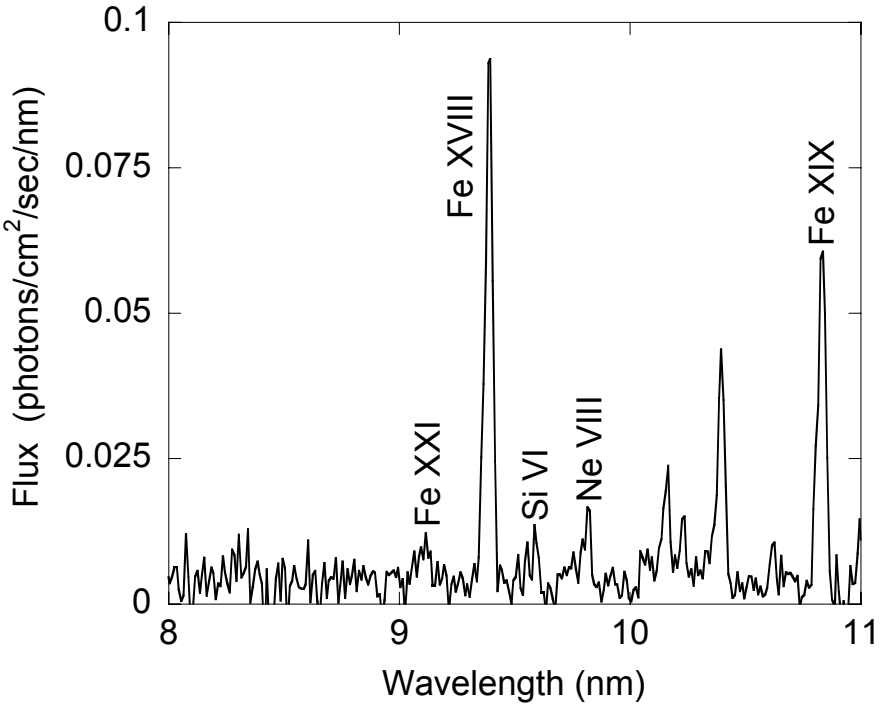

Figure 1.2. Intense EUV spectra observed from Capella during the all-sky survey by the EUVE mission.

also coated with Mo/Si and Mo_2C/Si multilayers, respectively, to record emissions at 17.1 nm, 19.5 nm, 28.4 nm, and 30.4 nm. However, there are still interesting portions of the EUV/soft x-ray region that have not been explored and that cannot be accessed by silicon-based multilayers. An example of the EUV spectra obtained from the Capella, a binary system star, is shown in Fig. 1.2. The most intense emission line is Fe XVIII at a wavelength around 9.4 nm.

Another challenging application of normal-incidence multilayer mirrors is photolithography using EUV radiation, termed Extreme Ultraviolet Lithography (EUVL).

Based on the same principle as that of a conventional camera, in which transmissive lenses are used to capture an original image that is transferred to a negative for development and reproduction, a semiconductor lithography stepper prints circuit patterns from a "mask" onto silicon wafer surfaces, which are further processed and developed into transistors.[18,19] The speed of computers has doubled every two years in the last four decades by steady shrinking the feature size of microchips. The minimum printable feature size scales according to the wavelength of illumination. Early generations of semiconductor technology used the mercury (Hg) lines at 436 nm and 365 nm as illumination sources. The Hg line at 248 nm, the krypton fluoride (KrF) line at 248 nm, and the argon fluoride (ArF) line at 193 nm, are used in production today and they are able to pattern circuits with feature sizes down to 130 nm. Increasing demand for faster and smaller transistors has driven the need for circuits as small as 30 nm for processors operating at 10 GHz or faster. The existing lithographic technologies will soon reach the point where moving toward EUV wavelengths will be required and there the refractive lenses currently used to focus light will no longer operate as has been explained in Section 1.1. A quest is therefore initiated by the semiconductor industry for a next-generation lithographic technology. EUVL has been voted the most suitable technology for the 30 nm resolution node by the semiconductor equipment manufacturers since it is considered the natural extension of optical lithography. EUVL operates at a wavelength around 13 nm where high reflectance (70%) is obtained from Mo/Si multilayers.[20] Fig. 1.3 shows a schematic of the Engineering Test Stand (ETS), a prototype laboratory system developed to demonstrate full-field printing of EUV images.[21] The most advanced set of Mo/Si-coated projection optics for this tool has achieved thickness control across

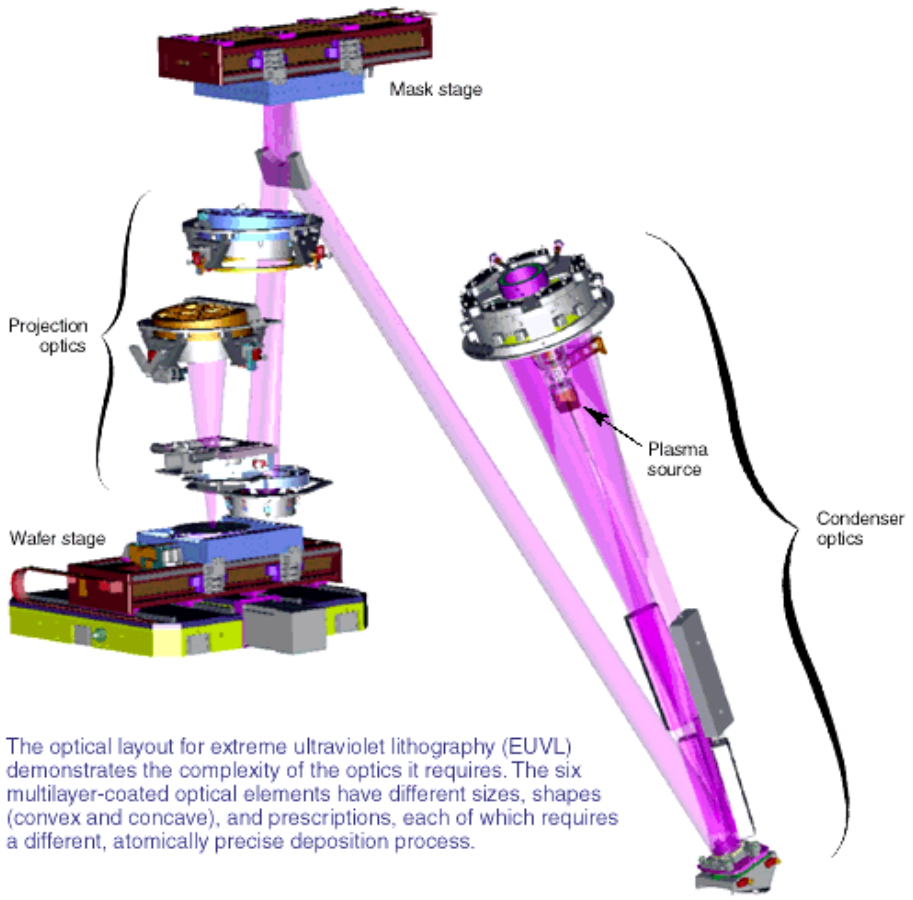

Figure 1.3. Engineering Test Stand (ETS) Image. Courtesy of Donald Sweeney, Lawrence Livermore National Laboratory

the optic surface equivalent to a quarter-diameter of a silicon atom and has printed images with 30 nm resolution (Fig. 1.3). To meet the required commercial EUVL throughput specifications, the EUV source must provide sufficient power at 13.4 nm wavelength. However, the currently used and developed Xenon jet laser-produced-plasma source has a maximum intensity at around 10.8 nm wavelength where Mo/Si multilayers provide low reflectance (30%). Therefore one needs to either optimize the source efficiency at 13.4 nm or alternatively search for new materials that would provide high reflectance at around 10.8 nm to obtain better throughput and resolution.

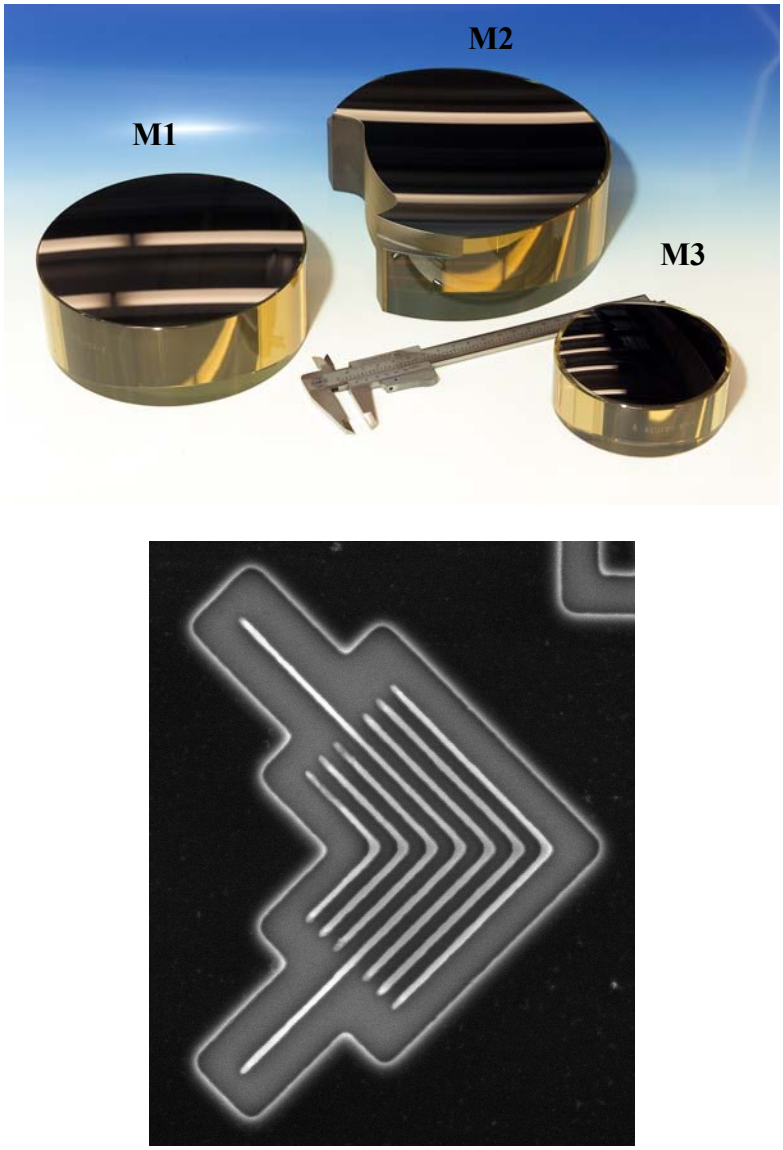

Figure 1.4. Three of the four camera mirrors (M1-M4) after being multilayer-coated (top). Courtesy of Regina Soufli, Lawrence Livermore National Laboratory. The 39-nm elbows pattern with the M1-M4 camera optics which represents the finest imaging resolution ever achieved with EUVL (bottom). These spectacular results demonstrate the feasibility of EUVL for printing circuits down to the 30 nm technology node. Courtesy of Patrick Naulleau, Lawrence Berkeley National Laboratory

1.3 Objective of This Study

In the wavelength region below 12.4 nm (silicon *L*-edge) where Mo/Si can no longer operate, multilayer pairs other than Mo/Si need to be developed for the applications discussed in the previous sections. Studies by Montcalm *et al.* have shown that Mo/Sr and Mo/Y are the most promising multilayers to operate below 12.4 nm down to the 8 nm region, thus Mo/Sr and Mo/Y have been selected for this study.[22] The goal of this dissertation is to develop a better understanding of both the optical properties and micro structural properties of Mo/Sr and Mo/Y multilayers in order to improve their reflectance and stability. Details about the multilayer deposition tool and the various characterization techniques applied throughout this work are given in Chapter 2. The fabrication and *in situ* reflectance characterization of Mo/Sr multilayer mirrors designed for the 8-12 nm wavelength region are described in Chapter 3. The determination of the complex index of refraction of yttrium and molybdenum in the 50-1300 eV energy region, by means of photoabsorption, is presented in Chapter 4. An accuracy validation of the new sets of yttrium and molybdenum refractive indices using sum rule tests is also described. The structural properties of Mo/Y are further investigated in Chapter 5. The stability of Mo/Y multilayers with different capping layers and the reflectance/structural changes after annealing are also discussed. The fabrication and efficiency measurements of a Mo/Y multilayer-coated diffraction grating, operating at 9 nm, are presented in Chapter 6. The multilayer principle, design, and modeling are described in Appendix A. The computer codes for dispersion and sum rule calculations and the newly measured optical constants (β,δ) of yttrium and molybdenum are given in Appendix B.

Chapter 2

Experimental Techniques

In this study, the magnetron-sputtering technique was used for multilayer fabrication. Details of the deposition system are presented in this chapter. Several methods used to characterize multilayer samples are briefly described.

2.1 Sample Deposition

An ultrahigh vacuum (UHV) magnetron-sputtering[23] deposition system was used for the fabrication of thin films and multilayers throughout this study. A picture of the complete system and its schematic (top view) are shown in Fig. 2.1. Three planar-magnetron-sputtering sources from US Inc. were mounted vertically on the chamber wall. Two were used for multilayer fabrication with shutter in front of each source to regulate the deposition flux. The third source was sometimes used for deposition of a capping layer of another material. The sputtering source was either powered with a dc power supply (MDX-500 or MDX-1000 from Advanced Energy) for conducting target materials or with an rf power supply (RFX-600 used in conjunction with ATX-600, both from Advanced Energy) for insulating target materials. The substrate, placed in the center of the chamber, was mounted on a rotary feedthrough attached to the chamber lid. The substrate-to-target distance could be varied from 7.5-15.5 cm. A substrate of up to 1 cm x 1cm in area could be inserted into the chamber through the loadlock without breaking

vacuum. The loadlock chamber was turbo pumped to $1x10^{-6}$ Torr within 15 min thus facilitating the procedure for substrate loading. However, the substrate holder could accommodate a substrate of up to 3.5 cm x 4.5 cm in area if the deposition chamber is vented.

The deposition chamber was cryogenically pumped to about $1x10^{-8}$ Torr in base pressure after an initial pumpdown with a mechanical pump. Pressures in 0.1 mTorr or above were measured with a convectron gauge and those below with a nude Bayard-Alpert type ion gauge. The convectron and the ion gauges were controlled with a Granville-Phillips vacuum process controller series 303. The chamber bakeout was done by using one of the programmable controls of the 303 unit so that the heating process was paused whenever the increased pressure due to outgassing was above the set point. A UHV base pressure of about $2x10^{-9}$ Torr was normally achieved after three days of bakeout at 130° C. A residual gas analyzer (RGA) was used to monitor the vacuum contaminant levels. The RGA was very useful for leak detection in the system. During the deposition, ultra-high purity argon process gas (99.999%) was used. The base pressure was monitored with a capacitance manometer and maintained at 2.0 mTorr by slightly closing the gate valve between the deposition chamber and the cryogenic pump and by adjusting the gas flow rate. A 10-minute presputtering of the targets was done before any deposition runs to remove surface contaminants. A multilayer was fabricated by alternatively facing the substrate toward each target and then opening the associated shutter for a predetermined time. The substrate could be spun around its center to achieve good thickness uniformity. The deposition process was completely controlled by computer and lasted about two hours for a typical multilayer.

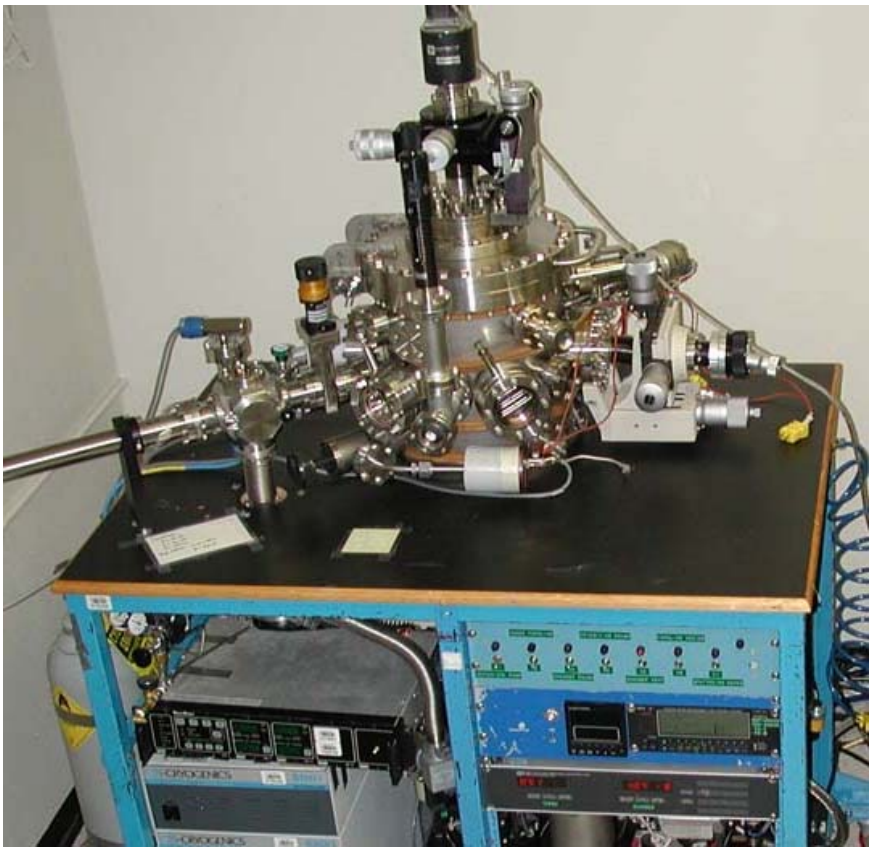

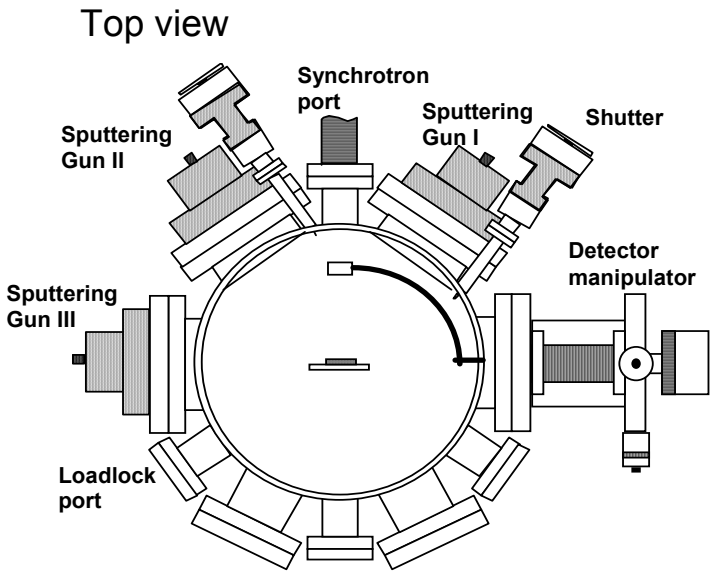

Figure 2.1. The dc magnetron-sputtering deposition-reflectometer system used for the fabrication of thin films and multilayers and for the *in situ* reflectance characterization with synchrotron radiation.

The deposition system was designed so that it could also be used as a reflectometer. The complete system was portable and could be attached to a synchrotron beamline or any other light source through the synchrotron port. Therefore, reflectance of as-deposited multilayers could be measured *in situ* before exposure to ambient air. As shown in Fig. 2.1, opposite to the synchrotron port was a viewport that was very useful for the alignment of the synchrotron beam. An XYZ-rotary manipulator mounted opposite to the third magnetron-sputtering source was used to position a photodiode detector. The reflectance measurements could be performed in a horizontal plane at any incidence angle from 3° to 8° with this configuration. During deposition, the detector was kept from being coated by placing it in a closed box located inside the chamber. Detailed information about the reflectance measurements is described in Section 2.3.

2.2 Characterization of Thin Films and Multilayer Structures with X-Ray Diffraction

X-ray diffraction[24] (XRD) was the main technique used to determine the period thickness of multilayers and the thickness of thin films for deposition rate calibration. The basic diagram of the XRD measurement is shown in Fig. 2.2, where the diffraction angle 2θ is the angle between the incident and the diffracted x-rays. At low incident angles, the XRD measurements were made on a Rigaku DMAXIIB powder diffractometer. The voltage and current setups for the rotating copper anode (x-ray source) were 40 kV and 40 mA, respectively. A collimated beam of x-rays from copper K_{α} emission at wavelength of 0.1546 nm was generated and incident on a sample. The intensity of the diffracted beam was measured with a NaI (Sodium Iodide) scintillation counter. For diffraction at small incident angles, the XRD reflectance was obtained by

measuring the diffracted beam intensity as a function of the diffraction angle over the angular range of 2θ from 0° to 12°. Examples of the measured XRD data from thin film and multilayer samples can be found in the following chapters. Due to variation of the deposition rates with the increasing wear of the sputtering targets, the rate calibration was performed before each set of deposition runs. The substrates used for rate calibration were silicon (100) wafers, 4 inches in diameter and cut to about 1 cm x 1 cm in size. There was no removal of the native oxide on the silicon substrate before using.

For multilayers, some material pairs may react and cause either contraction or expansion at the interface. Thus, the rate calibrations were done directly with multilayers

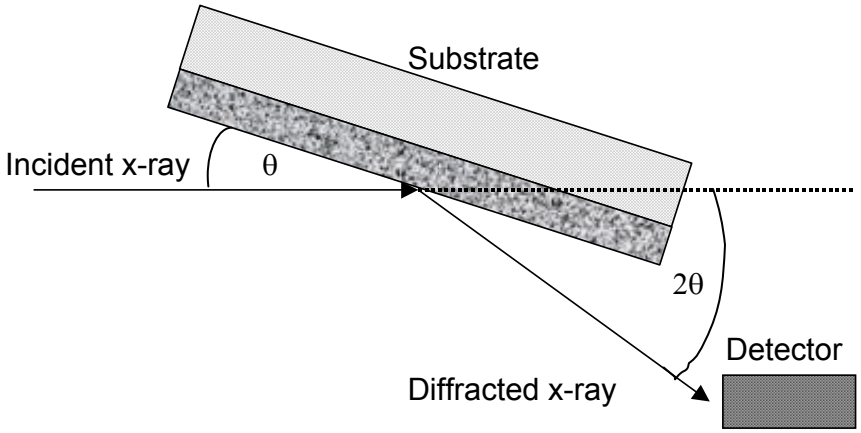

Figure 2.2. Basic diagram of a typical x-ray diffractometer.

rather than with separate single layers of the constituents. A series of multilayers having different thickness combinations was fabricated and the XRD reflectance was measured as a function of diffraction angle. From the reflectance spectrum, the n^{th} order Bragg diffraction peak occurs when the reflectance from all interfaces is in phase. The angular

positions of the diffracted peaks are related to the geometrical period thickness of the multilayer (d_{Bragg}) to the well known Bragg's law:

$$n\lambda = 2d_{\mathrm{Bragg}} \sin\theta, \qquad (2.1)$$

where n is the Bragg's diffraction order and λ is the wavelength of light. The refraction-corrected multilayer period (Λ) can then be determined using the modified Bragg's equation developed by Henke *et al.* [25]

$$n\lambda = 2d_{Bragg}\left(1-\frac{\delta}{\sin^2\theta}\right)\sin\theta = 2\Lambda\sin\theta\,, \qquad (2.2)$$

where δ is the decrement of the average refractive index of the multilayer. Equation (2.2) can be rewritten in the following form

$$\frac{1}{d_{Bragg}} = \frac{1}{\Lambda}\left(1-\frac{\delta}{\sin^2\theta}\right), \qquad (2.3)$$

where Λ can be determined from linear regression of $1/d_{\mathrm{Bragg}}$ versus $1/\sin^2\theta$. The slope is equal to $-\delta/\Lambda$ with y-axis interception of $1/\Lambda$. With the known deposition times of material I and II and the calculated period thicknesses, the deposition rates can be determined based on a two-layer model

$$\Lambda = r_{\mathrm{I}}\, t_{\mathrm{I}} + r_{\mathrm{II}}\, t_{\mathrm{II}} + \Delta\Lambda, \qquad (2.3)$$

where r_{I}, r_{II} and t_{I}, t_{II} are the deposition rates and times of material I, II, respectively and $\Delta\Lambda$ is the change (contraction or expansion) in the period thickness due to interface formation. Since there are only three unknowns in this equation, r_{I}, r_{II}, and $\Delta\Lambda$, thus at least three multilayers are needed to accurately determine the deposition rates. The accuracy of this method can be improved by having more than three deposited

multilayers when solving these equations. It is assumed that the deposition rates of both materials and the interface factor are constant in this model.

For a single layer film, the deposition rate can be accurately determined simply by growing a series of films under the same deposition conditions but different deposition times. By fitting the reflectance data obtained from XRD through Fresnel equations,[26] the film thickness can be determined. Parameters such as roughness were always included in the model in order to have a good fit (See Appendix A for fitting XRD data). The deposition rate can then be determined from the slope of fitted thickness versus time.

The XRD technique was sometimes performed at larger incident angles. Instead of the Rigaku diffractometer, an Intel curved position sensitive detector with copper K_α radiations was used. Such a system can scan the diffracted signals over the angular range of 2θ from 25° to 100° simultaneously. Several diffracted peaks with angular positions (θ) corresponding to atomic d-spacings can provide detailed information about the crystalline structure of the constituent materials under investigation.

2.3 EUV Reflectance Metrology

The most direct method in determining the multilayer performance is by measuring its EUV reflectance with the EUV/soft x-ray reflectometer. In this study, the reflectometer at beamline 6.3.2 of the Advanced Light Source at Lawrence Berkeley National Laboratory was used.[27] This beamline, shown in Fig. 2.3, is designed for high spectral purity and wavelength accuracy for the characterization of optical components and reflective coatings for a variety of applications, EUV lithography, for example. The reflectometer has served as an important tool throughout this work for both *in situ* and *ex situ* reflectance and transmittance measurements. The radiation obtained from a bending

magnet is in the energy range 50 to 1300 eV (25 nm down to 1 nm). The beam is first cut geometrically by the 4-jaw aperture, and then focuses horizontally and vertically with grazing incidence mirrors M-1 and M-2, respectively. A spectral resolution ($\Delta\lambda / \lambda$) of up to 3000 has been obtained using a varied-line-spacing plane grating monochromator. Energy is scanned by a simple rotation of the grating with a fixed exit slit. Energy was calibrated with a relative accuracy of 0.011% rms, and could be determined with a 0.007% repeatability. The fixed exit slit has a horizontal width of 1 cm and an adjustable vertical width of 1 to 400 μm. The M-3 mirror reflects the beam into the reflectometer chamber. The focal length of the M-3 mirror and the vertical position of the beam in the chamber are adjustable through three vacuum feedthroughs. A GaAsP photodiode with a 5 mm x 5 mm active area was used as a detector. A small photocurrent generated by photodiode is directly related to the beam intensity. A Keithley 428 amplifier is used to amplify such a small photocurrent. This current amplifier can measure currents in the mA to pA range and convert into 0-10 V output signal with a selectable amplification from 10^3 to 10^{11} V/mA. The current was also measured from the M-3 mirror to normalize the signal against the storage ring current decay. The same type of amplifier is also used to amplify the reference current obtained from the M-3 mirror. Second harmonic and stray light suppression at various energies were achieved with a selection of filters installed between the exit slit and the M-3 mirror. At low energies where higher harmonics are present, an order suppressor consisting of three grazing incidence mirrors was used in addition to filters to improve spectral purity. The angles and the coatings of the mirrors composing of the order suppressor can be changed to filter the desired energy. Table 2.1 summarizes the common settings of beamline 6.3.2 in order to obtain high spectral purity.

The reflectometer chamber is differentially pumped from the beamline and can be pumped to 1.2×10^{-6} Torr in half an hour. There are two goniometers installed in the chamber for rotating the detector and sample holders. The detector holder is usually equipped with a CCD camera. In addition to rotation, the sample holder is translatable in three axes. All axis motion is controlled by the LABVIEW based software. The reflectometer chamber can accommodate samples with size up to 8 inches, and has the

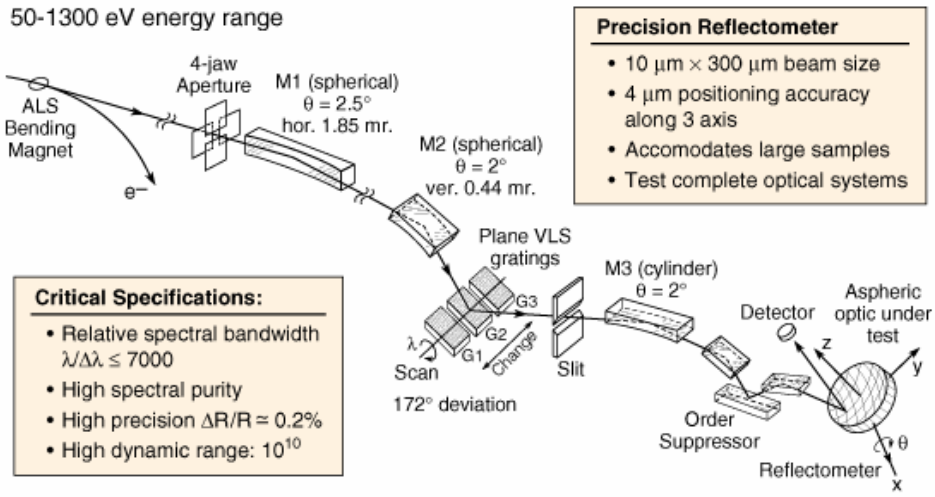

Figure 2.3. A schematic diagram of the reflectometer beamline 6.3.2. at the Advanced Light Sources (ALS), Lawrence Berkeley National Laboratory (LBNL). Courtesy of Eric Gullikson; Center for X-ray Optics (CXRO), LBNL.

capability of positioning the sample to within ±4 μm and setting the sample angular position to within 0.002°.

For an alignment of the reflectometer, the sample was first positioned at the center with visible light from the beamline by turning the grating monochromator to zero order. Then, the specular reflectance was measured at several incident angles under EUV radiation. For perfect alignment, the sample surface should be in the rotational axis of the

Table 2.1. Settings of beamline 6.3.2 for reflectance and transmittance measurements.

Grating (lines/mm)	Filter	Order Suppressor		Energy Range (eV)
		Coating	Angle	
200	Al	C	10°	50-72
200	Si	C	10°	68-96
200	Be	C	8°	94-110
200	B	C	8°	107-144
600	B	C	6.2°	141-181
600	C	Ni	8°	179-283
600	Ti	Ni	6.2°	260-450
1200	Cr	Ni	6.2°	440-570
1200	Co	-	-	560-760
1200	Cu	-	-	752-932

goniometer so that the reflected beam hits the same spot for different combinations of θ-2θ. This was done by monitoring the reflected beam with the internal CCD camera detector. Once the angular positions of sample and detector were aligned, the reflectance measurement was performed first by measuring the reflected beam intensity (I_r) as a function of wavelength. The direct beam intensity (I_0) was then measured after removing the sample from the optical path. The background intensities were subtracted from I_r and I_0 and then normalized by the intensity collected from M-3 mirror to account for the decay of incident light with the storage ring current decay. The reflectance R is defined as the ratio of normalized I_r and I_0. The reflectance calculations were done automatically using a user-friendly program available at the beamline right after the measurements.

2.4 Purity Analysis with Rutherford Backscattering Spectrometry

The quality of sputtering targets may be determined based on the purity quoted from their manufacturers. However, most vendors only factor in the metallic impurities and exclude the absorbed gas contents. For example, a 99.95% purity can have up to 500 ppm (parts per millions) metallic impurities plus thousands ppm of absorbed oxygen, nitrogen, and carbon. Since composition and density of materials are the main parameters for determining the refractive index used for multilayer design and simulation, purity verification is very important.

Yttrium is known to oxidize in air.[28] Therefore it is the most interesting material to be studied among all targets used in this work excluding strontium which is highly reactive material. Rutherford backscattering spectrometry[29] (RBS) was used to determine the oxygen content and any other elements in the yttrium target and the magnetron-sputtered yttrium films. RBS is a nondestructive method that can provide a quantitative depth profile of the upper 1 to 2 μm of the sample. Briefly, a 50-nm thick yttrium film was bombarded with 2.3 MeV He^{++} ions and the energies of the backward scattered ions were measured at 108°and 170° angles. The depth and the mass of the target atom are directly related to the energy of the backscattered ions. The atomic concentration is also proportional to the number of these ions. The detection limits of RBS range from a few ppm for heavy elements to a few percent for light elements.

2.5 Microstructure Imaging with Transmission Electron Microscopy

Transmission electron microscopy (TEM)[30] is one of the most powerful tools to study multilayer microstructure. This technique offers a tremendous range of signals from which one can obtain images, diffraction patterns, and several kinds of spectra from the same small region of the specimen. In TEM, a focused electron beam is incident on a thin sample. The undeflected and deflected electrons that penetrate the sample thickness generate signals. These signals are delivered to a detector such as a fluorescent screen, a film plate, or a video camera by a series of magnetic lenses at and below the sample position. As a result of using a highly focused electron beam as a probe on an extremely thin sample, highly magnified images of the sample with better than 0.2 nm lateral spatial resolution can be achieved. The resolution can be increased by increasing the voltage of the TEM instrument.

In this study, an ultra thin cross section of a multilayer was prepared following the steps shown in Fig. 2.4. Briefly, two pieces of multilayer were cleaved from the center and then cleaned with ethanol. These two pieces were glued together face-to-face with G-1 epoxy from Gatan Corp. Two blank silicon pieces were added on each side of the sample stack in order to increase the overall thickness before coring. A Gatan coring machine was used to core the stack to ¼ inches in length. The core was inserted into a brass tube (0.118 inches in diameter) which was then filled with the G-1 epoxy. The advantage of this step is that the final specimen has a thick ring of brass tube around it, which gives it mechanical stability. A low speed cut off saw was used to cut slices of about 600 μm thick. A lapping machine from Allied High Tech was used to polish the sample surface. A dimpling process was subsequently performed using a Gatan dimpler

until the end thickness at the sample center was about 8 to 12 μm. Ion milling was done with a Gatan 691 for final thinning (polishing). This finishing process involved bombarding a thin specimen with energetic ions of argon and sputtering material from the sample until it was thin enough to be studied. An increase in temperature during specimen preparation, for example the curing of epoxy at 130 $^{\circ}$C for 30 minutes, was insufficient to induce significant structural changes in the Mo/Y multilayer (See the annealing effect on Mo/Y multilayers in Section 5.5). Hence, it is believed that the structures observed in the TEM images are true representations of the samples and not artifacts of the specimen preparation. With the use of TEM, the interface profiles of multilayers such as interface reaction, interdiffusion, and interface roughness may be revealed. Fig. 2.5 shows an image from a Mo/Y sample. This image was intentionally taken at low magnification to reveal the ion milled surface (top), the multilayer stack (middle) and the silicon substrate (bottom). The exact thickness of each individual layer can be determined directly from the image itself. However, the thickness determination is not usually done this way because x-ray diffraction is more accurate. In addition to high resolution images, the diffraction patterns obtained from TEM can also be used to determine the microstructure of the specimen (e.g. amorphous or crystalline) and other crystallographic characteristics of the sample if it is crystalline (e.g. lattice parameter and symmetry). Detailed studies on micro structural properties of Mo/Y multilayers with TEM images and electron diffraction are described in Chapter 5.

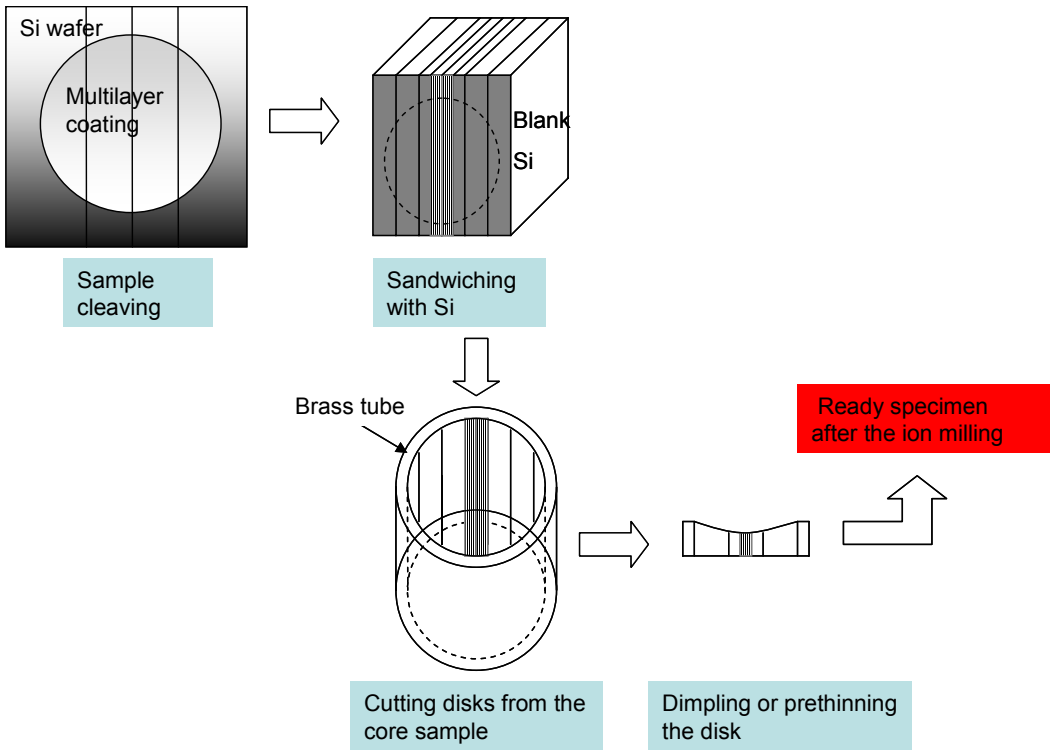

Figure 2.4. Sequence of steps for cross-section specimen preparation; the multilayer sample was cut into pieces normal to the interfaces which were glued together with blank silicon wafers so that the stack was wider. The sample was then glued into the brass tube, cut into slices, dimpled, and ion milled to perforation.

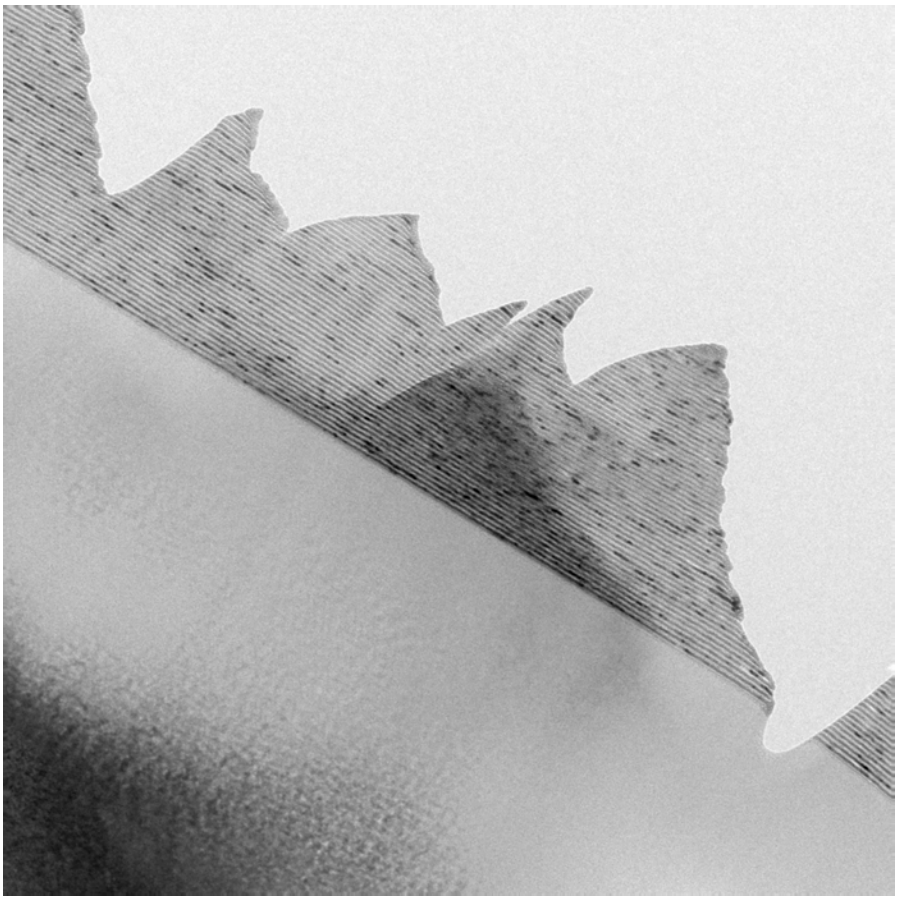

Figure 2.5. Low magnification TEM image of a Mo/Y multilayer.

2.6 Surface Roughness Determination with Atomic Force Microscopy

One of the factors limiting reflectance of multilayers is surface-interface roughness. With the use of an atomic force microscope (AFM), the roughness can be determined by scanning a sharp tip across the surface. This AFM was fitted with the following components: Digital Instruments Dimension 5000 equipped with an acoustic hood, type G scanner, and a Nanoscope IIIA Controller with a phase extender box. All measurements were performed in air using tapping mode which measured topography by

tapping the surface with an oscillating probe tip. The probe tip was etched silicon with a nominal tip radius of 5-10 nm. The roughness values (R_q) derived from AFM measurements are the root mean square (RMS) of height deviation (z) taken from the mean data plane and can be expressed as:

$$R_q = \sqrt{\frac{(z_1^2 + z_2^2 + z_3^2 + \ldots + z_N^2}{N}} . \qquad (2.4)$$

A number of scans were performed over the 1 to 5 μm square areas on each sample. The measurements had a lateral resolution of 10 nm limited by the finite size of the probe tip and a height resolution of 0.02 nm. The Fourier transform of the surface height gives the two-dimentional power spectral density (PSD) of the surface which can be calculated from the measured surface contour $Z(\vec{r}), \vec{r} = (x, y)$ using the standard relation:

$$\underset{\lim A \to \infty}{S_2(\vec{f})} = \frac{1}{A}\left|\int_A z(r) e^{2\pi i \vec{f} \bullet \vec{r}} d\vec{r}\right|^2 , \qquad (2.5)$$

where vector $\vec{f} = (f_x, f_y)$ is a vector of spatial frequencies f_x = 1/ Λ_x, f_y = 1/ Λ_y. The surface roughness is the integral of the power spectrum:

$$\sigma^2 = 2\pi \int_0^\infty S_2(f) f df , \qquad (2.6)$$

for an isotropic surface, where $f = \sqrt{f_x^2 + f_y^2}$. PSD represents the relative contributions of different frequency components of the roughness at the surface of a sample.

Chapter 3

Molybdenum/Strontium Multilayer Mirrors

3.1 Introduction

Very few material pairs are known to provide high normal-incidence reflectance in the wavelength region below 30 nm because of high absorption. To date, the reflectance of about 50% to as high as 70% is experimentally achieved from Mo/Si multilayers in the 13-15 nm region.[31] A few carbon- and yttrium-based material pairs were investigated for normal-incidence multilayer mirrors in the 8-12 nm wavelength region and the best reflectance in this spectral range was achieved with Mo/Y multilayers.[22,32] According to theoretical simulations, some strontium-based material pairs, in particular Mo/Sr, would provide equally high reflectance mirrors as Mo/Si multilayers. Because of their superior optical and chemical properties, Mo/Sr would also provide higher reflectance than Mo/Y multilayers in the region below the silicon *L*-absorption edge (at 12.4 nm) down to 8 nm where Mo/Si has low reflectance. However, strontium has not been considered as a possible material for multilayers mainly due to its high reactivity with oxygen and water vapor.[33] Even if it were deposited in ultrahigh vacuum (UHV) conditions to prevent oxidation during deposition, a strontium-based multilayer would most likely deteriorate rapidly after deposition when exposed to air. Nevertheless, it is of interest to investigate the Mo/Sr material pair for use in high-

reflectance multilayer mirrors. Achieving high *in situ* reflectance before exposure to air may justify efforts to develop surface passivation layers.

The fabrication and characterization of Mo/Sr multilayer mirrors designed for the 8-12 nm wavelength region are reported in this chapter. The multilayers were deposited in a UHV deposition-reflectometer system attached to a beamline at a synchrotron radiation facility so that the measurement of normal-incidence reflectance of the as-deposited multilayers could be measured before exposure to ambient air.

3.2 Multilayer Deposition

Mo/Sr multilayers were fabricated by using the UHV deposition-reflectometer system described previously in Section 2.1. Each multilayer was deposited onto a 1 cm x 1 cm piece of Si (100) wafer held on a rotating shaft at the center of the chamber at a distance of 19.5 cm from the sources. For a typical deposition run, ultrahigh-purity argon (99.999%) was flowed into the chamber, at a rate of 64 cm^3/min at STP, to maintain a pressure of 2.0 mTorr. A carbon target was added in this study to deposit capping layers. Molybdenum (99.99%), strontium (99%) and carbon (99.99%) magnetron sputtering sources were operated at dc powers of 50, 30, and 200 W, and the deposition rates under these conditions were 0.047, 0.166, and 0.012 nm/s, respectively. A Mo/Sr multilayer was deposited by alternate rotation of the substrate in front of either the molybdenum or strontium target and then opening of the associated shutter for a predetermined time. All multilayers had a first layer of strontium on the substrate and a last layer of molybdenum on the surface. Some samples were capped with carbon after the molybdenum and strontium sources were turned off.

Several precautions had to be taken to minimize the exposure of the strontium target to air during shipment, installation, and use. The target was shipped in mineral oil, which was removed by soaking the target in a bath of paint thinner (Klean-Strip) and then acetone. It is likely that this method of shipment contaminated the target with hydrocarbons. However, no chemical analysis was performed to verify this because the target was extremely unstable. Once exposed to air, the silvery appearance of the target turned into yellowish-color powder of strontium oxide immediately. Strontium does not absorb nitrogen below 380° C, thus the strontium target was mounted on the sputtering source inside a glove bag inflated with a large flow of nitrogen. The sputtering source itself was then quickly mounted on the chamber flange and a pumpdown was initiated as soon as a sufficient seal was made. Once a high vacuum was achieved, the system was baked at 130° C for three days and a base pressure in the low 10^{-9} Torr was reached after cool-down. After this, the strontium target was not exposed to air, as all the substrates were introduced into the chamber via a turbo-pumped loadlock. The strontium target was presputtered for several hours to clean its surface before starting multilayer deposition runs.

For these experiments, the deposition system was attached to the back of the reflectometer chamber of beamline 6.3.2 of the Advanced Light Source at the Lawrence Berkeley National Laboratory. All reflectance measurements were performed in the *p*-polarized plane at an angle of incidence of 3.6° to 7.2° from normal incidence. Details of the reflectance measurement procedure are described in Section 2.3.

3.3 Rate Calibration for Thin Carbon Films

Carbon is one of the materials having low optical contrast compared to silicon. For this reason, there is a small difference between the x-ray diffraction (XRD) spectrum obtained from a carbon film deposited on silicon substrate and the one obtained from bare

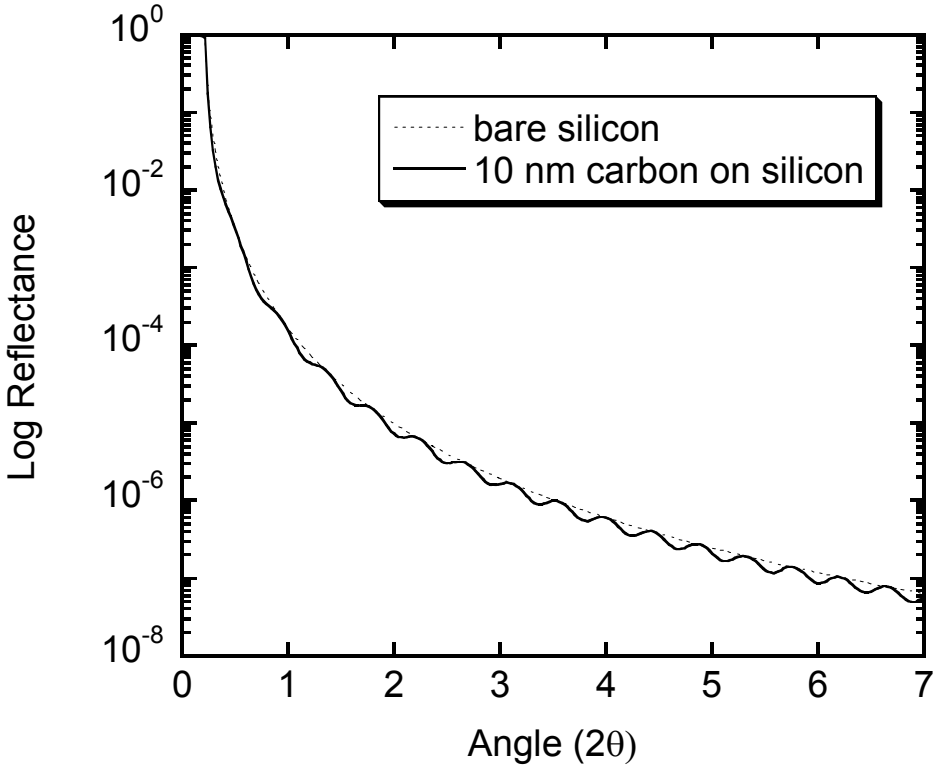

Figure 3.1. Calculated XRD reflectance of a thin carbon film deposited on a silicon wafer substrate in comparison to the reflectance obtained from bare-silicon.

silicon. As shown in Fig 3.1, the calculated XRD spectrum of a 10 nm thick carbon film deposited on a silicon substrate provides reflectance modulations with small amplitude because of low optical contrast. Increasing the carbon thickness only increases the frequency of modulations with very small increase in the reflectance amplitude. Therefore determining the thickness of carbon by fitting such a reflectance spectrum as

discussed in Section 2.2 is rather difficult. Instead of fitting the diffraction data of single layer carbon samples, fitting the data of bilayer Mo/C samples is one solution. Since carbon and silicon have higher optical contrast than molybdenum, molybdenum of known thickness can be used as an intermediate layer for the purpose of enhancing the optical contrast. Carbon deposition rates can then be determined from the slope of the fitted thickness versus deposition time.

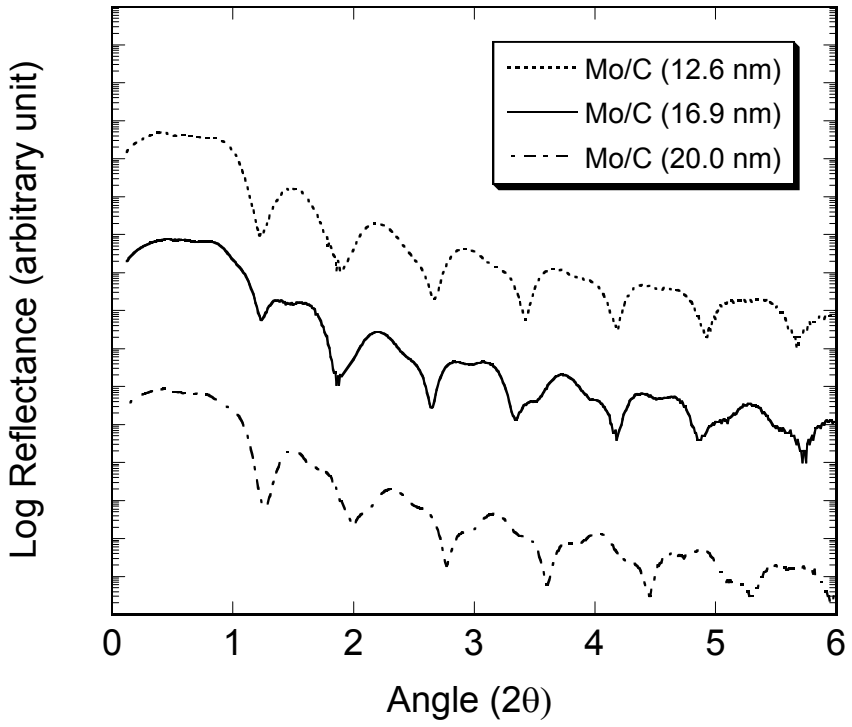

Figure 3.2 Measured XRD spectra of three bilayer samples having different thicknesses of carbon on 11-nm-thick molybdenum films on silicon substrate.

Examples of the measured reflectance data of various carbon thicknesses deposited on 11 nm thick molybdenum films are shown in Fig. 3.2. Adding a fixed thickness of molybdenum in between carbon and silicon substrate resulted in primary modulations of the same frequency. The secondary modulations of different frequencies

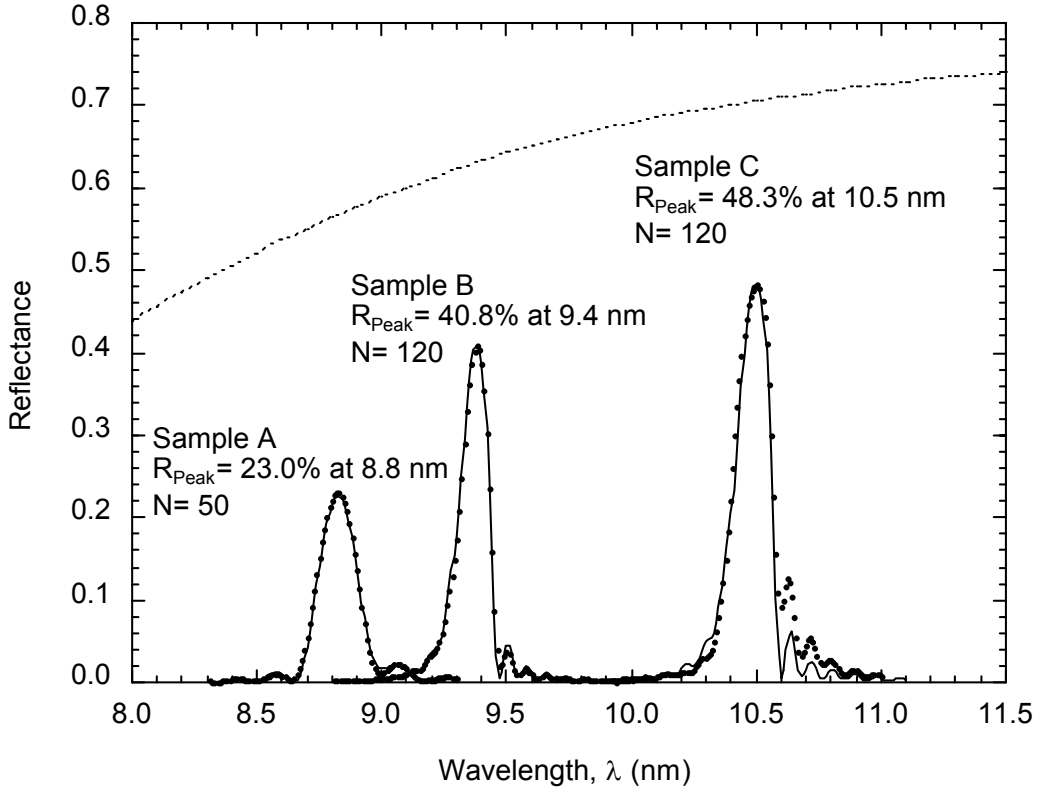

Figure 3.3. *In situ* normal-incidence (3.6°) reflectance of three Mo/Sr multilayer samples. Data points, measured reflectance; solid curves, best theoretical fits; dashed curves, maximum theoretical peak reflectance of an ideal Mo/Sr multilayer throughout the wavelength region of interest.

on top of the primary ones were the results of different carbon thicknesses. The fitted thicknesses corresponding to carbon deposition times of 900, 1200, and 1500 sec. were 12.6, 16.9, and 20.0 nm, respectively. The carbon deposition rate was thus 0.012 nm/sec.

3.4 Results and Discussion

A series of Mo/Sr multilayers were deposited and their EUV reflectances were measured *in situ* as a function of wavelength directly after the deposition. Fig. 3.3 shows the reflectance curves of three representative samples (A, B, and C) measured at 3.6° from normal incidence (data points), along with a theoretical fit for each set of data (solid curves). The dashed curve represents the maximum theoretical reflectance of Mo/Sr

multilayers with 500 bilayers achievable at each wavelength, assuming optimum layer thicknesses and ideal interfaces. Peak reflectances of 23.0, 40.8, and 48.3% were measured at 8.8, 9.4, and 10.5 nm, respectively. To our knowledge this is the best normal-incidence reflectance achieved to date in the 8-12 nm wavelength region. The reflectance of sample A is relatively lower than those of samples B and C because it had only 50 bilayers, whereas the other two samples had 120 bilayers. Sample A was one of the first multilayers deposited for rate calibration purposes and had only 50 bilayers to preserve the target life.

The theoretical fit for each sample was achieved with adjusting only the interface roughness factor, σ using TF Design. TF Design is a thin film computer program used to calculate the optical properties of the EUV multilayer mirrors, and written by the Thin Films Group, Institute of Microstructural Sciences, National Research Council of Canada. The interface roughness factor was assumed to be the same for each interface ($\sigma_{Mo\text{-}on\text{-}Si} = \sigma_{Si\text{-}on\text{-}Mo}$), and the interface profile was modeled by the Debye-Waller factor (See Appendix A). The average layer thicknesses d_{Sr} and d_{Mo} were fixed to values determined from the deposition-rate calibrations. The layer thicknesses were assumed to vary linearly throughout the multilayer by a small percentage Δd that was adjusted to yield the best fit to the oscillations on each side of the main reflectance peak. Parameter Δd takes into account the small drifts of the deposition rates during multilayer deposition. Note that equally good fits could have been obtained with other combinations of the layer thicknesses and interface roughness. No surface oxide was considered in the fits because the reflectance of all samples was measured *in situ* immediately after deposition. The agreement between the measured reflectance curve and the theoretical fit

Table 3.1. Fitting parameters for the three multilayer samples shown in Fig. 3.3.

Sample	*N*	d_{Sr} (nm)	d_{Mo} (nm)	Λ (nm)	Γ	Δd (%)
A	50	2.61	1.86	4.47	0.41	+1.2
B	120	3.06	1.77	4.83	0.37	-1.0
C	120	3.44	1.92	5.36	0.36	-1.2

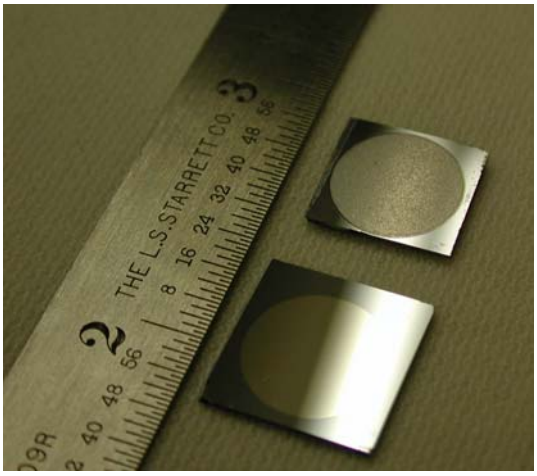

Figure 3.4. Physical appearance of a Mo/Sr multilayer before (left) and after (right) exposure to air.

is relatively good for all three multilayers, especially for sample A. A list of the fitting parameters for each multilayer is given in Table 3.1.

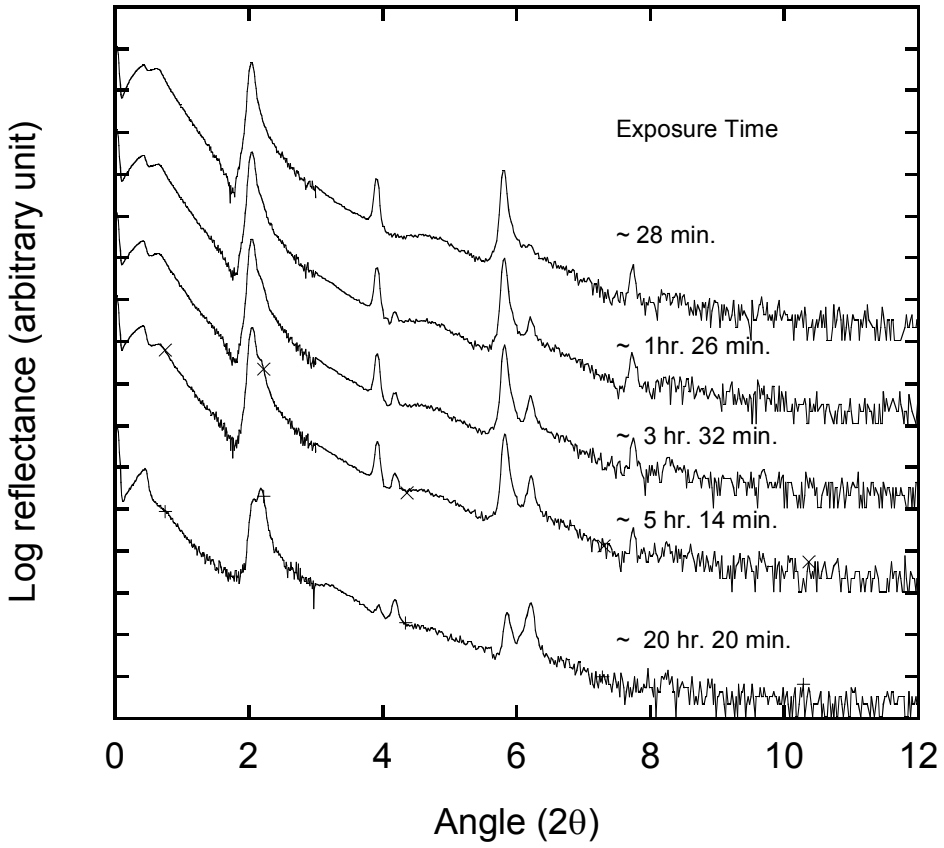

Figure 3.5. Series of measured x-ray diffraction data of the same Mo/Sr multilayer sample after various intervals of exposure to air.

Although the as-deposited Mo/Sr multilayers had good *in situ* reflectance, they were not stable when exposed to air. For example, the reflectance of a Mo/Sr sample decreased from 43% to 42% after a short 15 min. exposure to air. After 24 hours, the reflectance of this sample decreased to less than 1%. The most obvious cause of such reflectance loss is a reaction of the strontium layers with oxygen and water vapor after exposure to air. This assumption is supported by a visual change in the Mo/Sr multilayer surface color (Fig. 3.4), which changed from shiny silver (left) to dull gray (right) after a few hours of exposure to ambient air. Other causes such as broadening of the interfaces

as a result of inter-diffusion can be ruled out since the Mo/Sr multilayer kept in vacuum or dry nitrogen did not exhibit any significant decrease in the reflectance after 24 hours. The deterioration was investigated by repeatedly measuring the grazing incidence reflectance of a sample using XRD. Fig. 3.5 shows a series of grazing-incidence reflectance curves and confirms that the sample structure gradually deteriorated with time after exposure to air. The reflectance of an as-deposited sample shows a series of well-defined peaks, indicative of a good quality multilayer structure with a periodicity of 4.57 nm. However, with time the initial structure is replaced by a second structure with a periodicity of 4.14 nm. This change of periodicity is an indication of a chemical reaction in the multilayer, which propagates throughout the multilayer structure starting, most likely, from the surface of the sample. The decrease in period thickness that results from the reaction is puzzling, since the oxidation of metal layers usually results in a thicker oxide layer.

According to a simple model based on the density of materials[33] the ratio of the oxide to the metal thickness (assuming that the surface layer only expands in the direction perpendicular to the surface) is given by:

$$\frac{d_{Me_xO_y}}{d_{Me}} = \frac{1}{x}\frac{\rho_{Me}}{\rho_{ME_xO_y}}\frac{M_{Me_xO_y}}{M_{Me}} \quad , \qquad (3.1)$$

where d is the thickness, ρ is the density, and M is the atomic weight or molecular weight of the metal or oxide. The factor for expansion of a strontium layer into SrO or SrO_2 is 0.62 or 0.74, respectively, suggesting a *decrease* in thickness by less than a factor of 2. However, the factor of expansion of molybdenum into MoO_3 (the compound most likely to form) is 3.26, suggesting an *increase* in thickness by more than a factor of 3.0. If both

the strontium and molybdenum layers were fully oxidized, then one would expect an increase in the period thickness. Other oxidation models are possible, but unfortunately there is not enough information to speculate on them. After 24 hours, the multilayer had

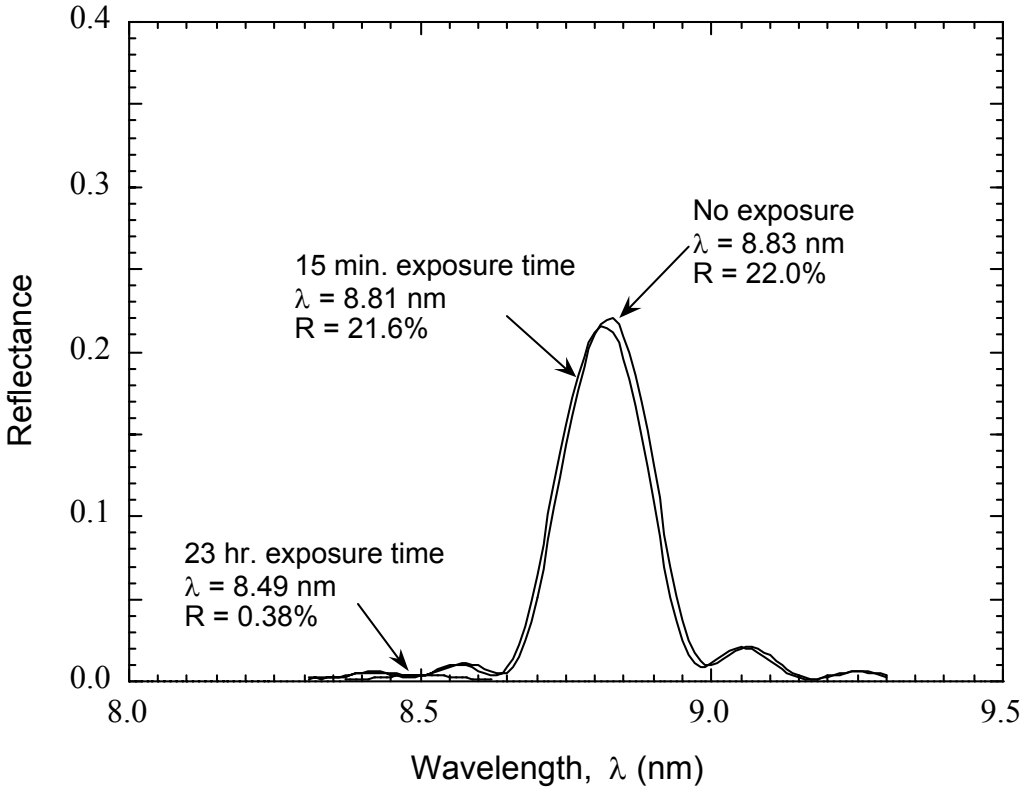

Figure 3.6. Repeated measurements of normal-incidence (3.6°) reflectance of a Mo/Sr multilayer having 7 nm thick carbon capping layer within one day of exposure to air.

completely lost its coherence, as can be seen from the disappearance of the 2θ peaks. It should be noted that similar measurements of a sample that was maintained in a relatively dry nitrogen environment did not exhibit such rapid deterioration.

Attempts to passivate the Mo/Sr multilayers and prevent their oxidation were made by deposition of a carbon capping layer on the surface. The normal-incidence (3.6°) reflectance of a freshly deposited Mo/Sr multilayer with bilayers was measured *in situ*

before and after the deposition of a 7.2±0.6 nm thick carbon capping layer. As shown in Fig. 3.6, the peak reflectance at 8.8 nm dropped from 23% to 22% after the deposition of the carbon layer. This carbon-capped sample was then exposed to air for 23 hours before its reflectance was re-measured. Measurements indicated that the reflectance had dropped from 22% to less than 1%, with slight decrease in the reflectance peak wavelength by 0.34 nm. The similar drop in reflectance that was observed for both capped and uncapped samples indicates that the 7 nm carbon layer was not successful in protecting the Mo/Sr multilayer when exposure to air.

3.5 Conclusions

Mo/Sr multilayer structures were fabricated for what is believed to be the first time, and high reflectance in the 8-12 nm wavelength region was measured *in situ*. However, these Mo/Sr multilayers were not stable in air, and oxidation processes rapidly degraded the multilayer structures. These multilayers therefore have rather limited applicability unless one can develop good capping layers that can prevent oxidation. Attempts to passivate the multilayers with carbon capping layers were unsuccessful, but other materials might prove more resistant. Also, using higher-energy deposition techniques may produce carbon layers with fewer pinholes or are otherwise more robust against corrosion. Future work should therefore focus on the development of a good capping layer that, in addition to providing high reflectance, will also allow the Mo/Sr multilayers to be investigated more thoroughly with chemical and physical analytical techniques.

Chapter 4

Index of Refraction of Yttrium and Molybdenum in the EUV and Soft X-Ray Region

4.1 Introduction

The need for high-reflectance multilayer coatings has been driven by rapid development of EUV/soft x-ray instrumentation for a number of applications such as microscopy, spectroscopy, EUV lithography, and astronomy. The 8-12 nm (155 eV down to 103 eV) region in particular has become important for astronomy due to the observation of intense emission lines from various cosmic sources.[14] High-reflectance multilayers would enable recording and high-resolution imaging of weak EUV spectra.

Mo/Y has proven to be one of the most promising material pairs for multilayers operating in this region due to its high and relatively stable reflectance.[31,32] A key parameter needed for modeling and designing of a reflective multilayer mirror is the refractive index of its constituent materials. The most comprehensive and up-to-date source for the refractive index of materials in the EUV/soft x-ray region is the angle-independent (forward) atomic scattering factors from the Center for X-Ray Optics (CXRO), Lawrence Berkeley National Laboratory.[34] An atomic scattering factor is defined as a ratio of the field amplitude coherently scattered by the whole atom to that

scattered by a free classical electron (Thomson scattering).[35] The forward atomic scattering factors have been compiled by the CXRO for the Z = 1 - 92 elements using available experimental and theoretical photoabsorption data in the energy region 10-30,000 eV.[36] Fairly accurate values of the refractive index of any material may be derived from these factors based on the independent atom approximation, where each atom in the material is assumed to interact with light in the same way as if the atom were free. However, it has been found experimentally that the atomic-like approximation for condensed matter is invalid at energies below about 50 eV where absorption is due to valence electrons and in the vicinity of absorption edges where the refractive index is sensitive to chemical environment and geometry of atoms within solid.[37] In the case of yttrium, the experimental results of refractive index have never been published in the region above 30 eV;[‡] therefore the values of the atomic scattering factors tabulated by the CXRO have relied exclusively on theoretical calculations. Moreover, the operating region of Mo/Y multilayers is in the vicinity of the yttrium-$M_{4,5}$ (155.8 eV) absorption edge, where fine features would be expected in the absorption spectrum. Thus it would be useful to experimentally determine the refractive index of yttrium in these energy regions in order to obtain more accurate values that can be applied in modeling the performance of yttrium-based x-ray optics. For molybdenum, although its refractive index has been measured several times by others using different methods, [38-41] these data are not often in good agreement. The only complete optical data were obtained with the transmittance

[‡] An unpublished experimental data set for the refractive index of yttrium in the 50-248 eV energy region has been included in IMD program by D. L. Windt and is available on the World Wide Web at http://www.cletus.phys.columbia.edu/~windt/imd/.

method in the 60-930 eV energy range by Soufli *et al*..[39] These data have been used to revise the atomic scattering factors that are now available on the CXRO World Wide Web. A comparison of these data with our measurements is nonetheless desirable.

There are several techniques for determination of the refractive index of materials such as reflectance, transmittance (photoabsorption), interferometry, and ellipsometry. Transmittance is one of the most robust and accurate methods if there is a capability to fabricate good quality ultra-thin samples to overcome strong absorption in the EUV and soft x-ray region. Hence transmittance was the experimental method chosen for this work.

4.2 Index of Refraction

The response of materials to electromagnetic radiation depends strongly on the energy region of interaction. In the EUV and soft x-ray region where photon energies are in the same order of magnitude as the binding energies of inner atomic electrons of low-*Z* and intermediate-*Z* elements (*Z*: atomic number), absorption becomes the dominant process when light interacts with matter. Different wavelengths propagate and disperse at different phase velocities. Both dispersive and absorptive properties of materials are commonly expressed in term of energy-dependent optical constants δ, β of a complex refractive index $\tilde{n} = 1 - \delta + i\beta$. As mentioned earlier, under the independent atom approximation, an index of refraction may be related to the forward atomic scattering factors, $f(0)$, of the individual atoms by:[37]

$$\tilde{n} = 1 - \delta + i\beta = 1 - \frac{r_e}{2\pi}\lambda^2 \sum_j n_j f_j(0) \qquad (4.1)$$

where r_e is the classical electron radius, λ is wavelength of light, n_j is the atomic density of the atoms of type j, and $f_j(0) = f_{1j} + i f_{2j}$. An atomic scattering factor is indeed dependent on the scattering angle, but it is equal to the forward scattering factor if atoms scatter as dipoles (the wavelengths are long compared to the atomic dimension and/or the scattering angles are small). Thus in the region where restrictions for the forward scattering and the independent atom are valid, it is interchangeable between atomic scattering factors f_1, f_2 and optical constants δ, β for any elements and compounds. In the high-energy limit where incident photon energies are well above the highest binding energy of a material (the *K*-shell binding energy), but are not so high that relativity corrections become important, the forward atomic scattering factor approaches Z. However, the forward scattering factor approaches Z^* which is slightly reduced from Z when relativistic effects are taken into account. The difference between Z^* and Z is approximately equal to E_{total} / mc^2, where E_{total} is the total atomic binding energy.[42] The expression of Z^* as a function of Z is given in Ref. 36 as:

$$Z^* = Z - \left(\frac{Z}{82.5}\right)^{2.37}. \qquad (4.2)$$

The difference $Z - Z^*$ is significant only for the high-Z elements. When light passes through matter, its intensity is exponentially attenuated in the following manner

$$I = I_o \exp\left(\frac{-4\pi\beta x}{\lambda}\right), \qquad (4.3)$$

where λ is the wavelength of radiation, x is the thickness of the material and I_0 and I are the incident and transmitted intensities, respectively. The transmittance T of a material can be expressed in terms of β as:

$$T = \frac{I}{I_o} = \exp(\frac{-4\pi\beta x}{\lambda}). \qquad (4.4)$$

This relation implies that β may be obtained experimentally from transmittance measurements if the film thickness of the material under investigation can be accurately determined. The dispersive δ can be calculated through a mathematical relationship between δ and β, generally referred to as the Kramers-Kronig relations.[43-45] For various physical problems, for example damped electrical circuits, scattering, and index of refraction, these rules relate the real and imaginary parts of the physical response to a stimulus in a linear, stable, and causal system. The real and imaginary parts of the complex index of refraction are related by

$$\delta(E) = \frac{2}{\pi}\int_0^\infty \frac{E'\beta(E')}{E^2 - E'^2} dE', \qquad (4.5)$$

where $E = hc / \lambda$ is the photon energy. The integral nature of Eq. (4.5) requires complete knowledge of β over a semi-infinite energy range in order to determine δ at a single photon energy E. A program written in IDL was used in these calculations (See Appendix B). Once the optical constants δ, β versus energy are determined, a set of integral constraints may be applied to evaluate their accuracy. These constraints, known as "sum rules", arise by translating into frequency space the causality and dynamic laws of motion governing the temporal response of matter to an applied electromagnetic field.[46] "Partial"sum rules may be written in terms of the effective number of electrons N_{eff,A_k} in the atom contributing to the absorption/dispersion up to energy E as

$$N_{eff,A_k}(E) = Z^* - \frac{2m\varepsilon_o}{n^2\pi e^2\hbar^2}\int_E^\infty E' A_k(E')dE' \qquad , k = 1, 2, 3 \qquad (4.6)$$

where optical data A_k are represented in one of the following forms: $A_1 = \varepsilon_2$, $A_2 = 2\beta$, and $A_3 = Im\,(\varepsilon^{-1})$, $\varepsilon(E) = \tilde{n}^2 = \varepsilon_1(E) + i\varepsilon_2(E)$ is the complex dielectric function, and n is the atomic density of the material. In this theoretical framework the model of Lorentzian oscillators is used to describe the electrons bound to the atom, where each electron has a characteristic resonant energy and acts as a dipole radiator at all energies. The term "oscillator strength" is thus used to describe the quantity inside the integral of Eq. (4.6). The N_{eff,ε_2}, $N_{eff,\beta}$, and $N_{eff,\varepsilon^{-1}}$ are not exactly equivalent quantities as they account for different physical processes; ε_2 is associated with the rate of energy dissipation from an electromagnetic wave, β with the amplitude decrease of the wave, and $Im\,(\varepsilon^{-1})$ (known as the energy-loss function) with the energy lost by fast charged particles going through the medium. The sum rules are valid only in the case of non-overlapping energy bands, i. e: when the absorptive/dispersive processes occurring up to energy E are sufficiently isolated from processes taking place in all other spectral regions. If an accurate and self-consistent set of optical data A_k is used to calculate the oscillator strength**,** all three versions of sum rules result in $N_{eff,A_k}(E = 0) = 0$. A non-zero result for $N_{eff,A_k}(E = 0)$ i.e. missing or excess oscillator strength would indicate that there are flaws in the optical data set in some region of the spectrum. By plotting N_{eff,A_k} versus energy and noting the energy levels where characteristic absorptions occur, it may be possible to identify the specific spectral regions where deficiencies exist in the optical values. Starting at zero for $E = 0$, the three sums increase monotonically, but on a different path until the onset of the lowest core level absorption where the three sums draw together and asymptotically approach Z^* at infinity. For intermediate values of E, the three sums generally do not coincide. Thus for any given material the sum rules are useful as guidelines for the

evaluation of data subsets and the construction of meaningful composite data sets covering the entire spectrum. Later in this chapter, the sum rules will be used to test a new set of optical data for both yttrium and molybdenum.

4.3 Experimental Procedure

4.3.1 Sample Preparation

Yttrium and molybdenum films were fabricated using the UHV deposition-reflectometer system described in Section 2.1. Base pressure in the deposition chamber was $2x10^{-9}$ Torr after three days bakeout at 130°C and maintained at 2.0 mTorr with 40 sccm flow of argon (99.999%) during deposition. Yttrium (99.5% from ACI Alloys, San Jose, CA) and molybdenum (99.99% from Angstrom Sciences Inc., Duquesne, PA) sputtering sources were operated at dc powers of 50 W, and the deposition rates under these conditions were 0.086 and 0.048 nm/sec, respectively.

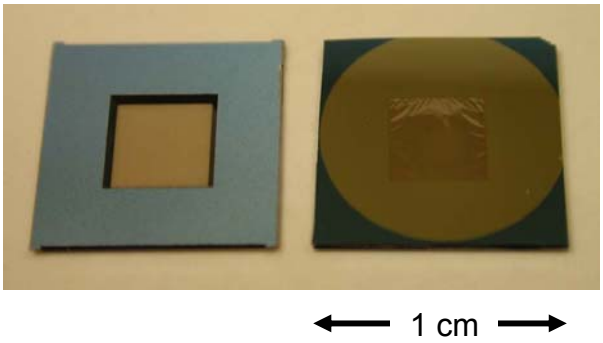

Figure 4.1. $Si_{10}N_{11}$ supporting membrane before (left) and after (right) yttrium film deposition.

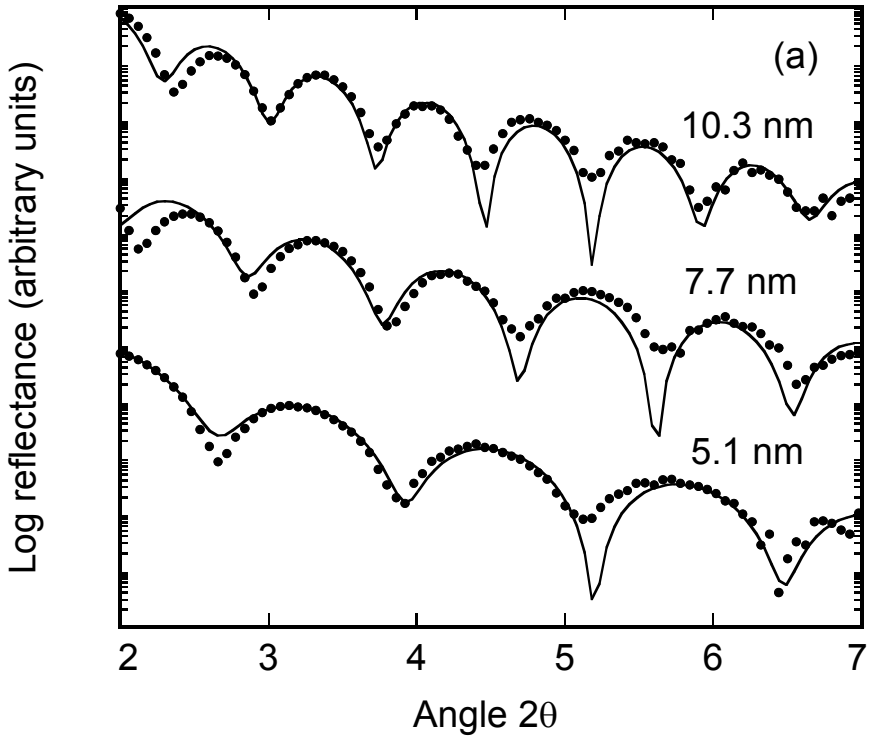

Figure 4.2. X-ray diffraction results from three yttrium films measured at copper K_α energy. The solid lines are fits to the data and were used to determine the yttrium film thickness.

Each yttrium or molybdenum film was magnetron-sputtered on a 5 x 5 mm^2 silicon nitride membrane (Fig. 4.1), fabricated by means of low-pressure chemical vapor deposition (LPCVD). The membrane fabrication involved 111 sccm of $Si_2Cl_2H_2$ (dichlorosilane) flow and 30 sccm of NH_3 (ammonia) flow at a temperature of 800° C and a pressure of 300 mTorr. The membrane deposition rate under this condition was 5 nm/min. The stoichiometry of the resulting membranes was $Si_{10}N_{11}$ with a density of 3.4 g/cm^3 and a thickness of 100±10 nm. As is going to be explained in Section 4.4, the contribution of the silicon nitride to the overall transmittance of the $Y/Si_{10}N_{11}$ or $Mo/Si_{10}N_{11}$ samples is normalized out in the measurements. Therefore, the 20%

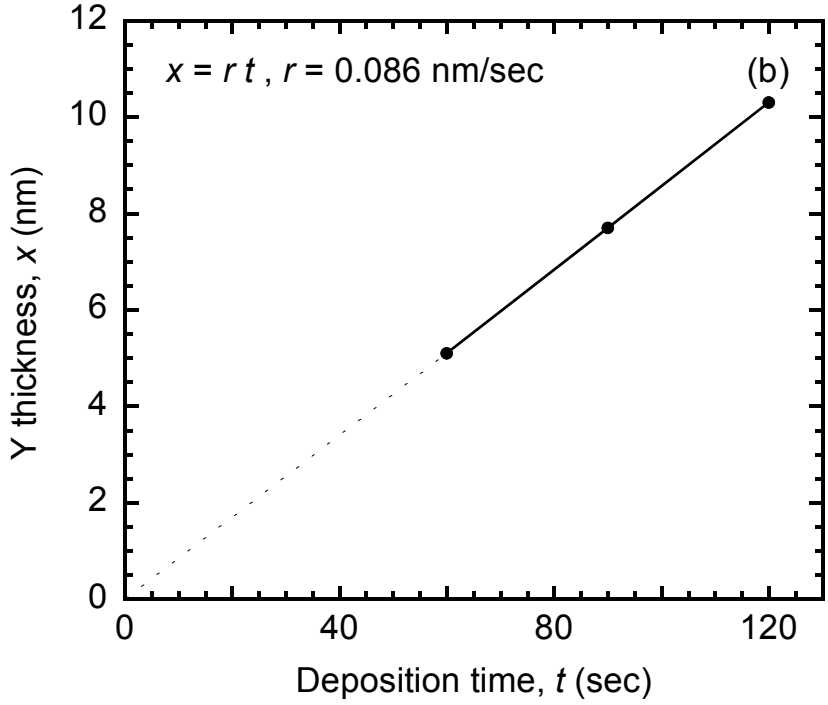

Figure 4.3. The yttrium sputtering deposition rate is determined using the three experimental thickness results shown in Fig. 4.2.

uncertainty in knowledge of the silicon nitride thickness does not ultimately affect the accuracy of the measured refractive index of yttrium and molybdenum.

The reliability of the transmittance method depends strongly on accurate knowledge of the film thickness and density of the material under investigation. In this study, the film thickness and density were determined using two independent methods. The deposition rate of yttrium and molybdenum was first determined by fitting the x-ray diffraction data as described in Section 2.2. Examples of reflectance versus diffraction angle of three yttrium films are plotted in Fig. 4.2. The data were fitted using the optical constants obtained from Ref. 34**.** The fitting parameters include the yttrium film thickness and the roughness of both silicon substrate and yttrium surface expressed in the form of

the Debye Waller factor (See Appendix A). Yttrium was assumed to have bulk density in the fitting calculations, given that the refractive index is relatively insensitive to small density variations at short wavelengths. The slope of the fitted thickness versus deposition time yields the deposition rate as is illustrated in Fig. 4.3. Based on this rate, any yttrium film thickness can be calculated from its known deposition time. Yttrium thickness determined in this manner is accurate to within ±2 nm. Although the minimum thickness that may be reliably determined using this method is limited by the nonlinearity of the deposition rate at very short deposition times, all yttrium films used in this study were well above the minimum thickness threshold.

Rutherford backscattering spectrometry (RBS) was used for determination of yttrium density. This test proved to be critical in this work due to difficulties encountered in obtaining a high-purity yttrium target. Prior to obtaining the yttrium target used in this study, two other targets from two different companies were tested (See details in Section 5.3.2). Both targets were dismissed as unacceptable for fabrication of pure yttrium samples due to high oxygen content detected in the films. On the other hand, the RBS-analyzed yttrium film from the third target that was eventually selected for this work contained an undetectable amount of oxygen (<3%), even though the film was left in air for several days before characterization. The aforementioned results show that yttrium films made from a pure target are extremely stable against oxidation. This conclusion is contradicting previous reports that yttrium oxidized readily[47] which could be a result of different deposition conditions or impurities included in the source material. Regarding contaminants other than oxygen, RBS analysis on yttrium films from the selected target showed atomic concentrations of 0.5% argon and 0.1% tungsten. The presence of argon

in the film is from the argon process gas used during the deposition (See Section 2.1). The negligible amount of tungsten is attributed to the tungsten filament used during target fabrication. An yttrium density of 4.43±0.18 g/cm^3, relatively close to the bulk density of 4.457 g/cm^3, was inferred from this method.

For molybdenum, the deposition rate of 0.048 nm/sec was determined using the same method as yttrium. The accuracy of the molybdenum thickness determined using this rate is ±1 nm. There was no attempt to verify the density (purity) of molybdenum because most magnetron-sputtered molybdenum films studied by several authors have density values which were very close to the bulk value (10.22 g/cm^3). Also, molybdenum targets have been used extensively so that the target purity and density are well calibrated by their manufacturers. Therefore, the molybdenum film density was assumed to be the same as bulk density throughout this study.

4.3.2 Transmittance Measurement Setup

Two instrumental setups for the transmittance measurements in this work are:

(a) The EUV and soft x-ray reflectometer of beamline 6.3.2 of the Advanced Light Sources, Lawrence Berkeley National Laboratory (LBNL) described in Section 2.3. Three yttrium films of 30, 52, and 90 nm thicknesses were fabricated on silicon nitride membranes. The exposure of yttrium films during transportation would have negligible effect regarding contamination based on RBS results as mentioned previously. Nonetheless, the samples were stored in a dessicator after deposition and transported to LBNL. Transmittance measurements on yttrium samples were performed in the 50-1300 eV energy region in 1.0 eV steps except for the energy regions around absorption edges where steps as small as 0.2 eV were used to better resolve the fine structures.

(b) The UHV deposition-reflectometer system described in Section 2.1. This system was attached to the back of the same reflectometer of beamline 6.3.2, thus all measurements for molybdenum films were done *in situ* without any exposure of samples to air. The transmittance measurements were performed on three molybdenum films of 36, 54, and 72 nm thicknesses in the 50-1300 eV energy range.

4.4 Results and Discussion

4.4.1 Yttrium

Transmittance versus energy measurements were performed on each of the three silicon nitride membranes that were used as substrates for the 30, 52, and 90-nm-thick yttrium films, respectively. Transmittance was also repeatedly measured after yttrium film deposition on each of the three samples. Fig. 4.4 illustrates the procedure applied in order to obtain pure yttrium transmittance. The advantage of this method is that the contribution of the membrane is normalized out in the transmittance results. Therefore any uncertainty in thickness, density, and composition of the membrane substrates did not ultimately affect the absorption results for yttrium. The yttrium transmittance results are plotted in Fig. 4.5. Fine structures due to the yttrium-$M_{4,5}$ edges (155.8 eV) and yttrium-$M_{2,3}$ edges (298.8 eV) are clearly resolved for the first time in the literature on this material. There is no evidence of any contaminants such as oxygen, nitrogen or carbon apparent in the transmittance spectra of the three yttrium films, which is in good agreement with the RBS results.

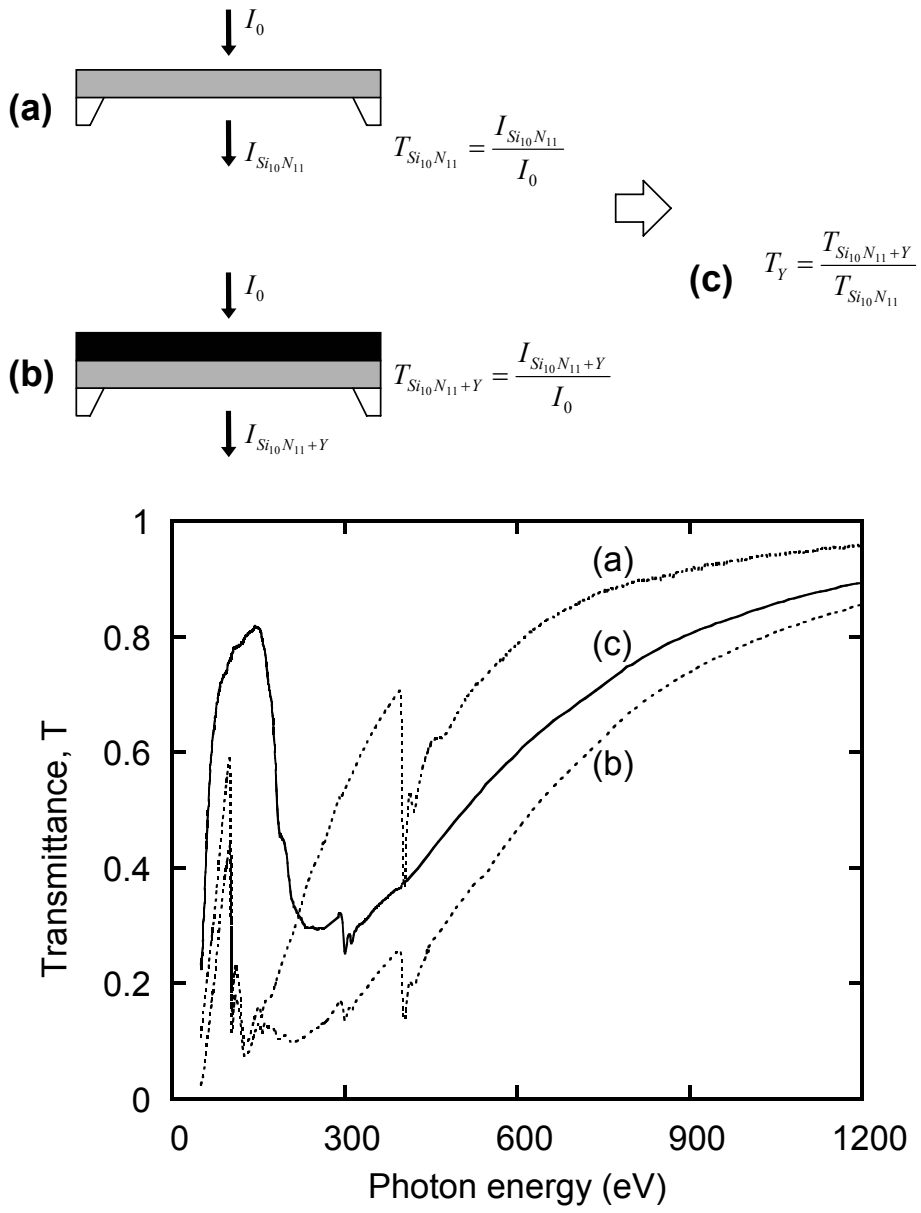

Figure 4.4. Top: Schematic diagram of the method used to obtain the transmittance of pure yttrium films. Bottom: Measured transmittance versus photon energy of: (a) a silicon nitride membrane (b) a silicon nitride membrane with a 90-nm-thick yttrium film (c) a 90-nm-thick yttrium film, obtained from the measurements in (a) and (b) as is explained in the diagram on the top. The silicon $L_{2,3}$-edge (99.8 eV) and nitrogen K_1-edge (409.9 eV) edges can be distinguished in (a), (b) due to the constituents of the membrane. The yttrium $M_{4,5}$ (155.8 eV) and yttrium $M_{2,3}$ (298.8 eV) edge features are present in (b), (c).

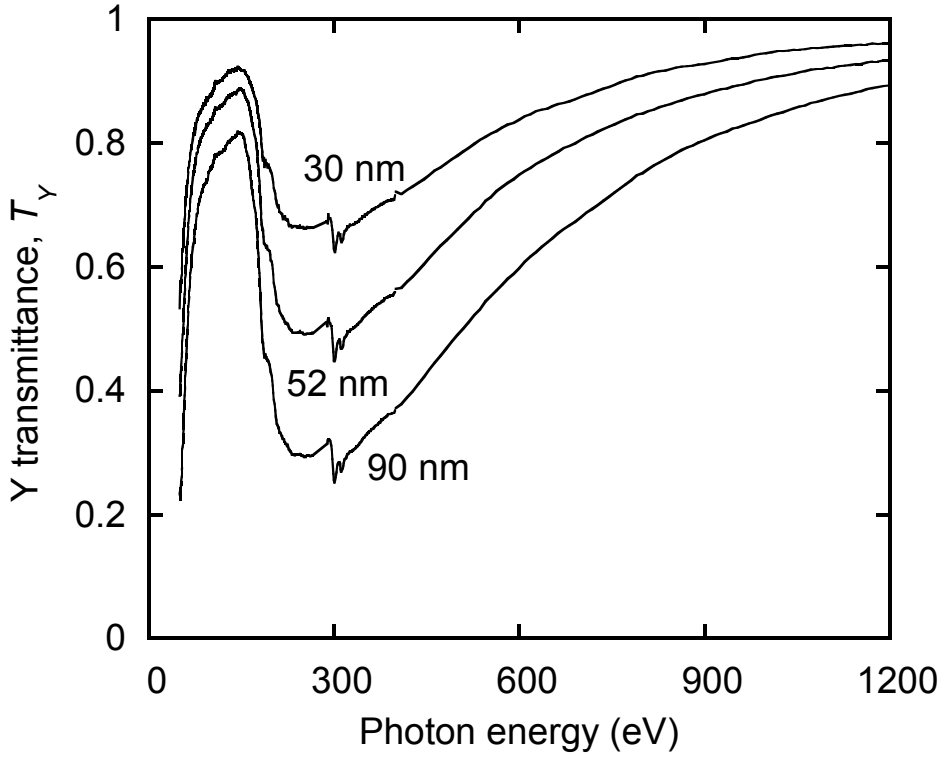

Figure 4.5. Transmittance versus photon energy obtained from 30, 52, and 90-nm-thick yttrium films.

Base on the transmittance results from the 30, 52, and 90-nm-thick yttrium films, the absorption β was determined using a linear regression of *ln* (*T*) versus *x*. As shown in Fig. 4.6, a straight line was formed and the slope of *ln* (*T*) was used to obtain β at each energy according to Eq. (4.4). In Fig. 4.7, the β values extracted from the measured transmittances in the 50-1300 eV region are plotted in comparison with the tabulated values derived from the atomic scattering factors, assuming bulk density of 4.457 g/cm^3. Significant differences between the measured and the tabulated results can be observed in the expanded plot from 50 eV to 250 eV, which includes the region of particular interest (100-155 eV) where Mo/Y multilayers operate. Fine structure is present in the measured β which was not resolved in the previously tabulated values.

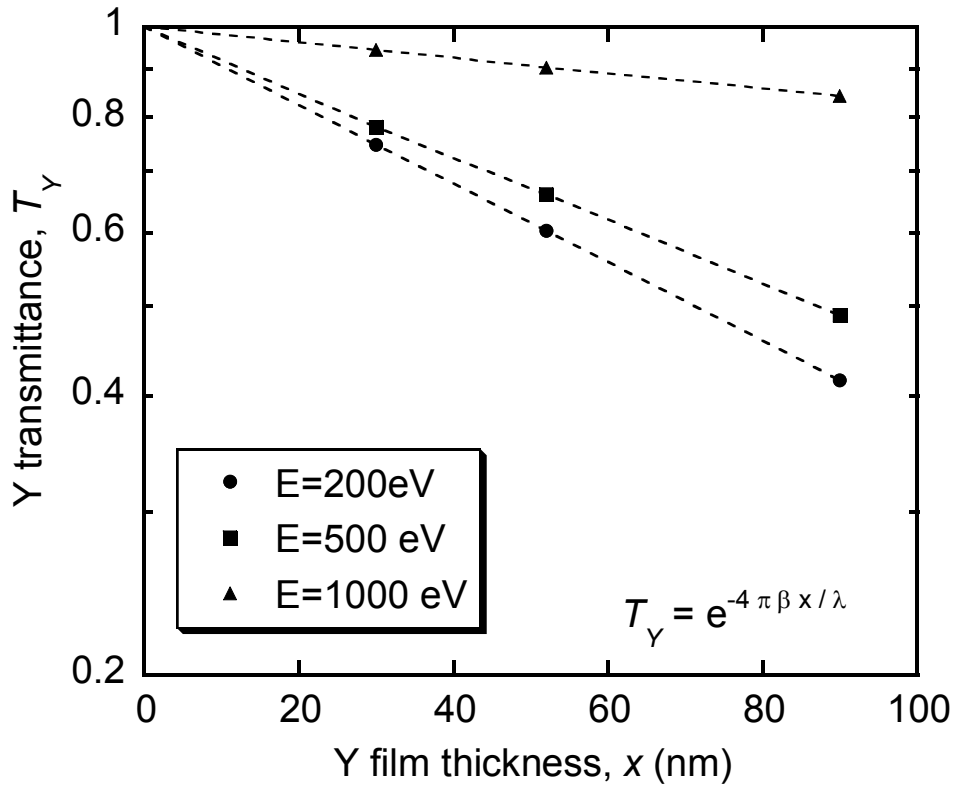

Figure 4.6. Transmittance (logarithmic axis) versus yttrium film thickness measured at 200, 500, and 1,000 eV for each of the 30, 52, and 90-nm-thick yttrium films. Transmittance curves at all energies result in $T_y = 1$ when extrapolated to zero film thickness, confirming the consistency between the film thickness determination and the experimental transmittance results.

To construct a set of absorption data covering the entire spectrum as needed for calculation of the dispersion δ according to Eq. (4.5), the present set of experimental β values were combined with data from other workers. In the 0.1-30 eV energy region, optical data have been available from Weaver *et al.* in terms of the polarized complex dielectric constants ε_s and ε_p.[48] Since polycrystalline yttrium structures (a hexagonal close-packed metal structure) have been observed from the TEM images of magnetron-sputtered yttrium films, the optical constant β is therefore dependent on the crystalline

orientation and was derived using the following expression: $\tilde{n}^2 = \varepsilon = (2\varepsilon_s + \varepsilon_p) / 3$. In the energy region 30-50 eV and above 1,300 eV, β values were again derived from the CXRO atomic scattering factors assuming bulk density. To verify the accuracy of the entire set of data for β, the partial sum rule $N_{eff,\beta}(E)$ of Eq. (4.6) was applied. This sum is particularly useful since it allows an independent accuracy check of β before δ calculation. The β-sum results are plotted in Fig. 4.8 in comparison with the β-sum results derived from the tabulated atomic scattering factors. At E = 0 eV, the new β values yield $N_{eff,\beta}(E) = 0$ while the tabulated values yield $N_{eff,\beta}(E) = 1.3$. As is discussed in Section 4.2, the nonzero result of $N_{eff,\beta}(E)$ at E = 0 indicates that there a systematic error in the tabulated yttrium absorption results in some spectral region. In this case, the integrated oscillator strength equivalent to 1.3 electrons is missing from the tabulated absorption values. The new measurements in the 50-1300 eV region appear to recover the 1.3-electron deficiency. After the validity of the new absorption data set was confirmed, δ was calculated using Kramers-Kronig integration of Eq. (4.5). Only slight differences between the new δ and the tabulated δ appear in the regions around yttrium absorption edges as can be seen in Fig. 4.9. The results of the ε_2- and $Im\ (\varepsilon^{-1})$-sum rules using the new set of yttrium data are also consistent, as shown in Fig. 4.10. The sum results plotted in Fig. 4.10 indicate that the new absorption measurements and dispersion calculations are consistent and result in an improved set of yttrium optical constants.

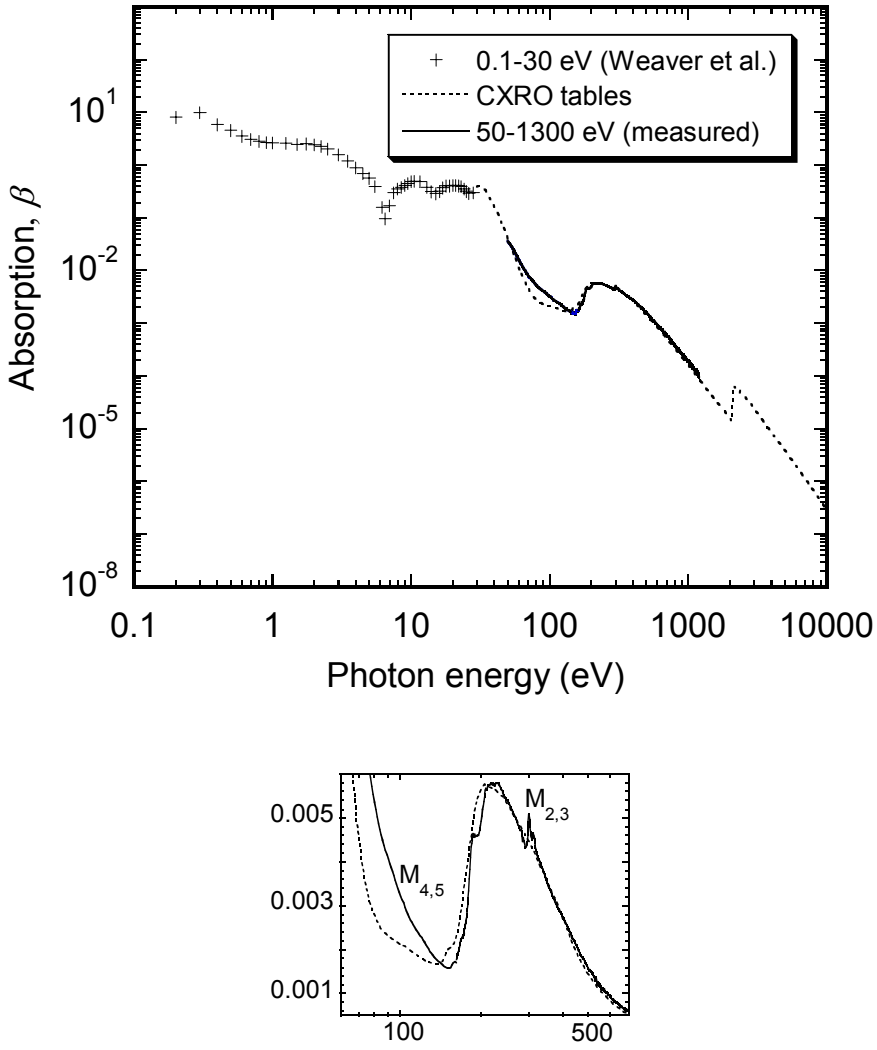

Figure 4.7. The absorption β of yttrium versus photon energy. The new measurement values shown as a solid curve are significantly different from the CXRO tables (dashed curve) in the yttrium $M_{2,3}$ and $M_{4,5}$ energy regions.

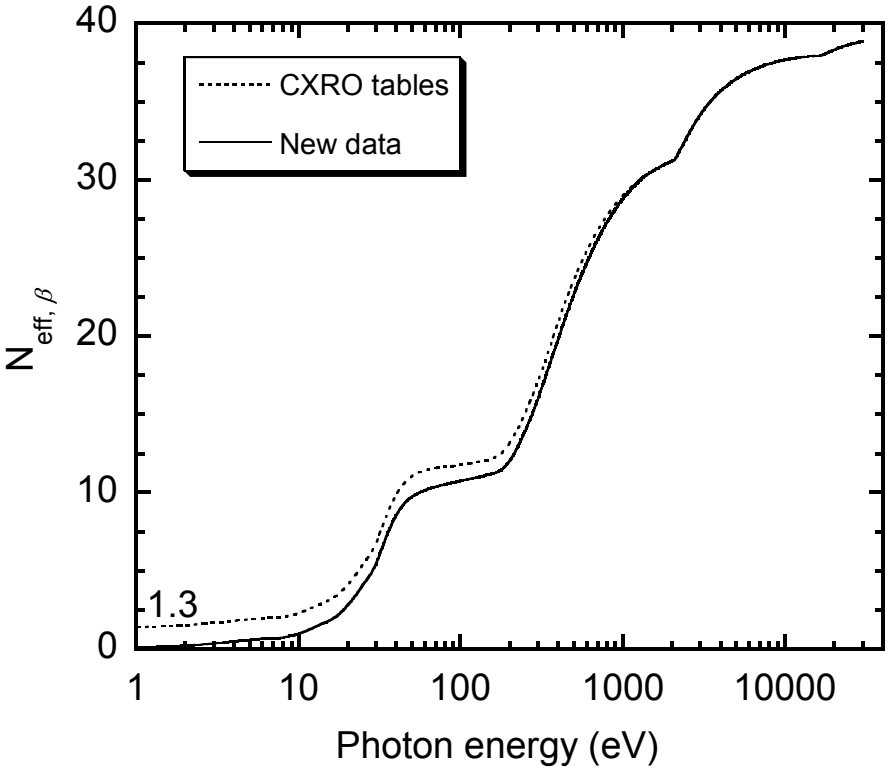

Figure 4.8. The β-sum rule is computed using (i) the new yttrium absorption data (solid curve) and (ii) the data from the CXRO tables. A 1.3-electron deficiency in the tabulated values is recovered with the new results.

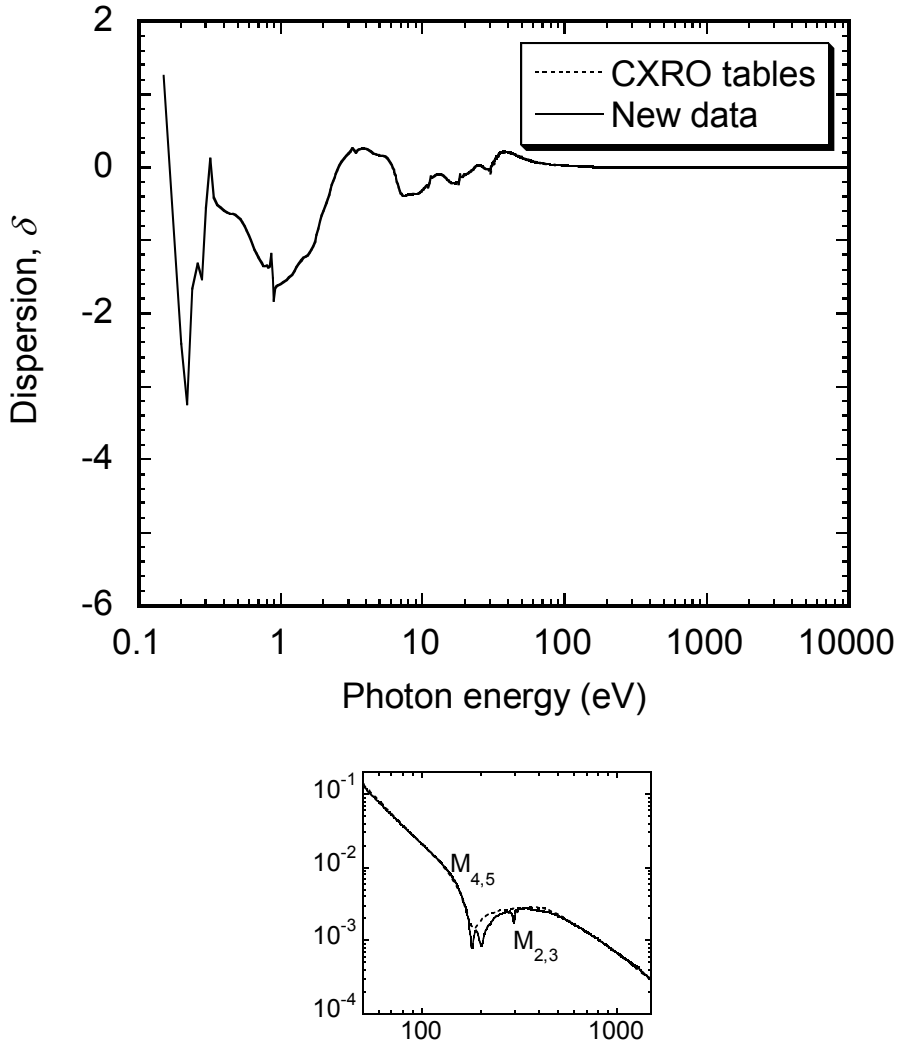

Figure 4.9. The yttrium dispersion coefficient δ is plotted versus photon energy. Only slight differences exist between the new results (solid curve) and the tabulated values (dash curve).

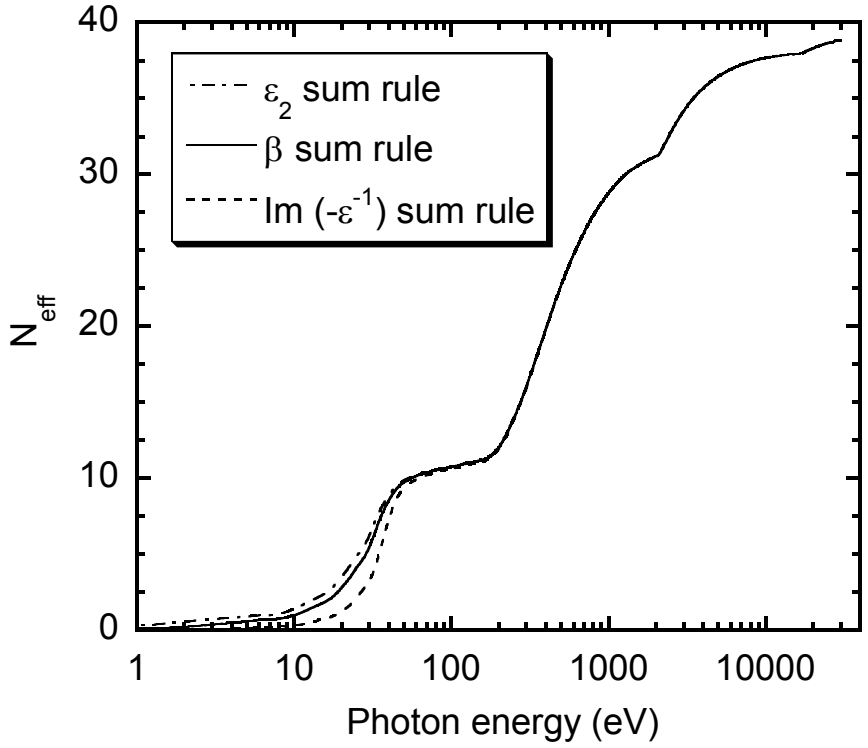

Figure 4.10. Sum rules are calculated with the new yttrium optical constants, expressed in terms of ε_2, β, and *Im* (ε^{-1}) are shown. The three sums rise monotonically with $N_{eff,\varepsilon_2} > N_{eff,\beta} > N_{eff,\varepsilon^{-1}}$, reaching the gradually rising plateaus where the onset of the lowest core-level of the absorption begin. The three sums show identical results from there on until they reach the value $N_{eff,\varepsilon_2} = N_{eff,\beta} = N_{eff,\varepsilon^{-1}} = Z^* = 38.83$ at $E \to \infty$.

4.4.2 Molybdenum

Transmittance versus photon energy of three molybdenum films was measured using the same technique as yttrium and is shown in Fig. 4.11. The most distinct features of the three transmittance curves are the dip at the molybdenum-$M_{4,5}$ edges (227.9 eV) and structures around molybdenum-$M_{2,3}$ edges (394.0 eV). Measured data in some regions including those in the 390-400 eV were excluded due to noisy signals in the measurements. Thus, the fine structure from the molybdenum-M_3 edge (394 eV) was missing as shown in the expanded plot. There is no evidence of any contaminants apparent in the transmittance spectra. Fig. 4.12 shows the experimental values of β obtained in this work in comparison with β derived from the CXRO atomic scattering factors, assuming bulk density of 10.22 g/cm^3. Slight different of β values (less than 2% relative) can be observed in the expanded plot which may be explained by the difference in film density or the error in thickness determination. Overall, our results are in excellent agreement with the CXRO values. These experimental values were combined with data from Juenker *et al*.[49] and data from the CXRO to obtain a semi-infinite data set ranged from 0 to 30,000 eV. δ was then calculated by the Kramers-Kronig formalism. The new δ values of molybdenum are also in excellent agreement with the CXRO as shown in Fig. 4.13.

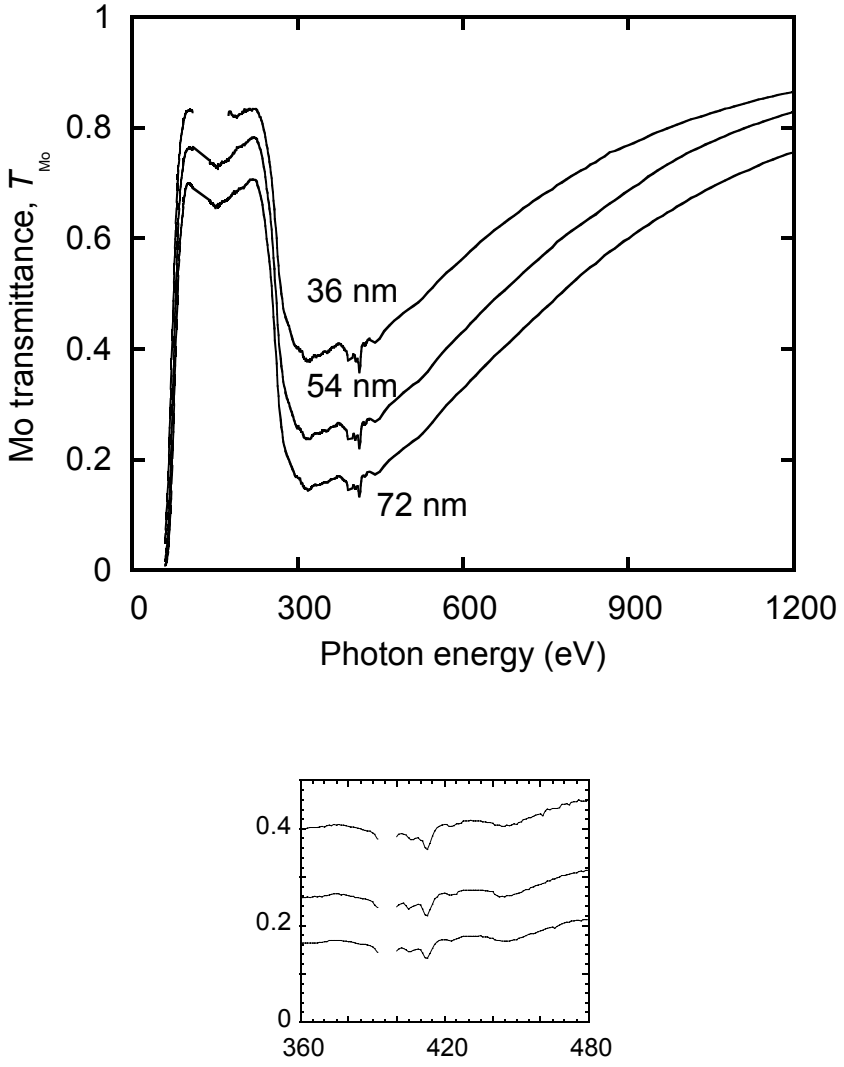

Figure 4.11. Transmittance versus photon energy obtained from 36, 54, and 74-nm-thick molybdenum films. Data from 390-400 eV region were removed due to noises during the measurements.

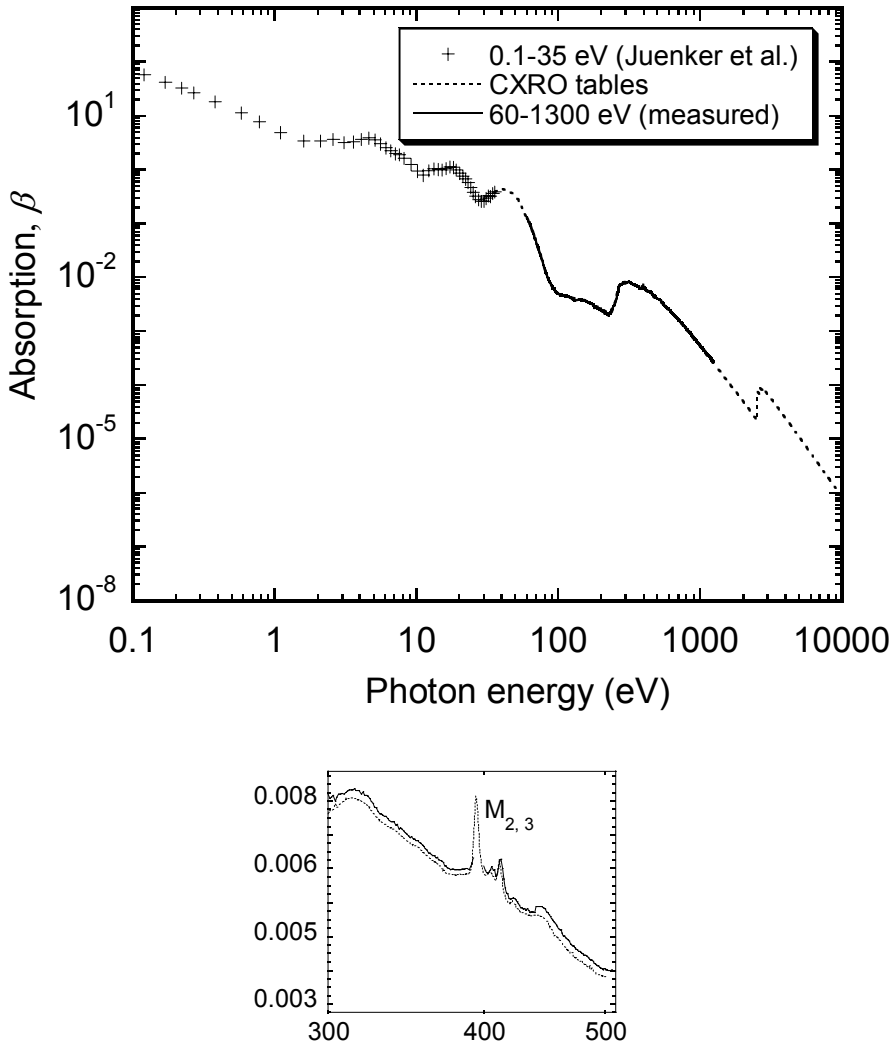

Figure 4.12. The absorption β of molybdenum versus photon energy. The measurement values, shown in solid curve, are in good agreement with those of the CXRO tables shown in dashed curve.

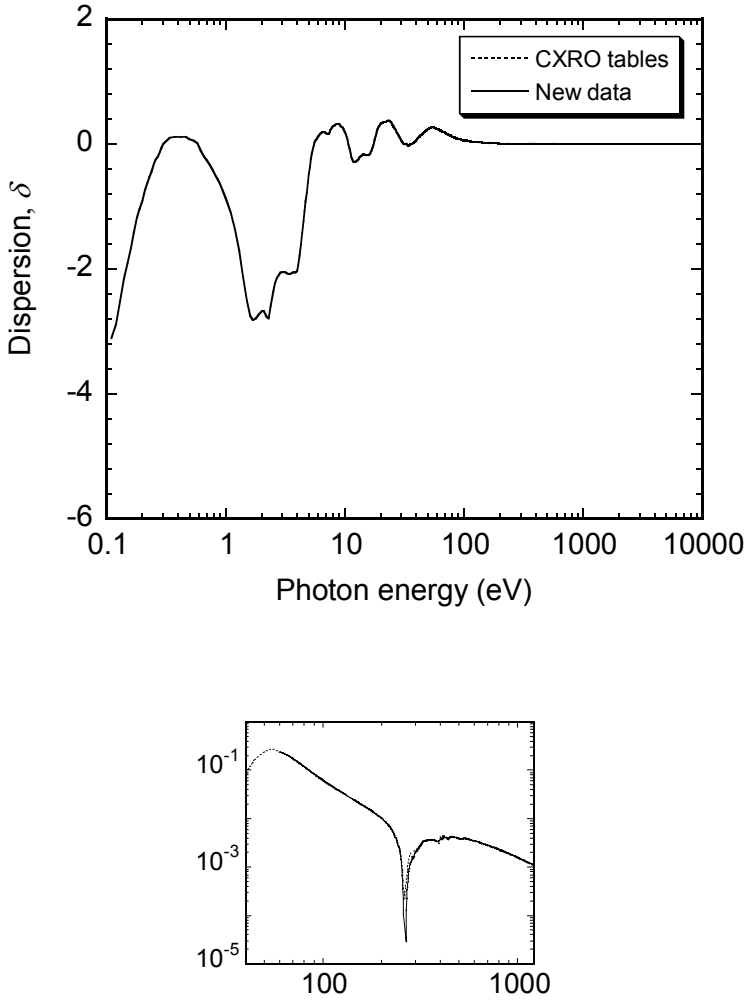

Figure 4.13. The dispersion δ of molybdenum versus photon energy. The new δ (solid curve) calculated from Kramers-Kronig integral exhibit excellent agreement and consistent with the CXRO values (dashed curve).

4.4.3 Modeling of Molybdenum/Yttrium Multilayers

A new set of optical constants β, δ of yttrium and molybdenum determined in this work was used to calculate the ideal reflectance of Mo/Y multilayers in the 95-155 eV region (13 nm down to 8 nm). The following parameters were applied: the number of bilayers N = 120, the thickness ratio of the absorber layer (molybdenum) to the period thickness Γ = 0.425. Perfectly smooth substrate surface and layer interfaces were assumed in these calculations. The reflectance results are plotted in comparison with

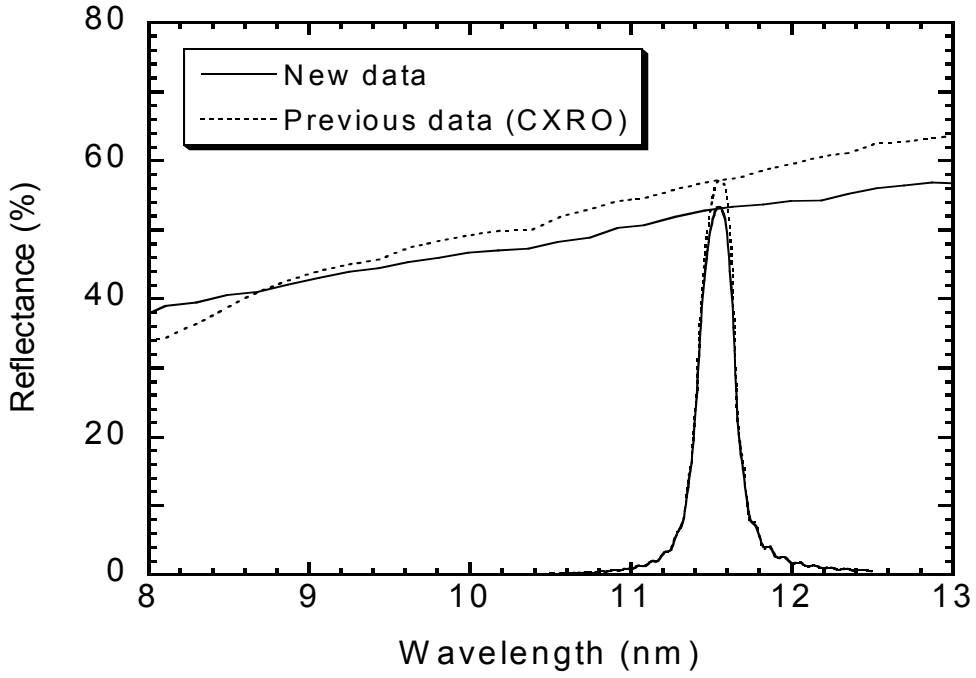

Figure 4.14. Normal-incidence reflectance of Mo/Y multilayer mirrors calculated using the IMD program with (i) new yttrium and molybdenum optical constants (solid curve) and (ii) the previously available optical constants from CXRO tables (dash curve). The calculated peak reflectance was shown in detail for a Mo/Y with 5.95 nm period.

those predicted using the previously available data in Fig. 4.14. At 11.5 nm wavelength for example, the difference between the reflectances obtained using the new and previous optical data is 4% and becomes even higher at longer wavelengths. Several parameters are often involved in the fitting of experimental reflectance data from multilayer optics operating in the EUV region. Using an accurate set of optical constants, when modeling these experimental results, is therefore critical in order to obtain meaningful values for fitted parameters such as surface oxide, interface roughness, and diffusion.

4.5 Conclusions

The experimental results on the refractive indices $\tilde{n} = 1 - \delta + i\beta$ of yttrium and molybdenum in the EUV/soft x-ray energy range are presented. The absorption β was obtained through transmission measurements on dc-magnetron sputtered films deposited under UHV conditions. For the case of yttrium, sum rule tests were applied on the absorption results and it was shown that the new set of yttrium data corrects deficiencies that existed in previously tabulated values. Absorption edge fine structure is also resolved for the first time in the yttrium $M_{4,5}$ (155.8 eV) and $M_{2,3}$ (298.8 eV) edge regions. The Kramers-Kronig calculations were used to obtain the dispersion δ. The new set of data for the refractive index of yttrium is more accurate and contains detailed fine structure information in the regions of the $M_{2,3}$ and $M_{4,5}$ absorption edges, where Y-based multilayer mirrors operate. For molybdenum, the new measured β and the calculated δ are in excellent agreement with the published CXRO values. The newly determined values for the refractive index of yttrium and the highly accurate refractive index of molybdenum are expected to lead to better modeling of the properties of yttrium- and molybdenum-based multilayer structures, operating in the EUV/soft x-ray energy range.

Chapter 5

Structural Characterization and Stability of Molybdenum/Yttrium Multilayer Mirrors

5.1 Introduction

Mo/Y has become one of the most promising material pairs for multilayers operating in the 8-12 nm wavelength region due to its high and relatively stable reflectance.[32] The maximum achievable reflectances reported by Montcalm *et al.* were 21.3%, 34.7%, and 46.1% at wavelengths of 7.9 nm, 9.7 nm, and 11.4 nm, respectively. This remarkable improvement of the multilayer reflectances compared to previous reports[22] is believed to be a result of fabricating the multilayers with an ultra high vacuum system and characterizing them *in situ* to prevent layer contamination and surface oxidation both during and after deposition. Though these results are encouraging, the reflectance of 34.7% at 9.7 nm, for example, is only 75% of the ideal reflectance calculated using the derived optical constants from the CXRO atomic scattering factors.[§] After using our newly measured molybdenum and yttrium optical constants discussed in Chapter 4, the experimental reflectance was still 77% of the ideal reflectance. The cause

[§] Ideal reflectance means that perfectly smooth substrate and interfaces, and a top layer with no contamination are assumed in the multilayer structure.

of this discrepancy will be studied in this Chapter. Montcalm *et al.* proposed that the main causes were interface imperfections, e.g. roughness, and/or interdiffusion. However, no experimental work was done to examine his hypothesis. A better understanding of Mo/Y structural properties would lead to an improved reflectance closer to the ideal value.

In addition to understanding the structure of the as-deposited Mo/Y multilayers, one would also like to know their stability. The study by Montcalm *et al.* showed approximately 10% relative loss in reflectance within one week after deposition. The multilayers were stored in air and the reflectance loss was attributed to the surface contamination and/or oxidation. The reflectance loss was more dramatic (16% relative loss) in the multilayers terminated with yttrium. Therefore it was concluded that Mo/Y multilayers terminated with molybdenum were more stable than the ones terminated with yttrium. However, the measurements done seven days after the deposition by Montcalm *et al.* were too short to truly test the lifetime of Mo/Y multilayers. Hence, further studies are required to validate their long term reflectance and structural stability. Moreover, it is desirable to develop a protection layer that can prevent reflectance decrease due to surface oxidation.

Thermal stability of these multilayers is also of interest because of their potential use as reflective coatings on gratings for high-resolution spectroscopy (See Chapter 6) that might expose them either to high temperatures for short periods of time during the launch or for extended periods of time during observations. There have been several studies investigating the effect of annealing on Mo/Y multilayers.[51,52] However, the focus of these studies was mainly the existence of solid-state amorphization i.e. the formation

of amorphous alloy from metallic molybdenum and yttrium layers. No previous work has been done on the thermal stability of Mo/Y multilayers. Several other multilayer systems have been studied for their thermal stability. For example, W/C[53,54] and Co/C[55] show an enhancement of grazing-incidence reflectance after annealing at any temperature below 400°C. The increase in reflectance in the W/C system is believed to result from improved lateral uniformity in the layers and/or sharper concentration gradients across the interfaces.[56] For Co/C, the back-interdiffusion of supersaturated Co-C alloy after annealing leads to an increase in the composition gradient at the interfaces and in multilayer reflectance as a whole. Mo/Si shows a significant degradation of both the grazing- and the normal-incidence reflectance at temperatures above 200° C.[57] In contrast to W/C and Co/C, the primary mechanism responsible for reflectance drops in Mo/Si multilayers at elevated temperatures is an increase in the silicide interlayer thickness along with an increase in the roughness associated with silicide crystallites. All the aforementioned results demonstrate that annealing effects are dependent on the microstructure of the multilayer materials and thus can be different for different multilayer systems. As a result it is important to determine the microstructure of Mo/Y multilayers in order to study any structural effects at elevated temperatures.

In this work, the structures of Mo/Y multilayers were studied in detail using small- and large-angle x-ray diffraction (XRD), transmission electron microscopy (TEM), and atomic force microscopy (AFM). These techniques enabled correlation of the multilayer microstructure with the EUV normal-incidence reflectance measurements. Lifetime stability of Mo/Y multilayers with various capping layers was also studied.

Multilayers that underwent thermal annealing were examined for any structural changes using XRD and TEM, and for reflectance changes using EUV reflectance measurements.

5.2 Multilayer Deposition

Mo/Y multilayers were fabricated using the UHV magnetron-sputtering deposition system described in Section 2.1. The base pressure in this cryogenic-pumped system was below $2x10^{-9}$ Torr prior to deposition. Ultra-high purity argon gas was used at a constant pressure of 2.0 mTorr during deposition. The operating powers for molybdenum and yttrium were 50 W. Substrates 1 x 1 cm^2 in size were cut from a polished single-crystal Si (100) wafer. Each multilayer sample consisted of 100 Mo/Y bilayers where the first layer was yttrium and the last layer was molybdenum. Unlike molybdenum, high-purity yttrium targets are not readily available. Therefore three yttrium targets quoted for 99.9% purity from three different companies were studied. The purity of the yttrium targets was tested on deposited films using Rutherford backscattering. All the samples were labeled *A*, *B*, and *C* corresponding to multilayers that were fabricated from yttrium targets of ACI Alloys (San Jose, CA), Plasmaterial Inc. (San Ramon, CA), and Research and PVD Materials Corp. (Wayne, NJ), respectively. A molybdenum target (99.999%) from Angstrom Science Inc. (Duquesne, PA) was used in all samples throughout this study.

5.3 Multilayer Characterizations

5.3.1 Deposition Rate Calibrations and EUV Reflectance Measurements

All the multilayers were designed to operate at a wavelength of 9.4 nm. To obtain wavelength calibration for each target, a set of multilayers of various thickness combinations was deposited on silicon wafer substrates. XRD measurements were

performed with the copper K_α (0.154 nm) source to determine the multilayer periods. The period thickness (Λ) can be calculated based on the modified Bragg's equation[25] using the measured angles of the m^{th}-order (m = 1, 2,…, 6) diffraction peaks. With known deposition times and period thicknesses, the deposition rates of molybdenum and yttrium were determined from the slope of thickness versus time. Due to interface formation, a parameter $\Delta\Lambda$ was included in a two-layer model, $\Lambda = d_{Si} + d_{Mo} + \Delta\Lambda$, where a positive $\Delta\Lambda$ value means expansion and a negative $\Delta\Lambda$ means contraction of the interlayer thickness (see detail in Section 2.2). In Mo/Y multilayers, the $\Delta\Lambda$ values were always negative and less than 0.1 nm, suggesting a small multilayer period contraction.

The EUV reflectance measurements were performed *ex situ* with the reflectometer at beamline 6.3.2 of the Advanced Light Source, LBNL. A detailed description of this beamline and the reflectance measurements is given in Section 2.4. The normal-incidence (3° off normal) reflectances obtained from three representative samples *A*, *B*, and *C* were 32.6% at 9.27 nm, 38.4% at 9.48 nm, and 29.6% at 9.46, respectively (Fig. 5.1). The slight differences among the peak wavelengths of these three multilayers were mainly due to the accuracy limitations of their deposition rate calibrations. However, the significant differences in reflectances of the three multilayers could not be explained by their slightly different wavelengths. Since all three multilayers were fabricated using the same design parameters and the same deposition conditions, the most likely cause for the reflectance differences was identified in the quality of yttrium targets.

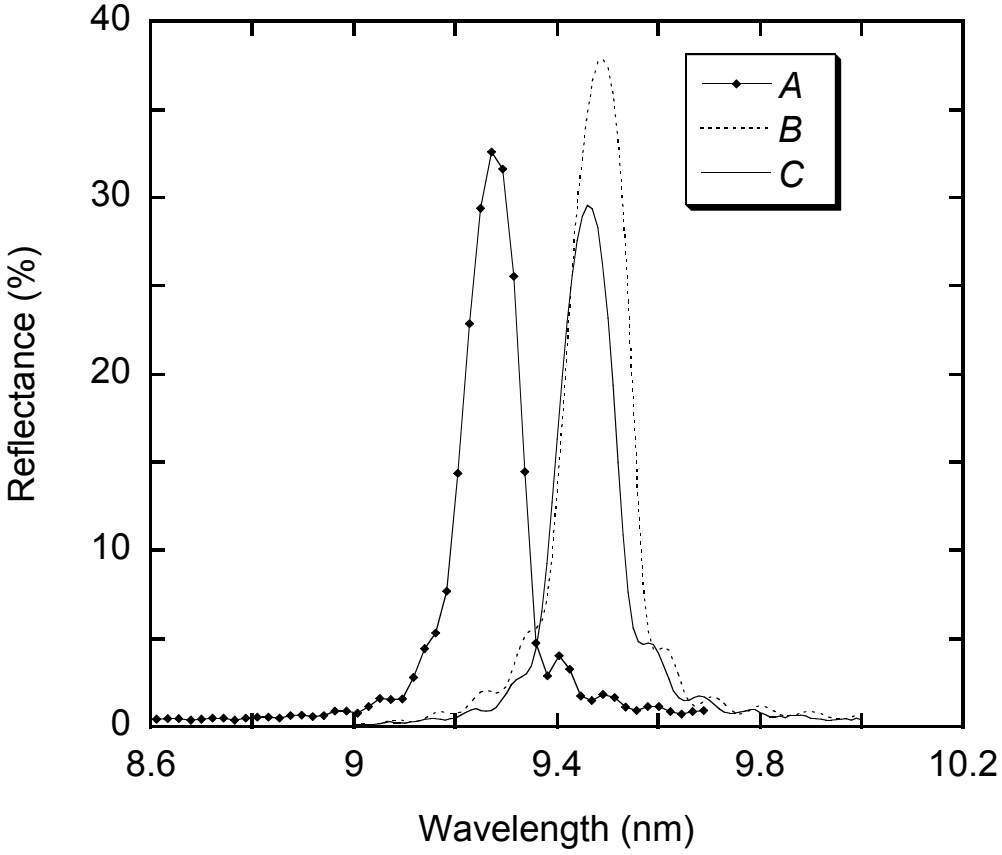

Figure 5.1. The EUV normal-incidence (3°) reflectance of three representative multilayers *A*, *B*, and *C*, which were fabricated from yttrium targets of ACI Alloys, Plasmaterial Inc., and Research and PVD Materials Corp., respectively

5.3.2 Yttrium Targets and Films Purity

To verify the aforementioned hypothesis regarding the quality of these yttrium targets, RBS measurements were performed on three magnetron-sputtered yttrium films from targets *A*, *B*, and C. The films were bombarded with 2.3 MeV He^{++} ions and the energies of the backscattered ions, directly related to the depth and the mass of the target atoms, were measured at two different angles. The RBS results revealed <3 %, 25 ± 3 % and 39 ± 3 % atomic oxygen content in the yttrium films from targets *A*, *B*, and *C*, respectively. Since all three films were deposited under the same conditions and were left

in air for several days before characterization, it was concluded that the amount of oxygen present in the yttrium films from targets *B* and *C* was incorporated in the targets and was not a result of film oxidation during or after deposition. The vacuum hot pressing method applied in the fabrication of the first two targets may explain the high amount of oxygen assimilated in these targets. This method is not as efficient to remove oxygen as the vacuum arc melting[58] applied in the fabrication of target *A*. In addition to oxygen, it was found that argon, tantalum, and tungsten in a total amount of less than 1% were present in all three yttrium films. The presence of argon was attributed to the argon processing gas used during film deposition. The presence of tantalum and tungsten was attributed to the target fabrication processes. The yttrium film densities were determined at 4.430 g/cm^3, 4.402 g/cm^3, and 4.088 (with ± 0.18 g/cm^3 accuracy) for samples from targets *A*, *B*, and C, respectively.

The ideally predicted reflectance for the three multilayers *A*, *B*, and C was calculated with IMD software[59] using the RBS results for yttrium compositions (0%, 25%, and 39% oxygen) and densities. The following structure parameters were applied: the period thickness $\Lambda = 4.78$ nm, the number of bilayers $N = 100$, and the thickness ratio of the absorber layer (molybdenum) to the period thickness, $\Gamma = 0.425$. The calculated reflectances are plotted in Fig. 5.2. These theoretical calculations predict that the multilayer with more oxygen should have lower reflectance than the one with less oxygen, as would be expected due to increasing absorption with oxygen content. However, instead of a trend of increasing reflectance in the order *C*, *B*, *A* as predicted by theory, the previous measurements show an increasing trend in the following order: *C*, *A*, *B* (Fig. 5.1). It should be noted that the reflectance of sample *B* is in fact the highest

reflectance obtained to date from a Mo/Y multilayer for the wavelength around 9.4 nm. The highest reflectance multilayer, sample *B* which contains ~25% of oxygen, indicates that oxygen contamination is not the only quality factor for the reflectance performance of Mo/Y multilayers. In order to further investigate this issue, a series of characterizations using various methods were performed.

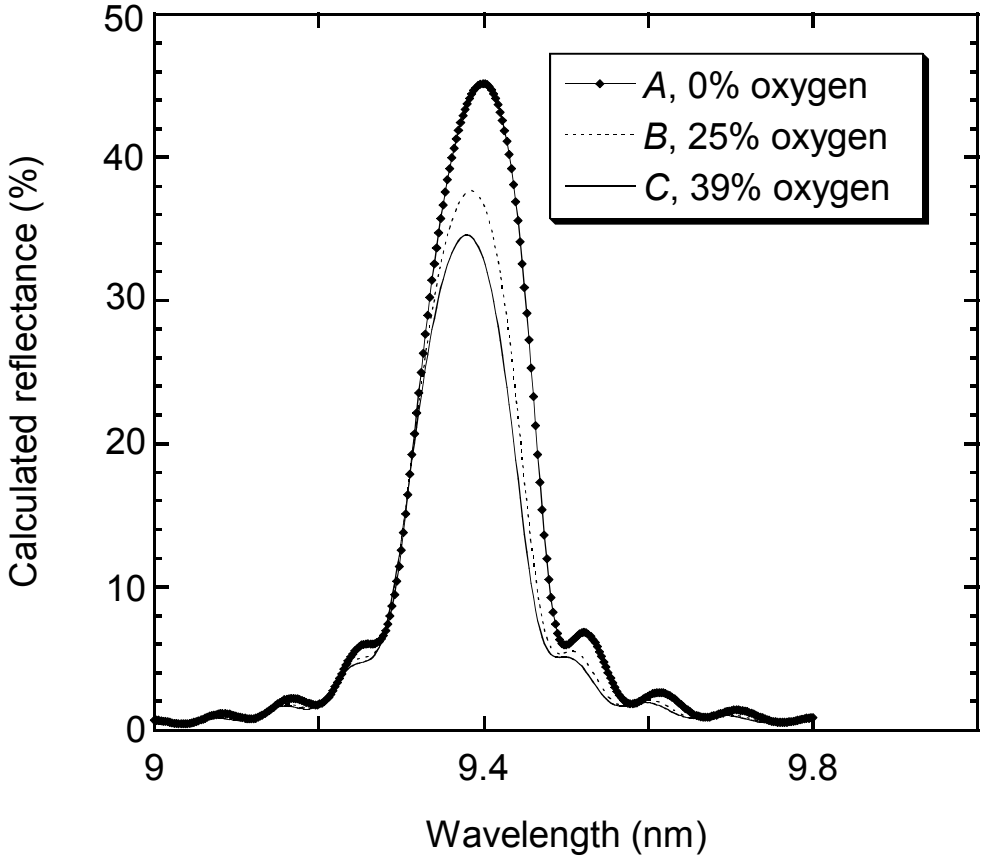

Figure 5.2. Calculated reflectances of three Mo/Y multilayers *A*, *B*, and *C* which have 0%, 25%, and 39% atomic oxygen content in their yttrium layers.

5.3.3 Small-Angle X-Ray Diffraction

The small-angle XRD spectra of multilayers *A*, *B*, and *C* are plotted in Fig. 5.3. All three samples exhibit a high-quality multilayer structure. A series of strong diffraction peaks indicates sharp interfaces between molybdenum and yttrium, in good

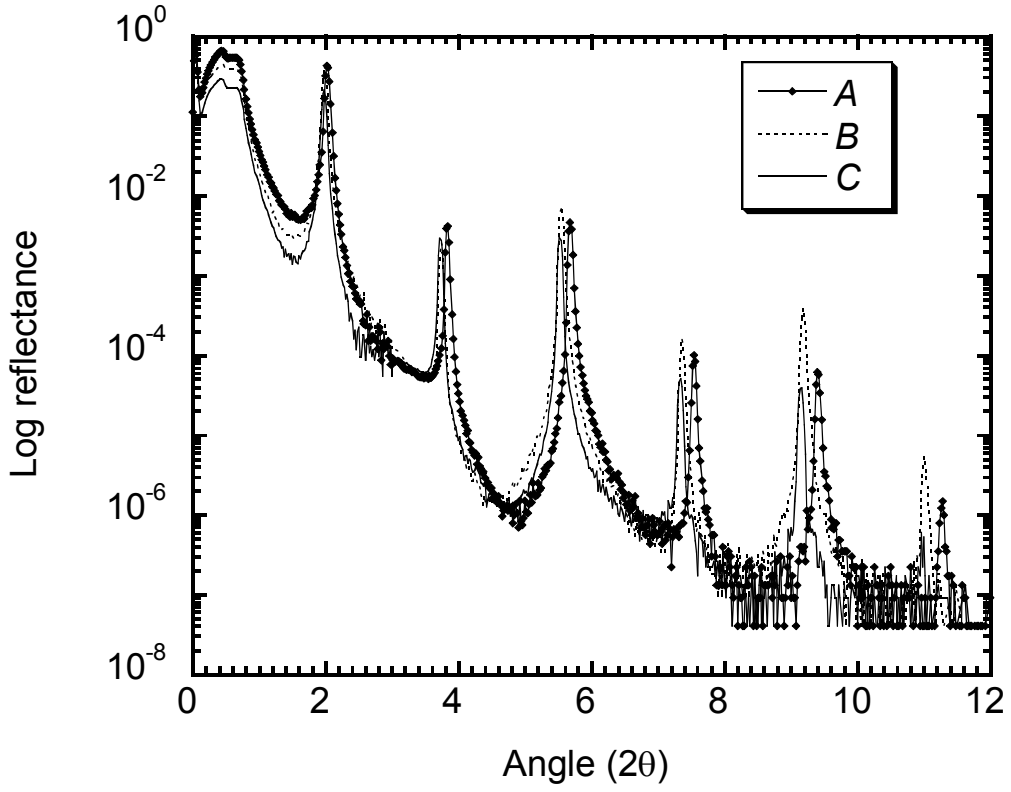

Figure 5.3. Specular reflectance versus incident angle of three representative Mo/Y multilayers *A* (< 3% oxygen), *B* (~25% oxygen), and *C* (~39% oxygen) showing many orders of Bragg reflections.

agreement with a small contraction mentioned previously. The periods of multilayers *A*, *B*, and *C* were 4.72 nm, 4.83 nm, and 4.85 nm, respectively. It is evident that the different amounts of oxygen present in the yttrium layers affect the reflectance performance of Mo/Y multilayers differently. At low incident angles, prior to the first order Bragg peak, the x-ray beam penetrates only a few topmost layers of the multilayer. The XRD

reflectance in *A* (< 3% oxygen) is higher than in *B* (~25% oxygen) and that of *B* is higher than in *C* (~39% oxygen) which is in good agreement with their optical properties. At high incident angles, where x-rays penetrate deeper into the sample, it appears that some structural modification occurred during the multilayer growth process so the overall reflectance performance of these samples follows the same trend (C, A, B) obtained at EUV wavelengths, as was discussed in Section 5.3.1.

Since any substantial interdiffusion on interfaces was already excluded, the only other parameter left that could affect the reflectance is the interface roughness. To study the interface roughness, "rocking scans" were performed on each sample around the first and the second order Bragg peaks by fixing the detector at an angle $2\theta = 2\theta_{Bragg}$ and scanning the sample angle θ symmetrically around θ_{Bragg}. The rocking curves can provide useful information about interface roughness. As shown in Fig. 5.4, scattering due to roughness is present in all samples since the substantial scattered intensities were observed around their specular peaks. The scattered intensity of sample *B* is lower than in *A* and that of *A* is lower than in *C* for both the first and second order Bragg peak. The rocking scan results show a trend of an increase in roughness in the order: *B*, *A*, *C*, which is consistent with EUV reflectance results. To determine the roughness values, the XRD spectra of these multilayers were fitted using an optimization program called GAXFIT which is based on a genetic algorithm.[60] In the fitting model for Mo/Y multilayers, each period was composed of only two layers: the pure yttrium and molybdenum layers, assuming the same roughness at both interfaces and no interdiffusion. Fig. 5.5 shows the best fits and the fitted parameters obtained for these samples where σ is the interface

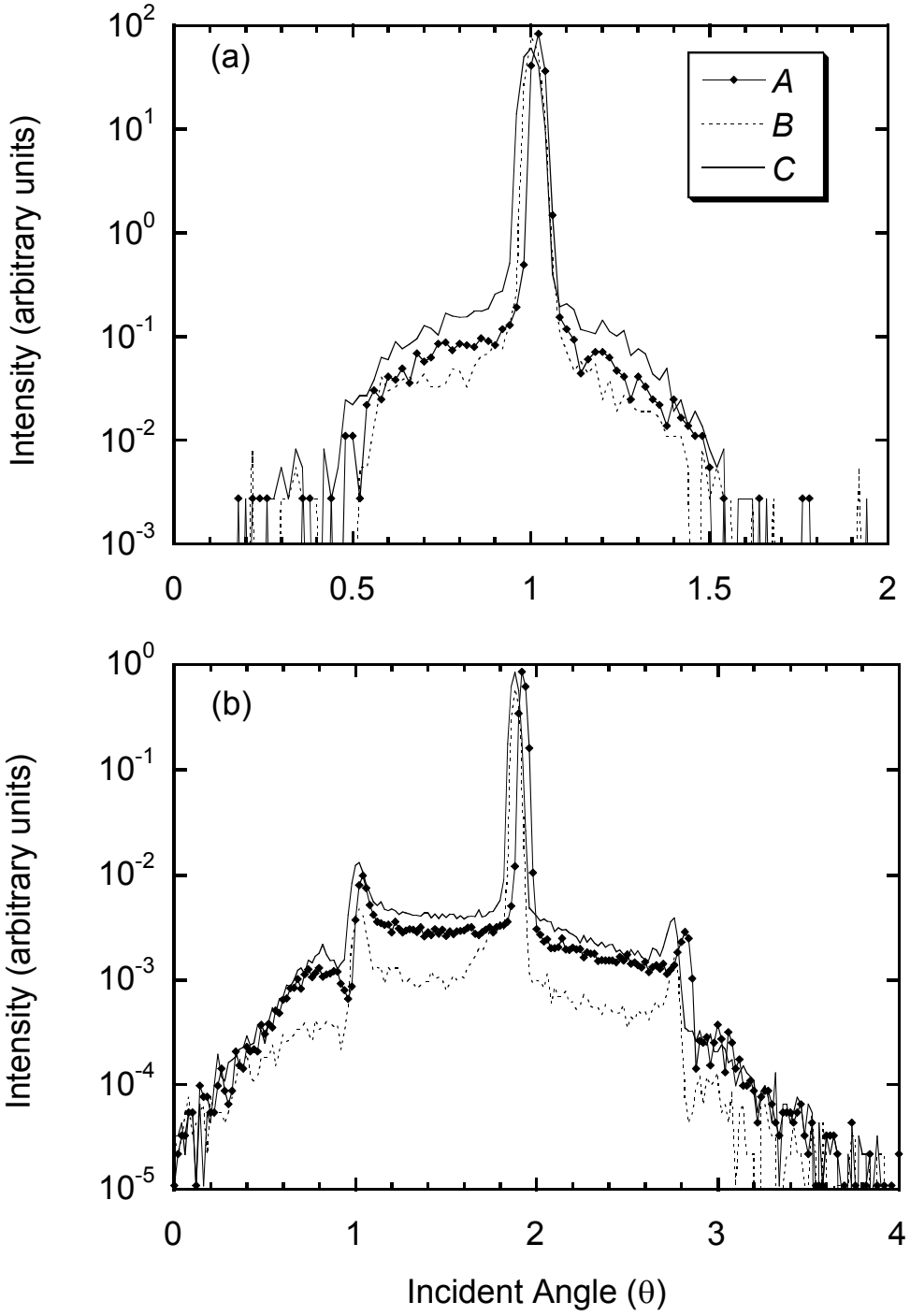

Figure 5.4. First- (a) and second-order (b) rocking curves of multilayers *A* (< 3% oxygen), *B* (~25% oxygen), and *C* (~39% oxygen) at x-ray copper K_α wavelength. The intensities away from the first and second order Bragg peaks drop because the input beam or the detector was shadowed by the sample.

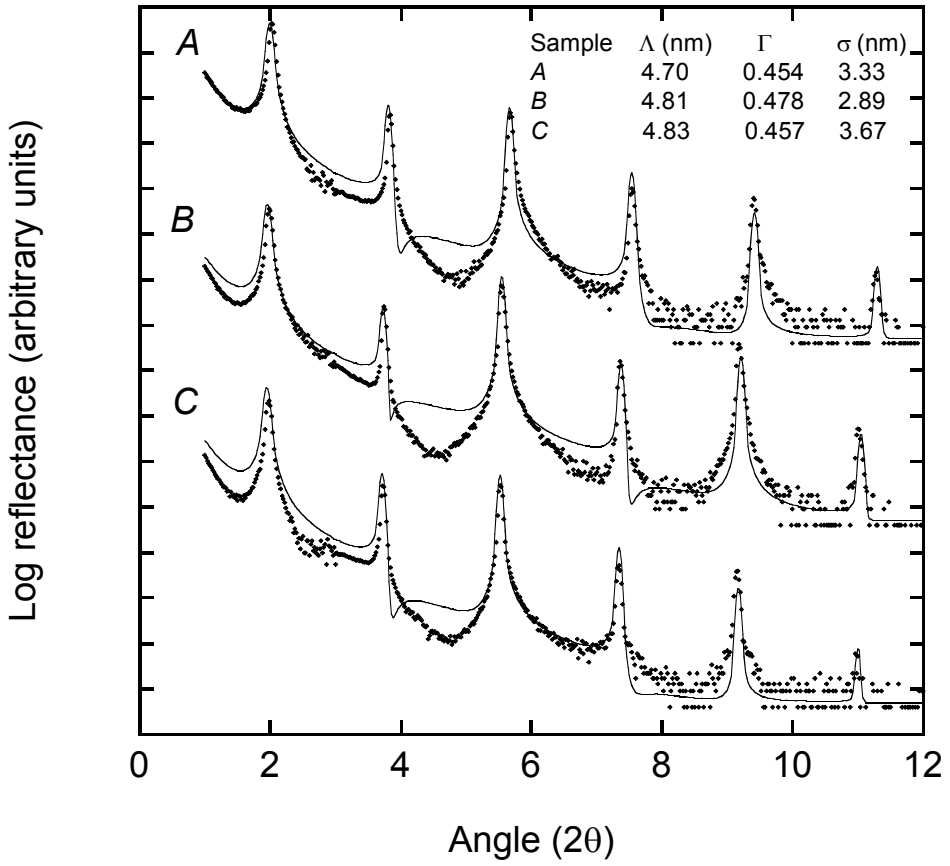

Figure 5.5. The best fits (line) to the XRD data of multilayer *A* (< 3% oxygen), *B* (~25% oxygen), and *C* (~39% oxygen) using GAXFIT.

roughness. The fitted results for interface roughness were 0.33 nm, 0.29 nm, and 0.37 nm for *A*, *B*, and *C*, respectively. These results are in good agreement with the trend of roughness predicted from the rocking scan data, where *B* showed the least amount of scattering. Other fitted parameters, e.g. Λ and Γ, were very close to the design values. Based on these results it was concluded that a Mo/Y multilayer made out of an yttrium target with ~25% atomic oxygen content has sharper and smoother interfaces and higher reflectance, as compared to a multilayer made out of a pure yttrium target.

5.3.4 Large-Angle X-Ray Diffraction

More XRD measurements were performed at larger incident angles to see if there are any other changes in crystalline structure or composition due to oxygen that could affect the roughness in these multilayers. It was found that it is important to do the large-angle XRD scans with and without the sample so that any diffraction peaks coming from the experimental setup can be identified and disregarded. Fig. 5.6 shows a comparison of the large-angle XRD spectra of these samples over the angular range of $2\theta = 10^{\circ}$ to 100°. Several broad peaks of polycrystalline materials were detected. To index all the peaks, all possible diffracting planes of yttrium, molybdenum, and their oxides have been surveyed based on the powder diffraction (PDF) data. This method includes all the diffraction peaks from a powder specimen with randomly oriented crystals. Only one prominent peak of yttrium at $2\theta = 32.35^{\circ}$ which corresponds to Y (101) and several other peaks that correspond to molybdenum, e.g. Mo (110) at $2\theta = 40.52^{\circ}$, Mo (200) at $2\theta = 58.61^{\circ}$, Mo (211) at $2\theta = 73.68^{\circ}$, and Mo (220) at $2\theta = 87.59^{\circ}$, were detected in all three samples. It appears that yttrium is strongly textured since yttrium crystallites are oriented mainly in the <101> direction. A significant shift toward lower angles of the Y (101) diffraction peak was noticed in sample *C*. This line shift may be due to either a uniform strain created by sufficiently high amount of oxygen atoms (~39%), which results in larger *d*-spacing (*d* increases from 0.276 nm to 0.292 nm) or due to Y_2O_3 formation or both. The change in the peak position from $2\theta = 32.35^{\circ}$ to $2\theta = 30.78^{\circ}$ in sample *C* as compared to sample *A* may actually be a result of two overlapping peaks of Y_2O_3 (222) at $2\theta = 29.15^{\circ}$ and Y (101) at $2\theta = 32.35^{\circ}$.

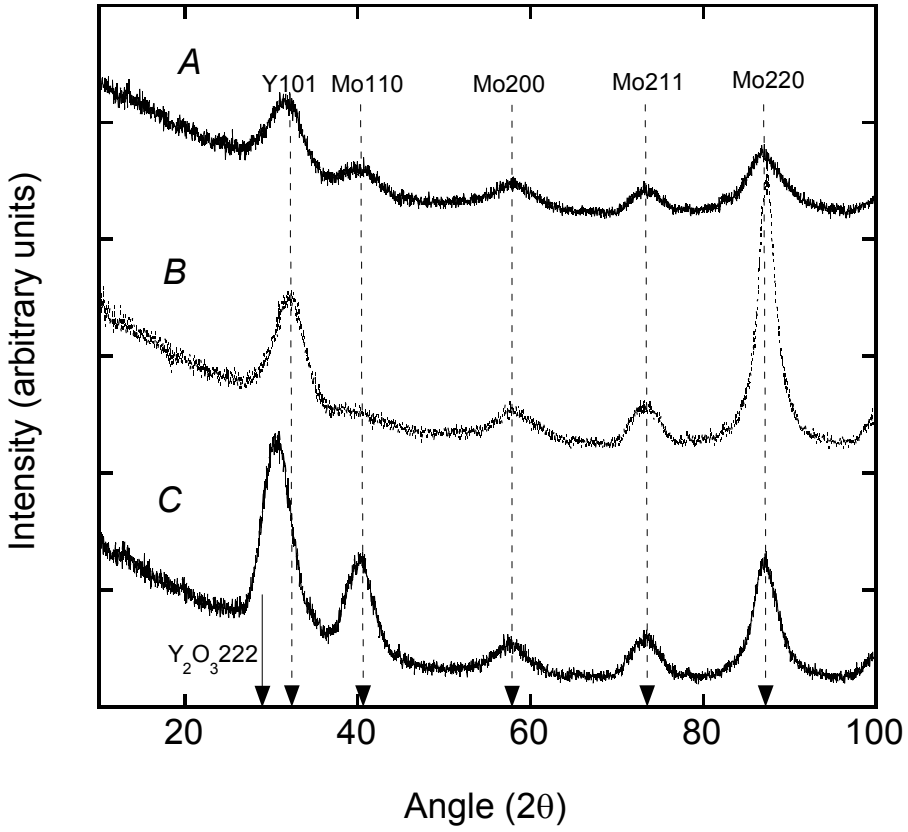

Figure 5.6. Comparison of large-angle XRD spectra of Mo/Y multilayer samples *A* (< 3% oxygen), *B* (~25% oxygen), and *C* (~39% oxygen). The *B* and *C* curves are displaced vertically by arbitrary amounts, for better viewing.

To estimate the minimum grain sizes of yttrium and molybdenum in the multilayer growth direction, the grain sizes were calculated using the measured peak widths based on the Scherrer formula:[24]

$$t = \frac{0.9\lambda}{b\cos\theta_B}, \qquad (5.1)$$

where t is the particle size in a direction perpendicular to the plane of Bragg reflection, b is the peak width measured in radians (in terms of 2θ) at the half of the maximum intensity, and θ_B is the Bragg peak angle. Using the above equation (5.1), the yttrium grain sizes are approximately 2.4±0.5 nm in all three samples. The grain size seems to be

correlated with the yttrium layer thickness of about 2.8 nm and it is likely that this is the main constraint of yttrium crystallite size in the growth direction. If yttrium in sample *C* (~39 % oxygen) is a combination of yttrium and yttrium oxide, it would be impossible to distinguish them since their grain sizes would still be the same in the multilayer growth direction. For the case of molybdenum, the highest peak intensities were always obtained from Mo (220) in these samples. PDF data indicate that if molybdenum crystallites had a completely random orientation, the maximum intensity would appear from the Mo (110) and not from the Mo (220). Therefore molybdenum in all three samples is definitely textured. The grain size of molybdenum crystallites was estimated using the peak widths of Mo (200) because the broadening effect due to the XRD instrument is smaller at lower incident angles and these peaks were clearly resolved in every sample. The average grain size is about 1.6±0.5 nm in all three samples where the molybdenum nominal thickness is 2.0 nm. These results suggest that having some oxygen in the yttrium layer, as is the case of sample *B*, does not significantly change the crystalline properties of yttrium and molybdenum in the multilayer growth direction. The ~25% atomic oxygen content may not be sufficient for yttrium to form an oxide but the oxygen atoms may be able to smooth out some roughness of the multilayer resulting in the high EUV reflectance (38.4%) that was measured for sample *B*. However, when the oxygen concentration is as high as in sample *C* (~39% oxygen), the yttrium microstructure changes either by increasing its *d*-spacing or by forming Y_2O_3. In both cases this would lead to increased interface roughness of the multilayer, consistent with the lower EUV reflectance (29.6%) that was measured for sample *C*.

5.3.5 Transmission Electron Microscopy and Selected Area Diffraction

High resolution TEM is a standard imaging technique used to check the quality of multilayers and their interfaces. Further structural characterization of Mo/Y samples *A* and *C* was conducted by TEM to furnish additional evidence of the layer structures. Detailed information about the specimen preparation and microscope operation is described in Section 2.5. High resolution TEM images of the Mo/Y cross section are shown in Fig. 5.7 for samples *A* (< 3% oxygen) and *C* (~39% oxygen). In general, relatively sharp interfaces (no intermixing layer at the molybdenum and yttrium interfaces) could be observed in both samples. This is consistent with the phase diagram of the Mo-Y system[61] that shows no mixture phase of these two materials at any temperature and a positive enthalpy of mixing[62] (ΔH = +35 kJ/mole in Mo/Y system). A major difference observed between these images is that yttrium grains in sample *A* are much smaller than those in sample *C*, in the direction normal to the multilayer growth direction. Obviously, the presence of a high amount of oxygen (~39%) in the yttrium target *C* led somehow to the formation of large crystallites in the direction perpendicular to the multilayer growth. Hence interfaces appear smoother (less roughness) in sample *A*.

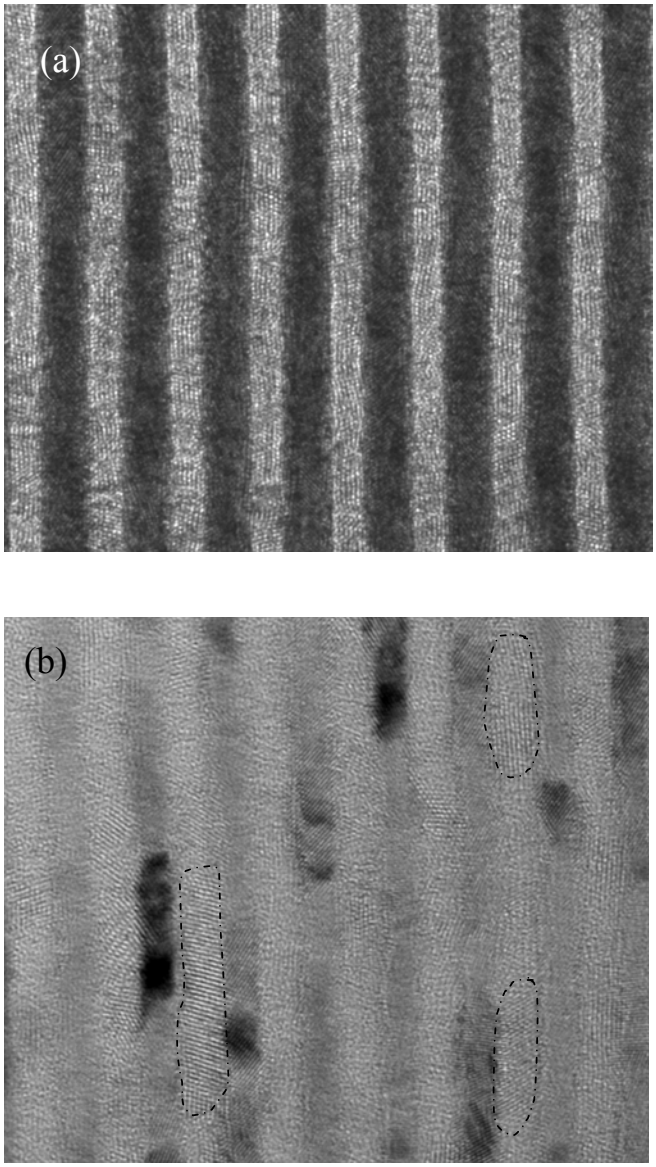

Figure 5.7. TEM images of (a) Mo/Y sample *A* (< 3% oxygen) and (b) Mo/Y sample *C* (~39% oxygen). A thicker sample or higher-*Z* material scatters more electrons than a thinner or lower-*Z* area. Therefore the originally thicker sample *A* has better contrast than sample *C* and the higher *Z* material (molybdenum, *Z* = 42) appears darker than the lighter *Z* material (yttrium, Z = 39). Few examples of large yttrium crystallites in the direction normal to the multilayer growth due to the presence of high amount of oxygen are outline in sample *C*.

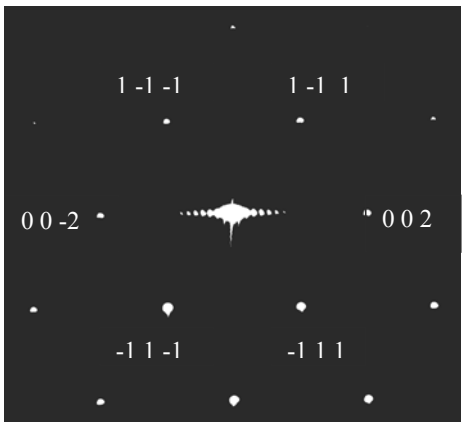

Figure 5.8. Diffraction pattern of the substrate, single-crystal Si (100). The multiple well-defined spots in the center are the results of the Mo/Y multilayer superlattice with spacing equal to its period thickness. The brightness of this image is adjusted to better reveal the silicon spots.

Electron diffraction images were collected in the same regions as those shown in Fig. 5.7. Since the electron beam is large as compared to the layer thickness, it was impossible to obtain electron diffraction from a single layer. In the area covering the multilayer and the silicon substrate, the diffraction pattern of silicon obtained with the electron beam in the [110] direction is shown in Fig. 5.8. The ring patterns due to the polycrystalline structure of molybdenum and yttrium are shown in Fig 5.9. The brightness of the rings is not uniform. At certain angular ranges, higher intensity arcs are present and can be interpreted as texture of either the molybdenum or the yttrium layers. To index these rings, the silicon (111) and (002) reflections were used as an internal calibration since their *d*-spacings are known, e.g. d = 3.1357 Å for Si (111) and d = 2.7153 Å for Si (002). The *d*-spacing of a material corresponding to any selected area diffraction (SAD) rings can be determined using the relation:

$$R_{Si}\, d_{Si} = R\, d, \qquad (5.2)$$

where R_{Si}, d_{Si} are the measured radius and *d*-spacing of either Si (111) or Si (002), and *R*, *d* correspond to the measured radius and the unknown *d*-spacing of material under study (molybdenum or yttrium). There were four prominent rings observed in both samples. The textured rings were identified to be the Y (101), Mo (110), Mo (200), and Mo (211) for the 1st to the 4th ring counting from the center, respectively. The two bright spots near the silicon (002), (00-2) reflections apparent in both samples indicate strong texture of Y (101) in the multilayer growth direction. In principle one can measure the width of the SAD ring and infer the crystallite size. However, the difference in the ring widths in sample *A* and *C* was too small to distinguish between the two samples. The SAD image of *A* is over exposed, making it more difficult to compare the two images in detail. It is also very hard to separate the rings of Y (d = 0.276 nm) and Y_2O_3 (d = 0.306 nm) in sample *C* in case there is one. However, these images confirm that both molybdenum and yttrium are polycrystalline and they are both strongly textured in these multilayers. Information about the interface roughness cannot be inferred from the SAD images.

In summary, the EUV reflectance of Mo/Y is dependent on both the optical and structural properties of Mo/Y multilayers. Oxygen (~25%) in the yttrium layers provides some kind of smoothing mechanism to the interfaces and thus improves the overall reflectance of the multilayer.

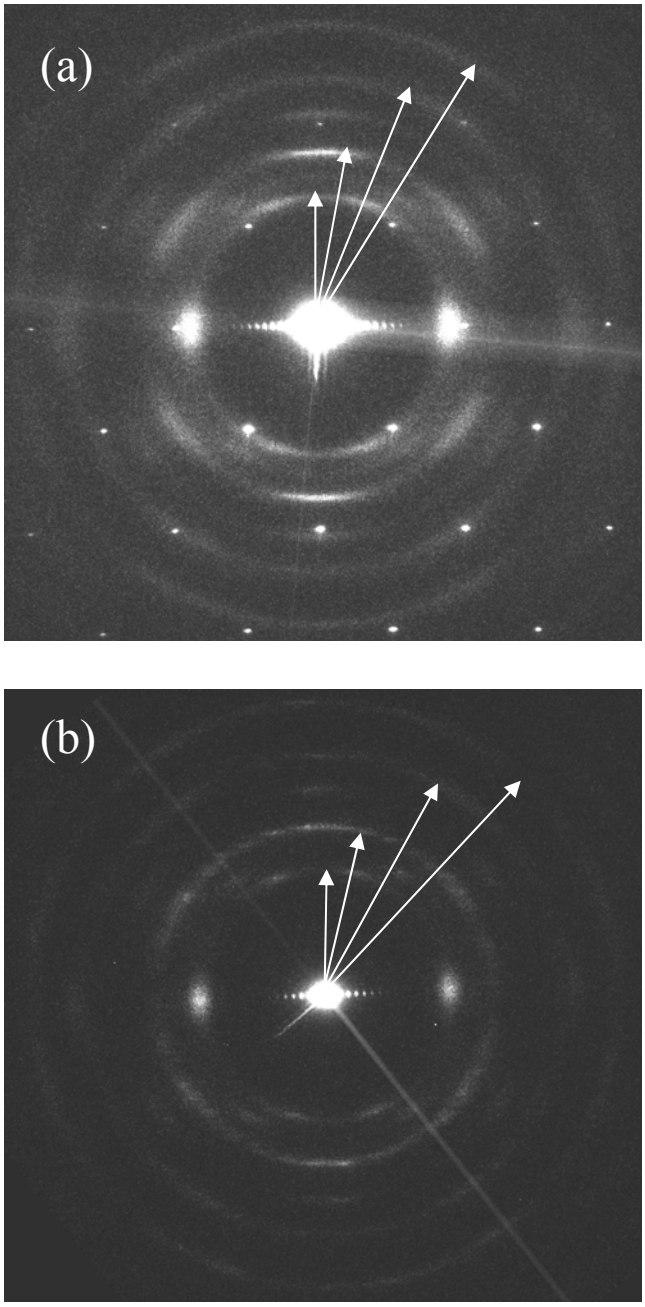

Figure 5.9. Ring diffraction patterns from polycrystalline layers of molybdenum and yttrium of (a) Mo/Y sample *A* (< 3%oxygen) and (b) Mo/Y sample *C* (~39% oxygen). The diffraction pattern of *C* was taken far from the substrate region so the diffraction spots from the silicon substrate (clearly visible as equally spaced dots in the diffraction pattern of *A*) cannot be seen.

5.4 Stability of Mo/Y Multilayers with Various Capping Layers

Earlier studies by Montcalm *et al.* have shown that Mo/Y multilayers, terminated with either molybdenum or yttrium, experienced some reflectance loss after several days of exposure to the air. In this study, multilayer samples with molybdenum, yttrium, and palladium capping layers were studied. Palladium was chosen as a capping material because it does not tarnish in air and it is a good absorber layer in the 8-12 nm wavelength region according to the literature.[28] A set of samples was made in which the palladium thicknesses varied from 2 nm to 6 nm. Fig. 5.10 shows the measured EUV reflectance as a function of palladium thickness. Superimposed is the calculated EUV reflectance. Based on these results, only the 5-nm-thick palladium capping layer was chosen for further stability tests since it exhibited the highest EUV reflectance. For the case of molybdenum and yttrium, the capping layer thicknesses were kept the same as the thickness of molybdenum (~ 2.1 nm) and yttrium (~ 2.7 nm) within the multilayer. It should be noted that the yttrium target *C* (~39% oxygen) was used in Mo/Y multilayer fabrication for all samples discussed in this section and was also used as a capping layer material in the comparison with molybdenum and palladium.

Surface roughness of the capping layer does not significantly affect the Mo/Y multilayer reflectance. Nevertheless, investigation of the capping layer surface may reveal information regarding the quality of the coverage and degree of protection that the capping material offers to the multilayer structure underneath. The surface roughness of the molybdenum-, yttrium-, and palladium-capped multilayers and also of a typical bare silicon substrate (that was used to deposit all three samples) was analyzed with AFM. The AFM results of 2 x 2 μm^2 scans are shown in Fig. 5.11 and 5.12. A typical Si (100)

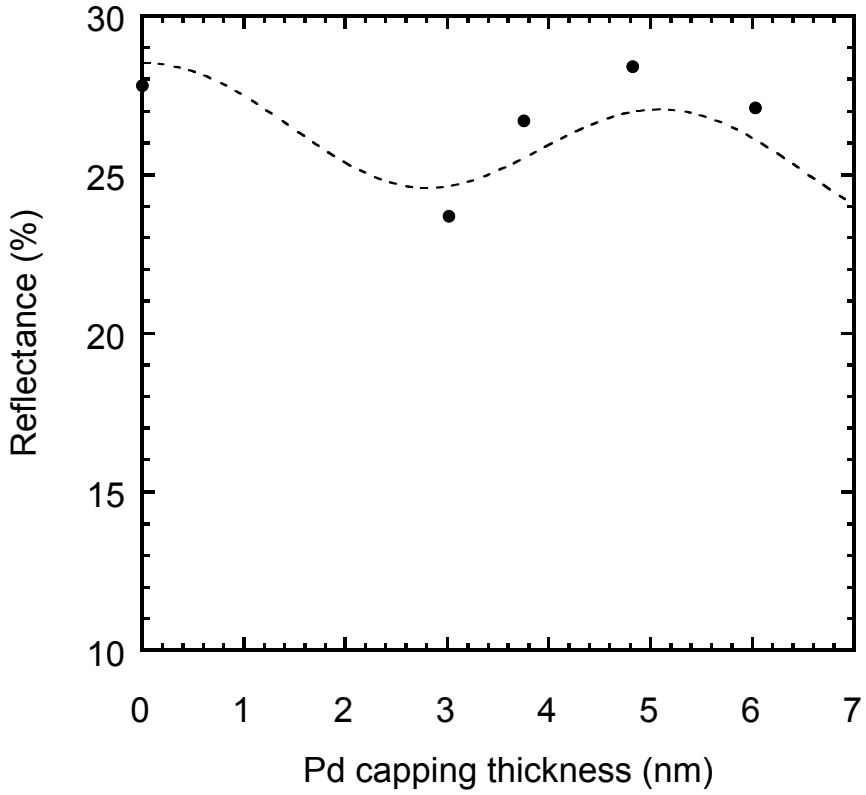

Figure 5.10. Measured (data points) and calculated (dash line) EUV reflectance as a function of palladium capping thickness from five Mo/Y multilayers. The palladium capping is coated on top of a molybdenum-finished Mo/Y multilayer.

substrate has high frequency roughness of about 0.1 nm rms. The surface roughness of the molybdenum-, yttrium-, and palladium-capped multilayers was 0.175 nm, 0.465 nm, and 0.183 nm, respectively, with an accuracy of ± 0.02 nm. Assuming that the roughness of the Mo/Y multilayer underneath the capping layer was the same in all three samples, the yttrium (~39% oxygen) capping layer appears to have a far worse surface quality, compared to the molybdenum and palladium capping layers.

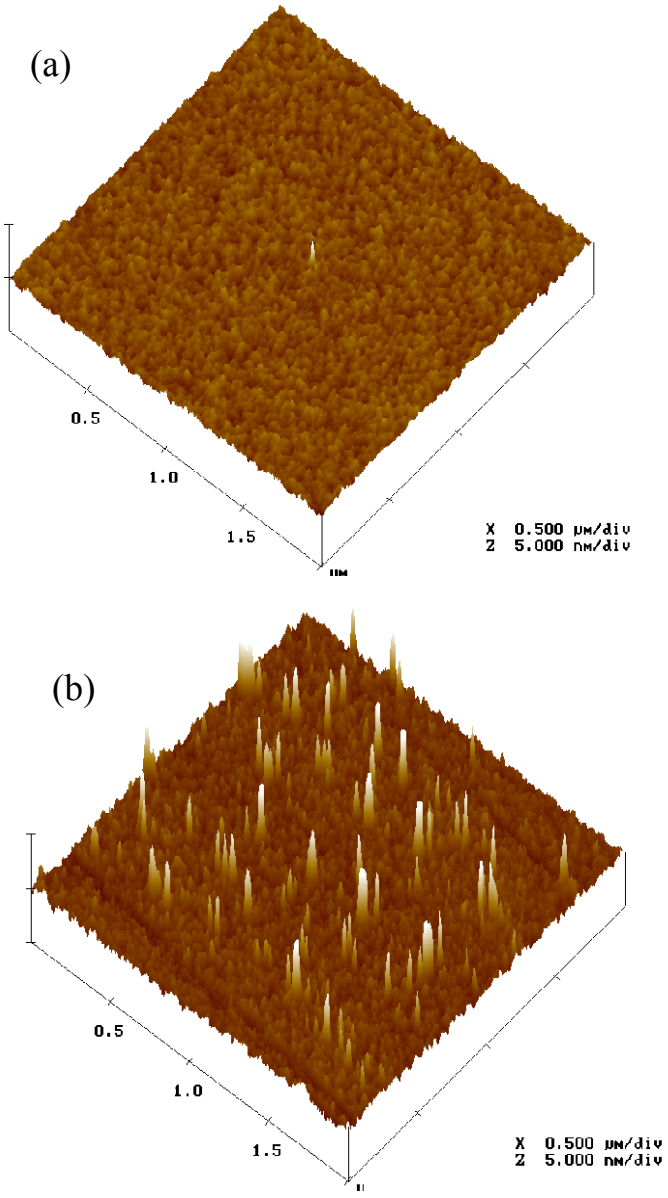

Figure 5.11. AFM images showing the surface profiles of (a) molybdenum-capped and (b) yttrium-capped Mo/Y multilayers.

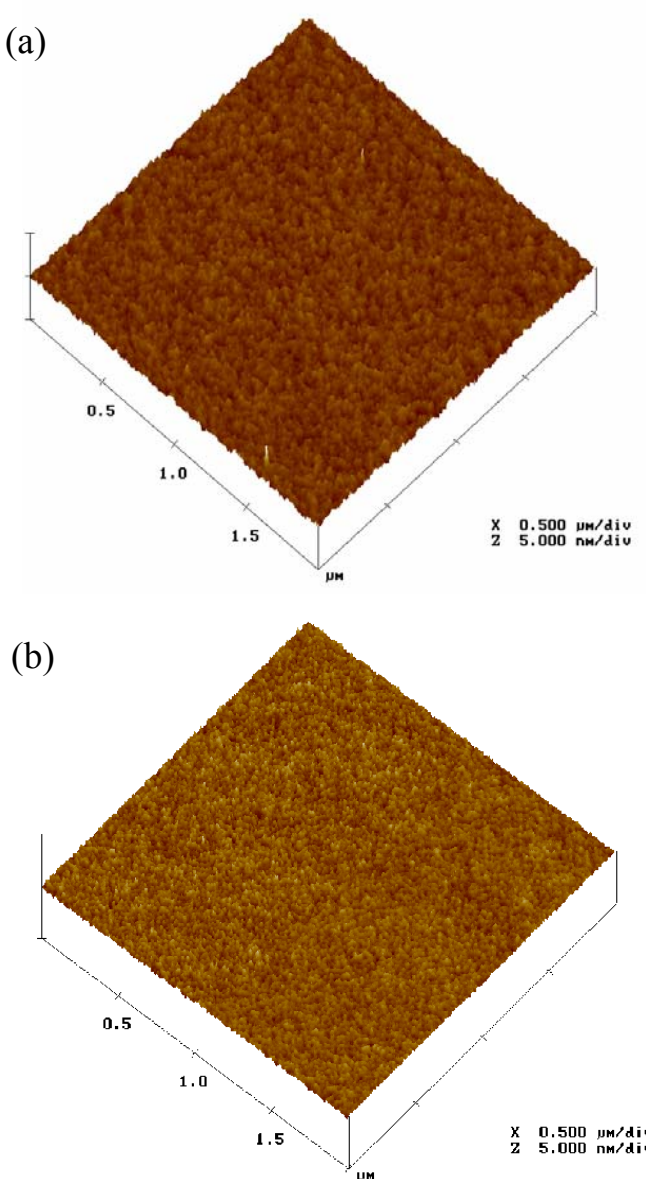

Figure 5.12. AFM images showing the surface profiles of (a) palladium-capped Mo/Y multilayer and (b) a bare silicon substrate.

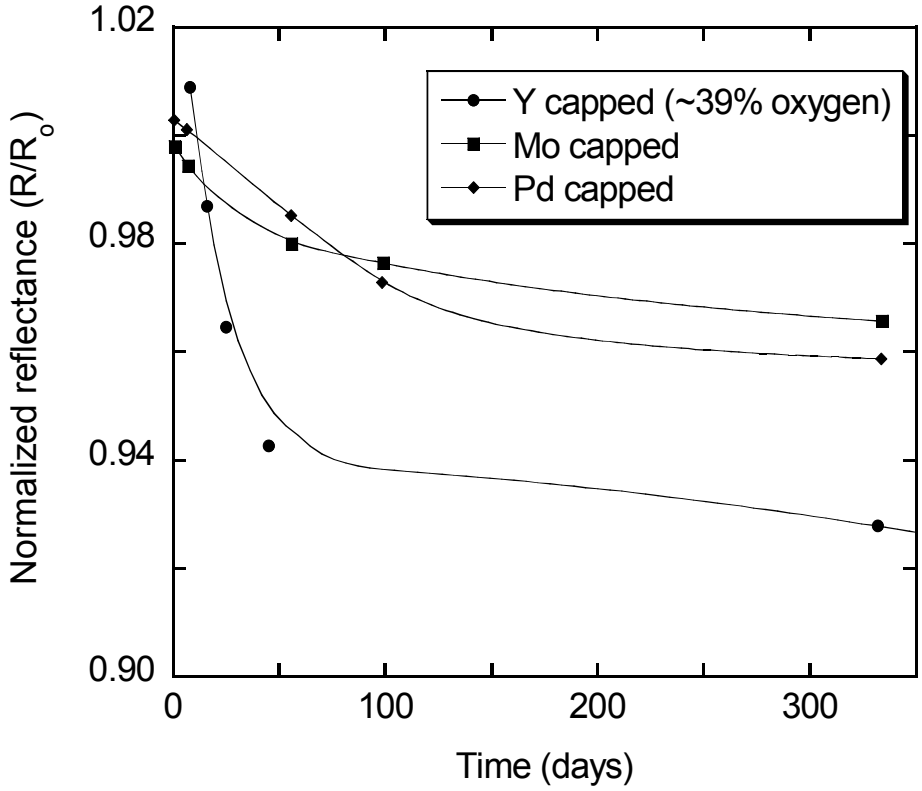

Figure 5.13. Measured EUV reflectances of molybdenum-, yttrium-, and palladium-capped Mo/Y multilayers (symbols) normalized to their initial values (immediately after deposition) as a function of time for a period of one year. The lines are interpolations of the measured results.

The EUV reflectances of these various capped Mo/Y multilayers were measured repeatedly over a period of one year. All the multilayers were kept in plastic containers at room temperature. Since the multilayer periods and their initial reflectances were not exactly the same, the measured reflectances at any given time were normalized to their initial values, for comparison purposes. The normalized reflectance plotted as a function of time is shown in Fig. 5.13 for three representative samples. As shown, all three multilayers had a significant reflectance drop in the first three months after deposition, followed by an extended period of time where the reflectance seemed to be fairly

constant. Small shifts (less than 0.1 nm) of the reflectance peaks toward shorter wavelengths were observed in the first three months after deposition indicating further period contraction in these samples. These wavelength shifts of less than 0.1 nm were indeed too small to be measured in the XRD spectra. After the first three months, the wavelength remained constant while the reflectance continued to decrease as a function of time. Molybdenum appears to be the best capping material among all three materials studied, with a reflectance drop of only 2.3% relative to its initial value in the first three months. Our last measurement, not shown in Fig. 5.12, on a three-year old molybdenum-capped multilayer showed 4.2% reflectance loss relative to the initial value, i.e. from 35.4% at 9.43 nm to 33.9% at 9.33 nm. Palladium also shows good lifetime stability (Fig 5.13). It should be emphasized once again that the yttrium capping material in this study came from target *C* (39% oxygen), which, as has been discussed in Section 5.3.5, formed a rough layer with large crystallites. Therefore the poor performance of yttrium target *C* in this capping layer study could be attributed to the presence of oxygen. A simple explanation for the loss in reflectance (Fig. 5.13) could be the following: in the case of molybdenum-capped sample, the molybdenum layer was mostly oxidized by the time the first measurement was done. No large reflectance loss could occur due to oxidation of the yttrium layer underneath since that layer already consisted of yttrium oxide. In the case of oxidized yttrium capping layer, the oxygen probably diffused through the yttrium oxide along the grain boundaries until it reached the molybdenum layer. The reflectance loss was mainly associated with the oxidation of the molybdenum layer underneath. The small reflectance loss in palladium-capped sample could be explained with palladium being a precious metal that formed a thin and stable oxide on it surface. As was demonstrated in

Section 5.3.2, pure yttrium films are very stable against oxidation. Thus pure yttrium could be a successful capping material for Mo/Y multilayers and should be the topic of further investigations.

5.5 Annealing Effect on Mo/Y Multilayers

Multilayer mirrors are often exposed to heat in most applications. It is therefore important to study their thermal stability in high temperature environments. A pyrolitic boron nitride heater (3 inch. in diameter) with a maximum temperature of 950° C was used to heat the multilayers in a vacuum chamber. The base pressure in the experimental chamber was ~2 x 10^{-8} Torr before the annealing process. The temperature stability was better than ± 2% and the uniformity was ± 8° C within 2.25 inches in sample diameter. In this study, all multilayers were made from yttrium target *C* (~39% oxygen). The multilayers were annealed at three temperatures 250° C, 380° C, and 480° C. Unless noted otherwise, the annealing time is one hour and this does not include the ramp time and the cool-down time. The ramp time to reach 480° C for example, was about 15 minutes and the cool-down time to room temperature was about 45 minutes in vacuum.

Annealing of Mo/Y samples resulted in an expansion of the multilayer periods (a shift toward longer peak wavelengths) and a reduction of the EUV reflectances. In Fig. 5.14, small-angle XRD data of three samples annealed at 250° C, 380° C and 480° C are shown. An increase in peak intensities in various diffraction orders after annealing indicates the sharpening of multilayer interfaces. A cross-sectional TEM image of the annealed sample at 480° C is shown in Fig. 5.15. The interfaces appear smoother and sharper compared to the as-deposited sample shown previously in Fig. 5.7 (b). The rocking scans on the multilayer that was annealed at 380° C for 24 hours showed less

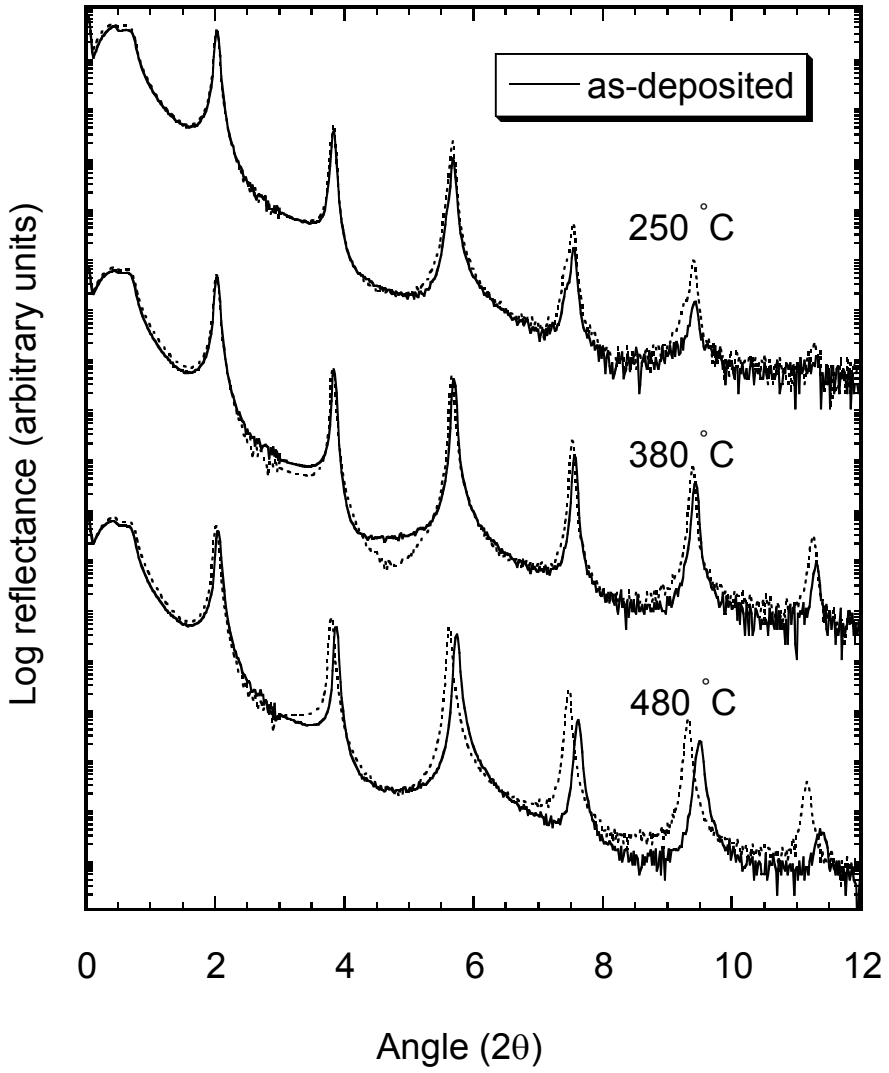

Figure 5.14 Small-angle XRD spectrum of multilayers from yttrium target *C* (~39% oxygen) heated to 250 °C, 380 °C, and 480 °C for one hour.

scattering than the as-deposited sample (see Figure 5.16). The scattering results indicate that the Mo/Y interface roughness improved after annealing. This is in good agreement with the modeling results from GAXFIT which predict the roughness of 0.32 nm in the annealed sample as compared to the roughness of 0.37 nm in the as-deposited sample. However, the EUV reflectance of the annealed samples is lower than the EUV reflectance

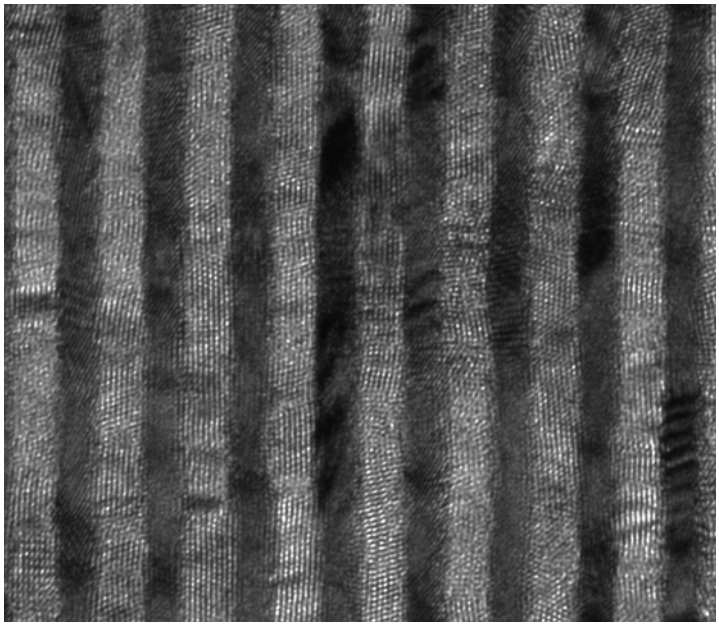

Figure 5.15. Cross section TEM image of Mo/Y multilayer *C* (~39% oxygen) after annealing at 480° C for one hour.

of the as-deposited samples. Fig. 5.17 shows the variation of the reflectance and the period thickness (normalized to their initial values) as a function of temperature. A maximum of 16% relative drop in reflectance and less than 2% relative increase in period thickness is measured in the sample annealed to 480° C. Since XRD and TEM data all show evidence that the annealed sample has sharper and smoother interfaces, the observed reflectance drop could only be explained with either surface oxidation/contamination or density/composition changes in the multilayer that could not be revealed by the XRD or TEM data. Given that all annealing was done in a clean and vacuum environment, the latter cause could be considered as the most probable cause for the reflectance loss. For the annealed multilayer at 380°C for 24 hours, the reflectance drop was only 9% relative to its initial value. These results indicate good thermal stability of Mo/Y multilayers at high temperatures.

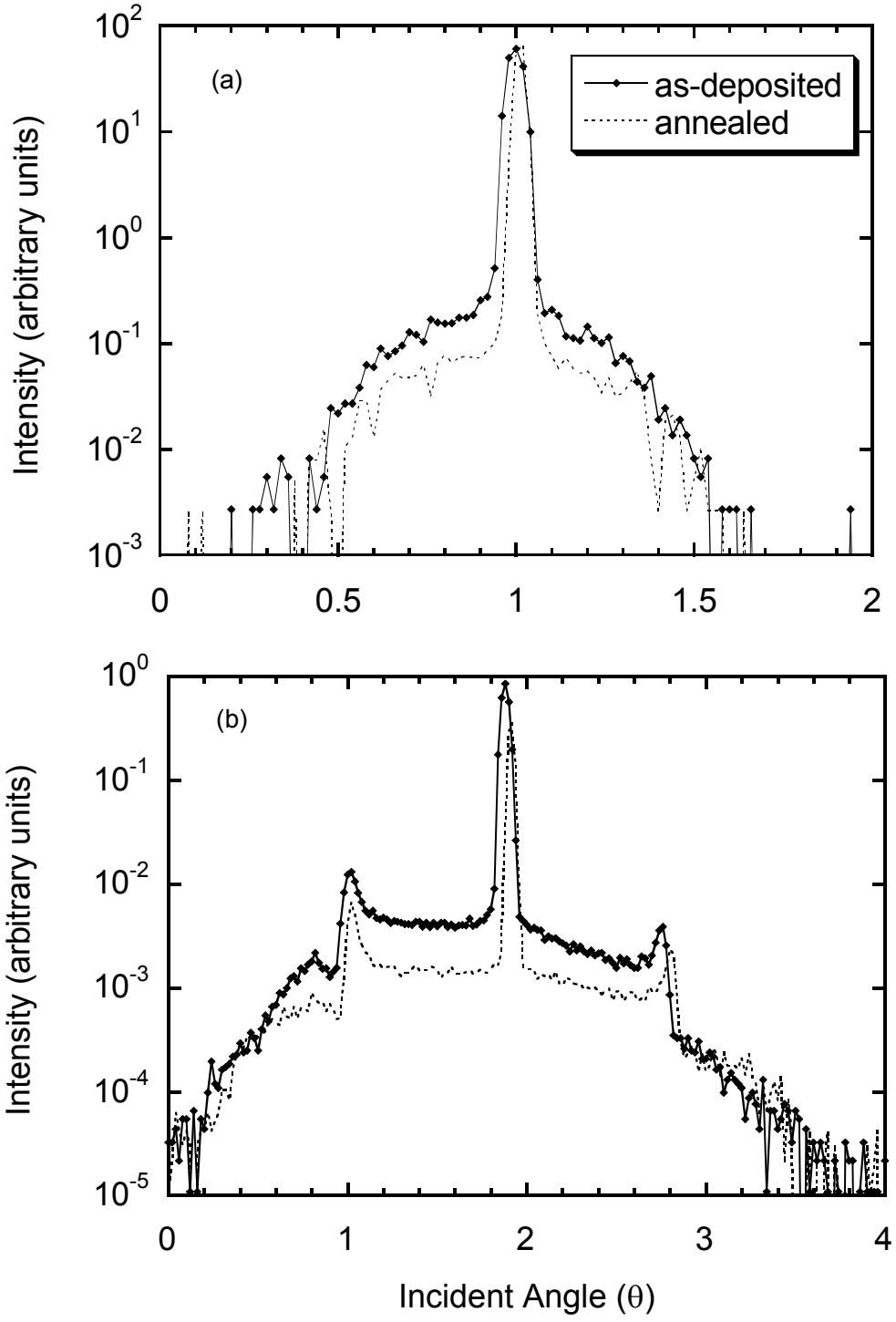

Figure 5.16. First- (a) and second-order (b) rocking curves of multilayers *C* (~39% oxygen) before and after annealing at 380° C for 24 hours.

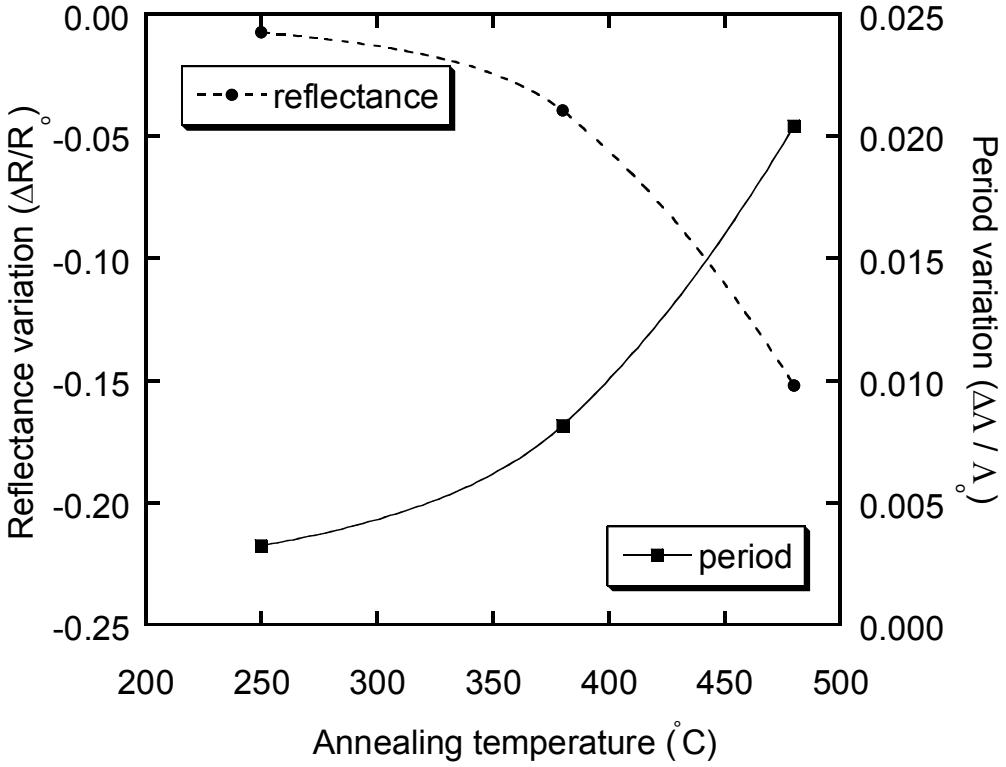

Figure 5.17. EUV reflectance variation (circle) and period thickness variation (square) of Mo/Y multilayers as a function of the annealing temperature. The annealing time of one hour was used for all samples.

5.6 Conclusions

Mo/Y multilayers were fabricated with an ultrahigh vacuum deposition system using three different yttrium targets which had < 3%, 25 ± 3%, and 39 ± 3% atomic oxygen in their yttrium layers. The highest multilayer reflectance of 38.4% at 9.48 nm was achieved from the yttrium target with ~25% oxygen in content. Less scattering was observed from this multilayer than from the < 3%- and ~39%-oxygen samples as a result of having lower interface roughness. These results confirm that in addition to changing in the optical properties, oxygen also causes some structural changes in the multilayer. It was found that yttrium and molybdenum are both polycrystalline and textured. The

crystallite size of both materials was similar in all three samples, in the direction parallel to the multilayer growth. The sample with the highest amount of oxygen (~39%) exhibited an increase in crystallite size in the direction perpendicular to the multilayer growth and/or formation of yttrium oxide. This effect caused increased interface roughness and loss in EUV reflectance. The optical and structural properties of the multilayers are thus competing in the reflectance results. To optimize the Mo/Y reflectance, more experiments are needed in order to determine the clear relationship between oxygen and multilayer structural properties.

Lifetime stability of Mo/Y multilayers fabricated from yttrium target *C* (~39% oxygen) and capped with molybdenum, oxidized yttrium (~39% oxygen), and palladium was monitored for up to one year. All samples experienced some reflectance drop in the first three months after the deposition due to the surface contamination/oxidation. Their reflectance peaks were also shifted toward shorter wavelengths due to multilayer contraction. The reflectance continued to drop slowly with time after the first three months. The molybdenum- and palladium-capped samples exhibited the best performance with about 4% relative loss in reflectance after one year. The oxidized yttrium-capped sample (~39% oxygen) performed poorer with 8% relative loss in reflectance in one year, most probably due to the presence of oxygen. Since pure yttrium films are very stable against oxidation, pure yttrium should be further explored as a capping layer. It is also discovered that the molybdenum-capped samples can withstand temperatures of up to 380° C for 14 hours with 9% relative reflectance loss and no degradation of the multilayer structure, thus proving that these multilayers also have relatively good thermal stability.

Chapter 6

Molybdenum/Yttrium Multilayer-Coated Diffraction Gratings

6.1 Introduction

There has been a continuing effort in the development of normal-incidence-multilayer coatings for extreme-ultraviolet (EUV) solar and astrophysical instruments such as telescopes and spectrographs. The high reflectance and wavelength-selective properties of multilayer-coated optics allow imaging and recording of distinct emission lines from solar regions. The solar coronal image dominated by the Si XII emission at 4.4 nm, recorded during a rocket flight on October 1985 by a W/C multilayer-coated telescope, represents the first successful use of multilayer technology for astrophysical observation.[63] Recent images of the sun (Fig. 6.1) obtained from the Solar and Heliospheric Observatory[16] (SOHO) and Transition Region and Coronal Explorer[17] (TRACE) missions have been made possible with the application of Mo/Si and Mo_2C/Si multilayer coatings, respectively. The operational wavelength of these multilayers was optimized to 17.1 nm, 19.5 nm, 28.4 nm, and 30.4 nm for the selected emission lines of Fe IX/X, Fe XII, Fe XV, and He II, respectively. Such observations provide sensitive temperature diagnostics in the range from 10^4 to 10^6 K and also the detailed information

about conditions on the Sun including plasma confinement, plasma heating, and solar flares.

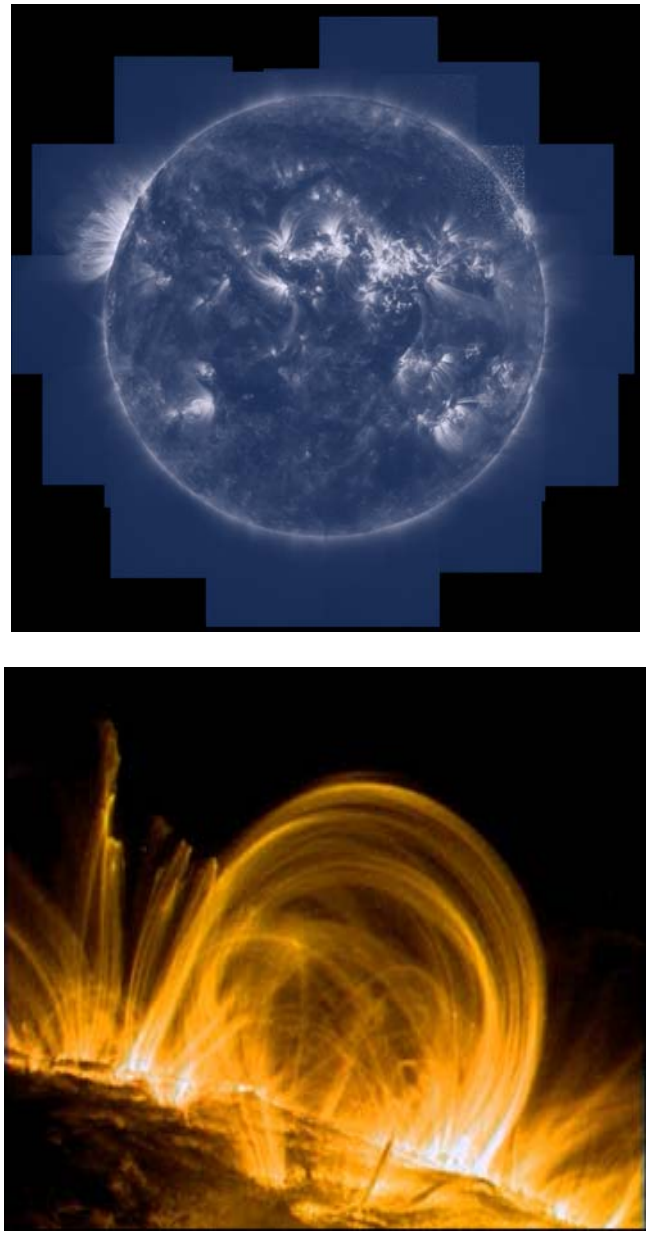

Figure 6.1. Images of the sun: whole body (top) and coronal region (bottom) obtained from Fe IX/X lines at 17.1 nm using Mo2C/Si multilayer-telescope during TRACE mission.

Multilayers were also applied on various types of grating to enhance the grating efficiency, especially for high-resolution spectroscopy of weak EUV sources. Gratings with Mo/Si multilayer coatings operating at wavelengths above the silicon *L*-edge have substantially higher efficiency than typical gold-coated gratings.[64] Recently, MoRu/Be multilayers enabled grating operation at normal-incidence with efficiencies of up to 10.4% in the 11.1-12.0 nm wavelength region.[65,66] However, there are still interesting portions of the EUV spectrum that have not yet been explored and that cannot be accessed by the above-mentioned multilayers.[67]

According to the all-sky survey conducted in the 7-80 nm wavelength region by the Extreme Ultraviolet Explorer (EUVE) mission,[14] there are over 700 bright objects in space, including hot white dwarfs, active and nearby late-type stars, cataclysmic variables, and various types of active galactic nuclei, that radiate EUV energy. In the 8-12 nm spectral range, the most intense emission line is Fe XVIII at 9.392 nm. This line was observed in rotating cool stars and white dwarf systems and can be used, for example, to study magnetic fields. It is therefore of interest to develop high-resolution spectroscopic instruments based on high-efficiency diffraction gratings that operate in this wavelength region. Experimental data on multilayers that can reflect at 9.4 nm at normal incidence include the Mo/Sr, Mo/Y, Ru/C, Pd/B_4C, Cr/C, and W/B_4C material pairs.[31] However, none of these multilayers was ever applied to a grating. Theoretical calculations predict much higher reflectance for Mo/Sr and Mo/Y multilayers than for the other multilayer pairs mentioned above. Even though Mo/Sr theoretical reflectance is the highest in this group, the experimental data revealed that this multilayer, if exposed to air, would completely loose its reflective properties within one day because of oxidation.[68]

Therefore the following study was limited to Mo/Y multilayers, which provide substantially high reflectance and long lifetime.[32,69]

In this chapter, the performance of a Mo/Y multilayer-coated diffraction grating operating at 9 nm was investigated. The grating principle and fabrication procedure are explained in Section 6.2. The experimental procedures are described in Section 6.3 followed by the results and discussion in Section 6.4. A comparison between the measured and calculated grating efficiencies is presented in Section 6.5. Finally, the conclusions are discussed in Section 6.6.

6.2 Grating Operation and Fabrication

Diffraction gratings are commonly used in spectroscopic instruments to disperse polychromatic light. The grating diffracts light into several orders given by the grating equation

$$m\lambda = d\,(\sin\alpha - \sin\beta), \tag{6.1}$$

where m is the grating order; d is the groove spacing; α and β are the incidence angle and the diffraction angle measured from the grating normal, respectively; and λ is the wavelength of light. The efficiency at each order depends strongly on the grating profile. The efficiency of one particular order can be maximized with the use of a blazed (sawtooth) line profile. The blaze angle ϕ_b is chosen so that the facets reflect light of a particular wavelength into the chosen diffracted order, which means that blazed gratings have a high peak efficiency at only specific wavelengths. The grating efficiency also depends on the quality of the line profile and the smoothness of the grating surface. For an on-blaze operation, the wavelength in the m grating order can be expressed as

$$\pm m\lambda = 2d \sin\phi_b \sin\theta, \tag{6.2}$$

where $\theta = \pi/2 - \alpha \pm \phi_b = \pi/2 - \beta \pm \phi_b$ is the grazing-incidence angle that corresponds to the facet normal (Fig. 6.2).

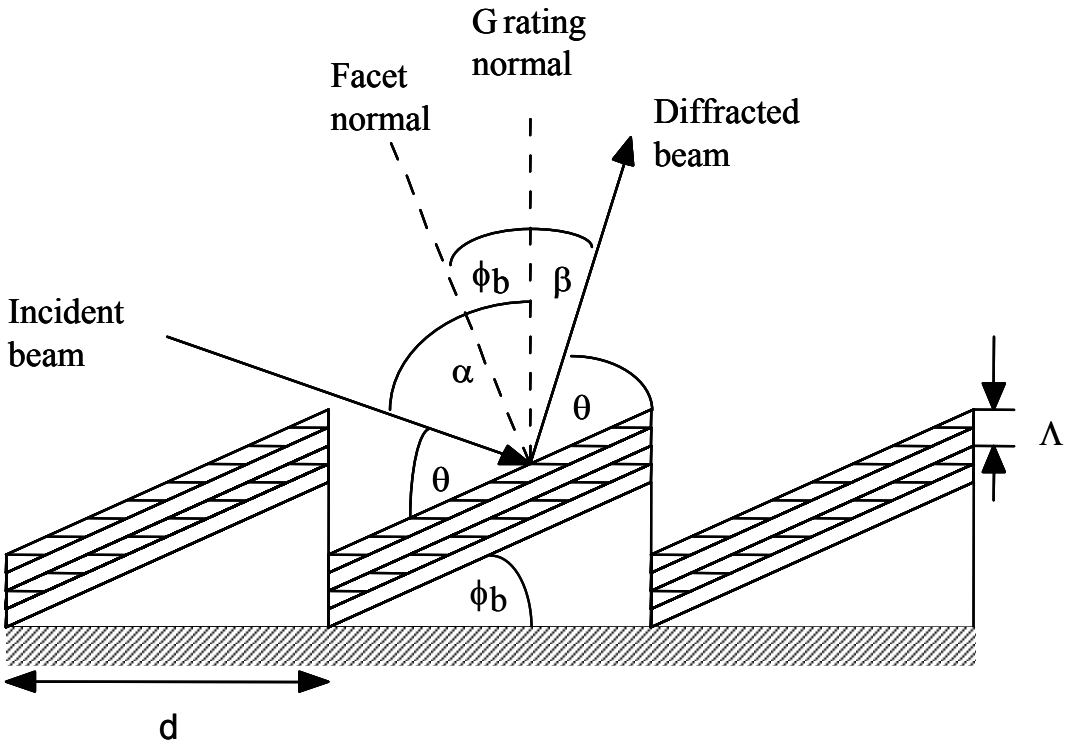

Figure 6.2. Schematic drawing of a multilayer blazed diffraction grating.

Let us now consider multilayer-coated gratings. Typical multilayers consist of a periodic stack of two alternating materials having high and low indices of refraction. When utilizing the well-known quarter-wave stack idea and ignoring the absorption,[11] the maximum reflectance occurs when the optical thickness of each layer is equal to a quarter of the wavelength of interest. In fact, the refraction-corrected multilayer period Λ can be determined through the modified Bragg's equation developed by Henke *et al.* (Section 2.2, Equation 2.2). For the first order multilayer interference at normal-

incidence, the optimum efficiency of an on-blaze operation of a multilayer-coated grating occurs when the blaze wavelength of the grating is equal to the peak wavelength of the multilayer. The following condition must be satisfied to achieve this:

$$\Lambda = d_{Bragg}(1-\delta) = \pm\frac{d\sin\phi_b}{m} \quad . \tag{6.3}$$

This condition relates the multilayer period to the diffraction order of the grating. It implies that the maximum efficiency is dependent on λ. Only in the region away from characteristic absorption edges of the multilayer materials, where δ is nearly constant, will the grating order remain constant with the change of wavelength.

In this study, a replica of a master holographic blazed grating produced by Spectrogon US Inc. with 2400 groves/mm was coated. The grating was concave with 2-m radius of curvature. The master grating was produced by a holographic process, in contrast to classical gratings that are mechanically ruled with a diamond tip. A photosensitive layer deposited on top of a glass substrate was exposed with the interference pattern formed by two laser beams, the layer was selectively dissolved, and ion-beam etching was used, which made it possible to produce almost sawtooth shaped grooves. The replica gratings, having almost equivalent properties and quality to the master grating, were made by Hyperfine Inc. The aluminum oxide surface resulting from the replication process was coated with a thin SiO_2 layer to reduce the microroughness of the oxidized aluminum surface.

6.3 Experimental Procedure

The UHV magnetron-sputtering deposition system described in Section 2.1 was used for the coating of the diffraction grating with Mo/Y multilayer. The typical base pressure after a bakeout and prior to deposition was $2\text{x}10^{-9}$ Torr. A series of Mo/Y

multilayers of various thickness combinations were deposited on silicon wafer substrates for the deposition-rate calibrations. Every multilayer started with yttrium and finished with molybdenum layer. The grating substrate was allowed to spin around its center to achieve good thickness uniformity. An atomic force microscope (AFM) was used to measure the grating groove profile before and after the multilayer coating. A number of scans were performed over the square areas of 1 and 5 μm in the center and near the edge of the grating. The multilayer reflectance and the grating efficiency were measured using the beamline 6.3.2 reflectometer of the Advanced Light Source. A detailed description about the reflectance measurements at this beamline was described in Section 2.3.

6.4 Results and Discussion

Mo/Y coatings exhibit a high-quality multilayer structure. A series of well-defined peaks obtained from small-angle XRD of a typical multilayer (Fig. 6.3) indicates sharp interfaces between molybdenum and yttrium, in good agreement with a small interface contraction of 0.055 nm obtained from rate calibration with a two-layer model. The deposition rates of molybdenum and yttrium operating at the same dc power of 50 W were 0.052 nm/sec and 0.095 nm/sec, respectively.

The multilayer design was based on calculations using IMD software[59] assuming an ideal Mo/Y structure. IMD is a computer program written with an interactive data language (IDL) that can calculate specular and non-specular (diffuse) optical functions of an arbitrary multilayer structure, i.e., a structure consisting of any number of layers of any thicknesses, and of any materials. The multilayer optimized parameters include the period thickness Λ, the thickness ratio of the absorber layer to the period thickness Γ, and the number of bilayers N. Theoretically, Γ of 0.425 and N = 120 bilayers would provide

the highest reflectance Mo/Y multilayer in the 8-12 nm wavelength region. The increase in reflectance with number of bilayers is limited by absorption because light penetrating too deep in the multilayer can no longer reflect to the top surface. This optimum number

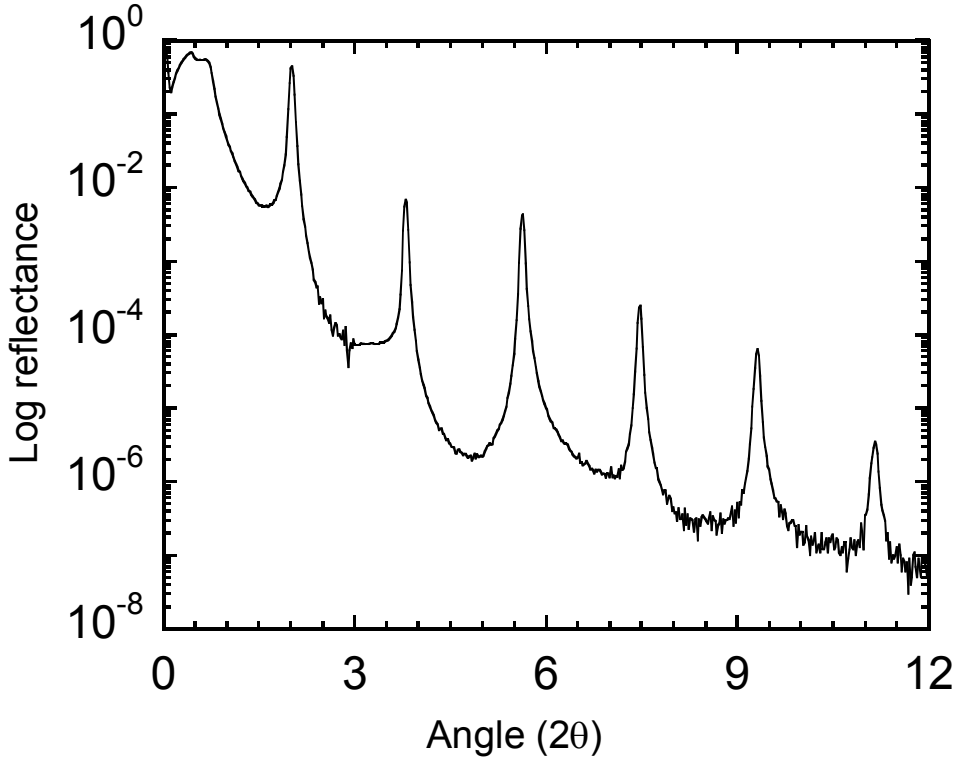

Figure 6.3. Typical XRD spectrum of a Mo/Y multilayer measured at small incident angles.

of N in reality was even lower because of surface-interface roughness of the multilayer that reduces the specular reflectance. The experimental optimum number of bilayers for Mo/Y seemed to be 100, and thus multilayers having only 100 bilayers were made. The reflectance of a Mo/Y multilayer deposited on a flat silicon wafer was 34.6% at 9.196 nm when the designed parameters Λ= 4.67 nm, Γ = 0.425, and N =100 bilayers were used. Fig. 6.4 shows also the best fit to the measured reflectance of this multilayer. The fit was performed using IMD software and the optical constants were derived from the Center

for X-Ray Optics (CXRO) atomic scattering factors.[36] Instead of bulk yttrium density (4.457 g/cm^3), the density of 4.402 g/cm^3 as measured with Rutherford backscattering spectrometry from yttrium films was used. Lower density can be explained with a high

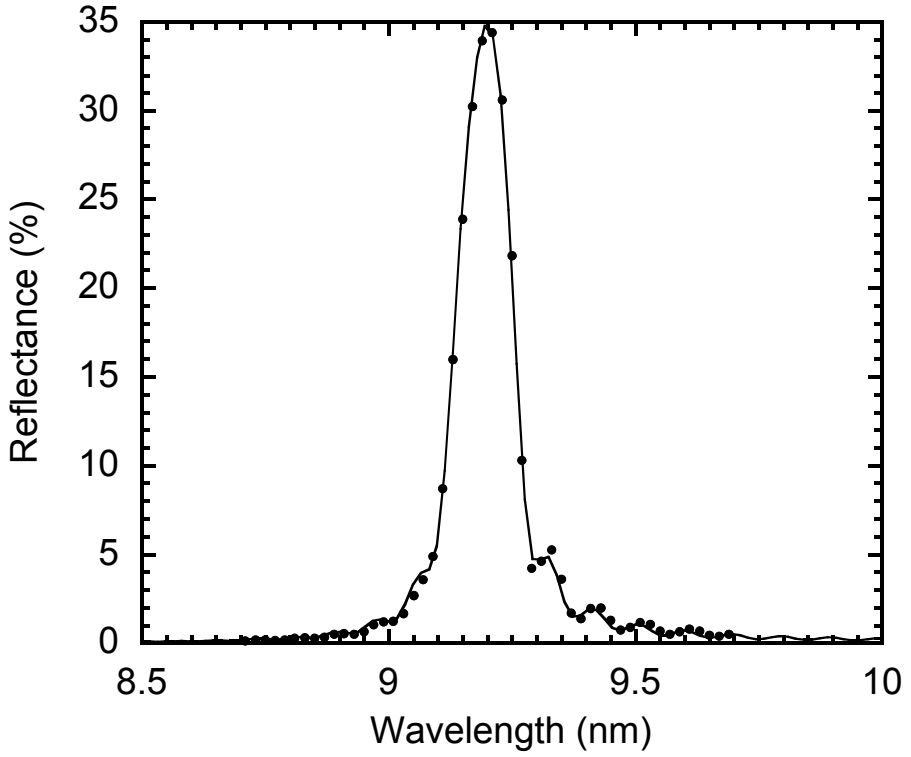

Figure 6.4. Measured normal-incidence (3°) reflectance of a Mo/Y multilayer deposited on a flat silicon wafer substrate. Experimental data (dots) and the best fit (solid line) are shown.

percentage of oxygen (~25%) and some other contaminants (~1% argon and ~0.3% tantalum). The best fit was obtained with Λ = 4.68 nm, Γ = 0.445, N = 100 bilayers, and the interface roughness of 0.55 nm, in good agreement with the designed parameters. The interface roughness in the fit was assumed to be the same for each interface. Because of the space limitation and the deposition geometry, the grating and the flat substrate could

not be coated simultaneously. Thus the reflectance of the coating on the grating was inferred from the above parameters.

AFM images of the grating before and after the application of the Mo/Y coating are compared in Fig 6.5. The vertical scale was adjusted to clearly reveal the texture of the grating image. Numerous spikes present on the substrate grating were smoothed out after the multilayer coating. The micro-roughness in the 4-40 μm^{-1} spatial frequency, excluding the low-frequency roughness from the groove pattern, was improved from 1.24 to 0.73 nm roughness. The smoothing properties of the Mo/Y multilayer enhanced the reflectance and substantially increased the grating efficiency without degrading the grating performance or affecting the blazed angle.

The grating efficiency was measured in the same configuration as the reflectance measurements using synchrotron radiation, however, with an additional 1.49-mm slit added in front of the detector. Grating efficiency is defined as the ratio of the diffracted intensity and the incident intensity, in which the incident radiation is monochromatic. Because this is a reflection grating, measuring the diffracted intensity is the same as measuring the reflected intensity. At fixed incident angles, the wavelength was scanned after the zero grating order was established. Approximately 0.89% grating efficiency at an 8.85 nm wavelength was measured at 8° from normal. This result implies that a higher grating efficiency could be obtained at 9.4 nm because of the increase of multilayer reflectance with wavelength in this spectral range**.**

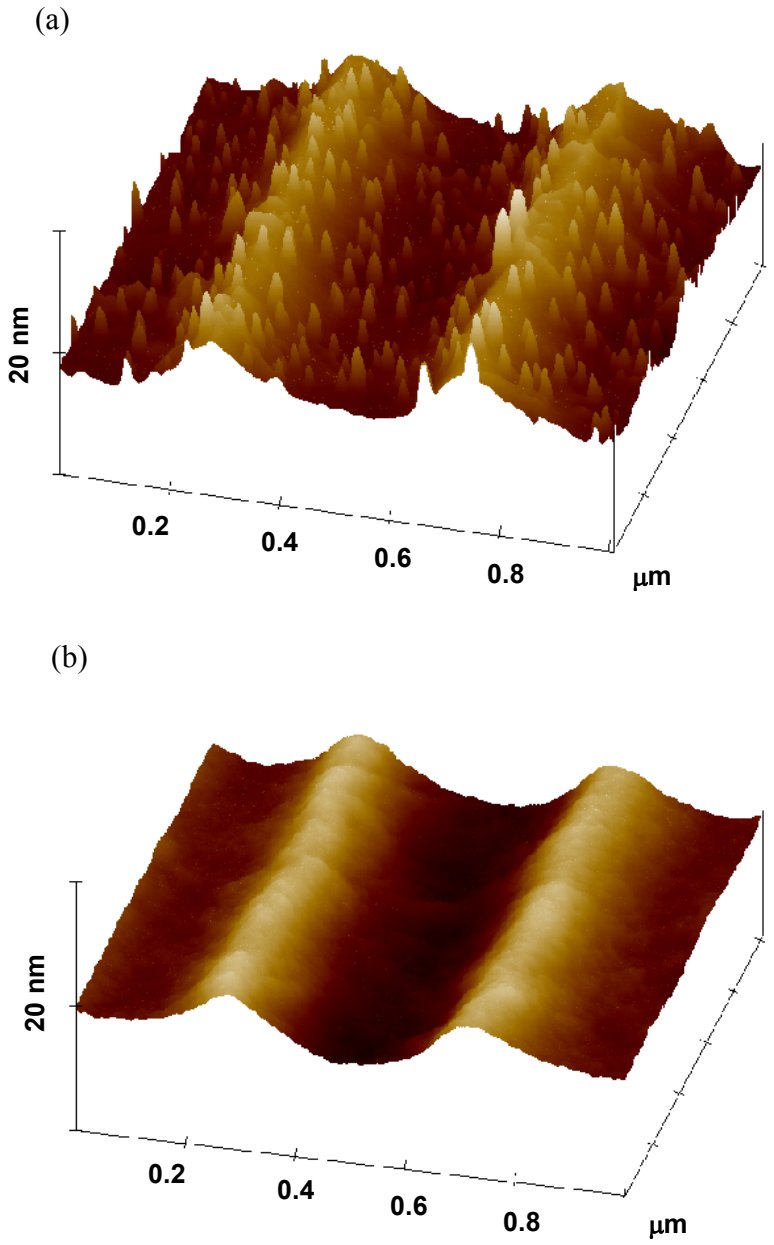

Figure 6.5. AFM images (1x1 μm^2) of the grating (a) before and (b) after the deposition of a Mo/Y multilayer coating.

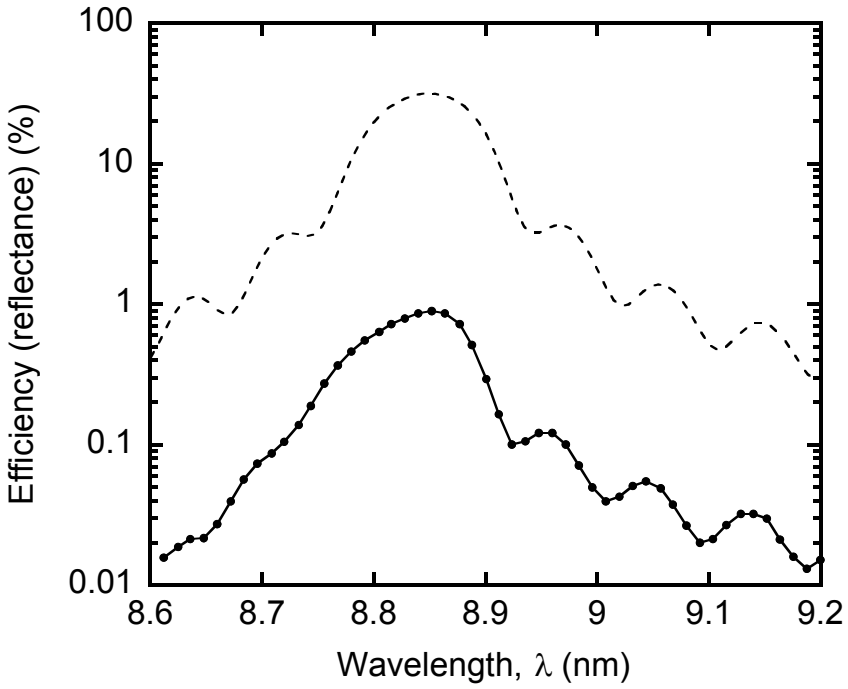

Figure 6.6. The zero order grating efficiency measured at 8° from normal-incidence (dotted curve) and the predicted reflectance (dashed curve) of the witness Mo/Y multilayer coating obtained from the fit.

In Fig. 6.6 the measured zero order efficiency at a normal-incidence angle of 8° is shown together with the predicted reflectance curve. This Mo/Y multilayer-coated grating had approximately 2.8% groove efficiency in the zero order at an 8.85 nm wavelength where the grating's groove efficiency is defined as the ratio of the grating efficiency and the coating reflectance. For a fixed wavelength, by scanning the detector around the specular angle where zero-order diffraction is located, the efficiencies in various diffraction orders were measured as displayed in Fig. 6.7. The positive-order numbers indicate the inside order, with the diffraction angle lying between the incident beam and the zero order, as opposed to the outside order.

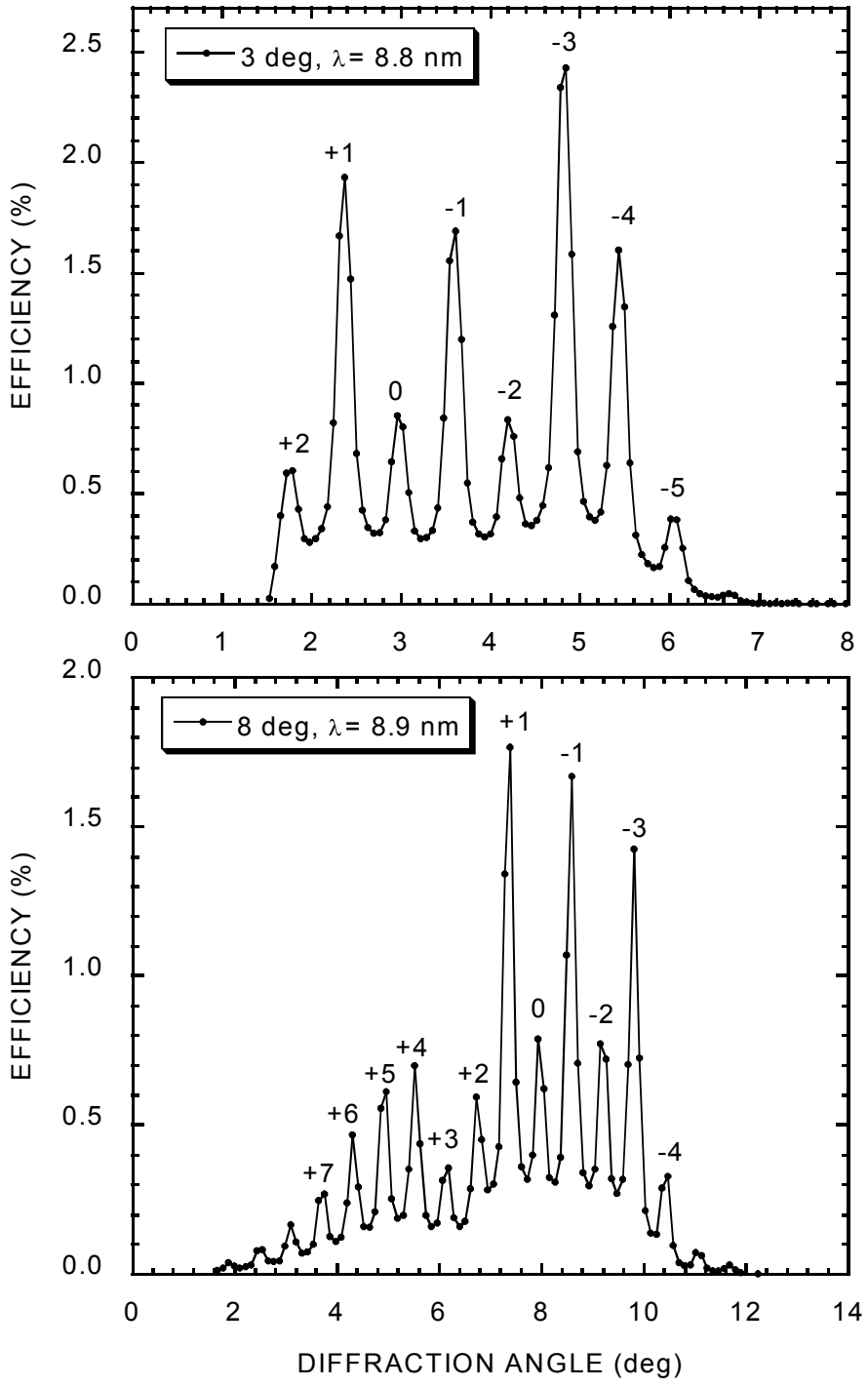

Figure 6.7. The efficiencies of the grating measured in various diffraction orders at 3° and 8° normal-incidence angles.

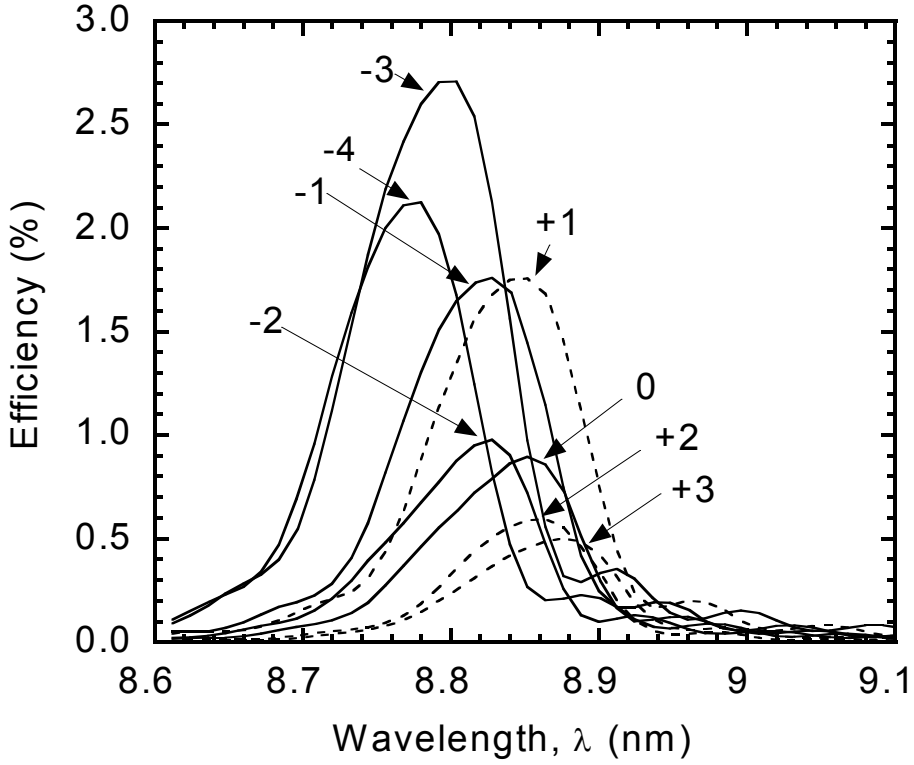

Figure 6.8. The peak efficiencies of the grating measured at 8° angle of incidence as a function of wavelength. The highest measured efficiency was 2.7% in the -3 order at a wavelength of 8.79 nm.

To optimize the peak efficiency of each order, the wavelength was scanned after the detector was aligned at peak angle. As shown in Fig. 6.8, the peak efficiencies as a function of wavelength were measured at 8° from normal incidence. The highest efficiency was 2.7% in the outside third order (m = -3) at a wavelength of 8.79 nm. It should be noted that this is the highest efficiency ever obtained at normal incidence in this wavelength region. Without the Mo/Y multilayer, the grating efficiency would have been zero (below the detection limit). The Mo/Y multilayer dramatically increased the grating efficiencies and enabled the grating to operate in this wavelength region.

6.5 Calculated Grating Efficiency

The multilayer grating efficiency was calculated with the computational model PCGrate developed by Goray and colleagues.[70] The computational model implements the

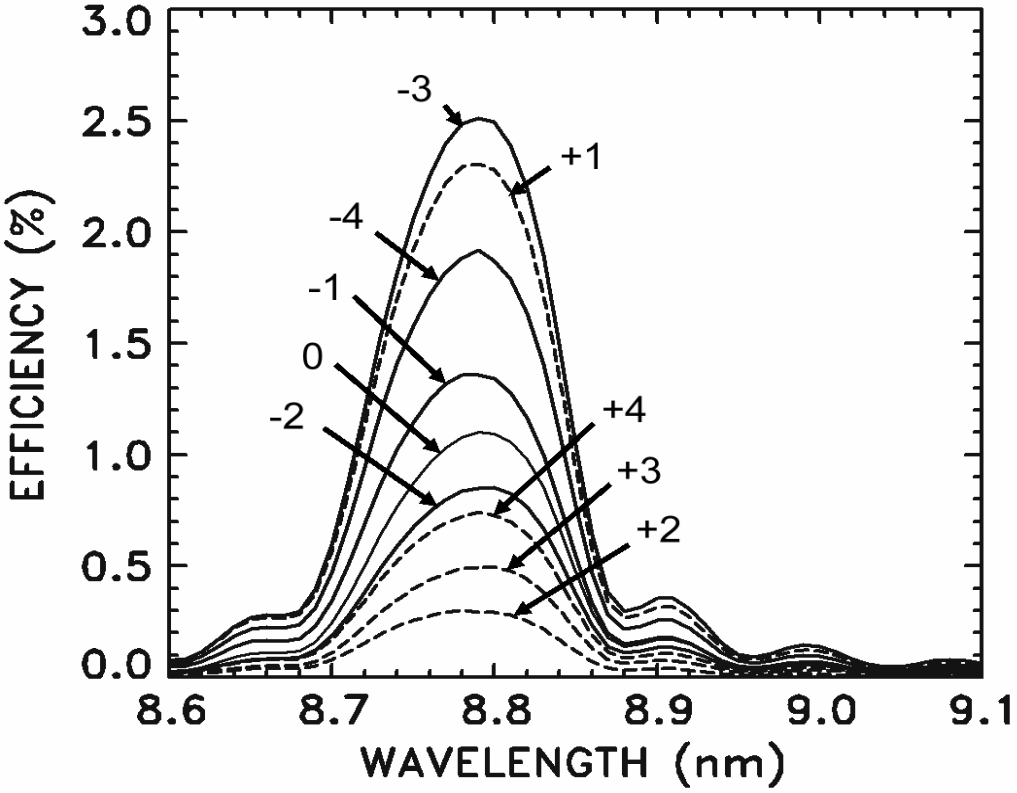

Figure 4.9. The grating efficiencies calculated for 8° angle of incidence as a function of wavelength.

modified integral method to solve the boundary-value problem of electromagnetic radiation incident on a multilayer grating. The calculation accounts for the groove profile of the grating substrate as determined with an AFM, the optical properties of the layers of the multilayer coating and the two polarization components of the incident radiation. The computational model was previously used to analyze the efficiency of MoRu/Be multilayer gratings of the same type as used in this study.[66]

The calculated efficiencies are shown in Fig. 6.9. The calculated peak efficiency in the -3 order is in good agreement with the measured peak efficiency. The calculated efficiencies of the weaker orders in some cases differ from the measured efficiencies in the same manner as found previously in Ref. 66. As discussed in Ref. 71 these differences indicate that the treatment of the micro-roughness in the computational model needs improvement, and this research is in progress.

6.6 Conclusions

The enhancement of the normal-incidence efficiency of a holographic blazed grating by the application of a Mo/Y multilayer coating is reported. The measured peak efficiency in the -3 order was 2.7% at a wavelength of 8.79 nm and is the highest normal-incidence efficiency measured in this wavelength region. The measured efficiency is high enough to make possible the utilization of multilayer gratings for high-resolution spectroscopic studies of solar and astrophysical objects in the 9-nm wavelength region. A flight instrument using such a grating could perform Doppler imaging that would reveal the magnetic fields and the structure of active regions. In addition, the spectra dispersed by the grating could be used to perform other studies such as solar abundance.

Appendix A

Multilayer Principle, Design, and Modeling

Many multilayer systems are well known for their high normal-incidence reflectance in the EUV and soft x-ray wavelength region. A substantial reflectance is attained as a result of addition of the reflected beams from a large number of interfaces. Based on the quarter wave stack idea, a multilayer system consists of alternating layers of high and low refractive index, each of the same optical thickness[**] which is equal to $\lambda/4$, such that the reflected beams perfectly add with equal phase at all boundaries. This geometry is best when both materials are absorption free so the reflectance can approach 100% with the smallest number of bilayers. On the other hand, there is always some absorption in materials in the EUV/soft x-ray region so the thickness of the absorber layer (the higher absorption material as opposed to the spacer for the lower absorption material) is usually reduced while the period thickness is kept constant. When the absorption is so high in the absorber compared to that of the spacer, the absorber layer is reduced to the limit of one atomic layer in analogous to the ideal Bragg crystal (different atomic planes are separated by $\lambda/2$ at normal incidence). Typical symbols used to describe the multilayer structure are the period or bilayer thickness Λ, the thickness ratio

[**] The optical thickness is the product of its geometrical thickness d with the refractive index $\tilde{n}$.

Γ which is defined as the ratio of the absorber thickness and the period thickness, and the surface roughness σ which will be discussed further.

A.1 Selection Rules for Multilayer Materials

The highest possible reflectance can be achieved with the following selection criteria:

(1) Select a material that has low absorption as a spacer material.

(2) Find another material with lowest possible absorption but provides large reflectance coefficient at the boundary with the first material.

(3) Make sure that the two materials do not react or form compound. Also, select the material pair that can be deposited with sharp and smooth boundaries. As a rule of thumb, the roughness $\sigma < 0.1\ \Lambda$ are recommended.

A.2 Reflectance Calculations

The amplitude r_{12} of the reflected field from a single boundary between two materials is given by the well known Fresnel equation[26]

$$r_{12}^{s} = \frac{\tilde{n}_1 \cos\alpha_1 - \tilde{n}_2 \cos\alpha_2}{\tilde{n}_1 \cos\alpha_1 + \tilde{n}_2 \cos\alpha_2}, \text{ for s polarization} \qquad (A.1)$$

$$r_{12}^{p} = \frac{\tilde{n}_1 \cos\alpha_2 - \tilde{n}_2 \cos\alpha_1}{\tilde{n}_1 \cos\alpha_2 + \tilde{n}_2 \cos\alpha_1}, \text{ for p polarization} \qquad (A.2)$$

where $\tilde{n}$ is the complex refractive index and α is the propagation angle with respect to the surface normal. For s polarization, the electric field E is perpendicular to the plane of incidence and the field is parallel to the plane of incidence for p polarization. The angle α_1 is related to α_2 according to the Snell's law

$$\tilde{n}_1 \sin\alpha_1 = \tilde{n}_2 \sin\alpha_2 \qquad (A.3)$$

Considering a multilayer stack that consists of a series of N layers (N+1 interfaces), where the i layer has thickness d_i, and refractive index $\tilde{n}_i$ The reflected amplitude of the i layer is given by

$$r_i = \frac{r_{ij} + r_j e^{2i\varphi_i}}{1 + r_{ij} r_j e^{2i\varphi_i}}, \qquad \text{(A.4)}$$

where $\varphi_i = 2\pi\, d_i \tilde{n}_i \cos\alpha_i / \lambda$; the reflection coefficient r_{ij} is computed from equation (A.1 or A.2). The net reflected amplitude of the multilayer stack can be calculated by applying equation (A.4) recursively. The reflectance (R) which measures the energy reflected from the multilayer is given by

$$R = \left| r^2 \right|. \qquad \text{(A.5)}$$

To account for reflectance loss due to interface imperfections e.g. surface roughness and interdiffusion, the Fresnel reflectance coefficient (equation A.1 and A.2) was multiplied by function w. This function is a Fourier transform of dp/dz, where p(z) is an interface profile function used to describe the change in refractive index across the interface developed by Stearns.[72] Stearns presents four particularly useful interface profiles e.g. error function, exponential, linear, and sinusoidal spatial profiles. The most common factor used to simulate non ideal interfaces is the error function

$$\mathrm{w} = e^{-s^2\sigma^2/2}, \qquad \text{(A.6)}$$

where $S = 4\pi\cos\alpha_i / \lambda$ and σ is the statistic width of the interface in the case of diffuse interface or the rms interfacial roughness in the case of rough interface. In the hard x-ray region, where the complex refractive index is close to unity, equation (A.6) can be simplified to the well-known Debye-Waller factor,

$$w = e^{-\frac{1}{2}\left(\frac{4\pi}{\lambda}\sigma\sin\theta\right)^2}, \qquad (A.7)$$

where the grazing angle in the incidence medium θ is used instead of the angle α.

A.3 Modeling of Multilayers

Three computer programs used to calculate the optical properties of the multilayer mirrors are TF Design, IMD and GIXFIT. TF Design is a DOS-based program written by the Thin Films Group, National Research Council of Canada. This program can calculate the reflectance, transmittance, absorptance, and phase properties of any multilayer systems. In addition to the design, analysis and characterization of multilayers, TF Design was also used to control the magnetron sputtering process throughout this study. A good thing about this program is that it allows calculations both in optical mode where the layer thickness is defined as optical thickness and in metric mode where the thickness is just the geometrical thickness. In metric mode, peak wavelength of a multilayer changes with the thickness ratio Γ. Therefore an optimization for Γ for a specific wavelength can be done more accurately in optical mode with the use of TF Design.

IMD is a program written in IDL which can also be used in the design and simulation of various optical properties of multilayer films including the previously mentioned properties. IMD provides several built-in optimization routines which allow fitting of the reflectance data at grazing and normal incidence at any wavelengths of interest. The user-defined optical constants can be used in addition to the ones that can be generated within the program using the atomic scattering factors. Imperfections at the interface, those that introduced by Stearns, are also included in IMD. An interactive visualization tool, IMDXPLOT is used to display the results so that one can vary any

given parameter and see the resulting effect on the optical functions (in one or two dimensions) in real time.

GAXFIT is a program written in FORTRAN and is adapted from a generic genetic algorithm (GA) code written by Carol at the Universities of Illinois.[73] This program has been proved to provide reliable global solution for the analysis of XRD data which have complex solution space. About GAXFIT, it was originally applied to Mo/Si multilayer based on the following model: for each bilayer period, a multilayer is composed of four layers: the pure molybdenum and silicon, and the two $MoSi_2$ interlayers. The interface roughness is assumed to produce a Gaussian composition gradient of width σ and assumed to be the same at all interfaces. In addition, the program allows adding two more layers at the top which correspond to a partially oxidized top layer of silicon. The x-ray reflectance is calculated based on the standard matrix method.[74] In order to fit XRD data for other multilayer systems e.g. Mo/Y, a zero thickness for the two $MoSi_2$ interlayers was assumed and a reasonably good fit was achieved with very short calculation time.

Appendix B

IDL Computer Codes and Optical Constant Data of Yttrium and Molybdenum

This appendix contains computer codes written in Interactive Data Language (IDL) for dispersion and sum rules calculations. IDL is software for data analysis and visualization which is available from Research Systems, Inc. (http://www.rsinc.com). The measured absorption β and the calculated dispersion δ of yttrium in the 50-1300 eV and molybdenum in the 60-1300 eV region are also given.

B. 1 Kramers-Kronig Integral

The following IDL code calculates the dispersive part δ from the absorption part β of the complex refractive index $\tilde{n} = 1 - \delta + i\beta$, based on the Kramers-Kronig integral given in Eq. 4.5 assuming that β is a piecewise linear function within the energy interval [E(j), E(j+1)]. A complete set of β from energy zero to infinity is required in this calculation.

```
;The program reads two-column data of Energy and Beta
;Then calculates Delta at energy Eo(j) using the Kramers-Kronig Integral
;Assuming Beta is a piecewise linear function within the energy interval [E(j), E(j+1)]
;E(0) is the minimum input energy and Beta is assumed to be constant between E=0 eV to E=E(0) eV
;Benjawan Kjornrattanawanich 8/31/2000
pro caldelta2
close, 1 & openr, 1, 'betafile.txt'  ;Open a formatted file name betafile on file unit 1
i=0 & dat=''
while not eof(1) do begin
        readf, 1, dat
        i=i+1                   ;Count lines
```

```
endwhile
close, 1
print,'the number of lines are', i
print, format=' (7x,"I", 4x, "Energy(eV)", 2x, "Beta") ' ; Format the header
print,'=========================================='
E =fltarr(i)                    ;Energy E
Eo =fltarr(i)
Beta =fltarr(i)                 ;Beta value
Bo =fltarr(i)
openr,1,'betafile.txt'
i= 0 & dat=''
while not eof(1) do begin
        readf, 1, dat
        reads,dat,a,b           ;Read string dat and write into 2 variables a and b
        E(i)= a & Eo(i)= a & Beta(i)= b*E(i) & Bo(i)=b*E(i)
        i=i+1
        print,i,E(i-1),Beta(i-1)
endwhile
close,1
openw,1,'deltafile2'            ;open the result file name deltafile2
For j=1, i-1 do begin
;Integration from 0 to E(0)
a1= (Eo(j)+E(0))/(Eo(j)-E(0))
a1=alog(abs(a1))
sum=a1*(Beta(0)-Bo(j))/2/Eo(j)
;Piecewise integration from E(0) to E(i)
For k=0,i-2  do begin
        m= (Beta(k+1)-Beta(k))/(E(k+1)-E(k))
        c= Beta(k)-(m*E(k))
If (Eo(j) GE E(k)) and (Eo(j) LE E(k+1)) then begin
a1=(E(k+1)+Eo(j))/(E(k)+Eo(j))
sum=sum-(m*alog(abs(a1)))
endif else begin
a1= (E(k+1)^2-Eo(j)^2)/(E(k)^2-Eo(j)^2)
a1=alog(abs(a1))
b1=(Eo(j)+E(k+1))*(Eo(j)-E(k))/(Eo(j)-E(k+1))/(Eo(j)+E(k))
b1=alog(abs(b1))
sum=sum-(m*0.5*a1)+(b1*(c- Bo(j))/2/Eo(j))
endelse
endfor
; pi=3.141592654, delta=sum*2/pi
delta= sum*2/3.141592654
printf, 1 ,j,Eo(j),delta
print, j, Eo(j), delta
endfor
close, 1
end
```

B.2 Optical Sum Rules Integral

This IDL code calculates the sum rule in terms of β , ε_2, and Im(ε^{-1}). Different forms of sum rule provide a means of relating different physical properties without model fits to spectra and are valuable as self-consistency tests.

```
pro sumrules
;z= 39 ; atomic number of Y
z= 42 ; atomic number for Mo
z= z-((z/82.5)^2.37)
print, z
close, 1 & openr, 1, 'betafile.txt'  ;open a formatted file name betafile on file unit 1
i=0 & dat=''
while not eof(1) do begin
        readf, 1, dat
        i=i+1                   ;count lines
endwhile
close, 1
E =fltarr(i)                            ;energy E
Eo =fltarr(i)
Beta =fltarr(i)             ;Beta value
Bo =fltarr(i)
openr,1,'betafile.txt'
i= 0 & dat=''
while not eof(1) do begin
        readf, 1, dat
        reads,dat,a,b           ; read string dat and write into 2 variables a and b
        E(i)= a & Eo(i)= a & Beta(i)= b & Bo(i)=b
        i=i+1
endwhile
close,1
openw,1,'sumdata'
For j=0, i-1 do begin
;piecewise integration from E(0) to E(I)
sum= 0
For k=j,i-2  do begin
        m= (Beta(k+1)-Beta(k))/(E(k+1)-E(k))
        c= Beta(k)-(m*E(k))
sum=sum+(m*(E(k+1)^3-E(k)^3)/3)+(c*(E(k+1)^2-E(k)^2)/2)
endfor
;Neff= z-(sum*0.030571949) ; for Y (beta sum), bulk density= 4.457
;Neff= z-(sum*0.030571949*0.5) ; for Y (e2,Im(-1/e) sum)
Neff= z-(sum*0.014392381) ; for Mo (beta sum)
;Neff= z-(sum*0.014392381*0.5) ; for Mo (e2,Im(-1/e) sum)
printf, 1 ,j,Eo(j),Neff
print, j, Eo(j), Neff
endfor
close, 1
end
```

B.3 Measured Optical Constants of Yttrium and Molybdenum

Energy (eV)	Yttrium-β	Yttrium-δ	Energy (eV)	Molybdenum-β	Molybdenum-δ
50.00	3.6130E-02	1.4074E-01	60.00	1.3099E-01	2.3090E-01
50.40	3.4444E-02	1.2862E-01	60.40	1.2766E-01	2.3528E-01
50.80	3.4008E-02	1.2426E-01	60.80	1.2242E-01	2.3448E-01
51.20	3.2630E-02	1.2064E-01	61.21	1.1720E-01	2.3231E-01
51.60	3.2580E-02	1.1759E-01	61.61	1.1319E-01	2.3010E-01
52.00	3.1357E-02	1.1511E-01	62.01	1.0835E-01	2.2793E-01
52.40	3.0725E-02	1.1270E-01	62.41	1.0414E-01	2.2542E-01
52.80	2.9443E-02	1.1046E-01	62.81	9.9726E-02	2.2267E-01
53.20	2.8467E-02	1.0800E-01	63.20	9.6440E-02	2.2015E-01
53.60	2.7961E-02	1.0600E-01	63.61	9.2204E-02	2.1783E-01
54.00	2.6550E-02	1.0407E-01	64.01	8.8240E-02	2.1481E-01
54.41	2.5538E-02	1.0173E-01	64.40	8.5387E-02	2.1193E-01
54.80	2.4994E-02	9.9584E-02	64.81	8.2508E-02	2.0988E-01
55.20	2.4452E-02	9.7848E-02	65.20	7.8462E-02	2.0749E-01
55.61	2.3551E-02	9.6199E-02	65.60	7.5579E-02	2.0471E-01
56.00	2.2725E-02	9.4457E-02	66.01	7.2663E-02	2.0242E-01
56.40	2.2002E-02	9.2824E-02	66.41	6.9268E-02	1.9995E-01
56.80	2.1050E-02	9.1151E-02	66.81	6.6591E-02	1.9746E-01
57.20	2.0351E-02	8.9411E-02	67.21	6.3359E-02	1.9501E-01
57.60	1.9720E-02	8.7790E-02	67.60	6.0617E-02	1.9237E-01
58.00	1.9065E-02	8.6266E-02	68.01	5.7885E-02	1.8983E-01
58.40	1.8353E-02	8.4722E-02	68.41	5.5195E-02	1.8726E-01
58.80	1.7792E-02	8.3223E-02	68.81	5.2604E-02	1.8466E-01
59.20	1.7140E-02	8.1774E-02	69.21	5.0133E-02	1.8207E-01
59.60	1.6590E-02	8.0347E-02	69.61	4.7717E-02	1.7945E-01
60.00	1.5921E-02	7.8896E-02	70.01	4.5731E-02	1.7736E-01
60.40	1.5508E-02	7.7464E-02	70.40	4.1863E-02	1.7454E-01
60.80	1.5049E-02	7.6193E-02	70.81	3.9998E-02	1.7069E-01
61.20	1.4427E-02	7.4859E-02	71.20	3.9026E-02	1.6784E-01
61.60	1.4060E-02	7.3535E-02	71.61	3.7082E-02	1.6538E-01
62.00	1.3543E-02	7.2244E-02	72.00	3.5481E-02	1.6265E-01
62.40	1.3262E-02	7.1003E-02	72.40	3.4040E-02	1.6004E-01
62.80	1.2820E-02	6.9853E-02	72.81	3.2644E-02	1.5752E-01
63.20	1.2431E-02	6.8701E-02	73.21	3.1352E-02	1.5512E-01
63.60	1.1937E-02	6.7484E-02	73.60	2.9925E-02	1.5270E-01
64.00	1.1703E-02	6.6252E-02	74.01	2.8861E-02	1.5032E-01
64.40	1.1497E-02	6.5212E-02	74.40	2.7709E-02	1.4814E-01
64.80	1.1101E-02	6.4182E-02	74.81	2.6577E-02	1.4608E-01
65.20	1.0841E-02	6.3136E-02	75.21	2.5073E-02	1.4384E-01
65.60	1.0494E-02	6.2107E-02	75.61	2.4138E-02	1.4149E-01
66.00	1.0254E-02	6.1070E-02	76.01	2.3233E-02	1.3941E-01
66.40	1.0017E-02	6.0095E-02	76.41	2.2231E-02	1.3745E-01
66.80	9.7792E-03	5.9145E-02	76.81	2.1088E-02	1.3542E-01
67.20	9.5533E-03	5.8218E-02	77.21	2.0052E-02	1.3324E-01
67.60	9.3458E-03	5.7326E-02	77.61	1.9350E-02	1.3116E-01
68.00	9.0999E-03	5.6444E-02	78.01	1.8515E-02	1.2928E-01
68.41	8.8999E-03	5.5566E-02	78.41	1.7505E-02	1.2724E-01
68.81	8.7049E-03	5.4712E-02	78.81	1.7022E-02	1.2529E-01
69.21	8.5264E-03	5.3882E-02	79.21	1.6102E-02	1.2345E-01
69.61	8.3824E-03	5.3106E-02	79.61	1.5514E-02	1.2155E-01
70.00	8.2079E-03	5.2434E-02	80.01	1.4768E-02	1.1970E-01
70.40	7.7470E-03	5.1617E-02	80.41	1.4265E-02	1.1789E-01

72.01	7.3371E-03	4.8360E-02	80.81	1.3595E-02	1.1614E-01
72.40	7.3524E-03	4.7684E-02	81.21	1.3059E-02	1.1439E-01
72.80	7.2528E-03	4.7099E-02	81.61	1.2401E-02	1.1261E-01
73.20	7.1251E-03	4.6547E-02	82.01	1.2002E-02	1.1078E-01
73.60	6.8154E-03	4.5896E-02	82.41	1.1760E-02	1.0919E-01
74.00	6.7027E-03	4.5135E-02	82.81	1.1139E-02	1.0761E-01
74.40	6.7301E-03	4.4506E-02	83.21	1.0827E-02	1.0593E-01
74.80	6.6161E-03	4.3958E-02	83.61	1.0555E-02	1.0441E-01
75.20	6.5224E-03	4.3426E-02	84.01	1.0115E-02	1.0293E-01
75.61	6.2752E-03	4.2817E-02	84.41	9.7942E-03	1.0137E-01
76.00	6.2738E-03	4.2202E-02	84.81	9.5408E-03	9.9869E-02
76.40	6.1697E-03	4.1675E-02	85.21	9.3540E-03	9.8466E-02
76.80	6.0911E-03	4.1187E-02	85.61	9.0634E-03	9.7113E-02
77.21	5.8397E-03	4.0633E-02	86.01	8.8449E-03	9.5770E-02
77.60	5.7757E-03	4.0014E-02	86.41	8.5335E-03	9.4399E-02
78.00	5.7449E-03	3.9484E-02	86.81	8.4652E-03	9.3087E-02
78.41	5.6576E-03	3.8990E-02	87.21	8.2544E-03	9.1883E-02
78.80	5.5600E-03	3.8486E-02	87.61	8.0431E-03	9.0667E-02
79.20	5.4761E-03	3.7970E-02	88.01	7.8382E-03	8.9445E-02
79.60	5.4436E-03	3.7496E-02	88.41	7.7483E-03	8.8303E-02
80.01	5.3310E-03	3.7036E-02	88.81	7.4490E-03	8.7156E-02
80.41	5.2400E-03	3.6539E-02	89.21	7.3660E-03	8.5992E-02
80.81	5.2274E-03	3.6090E-02	89.61	7.1798E-03	8.4899E-02
81.21	5.1002E-03	3.5645E-02	90.01	7.0409E-03	8.3816E-02
81.61	5.0691E-03	3.5196E-02	90.41	6.8684E-03	8.2728E-02
82.01	4.9590E-03	3.4742E-02	90.81	6.7898E-03	8.1674E-02
82.41	4.9773E-03	3.4320E-02	91.21	6.6486E-03	8.0664E-02
82.80	4.8596E-03	3.3922E-02	91.60	6.5542E-03	7.9671E-02
83.20	4.8081E-03	3.3497E-02	92.01	6.4239E-03	7.8706E-02
83.61	4.7344E-03	3.3074E-02	92.41	6.2860E-03	7.7749E-02
84.01	4.7093E-03	3.2672E-02	92.81	6.1622E-03	7.6788E-02
84.41	4.6297E-03	3.2274E-02	93.21	6.0655E-03	7.5836E-02
84.81	4.6081E-03	3.1876E-02	93.61	6.0125E-03	7.4943E-02
85.21	4.5545E-03	3.1495E-02	94.01	5.8547E-03	7.4065E-02
85.61	4.5391E-03	3.1130E-02	94.41	5.7636E-03	7.3157E-02
86.01	4.4824E-03	3.0778E-02	94.60	5.7419E-03	7.2742E-02
86.40	4.4539E-03	3.0434E-02	94.80	5.6391E-03	7.2302E-02
86.80	4.3641E-03	3.0079E-02	95.00	5.6169E-03	7.1839E-02
87.20	4.3533E-03	2.9722E-02	95.20	5.6099E-03	7.1433E-02
87.60	4.3158E-03	2.9393E-02	95.40	5.5152E-03	7.1011E-02
88.00	4.2621E-03	2.9067E-02	95.60	5.4943E-03	7.0560E-02
88.41	4.2087E-03	2.8729E-02	95.80	5.4994E-03	7.0165E-02
88.80	4.1839E-03	2.8398E-02	96.01	5.3858E-03	6.9742E-02
89.21	4.1465E-03	2.8073E-02	96.20	5.4145E-03	6.9320E-02
89.60	4.1318E-03	2.7774E-02	96.40	5.3344E-03	6.8915E-02
90.01	4.0618E-03	2.7462E-02	96.60	5.3465E-03	6.8493E-02
90.41	4.0604E-03	2.7152E-02	96.80	5.3326E-03	6.8120E-02
90.81	4.0189E-03	2.6871E-02	97.00	5.2457E-03	6.7711E-02
91.20	3.9818E-03	2.6581E-02	97.20	5.3014E-03	6.7325E-02
91.60	3.9530E-03	2.6300E-02	97.41	5.2021E-03	6.6951E-02
92.00	3.8981E-03	2.6012E-02	97.60	5.1954E-03	6.6549E-02
92.41	3.8926E-03	2.5726E-02	97.80	5.1703E-03	6.6165E-02
92.80	3.8560E-03	2.5459E-02	98.00	5.1742E-03	6.5792E-02
93.20	3.8468E-03	2.5208E-02	98.20	5.1278E-03	6.5445E-02
93.61	3.7821E-03	2.4944E-02	98.40	5.0574E-03	6.5041E-02
94.01	3.7869E-03	2.4700E-02	98.60	5.0897E-03	6.4647E-02

94.40	3.6935E-03	2.4439E-02	98.80	5.0691E-03	6.4299E-02
94.81	3.7203E-03	2.4177E-02	99.00	5.0664E-03	6.3932E-02
95.21	3.6670E-03	2.3953E-02	99.20	5.0615E-03	6.3590E-02
95.61	3.6572E-03	2.3747E-02	99.40	5.0498E-03	6.3271E-02
96.01	3.5178E-03	2.3502E-02	99.60	4.9813E-03	6.2938E-02
96.40	3.5049E-03	2.3214E-02	99.80	4.9118E-03	6.2533E-02
96.81	3.4831E-03	2.2968E-02	100.00	4.9906E-03	6.2178E-02
97.21	3.4650E-03	2.2734E-02	100.20	4.9472E-03	6.1869E-02
97.61	3.4312E-03	2.2508E-02	100.40	4.9038E-03	6.1511E-02
98.00	3.3906E-03	2.2279E-02	100.60	4.9258E-03	6.1170E-02
98.41	3.3553E-03	2.2045E-02	100.80	4.8900E-03	6.0831E-02
98.81	3.3391E-03	2.1820E-02	101.01	4.9226E-03	6.0495E-02
99.21	3.2924E-03	2.1591E-02	101.20	4.9183E-03	6.0199E-02
99.61	3.2794E-03	2.1348E-02	101.40	4.9056E-03	5.9919E-02
100.01	3.3097E-03	2.1160E-02	101.61	4.8097E-03	5.9574E-02
100.41	3.2359E-03	2.0970E-02	101.80	4.8612E-03	5.9239E-02
100.80	3.2134E-03	2.0742E-02	102.00	4.8295E-03	5.8937E-02
101.21	3.2251E-03	2.0548E-02	102.20	4.8344E-03	5.8628E-02
101.61	3.1683E-03	2.0356E-02	102.40	4.8089E-03	5.8330E-02
102.00	3.1682E-03	2.0158E-02	102.60	4.7935E-03	5.8022E-02
102.41	3.1379E-03	1.9975E-02	102.80	4.7948E-03	5.7720E-02
102.80	3.1286E-03	1.9812E-02	103.00	4.7970E-03	5.7450E-02
103.21	3.0641E-03	1.9648E-02	103.20	4.7425E-03	5.7176E-02
103.61	2.9972E-03	1.9452E-02	103.40	4.7135E-03	5.6897E-02
104.00	2.9677E-03	1.9254E-02	103.60	4.6187E-03	5.6591E-02
104.41	2.9168E-03	1.9057E-02	103.80	4.5730E-03	5.6238E-02
104.81	2.8960E-03	1.8858E-02	104.00	4.5744E-03	5.5883E-02
105.20	2.8603E-03	1.8667E-02	104.20	4.6062E-03	5.5565E-02
105.61	2.8516E-03	1.8482E-02	104.40	4.6233E-03	5.5285E-02
106.00	2.8259E-03	1.8315E-02	104.60	4.5715E-03	5.4967E-02
106.41	2.8004E-03	1.8162E-02	104.80	4.6321E-03	5.4636E-02
106.80	2.7091E-03	1.7998E-02	105.00	4.6802E-03	5.4355E-02
106.98	2.6634E-03	1.7891E-02	105.20	4.7428E-03	5.4122E-02
107.50	2.6470E-03	1.7600E-02	105.40	4.7056E-03	5.3894E-02
108.01	2.6371E-03	1.7347E-02	105.61	4.6920E-03	5.3627E-02
108.51	2.6591E-03	1.7128E-02	105.80	4.6569E-03	5.3326E-02
109.01	2.6291E-03	1.6926E-02	106.00	4.7791E-03	5.3082E-02
109.50	2.6111E-03	1.6703E-02	106.20	4.6876E-03	5.2863E-02
110.01	2.6311E-03	1.6503E-02	106.40	4.7255E-03	5.2590E-02
110.51	2.5994E-03	1.6318E-02	106.60	4.7327E-03	5.2371E-02
111.01	2.5964E-03	1.6130E-02	106.80	4.7083E-03	5.2150E-02
111.51	2.5544E-03	1.5938E-02	107.00	4.6539E-03	5.1908E-02
112.01	2.5623E-03	1.5746E-02	107.20	4.6206E-03	5.1625E-02
112.51	2.5338E-03	1.5572E-02	107.40	4.6627E-03	5.1379E-02
113.01	2.5135E-03	1.5390E-02	107.61	4.6096E-03	5.1142E-02
113.51	2.4916E-03	1.5206E-02	107.80	4.6163E-03	5.0896E-02
114.01	2.4724E-03	1.5027E-02	108.00	4.5716E-03	5.0641E-02
114.51	2.4555E-03	1.4843E-02	108.20	4.5894E-03	5.0392E-02
115.01	2.4614E-03	1.4683E-02	108.40	4.5352E-03	5.0136E-02
115.51	2.4004E-03	1.4510E-02	108.60	4.5581E-03	4.9855E-02
116.01	2.4164E-03	1.4323E-02	108.80	4.5936E-03	4.9615E-02
116.51	2.4010E-03	1.4162E-02	109.00	4.6055E-03	4.9397E-02
117.01	2.3958E-03	1.4003E-02	109.01	4.6043E-03	4.9388E-02
117.51	2.3856E-03	1.3853E-02	109.51	4.6078E-03	4.8834E-02
118.01	2.3591E-03	1.3700E-02	110.01	4.6205E-03	4.8318E-02
118.51	2.3457E-03	1.3543E-02	110.51	4.5190E-03	4.7780E-02

119.01	2.3350E-03	1.3398E-02	111.01	4.5099E-03	4.7201E-02
119.51	2.3057E-03	1.3248E-02	111.51	4.5126E-03	4.6687E-02
120.01	2.2991E-03	1.3101E-02	112.01	4.4330E-03	4.6142E-02
120.51	2.2741E-03	1.2962E-02	112.51	4.4690E-03	4.5622E-02
121.01	2.2464E-03	1.2816E-02	113.01	4.3797E-03	4.5103E-02
121.51	2.2243E-03	1.2659E-02	113.51	4.4132E-03	4.4574E-02
122.01	2.2309E-03	1.2525E-02	114.01	4.3892E-03	4.4091E-02
122.51	2.1891E-03	1.2388E-02	114.51	4.3450E-03	4.3580E-02
123.01	2.1910E-03	1.2257E-02	115.01	4.3813E-03	4.3079E-02
123.51	2.1458E-03	1.2128E-02	115.51	4.3772E-03	4.2629E-02
124.01	2.1176E-03	1.1982E-02	116.01	4.3420E-03	4.2157E-02
124.50	2.0980E-03	1.1843E-02	116.51	4.3632E-03	4.1677E-02
125.01	2.0627E-03	1.1698E-02	117.01	4.4212E-03	4.1281E-02
125.51	2.0501E-03	1.1547E-02	117.51	4.3291E-03	4.0873E-02
126.01	2.0443E-03	1.1408E-02	118.01	4.3223E-03	4.0417E-02
126.51	2.0418E-03	1.1289E-02	118.51	4.3196E-03	3.9982E-02
127.01	1.9993E-03	1.1162E-02	119.01	4.3391E-03	3.9583E-02
127.51	1.9902E-03	1.1026E-02	119.51	4.3181E-03	3.9203E-02
128.01	1.9627E-03	1.0902E-02	120.01	4.2812E-03	3.8811E-02
128.51	1.9383E-03	1.0763E-02	120.51	4.2657E-03	3.8417E-02
129.01	1.9199E-03	1.0612E-02	121.01	4.2394E-03	3.8049E-02
129.51	1.9420E-03	1.0481E-02	121.51	4.1591E-03	3.7632E-02
130.01	1.9245E-03	1.0370E-02	122.01	4.2114E-03	3.7238E-02
130.51	1.9110E-03	1.0247E-02	122.51	4.1615E-03	3.6877E-02
131.01	1.9045E-03	1.0131E-02	123.01	4.1778E-03	3.6514E-02
131.50	1.8758E-03	1.0007E-02	123.51	4.1337E-03	3.6173E-02
132.01	1.8848E-03	9.8878E-03	124.01	4.0999E-03	3.5822E-02
132.51	1.8532E-03	9.7766E-03	124.51	4.0321E-03	3.5441E-02
133.01	1.8394E-03	9.6501E-03	125.01	4.0714E-03	3.5079E-02
133.51	1.8354E-03	9.5325E-03	125.51	4.0207E-03	3.4754E-02
134.01	1.8256E-03	9.4253E-03	126.01	3.9929E-03	3.4409E-02
134.51	1.7976E-03	9.3074E-03	126.51	3.9533E-03	3.4061E-02
135.01	1.7944E-03	9.1900E-03	127.01	3.9316E-03	3.3707E-02
135.51	1.7709E-03	9.0720E-03	127.51	3.9116E-03	3.3352E-02
136.01	1.7751E-03	8.9561E-03	128.01	3.9527E-03	3.3036E-02
136.51	1.7547E-03	8.8423E-03	128.51	3.9055E-03	3.2752E-02
137.01	1.7589E-03	8.7314E-03	129.01	3.8551E-03	3.2429E-02
137.51	1.7410E-03	8.6197E-03	129.51	3.8319E-03	3.2111E-02
138.01	1.7513E-03	8.5118E-03	130.01	3.7805E-03	3.1795E-02
138.51	1.7431E-03	8.4190E-03	130.51	3.7403E-03	3.1461E-02
139.01	1.7215E-03	8.3209E-03	131.01	3.6936E-03	3.1110E-02
139.50	1.6919E-03	8.2051E-03	140.98	3.9104E-03	2.5754E-02
140.01	1.7045E-03	8.0918E-03	141.50	3.9202E-03	2.5536E-02
140.51	1.6925E-03	7.9962E-03	142.01	3.9252E-03	2.5334E-02
141.00	1.6784E-03	7.8886E-03	142.51	3.9120E-03	2.5138E-02
141.51	1.6878E-03	7.7920E-03	143.01	3.8854E-03	2.4918E-02
142.01	1.6719E-03	7.7111E-03	143.51	3.9058E-03	2.4699E-02
142.51	1.6316E-03	7.6067E-03	144.01	3.9222E-03	2.4523E-02
143.01	1.6362E-03	7.4954E-03	144.51	3.8698E-03	2.4325E-02
143.51	1.6464E-03	7.4368E-03	145.01	3.8774E-03	2.4106E-02
144.01	1.5386E-03	7.4262E-03	145.51	3.8863E-03	2.3918E-02
144.01	1.4804E-03	7.4269E-03	146.01	3.8648E-03	2.3732E-02
144.51	1.5585E-03	7.1408E-03	146.51	3.8406E-03	2.3520E-02
145.01	1.5252E-03	7.0211E-03	147.01	3.8806E-03	2.3335E-02
145.51	1.5914E-03	6.9009E-03	147.51	3.8403E-03	2.3163E-02
146.01	1.6056E-03	6.8387E-03	148.51	3.8258E-03	2.2776E-02

146.50	1.5761E-03	6.7557E-03	149.01	3.8312E-03	2.2596E-02
147.01	1.5713E-03	6.6657E-03	149.51	3.8064E-03	2.2414E-02
147.50	1.5202E-03	6.5522E-03	150.01	3.8195E-03	2.2234E-02
148.01	1.5458E-03	6.4331E-03	150.51	3.7999E-03	2.2062E-02
148.51	1.5198E-03	6.3186E-03	151.01	3.8047E-03	2.1889E-02
149.01	1.5645E-03	6.2090E-03	151.51	3.7929E-03	2.1721E-02
149.51	1.5731E-03	6.1381E-03	152.01	3.7952E-03	2.1563E-02
150.01	1.5444E-03	6.0500E-03	152.51	3.7606E-03	2.1401E-02
150.51	1.5269E-03	5.9209E-03	153.01	3.7594E-03	2.1230E-02
151.00	1.6139E-03	5.8545E-03	153.51	3.7417E-03	2.1070E-02
151.51	1.5171E-03	5.7854E-03	154.01	3.7265E-03	2.0905E-02
152.01	1.5442E-03	5.6838E-03	154.51	3.7191E-03	2.0744E-02
152.51	1.4626E-03	5.5675E-03	155.01	3.6996E-03	2.0584E-02
153.01	1.5059E-03	5.4303E-03	155.51	3.6969E-03	2.0424E-02
153.51	1.4980E-03	5.3304E-03	156.01	3.6979E-03	2.0289E-02
154.01	1.4970E-03	5.2247E-03	156.51	3.6317E-03	2.0132E-02
154.51	1.4505E-03	5.0791E-03	157.01	3.6409E-03	1.9951E-02
155.01	1.4715E-03	4.8536E-03	157.51	3.6413E-03	1.9804E-02
155.51	1.7247E-03	4.7640E-03	158.01	3.6392E-03	1.9672E-02
156.01	1.7205E-03	4.7777E-03	158.51	3.5968E-03	1.9532E-02
156.51	1.7437E-03	4.7556E-03	159.01	3.5770E-03	1.9373E-02
157.01	1.6261E-03	4.6366E-03	159.51	3.5724E-03	1.9227E-02
157.51	1.7913E-03	4.5432E-03	160.01	3.5473E-03	1.9089E-02
158.01	1.7184E-03	4.5012E-03	160.51	3.5195E-03	1.8934E-02
158.51	1.8033E-03	4.4595E-03	161.01	3.5190E-03	1.8791E-02
159.01	1.6531E-03	4.3820E-03	161.51	3.4858E-03	1.8651E-02
159.51	1.7265E-03	4.2540E-03	162.01	3.4714E-03	1.8499E-02
160.01	1.6925E-03	4.1857E-03	162.51	3.4645E-03	1.8359E-02
160.51	1.6458E-03	4.0479E-03	163.01	3.4449E-03	1.8229E-02
161.01	1.7030E-03	3.9148E-03	163.51	3.3990E-03	1.8079E-02
161.51	1.7082E-03	3.7962E-03	164.01	3.4027E-03	1.7923E-02
162.01	1.7743E-03	3.6787E-03	164.51	3.3945E-03	1.7789E-02
162.51	1.8174E-03	3.5812E-03	165.01	3.3756E-03	1.7653E-02
163.01	1.8920E-03	3.5117E-03	165.51	3.3663E-03	1.7515E-02
163.51	1.8864E-03	3.4393E-03	166.01	3.3517E-03	1.7381E-02
164.01	1.9297E-03	3.3380E-03	166.51	3.3407E-03	1.7245E-02
164.51	1.9695E-03	3.2445E-03	167.01	3.3258E-03	1.7110E-02
165.01	2.0528E-03	3.1858E-03	167.51	3.3257E-03	1.6982E-02
165.51	2.0409E-03	3.1186E-03	168.01	3.3072E-03	1.6858E-02
166.01	2.1023E-03	3.0272E-03	168.51	3.2984E-03	1.6732E-02
166.51	2.1539E-03	2.9622E-03	169.01	3.2822E-03	1.6611E-02
167.01	2.2069E-03	2.9100E-03	169.51	3.2600E-03	1.6484E-02
167.51	2.2525E-03	2.8865E-03	170.01	3.2524E-03	1.6356E-02
168.01	2.2186E-03	2.8391E-03	170.51	3.2358E-03	1.6233E-02
168.51	2.2357E-03	2.7496E-03	171.01	3.2263E-03	1.6111E-02
169.01	2.2854E-03	2.6918E-03	171.51	3.2091E-03	1.5990E-02
169.51	2.2674E-03	2.6303E-03	172.01	3.2012E-03	1.5868E-02
170.01	2.3060E-03	2.5637E-03	172.51	3.1998E-03	1.5760E-02
170.51	2.2802E-03	2.4965E-03	173.01	3.1634E-03	1.5648E-02
171.01	2.2726E-03	2.3784E-03	173.51	3.1511E-03	1.5522E-02
171.51	2.3433E-03	2.2877E-03	174.01	3.1406E-03	1.5403E-02
172.01	2.3290E-03	2.1978E-03	174.51	3.1360E-03	1.5295E-02
172.51	2.4028E-03	2.1144E-03	175.01	3.1127E-03	1.5192E-02
173.01	2.3630E-03	2.0060E-03	175.51	3.0859E-03	1.5079E-02
173.51	2.4689E-03	1.8888E-03	176.01	3.0685E-03	1.4962E-02
174.01	2.4898E-03	1.8032E-03	176.51	3.0422E-03	1.4842E-02

174.50	2.5682E-03	1.7088E-03	177.01	3.0452E-03	1.4729E-02
175.01	2.6089E-03	1.6262E-03	177.51	3.0233E-03	1.4625E-02
175.51	2.6591E-03	1.5273E-03	178.01	3.0131E-03	1.4524E-02
176.01	2.7278E-03	1.4276E-03	178.51	2.9757E-03	1.4413E-02
176.51	2.8056E-03	1.3359E-03	179.01	2.9880E-03	1.4317E-02
177.01	2.8792E-03	1.2527E-03	179.51	2.9508E-03	1.4281E-02
177.51	2.9342E-03	1.1503E-03	180.01	2.7121E-03	1.4090E-02
178.01	3.0363E-03	1.0292E-03	181.01	2.9349E-03	1.3735E-02
178.51	3.1720E-03	9.2169E-04	182.01	2.9163E-03	1.3617E-02
178.98	3.3384E-03	8.6209E-04	183.01	2.7939E-03	1.3388E-02
180.01	3.6198E-03	8.2603E-04	184.01	2.8613E-03	1.3167E-02
181.01	3.8236E-03	7.9843E-04	185.01	2.7591E-03	1.2952E-02
182.02	4.0978E-03	8.0021E-04	186.01	2.8384E-03	1.2735E-02
183.02	4.3389E-03	9.1500E-04	187.01	2.8162E-03	1.2609E-02
184.01	4.4218E-03	1.0415E-03	188.01	2.7039E-03	1.2423E-02
185.01	4.4935E-03	1.1136E-03	189.01	2.6521E-03	1.2156E-02
186.01	4.5748E-03	1.1791E-03	190.01	2.7433E-03	1.1962E-02
187.01	4.6485E-03	1.2913E-03	191.01	2.6914E-03	1.1833E-02
188.01	4.5594E-03	1.3382E-03	192.01	2.6142E-03	1.1637E-02
189.01	4.6277E-03	1.3497E-03	193.01	2.6321E-03	1.1468E-02
190.01	4.5686E-03	1.3672E-03	194.01	2.4763E-03	1.1252E-02
191.01	4.5887E-03	1.3347E-03	195.01	2.5338E-03	1.0992E-02
192.01	4.5993E-03	1.3248E-03	196.01	2.5600E-03	1.0835E-02
193.01	4.5831E-03	1.2892E-03	197.01	2.4946E-03	1.0654E-02
194.01	4.6140E-03	1.2437E-03	198.01	2.5120E-03	1.0434E-02
195.01	4.6069E-03	1.1878E-03	199.01	2.5962E-03	1.0328E-02
196.01	4.6593E-03	1.1118E-03	200.01	2.4190E-03	1.0163E-02
197.01	4.7231E-03	1.0613E-03	201.01	2.5116E-03	9.9646E-03
198.01	4.7686E-03	1.0098E-03	202.01	2.4248E-03	9.8078E-03
199.01	4.8372E-03	9.4907E-04	203.02	2.4807E-03	9.6482E-03
200.01	4.9206E-03	8.8829E-04	204.01	2.3956E-03	9.4999E-03
201.01	5.0355E-03	8.3618E-04	205.01	2.4249E-03	9.3548E-03
202.01	5.1938E-03	8.3814E-04	206.01	2.2814E-03	9.1663E-03
203.01	5.2777E-03	8.6990E-04	207.02	2.3795E-03	8.9884E-03
204.01	5.3743E-03	8.8859E-04	208.01	2.2544E-03	8.8217E-03
205.01	5.4834E-03	9.3220E-04	209.02	2.3484E-03	8.6546E-03
206.01	5.5595E-03	9.9499E-04	210.01	2.2524E-03	8.5257E-03
207.01	5.6315E-03	1.0662E-03	211.02	2.2552E-03	8.3703E-03
208.01	5.6739E-03	1.1573E-03	212.01	2.1294E-03	8.1680E-03
209.01	5.6529E-03	1.2186E-03	213.01	2.2211E-03	7.9844E-03
210.01	5.6510E-03	1.2171E-03	214.01	2.0955E-03	7.7948E-03
211.01	5.7589E-03	1.2621E-03	215.02	2.2160E-03	7.5977E-03
212.01	5.7425E-03	1.3393E-03	216.02	2.1803E-03	7.4743E-03
213.01	5.7520E-03	1.3780E-03	217.01	2.2016E-03	7.3374E-03
214.01	5.7599E-03	1.4176E-03	218.02	2.1406E-03	7.2070E-03
215.01	5.7579E-03	1.4495E-03	219.02	2.0767E-03	7.0048E-03
216.01	5.7735E-03	1.4783E-03	220.01	2.1440E-03	6.8356E-03
217.01	5.7879E-03	1.5201E-03	221.02	2.0894E-03	6.7053E-03
218.01	5.7741E-03	1.5523E-03	222.01	2.0495E-03	6.5131E-03
219.01	5.7980E-03	1.5935E-03	223.02	2.0895E-03	6.3578E-03
220.01	5.7543E-03	1.6166E-03	224.01	1.9959E-03	6.1838E-03
221.01	5.7956E-03	1.6422E-03	225.01	2.0298E-03	5.9771E-03
222.01	5.7537E-03	1.6728E-03	226.01	2.0280E-03	5.8254E-03
223.01	5.7828E-03	1.7004E-03	227.01	1.9315E-03	5.5819E-03
224.01	5.7240E-03	1.7166E-03	228.02	2.0807E-03	5.3448E-03
225.02	5.7426E-03	1.6951E-03	229.01	2.1317E-03	5.2253E-03

226.02	5.7959E-03	1.7180E-03	230.01	2.1106E-03	5.0661E-03
227.01	5.8038E-03	1.7718E-03	231.02	2.1485E-03	4.8652E-03
228.01	5.7928E-03	1.8132E-03	232.01	2.2574E-03	4.7362E-03
229.01	5.7802E-03	1.8396E-03	233.02	2.2236E-03	4.6265E-03
230.01	5.7812E-03	1.8650E-03	234.01	2.2156E-03	4.4585E-03
231.01	5.7890E-03	1.9031E-03	235.02	2.2297E-03	4.2799E-03
232.01	5.7782E-03	1.9510E-03	236.02	2.2518E-03	4.1112E-03
233.01	5.7508E-03	1.9915E-03	237.01	2.2436E-03	3.9293E-03
234.01	5.7229E-03	2.0238E-03	238.01	2.2504E-03	3.6967E-03
235.01	5.6908E-03	2.0443E-03	239.02	2.3521E-03	3.4720E-03
236.01	5.6726E-03	2.0634E-03	240.02	2.4450E-03	3.2899E-03
237.01	5.6475E-03	2.0820E-03	241.01	2.5470E-03	3.1347E-03
238.01	5.6295E-03	2.0970E-03	242.02	2.6105E-03	2.9776E-03
239.01	5.6138E-03	2.1196E-03	243.01	2.7036E-03	2.8025E-03
240.01	5.5838E-03	2.1392E-03	244.02	2.8629E-03	2.6771E-03
241.01	5.5649E-03	2.1578E-03	245.01	2.9507E-03	2.6228E-03
242.01	5.5297E-03	2.1718E-03	246.01	2.9340E-03	2.5239E-03
243.01	5.5109E-03	2.1860E-03	247.02	2.9809E-03	2.3791E-03
244.01	5.4586E-03	2.1773E-03	248.02	3.0056E-03	2.2349E-03
245.01	5.4842E-03	2.1775E-03	249.02	3.0482E-03	2.0794E-03
246.01	5.4532E-03	2.2002E-03	250.01	3.0527E-03	1.8906E-03
247.01	5.4393E-03	2.2092E-03	251.02	3.1280E-03	1.6656E-03
248.01	5.4145E-03	2.2172E-03	252.02	3.2421E-03	1.4594E-03
249.01	5.4049E-03	2.2206E-03	253.01	3.3560E-03	1.2737E-03
250.02	5.4014E-03	2.2360E-03	254.01	3.4676E-03	1.0742E-03
251.02	5.3862E-03	2.2619E-03	255.02	3.6251E-03	8.7395E-04
252.01	5.3533E-03	2.2750E-03	256.02	3.8041E-03	6.9916E-04
253.01	5.3482E-03	2.2916E-03	257.01	3.9686E-03	5.3103E-04
254.01	5.3131E-03	2.3153E-03	258.01	4.1703E-03	3.6120E-04
255.02	5.2796E-03	2.3240E-03	259.02	4.4026E-03	2.1584E-04
256.01	5.2485E-03	2.3233E-03	260.01	4.6416E-03	1.0855E-04
257.02	5.2421E-03	2.3280E-03	261.01	4.8540E-03	1.7142E-07
258.01	5.2128E-03	2.3385E-03	262.01	5.1443E-03	
259.01	5.1958E-03	2.3423E-03	263.02	5.3991E-03	-1.0270E-04
260.02	5.1776E-03	2.3491E-03	264.02	5.6301E-03	-1.2364E-04
261.02	5.1649E-03	2.3627E-03	265.02	5.9002E-03	-1.1970E-04
262.01	5.1323E-03	2.3720E-03	266.01	6.1538E-03	
263.01	5.1181E-03	2.3794E-03	267.01	6.3583E-03	2.8904E-05
264.01	5.0862E-03	2.3843E-03	268.02	6.5339E-03	1.2560E-04
265.02	5.0804E-03	2.3921E-03	269.01	6.6815E-03	2.2864E-04
266.02	5.0518E-03	2.4078E-03	270.02	6.7920E-03	3.2643E-04
267.02	5.0252E-03	2.4120E-03	271.01	6.8743E-03	3.9179E-04
268.02	5.0127E-03	2.4236E-03	272.02	6.9868E-03	4.3483E-04
269.01	4.9821E-03	2.4422E-03	273.01	7.1242E-03	5.0284E-04
270.02	4.9438E-03	2.4515E-03	274.01	7.2208E-03	5.7976E-04
271.02	4.9062E-03	2.4476E-03	275.02	7.3481E-03	6.6360E-04
272.02	4.8899E-03	2.4495E-03	276.02	7.4555E-03	8.0279E-04
273.01	4.8508E-03	2.4513E-03	277.01	7.4261E-03	8.9007E-04
274.02	4.8299E-03	2.4528E-03	278.02	7.5234E-03	9.3667E-04
275.01	4.7788E-03	2.4401E-03	279.02	7.5916E-03	1.0416E-03
276.02	4.7829E-03	2.4331E-03	280.02	7.5893E-03	1.1230E-03
277.02	4.7366E-03	2.4293E-03	281.01	7.6343E-03	1.1914E-03
278.01	4.7264E-03	2.4134E-03	282.02	7.6181E-03	1.2521E-03
279.02	4.7049E-03	2.3985E-03	283.02	7.6150E-03	1.2437E-03
280.01	4.7259E-03	2.4002E-03	284.01	7.7574E-03	1.3086E-03
281.02	4.7057E-03	2.4190E-03	285.02	7.6595E-03	1.3609E-03

282.02	4.7150E-03	2.4725E-03	286.02	7.7183E-03	1.2677E-03
283.02	4.5907E-03	2.5148E-03	287.02	8.0672E-03	1.4343E-03
284.02	4.4651E-03	2.4259E-03	288.02	7.8297E-03	1.6454E-03
285.01	4.5503E-03	2.3646E-03	289.02	7.7669E-03	1.6189E-03
286.01	4.5266E-03	2.3912E-03	290.01	7.7340E-03	1.5436E-03
287.02	4.4705E-03	2.3730E-03	291.02	7.8836E-03	1.5113E-03
288.01	4.4815E-03	2.3680E-03	292.01	7.9575E-03	1.5768E-03
289.01	4.4036E-03	2.3754E-03	293.02	7.9779E-03	1.6186E-03
290.01	4.3070E-03	2.2989E-03	294.02	8.0337E-03	1.6011E-03
291.01	4.3236E-03	2.2023E-03	295.02	8.3076E-03	1.7687E-03
292.01	4.3430E-03	2.1477E-03	296.02	8.1211E-03	1.9801E-03
293.02	4.3408E-03	2.0862E-03	297.02	8.0087E-03	1.9401E-03
294.02	4.3800E-03	2.0263E-03	298.02	8.1441E-03	1.9480E-03
295.01	4.3899E-03	1.9557E-03	299.02	8.1097E-03	2.0224E-03
296.02	4.4540E-03	1.8449E-03	300.02	8.1616E-03	2.0992E-03
297.02	4.6079E-03	1.7417E-03	301.02	8.0528E-03	2.1422E-03
298.01	4.9056E-03	1.7786E-03	302.02	8.0930E-03	2.1333E-03
299.02	5.0675E-03	1.9782E-03	303.02	8.1323E-03	2.2121E-03
300.02	5.0912E-03	2.1932E-03	304.02	7.9985E-03	2.2133E-03
301.01	5.0464E-03	2.3690E-03	305.02	8.0889E-03	2.1618E-03
302.02	4.9652E-03	2.5211E-03	306.01	8.1619E-03	2.2120E-03
303.01	4.7985E-03	2.5991E-03	307.02	8.1717E-03	2.2767E-03
304.01	4.6878E-03	2.5975E-03	308.02	8.1858E-03	2.3345E-03
305.01	4.6108E-03	2.5740E-03	309.02	8.1568E-03	2.3635E-03
306.01	4.5714E-03	2.5515E-03	310.02	8.1996E-03	2.3823E-03
307.01	4.5254E-03	2.5256E-03	311.02	8.2272E-03	2.4282E-03
308.02	4.5097E-03	2.4832E-03	312.02	8.2601E-03	2.4896E-03
309.02	4.5288E-03	2.4382E-03	313.02	8.2712E-03	2.5611E-03
310.02	4.6263E-03	2.4523E-03	314.02	8.2644E-03	2.6210E-03
311.01	4.6567E-03	2.5382E-03	315.02	8.2856E-03	2.6949E-03
312.01	4.6339E-03	2.6251E-03	316.02	8.2482E-03	2.7674E-03
313.01	4.5819E-03	2.6941E-03	317.01	8.2366E-03	2.8131E-03
314.02	4.5234E-03	2.7500E-03	318.02	8.2430E-03	2.8927E-03
315.02	4.4297E-03	2.7761E-03	319.02	8.1604E-03	2.9347E-03
316.02	4.3678E-03	2.7698E-03	320.02	8.2052E-03	2.9833E-03
317.02	4.3213E-03	2.7606E-03	321.01	8.1360E-03	3.0502E-03
318.02	4.2902E-03	2.7550E-03	322.02	8.1279E-03	3.0856E-03
319.02	4.2547E-03	2.7554E-03	323.02	8.1225E-03	3.1597E-03
320.02	4.2211E-03	2.7567E-03	324.02	8.0644E-03	3.2390E-03
321.02	4.1807E-03	2.7538E-03	325.02	7.9887E-03	3.2861E-03
322.02	4.1465E-03	2.7415E-03	326.02	7.9356E-03	3.3200E-03
323.01	4.1292E-03	2.7335E-03	327.02	7.8640E-03	3.3386E-03
324.01	4.1064E-03	2.7342E-03	328.03	7.8380E-03	3.3635E-03
325.02	4.0721E-03	2.7298E-03	329.01	7.7606E-03	3.3867E-03
326.01	4.0542E-03	2.7179E-03	330.02	7.7029E-03	3.3749E-03
327.02	4.0428E-03	2.7157E-03	331.02	7.6863E-03	3.3655E-03
328.01	4.0238E-03	2.7183E-03	332.01	7.6689E-03	3.3787E-03
329.02	4.0031E-03	2.7175E-03	333.02	7.6349E-03	3.3852E-03
330.02	3.9931E-03	2.7249E-03	334.02	7.6406E-03	3.4111E-03
331.01	3.9608E-03	2.7280E-03	335.01	7.5854E-03	3.4468E-03
332.02	3.9492E-03	2.7302E-03	336.02	7.5360E-03	3.4512E-03
333.01	3.9204E-03	2.7357E-03	337.02	7.5055E-03	3.4426E-03
334.01	3.8984E-03	2.7326E-03	338.02	7.5016E-03	3.4436E-03
335.02	3.8861E-03	2.7376E-03	339.02	7.5053E-03	3.4824E-03
336.01	3.8564E-03	2.7419E-03	340.02	7.4323E-03	3.5017E-03
337.01	3.8410E-03	2.7436E-03	341.02	7.4456E-03	3.5273E-03

338.02	3.8169E-03	2.7499E-03	342.02	7.3427E-03	3.5332E-03
339.01	3.7919E-03	2.7531E-03	343.02	7.3730E-03	3.5275E-03
340.02	3.7710E-03	2.7574E-03	344.02	7.3271E-03	3.5628E-03
341.01	3.7380E-03	2.7583E-03	345.02	7.2829E-03	3.5732E-03
342.01	3.7172E-03	2.7546E-03	346.02	7.2478E-03	3.5753E-03
343.02	3.6984E-03	2.7583E-03	347.02	7.2206E-03	3.5831E-03
344.02	3.6647E-03	2.7596E-03	348.02	7.1795E-03	3.5893E-03
345.02	3.6414E-03	2.7527E-03	349.02	7.1335E-03	3.5685E-03
346.01	3.6213E-03	2.7472E-03	350.02	7.1624E-03	3.5754E-03
347.02	3.5996E-03	2.7445E-03	351.01	7.1013E-03	3.5914E-03
348.02	3.5847E-03	2.7471E-03	352.02	7.1013E-03	3.5896E-03
349.01	3.5464E-03	2.7414E-03	353.02	7.0680E-03	3.5977E-03
350.02	3.5394E-03	2.7346E-03	354.01	7.0749E-03	3.6203E-03
351.02	3.5116E-03	2.7335E-03	355.02	7.0156E-03	3.6393E-03
352.02	3.4972E-03	2.7311E-03	356.02	7.0089E-03	3.6534E-03
353.02	3.4686E-03	2.7299E-03	357.02	6.9530E-03	3.6702E-03
354.01	3.4468E-03	2.7198E-03	358.02	6.9307E-03	3.6826E-03
355.02	3.4324E-03	2.7136E-03	359.02	6.8658E-03	3.6903E-03
356.03	3.4150E-03	2.7091E-03	360.02	6.8351E-03	3.6864E-03
357.01	3.4008E-03	2.7064E-03	361.02	6.7721E-03	3.6686E-03
358.01	3.3840E-03	2.7072E-03	362.02	6.7717E-03	3.6527E-03
359.02	3.3615E-03	2.7063E-03	363.02	6.7347E-03	3.6551E-03
360.01	3.3381E-03	2.6994E-03	364.02	6.6962E-03	3.6335E-03
361.02	3.3250E-03	2.6948E-03	365.02	6.7073E-03	3.6299E-03
362.02	3.3049E-03	2.6916E-03	366.02	6.6592E-03	3.6294E-03
363.01	3.2895E-03	2.6845E-03	367.02	6.6665E-03	3.6309E-03
364.02	3.2645E-03	2.6790E-03	368.02	6.6128E-03	3.6384E-03
365.02	3.2544E-03	2.6702E-03	369.02	6.5937E-03	3.6246E-03
366.02	3.2394E-03	2.6682E-03	370.02	6.5783E-03	3.6286E-03
367.01	3.2210E-03	2.6645E-03	371.02	6.5441E-03	3.6445E-03
368.02	3.2029E-03	2.6598E-03	372.02	6.4651E-03	3.6210E-03
369.01	3.1899E-03	2.6552E-03	373.02	6.4736E-03	3.5955E-03
370.01	3.1750E-03	2.6534E-03	374.02	6.4190E-03	3.5801E-03
371.02	3.1560E-03	2.6513E-03	375.02	6.4076E-03	3.5486E-03
372.01	3.1401E-03	2.6460E-03	376.01	6.3804E-03	3.5169E-03
373.01	3.1244E-03	2.6421E-03	377.01	6.3861E-03	3.4847E-03
374.01	3.1128E-03	2.6422E-03	378.02	6.3919E-03	3.4745E-03
375.02	3.0877E-03	2.6372E-03	379.02	6.3706E-03	3.4557E-03
376.01	3.0795E-03	2.6312E-03	380.02	6.3838E-03	3.4357E-03
377.01	3.0604E-03	2.6304E-03	381.01	6.3816E-03	3.4291E-03
378.02	3.0425E-03	2.6228E-03	382.02	6.3771E-03	3.4170E-03
379.02	3.0366E-03	2.6223E-03	383.02	6.3720E-03	3.3986E-03
380.02	3.0104E-03	2.6203E-03	384.01	6.3940E-03	3.3897E-03
381.01	2.9992E-03	2.6149E-03	385.01	6.3890E-03	3.3892E-03
382.02	2.9789E-03	2.6084E-03	386.02	6.3861E-03	3.3761E-03
383.02	2.9698E-03	2.6024E-03	387.02	6.4010E-03	3.3666E-03
384.02	2.9520E-03	2.5997E-03	388.01	6.4064E-03	3.3669E-03
385.02	2.9355E-03	2.5907E-03	389.02	6.3776E-03	3.3292E-03
386.01	2.9309E-03	2.5853E-03	390.02	6.4509E-03	3.2860E-03
387.01	2.9133E-03	2.5830E-03	391.01	6.5135E-03	3.2759E-03
388.01	2.9006E-03	2.5770E-03	392.02	6.6521E-03	3.3473E-03
389.03	2.8895E-03	2.5712E-03	400.01	6.4678E-03	3.7565E-03
390.03	2.8771E-03	2.5653E-03	401.02	6.3562E-03	3.7745E-03
391.01	2.8715E-03	2.5607E-03	402.01	6.3103E-03	3.7316E-03
392.02	2.8632E-03	2.5610E-03	403.02	6.3049E-03	3.6879E-03
393.02	2.8537E-03	2.5613E-03	404.02	6.3350E-03	3.6669E-03

394.02	2.8451E-03	2.5633E-03	405.02	6.3687E-03	3.6682E-03
395.02	2.8334E-03	2.5686E-03	406.02	6.4460E-03	3.7415E-03
396.01	2.8149E-03	2.5729E-03	407.02	6.3534E-03	3.8015E-03
397.02	2.8067E-03	2.5835E-03	408.02	6.3763E-03	3.8458E-03
398.01	2.7657E-03	2.5930E-03	409.01	6.2220E-03	3.8315E-03
399.02	2.7193E-03	2.5689E-03	410.02	6.2837E-03	3.7341E-03
400.01	2.7220E-03	2.5436E-03	411.02	6.4020E-03	3.7154E-03
401.02	2.7062E-03	2.5231E-03	412.01	6.6136E-03	3.8577E-03
402.02	2.7321E-03	2.5157E-03	413.02	6.6255E-03	4.1579E-03
403.02	2.7153E-03	2.5200E-03	414.02	6.3960E-03	4.3818E-03
404.02	2.7253E-03	2.5249E-03	415.02	6.1471E-03	4.4415E-03
405.02	2.7082E-03	2.5362E-03	416.01	5.9531E-03	4.4031E-03
406.01	2.6989E-03	2.5433E-03	417.02	5.8171E-03	4.3056E-03
407.03	2.6756E-03	2.5484E-03	418.02	5.8038E-03	4.2458E-03
408.01	2.6608E-03	2.5491E-03	419.02	5.7014E-03	4.1989E-03
409.00	2.6464E-03	2.5518E-03	420.02	5.6819E-03	4.1176E-03
410.02	2.6234E-03	2.5526E-03	421.02	5.6887E-03	4.0673E-03
411.03	2.6035E-03	2.5467E-03	422.01	5.7135E-03	4.0596E-03
412.02	2.5954E-03	2.5465E-03	423.02	5.6949E-03	4.0757E-03
413.03	2.5673E-03	2.5440E-03	424.02	5.6689E-03	4.0886E-03
414.02	2.5576E-03	2.5360E-03	425.02	5.6239E-03	4.0943E-03
415.03	2.5410E-03	2.5314E-03	426.02	5.5758E-03	4.0858E-03
416.02	2.5299E-03	2.5257E-03	427.02	5.5397E-03	4.0741E-03
417.02	2.5173E-03	2.5245E-03	428.02	5.4828E-03	4.0458E-03
418.02	2.5023E-03	2.5217E-03	429.02	5.4691E-03	4.0071E-03
419.01	2.4885E-03	2.5178E-03	430.02	5.4529E-03	3.9804E-03
420.03	2.4745E-03	2.5129E-03	431.02	5.4555E-03	3.9690E-03
421.02	2.4639E-03	2.5087E-03	432.01	5.4096E-03	3.9392E-03
422.02	2.4523E-03	2.5089E-03	433.01	5.4618E-03	3.9316E-03
423.02	2.4351E-03	2.5052E-03	434.02	5.4058E-03	3.9492E-03
424.02	2.4239E-03	2.5002E-03	435.02	5.3650E-03	3.9116E-03
425.02	2.4120E-03	2.4975E-03	436.02	5.3769E-03	3.8750E-03
426.01	2.3962E-03	2.4936E-03	437.02	5.3750E-03	3.8530E-03
427.01	2.3891E-03	2.4911E-03	438.01	5.3858E-03	3.8383E-03
428.01	2.3735E-03	2.4887E-03	439.02	5.3556E-03	3.7760E-03
429.02	2.3648E-03	2.4868E-03	439.93	5.5022E-03	3.7681E-03
430.02	2.3476E-03	2.4863E-03	441.00	5.5012E-03	3.8398E-03
431.02	2.3342E-03	2.4826E-03	442.02	5.5005E-03	3.8692E-03
432.00	2.3227E-03	2.4808E-03	443.02	5.5116E-03	3.8991E-03
433.02	2.3029E-03	2.4755E-03	444.02	5.5132E-03	3.9403E-03
434.02	2.2971E-03	2.4715E-03	445.02	5.5033E-03	3.9867E-03
435.01	2.2776E-03	2.4685E-03	446.02	5.4716E-03	4.0202E-03
436.03	2.2708E-03	2.4633E-03	447.02	5.4606E-03	4.0503E-03
437.02	2.2520E-03	2.4611E-03	448.02	5.4374E-03	4.0942E-03
438.02	2.2437E-03	2.4561E-03	449.02	5.3884E-03	4.1238E-03
439.02	2.2275E-03	2.4505E-03	450.02	5.3664E-03	4.1485E-03
440.01	2.2230E-03	2.4472E-03	451.02	5.3206E-03	4.1781E-03
441.02	2.2053E-03	2.4453E-03	452.02	5.2816E-03	4.2006E-03
442.02	2.1958E-03	2.4411E-03	453.02	5.2276E-03	4.2159E-03
443.01	2.1830E-03	2.4385E-03	454.02	5.1884E-03	4.2234E-03
444.02	2.1710E-03	2.4331E-03	455.02	5.1433E-03	4.2292E-03
445.02	2.1645E-03	2.4323E-03	456.02	5.1055E-03	4.2316E-03
446.01	2.1462E-03	2.4322E-03	457.02	5.0697E-03	4.2371E-03
447.02	2.1311E-03	2.4235E-03	458.02	5.0268E-03	4.2393E-03
448.02	2.1281E-03	2.4219E-03	459.02	4.9878E-03	4.2340E-03
449.02	2.1086E-03	2.4186E-03	460.02	4.9612E-03	4.2254E-03

450.02	2.1086E-03	2.4193E-03	461.02	4.9575E-03	4.2487E-03
451.01	2.0842E-03	2.4224E-03	462.02	4.8759E-03	4.2677E-03
452.02	2.0678E-03	2.4132E-03	463.02	4.8196E-03	4.2390E-03
453.01	2.0632E-03	2.4106E-03	464.02	4.8102E-03	4.2225E-03
454.01	2.0435E-03	2.4117E-03	465.02	4.7670E-03	4.2115E-03
455.02	2.0330E-03	2.4117E-03	466.01	4.7637E-03	4.2070E-03
456.01	2.0025E-03	2.4086E-03	467.02	4.7237E-03	4.2153E-03
457.01	1.9803E-03	2.3906E-03	468.01	4.6933E-03	4.2194E-03
458.01	1.9707E-03	2.3634E-03	469.02	4.6275E-03	4.2061E-03
459.02	1.9947E-03	2.3605E-03	470.01	4.6118E-03	4.1805E-03
460.02	1.9762E-03	2.3730E-03	471.02	4.5799E-03	4.1628E-03
461.01	1.9627E-03	2.3780E-03	472.02	4.5776E-03	4.1590E-03
462.01	1.9262E-03	2.3692E-03	473.02	4.5277E-03	4.1572E-03
463.01	1.9208E-03	2.3510E-03	474.02	4.4998E-03	4.1339E-03
464.02	1.9109E-03	2.3395E-03	475.02	4.4862E-03	4.1222E-03
465.01	1.9096E-03	2.3308E-03	476.01	4.4491E-03	4.1029E-03
466.01	1.9058E-03	2.3324E-03	477.02	4.4504E-03	4.0849E-03
467.02	1.8855E-03	2.3271E-03	478.02	4.4317E-03	4.0827E-03
468.01	1.8866E-03	2.3229E-03	479.02	4.4125E-03	4.0775E-03
469.02	1.8688E-03	2.3230E-03	480.02	4.3898E-03	4.0726E-03
470.02	1.8538E-03	2.3145E-03	481.02	4.3607E-03	4.0561E-03
471.02	1.8427E-03	2.3018E-03	482.02	4.3594E-03	4.0446E-03
472.02	1.8436E-03	2.2945E-03	483.02	4.3443E-03	4.0489E-03
473.02	1.8371E-03	2.2942E-03	484.01	4.3156E-03	4.0470E-03
474.01	1.8343E-03	2.3007E-03	485.02	4.2943E-03	4.0411E-03
475.02	1.7958E-03	2.2889E-03	486.02	4.2664E-03	4.0319E-03
476.01	1.8210E-03	2.2826E-03	487.02	4.2481E-03	4.0151E-03
477.02	1.7877E-03	2.2874E-03	488.02	4.2482E-03	4.0174E-03
478.01	1.7878E-03	2.2780E-03	489.02	4.2064E-03	4.0242E-03
479.01	1.7732E-03	2.2766E-03	490.02	4.1715E-03	4.0068E-03
480.01	1.7708E-03	2.2768E-03	491.01	4.1544E-03	3.9902E-03
481.01	1.7443E-03	2.2733E-03	492.02	4.1292E-03	3.9745E-03
482.01	1.7393E-03	2.2647E-03	493.02	4.1138E-03	3.9540E-03
483.02	1.7208E-03	2.2540E-03	494.02	4.1057E-03	3.9453E-03
484.02	1.7275E-03	2.2498E-03	495.02	4.0788E-03	3.9347E-03
485.01	1.7040E-03	2.2469E-03	496.02	4.0635E-03	3.9172E-03
486.02	1.7047E-03	2.2383E-03	497.02	4.0498E-03	3.9050E-03
487.02	1.6958E-03	2.2413E-03	498.02	4.0191E-03	3.8770E-03
488.02	1.6765E-03	2.2379E-03	499.02	4.0392E-03	3.8532E-03
489.02	1.6663E-03	2.2297E-03	500.02	4.0365E-03	3.8572E-03
490.02	1.6496E-03	2.2160E-03	501.01	4.0098E-03	3.8469E-03
491.02	1.6546E-03	2.2033E-03	502.02	4.0121E-03	3.8323E-03
492.02	1.6616E-03	2.2104E-03	503.02	4.0006E-03	3.8269E-03
493.02	1.6361E-03	2.2133E-03	504.01	3.9858E-03	3.8095E-03
494.02	1.6354E-03	2.2164E-03	505.02	3.9961E-03	3.7908E-03
495.02	1.5970E-03	2.2121E-03	506.01	4.0147E-03	3.7981E-03
496.02	1.5916E-03	2.1933E-03	507.02	3.9897E-03	3.8064E-03
497.01	1.5847E-03	2.1830E-03	508.01	3.9832E-03	3.7984E-03
498.02	1.5772E-03	2.1703E-03	509.02	3.9835E-03	3.7997E-03
499.02	1.5863E-03	2.1698E-03	510.02	3.9620E-03	3.7931E-03
500.02	1.5648E-03	2.1725E-03	511.02	3.9717E-03	3.7835E-03
501.01	1.5511E-03	2.1607E-03	512.01	3.9832E-03	3.7969E-03
502.02	1.5491E-03	2.1559E-03	513.02	3.9585E-03	3.8094E-03
503.02	1.5243E-03	2.1381E-03	514.02	3.9542E-03	3.8154E-03
504.01	1.5490E-03	2.1283E-03	515.02	3.9255E-03	3.8112E-03
505.03	1.5374E-03	2.1368E-03	516.01	3.9363E-03	3.8075E-03

506.02	1.5256E-03	2.1358E-03	517.02	3.9260E-03	3.8175E-03
507.02	1.5124E-03	2.1279E-03	518.02	3.9186E-03	3.8257E-03
508.01	1.5110E-03	2.1211E-03	519.02	3.9106E-03	3.8396E-03
509.02	1.5084E-03	2.1243E-03	520.01	3.8784E-03	3.8394E-03
510.02	1.4818E-03	2.1179E-03	521.02	3.8844E-03	3.8365E-03
511.02	1.4855E-03	2.1050E-03	522.02	3.8801E-03	3.8545E-03
512.02	1.4859E-03	2.1123E-03	523.02	3.8606E-03	3.8732E-03
513.02	1.4599E-03	2.1035E-03	524.02	3.8332E-03	3.8785E-03
514.02	1.4798E-03	2.0985E-03	525.02	3.8264E-03	3.8848E-03
515.02	1.4619E-03	2.1122E-03	526.01	3.8046E-03	3.8966E-03
516.01	1.4358E-03	2.0999E-03	527.02	3.7882E-03	3.9066E-03
517.01	1.4475E-03	2.0903E-03	528.02	3.7626E-03	3.9164E-03
518.02	1.4364E-03	2.0952E-03	529.01	3.7409E-03	3.9205E-03
519.02	1.4270E-03	2.0962E-03	530.02	3.7305E-03	3.9374E-03
520.02	1.4084E-03	2.0935E-03	531.02	3.6829E-03	3.9468E-03
521.01	1.3990E-03	2.0849E-03	532.02	3.6645E-03	3.9443E-03
522.02	1.3939E-03	2.0835E-03	533.01	3.6440E-03	3.9546E-03
523.01	1.3694E-03	2.0721E-03	534.02	3.6042E-03	3.9598E-03
524.02	1.3868E-03	2.0709E-03	535.03	3.5823E-03	3.9633E-03
525.01	1.3491E-03	2.0715E-03	536.01	3.5349E-03	3.9615E-03
526.01	1.3488E-03	2.0585E-03	537.02	3.5143E-03	3.9501E-03
527.02	1.3253E-03	2.0447E-03	538.02	3.5042E-03	3.9811E-03
528.01	1.3378E-03	2.0374E-03	539.02	3.3554E-03	3.9344E-03
529.01	1.2986E-03	2.0198E-03	540.01	3.4337E-03	3.8656E-03
530.03	1.3278E-03	1.9876E-03	541.03	3.4325E-03	3.8864E-03
531.01	1.3593E-03	1.9995E-03	542.02	3.4098E-03	3.8961E-03
532.02	1.3479E-03	2.0197E-03	543.01	3.3915E-03	3.9098E-03
533.01	1.3502E-03	2.0471E-03	544.02	3.3133E-03	3.8832E-03
534.02	1.2725E-03	2.0310E-03	545.02	3.3539E-03	3.8602E-03
535.02	1.3413E-03	2.0357E-03	546.02	3.3156E-03	3.8699E-03
536.01	1.2534E-03	2.0608E-03	547.02	3.3101E-03	3.8721E-03
537.01	1.2356E-03	2.0328E-03	548.01	3.2590E-03	3.8709E-03
538.02	1.1957E-03	1.9935E-03	549.02	3.2219E-03	3.8298E-03
539.02	1.2331E-03	1.9673E-03	550.02	3.2562E-03	3.8153E-03
540.02	1.2095E-03	1.9492E-03	551.02	3.2175E-03	3.8082E-03
541.01	1.2669E-03	1.9519E-03	552.02	3.2507E-03	3.8040E-03
542.01	1.2170E-03	1.9636E-03	553.02	3.2418E-03	3.8490E-03
543.02	1.2393E-03	1.9646E-03	554.02	3.1576E-03	3.8574E-03
544.02	1.1744E-03	1.9502E-03	555.02	3.1275E-03	3.8244E-03
545.01	1.2050E-03	1.9117E-03	556.01	3.1088E-03	3.7863E-03
546.01	1.2275E-03	1.9212E-03	557.02	3.1607E-03	3.8068E-03
547.01	1.2017E-03	1.9249E-03	558.02	3.0629E-03	3.8260E-03
548.02	1.2116E-03	1.9155E-03	559.01	3.0430E-03	3.7875E-03
549.02	1.2101E-03	1.9199E-03	560.02	3.0352E-03	3.7699E-03
550.01	1.2185E-03	1.9452E-03	560.98	3.0137E-03	3.7612E-03
551.02	1.1459E-03	1.9418E-03	562.02	2.9884E-03	3.7440E-03
552.02	1.1478E-03	1.9016E-03	563.02	2.9685E-03	3.7183E-03
553.01	1.1602E-03	1.8818E-03	564.02	2.9700E-03	3.6984E-03
554.02	1.1915E-03	1.8953E-03	565.01	2.9649E-03	3.6938E-03
555.01	1.1656E-03	1.9240E-03	566.02	2.9427E-03	3.6826E-03
556.01	1.1104E-03	1.9035E-03	567.02	2.9414E-03	3.6709E-03
557.02	1.1438E-03	1.8931E-03	568.02	2.9225E-03	3.6608E-03
558.01	1.0826E-03	1.8813E-03	569.00	2.9222E-03	3.6513E-03
559.92	1.1278E-03	1.8425E-03	570.02	2.9016E-03	3.6444E-03
561.00	1.1180E-03	1.8534E-03	571.01	2.8986E-03	3.6365E-03
562.01	1.0929E-03	1.8364E-03	572.02	2.8808E-03	3.6334E-03

563.03	1.1246E-03	1.8280E-03	573.02	2.8640E-03	3.6230E-03
564.00	1.1120E-03	1.8400E-03	574.02	2.8543E-03	3.6092E-03
565.02	1.0977E-03	1.8352E-03	575.01	2.8576E-03	3.6109E-03
566.01	1.0930E-03	1.8257E-03	576.02	2.8216E-03	3.6112E-03
567.02	1.0945E-03	1.8196E-03	577.01	2.8016E-03	3.5926E-03
568.01	1.0992E-03	1.8269E-03	578.02	2.7857E-03	3.5710E-03
569.01	1.0717E-03	1.8285E-03	579.02	2.7852E-03	3.5495E-03
570.02	1.0608E-03	1.8133E-03	580.01	2.7882E-03	3.5406E-03
571.02	1.0546E-03	1.7944E-03	581.02	2.7838E-03	3.5375E-03
572.01	1.0687E-03	1.7784E-03	582.02	2.7733E-03	3.5328E-03
573.03	1.1046E-03	1.8059E-03	583.01	2.7681E-03	3.5296E-03
574.01	1.0380E-03	1.8217E-03	584.02	2.7535E-03	3.5263E-03
575.02	1.0279E-03	1.7874E-03	585.02	2.7417E-03	3.5188E-03
576.02	1.0481E-03	1.7749E-03	586.02	2.7274E-03	3.5063E-03
577.01	1.0519E-03	1.7898E-03	587.02	2.7328E-03	3.5003E-03
578.02	1.0153E-03	1.7865E-03	588.02	2.7166E-03	3.4994E-03
579.02	1.0184E-03	1.7704E-03	589.02	2.7060E-03	3.4908E-03
580.02	1.0091E-03	1.7635E-03	590.02	2.6997E-03	3.4827E-03
581.02	9.9949E-04	1.7430E-03	591.02	2.6983E-03	3.4821E-03
582.01	1.0300E-03	1.7422E-03	592.01	2.6835E-03	3.4829E-03
583.01	1.0010E-03	1.7438E-03	593.03	2.6700E-03	3.4784E-03
584.03	1.0166E-03	1.7354E-03	594.02	2.6578E-03	3.4716E-03
585.01	1.0054E-03	1.7368E-03	595.02	2.6541E-03	3.4684E-03
586.02	1.0073E-03	1.7359E-03	596.01	2.6365E-03	3.4638E-03
587.02	9.9038E-04	1.7289E-03	597.02	2.6336E-03	3.4608E-03
588.01	1.0125E-03	1.7334E-03	598.03	2.6120E-03	3.4561E-03
589.02	9.7122E-04	1.7292E-03	599.02	2.6101E-03	3.4491E-03
590.02	1.0053E-03	1.7287E-03	600.01	2.5938E-03	3.4417E-03
591.01	9.5825E-04	1.7323E-03	601.02	2.5980E-03	3.4384E-03
592.02	9.6733E-04	1.7107E-03	602.03	2.5850E-03	3.4442E-03
593.02	9.6539E-04	1.7089E-03	603.02	2.5679E-03	3.4437E-03
594.01	9.5884E-04	1.7037E-03	604.02	2.5511E-03	3.4371E-03
595.02	9.6045E-04	1.7009E-03	605.01	2.5466E-03	3.4335E-03
596.01	9.5360E-04	1.7041E-03	606.01	2.5299E-03	3.4328E-03
597.03	9.3269E-04	1.6949E-03	607.03	2.5193E-03	3.4301E-03
598.01	9.3443E-04	1.6768E-03	608.02	2.5023E-03	3.4272E-03
599.02	9.4495E-04	1.6688E-03	609.02	2.4912E-03	3.4239E-03
600.02	9.5861E-04	1.6806E-03	610.02	2.4731E-03	3.4198E-03
601.01	9.3409E-04	1.6903E-03	611.01	2.4600E-03	3.4134E-03
602.02	9.2366E-04	1.6799E-03	612.02	2.4487E-03	3.4072E-03
603.01	9.2904E-04	1.6794E-03	613.01	2.4353E-03	3.4049E-03
604.02	9.1223E-04	1.6834E-03	614.02	2.4178E-03	3.3997E-03
605.01	8.9310E-04	1.6711E-03	615.02	2.4058E-03	3.3949E-03
606.03	8.9827E-04	1.6595E-03	616.03	2.3841E-03	3.3878E-03
607.00	8.9173E-04	1.6583E-03	617.01	2.3744E-03	3.3790E-03
608.02	8.7514E-04	1.6422E-03	618.03	2.3547E-03	3.3672E-03
609.01	8.9825E-04	1.6359E-03	619.01	2.3541E-03	3.3589E-03
610.02	8.8448E-04	1.6429E-03	620.03	2.3370E-03	3.3570E-03
611.02	8.7495E-04	1.6375E-03	621.02	2.3202E-03	3.3487E-03
612.01	8.6353E-04	1.6228E-03	622.00	2.3067E-03	3.3356E-03
613.02	8.8231E-04	1.6193E-03	623.03	2.3040E-03	3.3284E-03
614.01	8.6560E-04	1.6227E-03	624.02	2.2867E-03	3.3227E-03
615.02	8.6260E-04	1.6155E-03	625.02	2.2750E-03	3.3120E-03
616.00	8.5406E-04	1.6086E-03	626.01	2.2656E-03	3.3011E-03
617.02	8.5441E-04	1.5957E-03	627.02	2.2605E-03	3.2949E-03
618.01	8.6710E-04	1.5928E-03	628.01	2.2487E-03	3.2903E-03

619.02	8.6723E-04	1.5983E-03	629.02	2.2386E-03	3.2859E-03
620.02	8.7029E-04	1.6134E-03	630.02	2.2191E-03	3.2761E-03
621.02	8.3167E-04	1.6136E-03	631.02	2.2140E-03	3.2640E-03
622.02	8.3086E-04	1.5958E-03	632.00	2.2089E-03	3.2589E-03
623.02	8.3238E-04	1.5950E-03	633.02	2.1961E-03	3.2543E-03
624.00	8.0830E-04	1.5828E-03	634.02	2.1858E-03	3.2474E-03
625.03	8.3160E-04	1.5764E-03	635.03	2.1744E-03	3.2406E-03
626.03	8.0653E-04	1.5757E-03	636.01	2.1635E-03	3.2320E-03
627.02	8.1581E-04	1.5677E-03	637.02	2.1554E-03	3.2236E-03
628.02	7.9604E-04	1.5561E-03	638.01	2.1446E-03	3.2166E-03
629.01	8.2231E-04	1.5518E-03	639.02	2.1347E-03	3.2092E-03
630.02	8.0441E-04	1.5591E-03	640.03	2.1254E-03	3.2019E-03
631.01	7.9936E-04	1.5530E-03	641.02	2.1145E-03	3.1950E-03
632.02	7.9027E-04	1.5448E-03	642.02	2.1046E-03	3.1863E-03
633.02	7.9394E-04	1.5342E-03	643.02	2.0965E-03	3.1790E-03
634.02	8.0324E-04	1.5376E-03	644.01	2.0854E-03	3.1708E-03
635.02	7.8615E-04	1.5386E-03	645.03	2.0777E-03	3.1606E-03
636.01	7.8674E-04	1.5325E-03	646.02	2.0750E-03	3.1552E-03
637.01	7.7683E-04	1.5280E-03	647.02	2.0626E-03	3.1519E-03
638.03	7.7631E-04	1.5192E-03	648.02	2.0518E-03	3.1429E-03
639.01	7.7972E-04	1.5191E-03	649.01	2.0457E-03	3.1349E-03
640.02	7.6291E-04	1.5107E-03	650.03	2.0389E-03	3.1312E-03
641.01	7.8302E-04	1.5087E-03	651.02	2.0230E-03	3.1229E-03
642.02	7.6249E-04	1.5144E-03	652.02	2.0200E-03	3.1143E-03
643.00	7.5769E-04	1.5055E-03	653.02	2.0072E-03	3.1072E-03
644.01	7.4986E-04	1.4925E-03	654.02	2.0035E-03	3.0999E-03
645.02	7.6939E-04	1.4922E-03	655.02	1.9922E-03	3.0940E-03
646.02	7.5087E-04	1.4987E-03	656.02	1.9850E-03	3.0861E-03
647.01	7.3828E-04	1.4821E-03	657.01	1.9773E-03	3.0797E-03
648.03	7.5929E-04	1.4742E-03	658.03	1.9689E-03	3.0725E-03
649.00	7.5997E-04	1.4867E-03	659.02	1.9613E-03	3.0652E-03
650.03	7.3758E-04	1.4858E-03	660.02	1.9568E-03	3.0603E-03
651.01	7.4788E-04	1.4856E-03	661.02	1.9444E-03	3.0544E-03
652.02	7.1496E-04	1.4779E-03	662.02	1.9387E-03	3.0462E-03
653.00	7.3216E-04	1.4623E-03	663.02	1.9343E-03	3.0447E-03
654.02	7.3124E-04	1.4649E-03	664.00	1.9135E-03	3.0367E-03
655.00	7.2962E-04	1.4702E-03	665.03	1.9143E-03	3.0247E-03
656.02	7.0286E-04	1.4577E-03	666.00	1.9077E-03	3.0206E-03
657.02	7.2562E-04	1.4446E-03	667.03	1.8978E-03	3.0156E-03
658.02	7.2702E-04	1.4531E-03	668.02	1.8877E-03	3.0087E-03
659.01	7.1995E-04	1.4622E-03	669.02	1.8778E-03	2.9983E-03
660.01	6.9294E-04	1.4521E-03	670.02	1.8761E-03	2.9910E-03
661.03	7.1106E-04	1.4455E-03	671.01	1.8675E-03	2.9867E-03
662.01	6.8836E-04	1.4452E-03	672.03	1.8580E-03	2.9786E-03
663.02	6.9033E-04	1.4339E-03	673.02	1.8532E-03	2.9703E-03
664.01	6.8092E-04	1.4200E-03	674.02	1.8475E-03	2.9641E-03
665.02	7.0794E-04	1.4175E-03	675.01	1.8422E-03	2.9595E-03
666.01	6.9868E-04	1.4325E-03	676.03	1.8320E-03	2.9528E-03
667.02	6.7907E-04	1.4306E-03	677.01	1.8288E-03	2.9469E-03
668.01	6.7591E-04	1.4219E-03	678.03	1.8186E-03	2.9403E-03
669.03	6.6980E-04	1.4163E-03	679.01	1.8149E-03	2.9327E-03
670.01	6.6689E-04	1.4095E-03	680.03	1.8090E-03	2.9261E-03
671.00	6.6336E-04	1.4009E-03	681.01	1.8066E-03	2.9225E-03
672.04	6.6709E-04	1.3960E-03	682.01	1.7975E-03	2.9182E-03
673.00	6.6003E-04	1.3872E-03	683.02	1.7926E-03	2.9138E-03
674.04	6.7796E-04	1.3859E-03	684.02	1.7804E-03	2.9078E-03

675.00	6.7116E-04	1.3952E-03	685.02	1.7788E-03	2.9015E-03
676.03	6.6194E-04	1.3996E-03	686.01	1.7700E-03	2.8979E-03
677.00	6.3757E-04	1.3899E-03	687.04	1.7620E-03	2.8907E-03
678.03	6.4073E-04	1.3690E-03	688.01	1.7593E-03	2.8861E-03
679.02	6.5198E-04	1.3600E-03	689.01	1.7509E-03	2.8819E-03
680.03	6.6425E-04	1.3645E-03	690.04	1.7449E-03	2.8765E-03
681.01	6.6140E-04	1.3789E-03	691.01	1.7391E-03	2.8718E-03
682.02	6.3030E-04	1.3727E-03	692.01	1.7337E-03	2.8678E-03
683.03	6.4375E-04	1.3597E-03	693.03	1.7274E-03	2.8663E-03
684.01	6.3803E-04	1.3607E-03	694.02	1.7159E-03	2.8621E-03
685.03	6.3088E-04	1.3522E-03	695.01	1.7107E-03	2.8570E-03
686.02	6.4215E-04	1.3535E-03	696.02	1.7012E-03	2.8534E-03
687.02	6.1487E-04	1.3443E-03	697.02	1.6925E-03	2.8477E-03
688.02	6.4079E-04	1.3335E-03	698.01	1.6860E-03	2.8416E-03
689.02	6.3138E-04	1.3356E-03	699.03	1.6809E-03	2.8375E-03
690.02	6.4439E-04	1.3401E-03	700.02	1.6680E-03	2.8321E-03
691.02	6.2519E-04	1.3413E-03	701.01	1.6653E-03	2.8253E-03
692.04	6.3407E-04	1.3373E-03	702.03	1.6589E-03	2.8235E-03
693.02	6.2822E-04	1.3443E-03	703.01	1.6478E-03	2.8201E-03
694.02	6.1067E-04	1.3405E-03	704.03	1.6399E-03	2.8146E-03
695.04	6.1077E-04	1.3282E-03	705.02	1.6298E-03	2.8098E-03
696.02	6.1944E-04	1.3298E-03	706.01	1.6190E-03	2.8027E-03
697.02	6.0199E-04	1.3290E-03	707.02	1.6075E-03	2.7910E-03
698.03	6.0390E-04	1.3205E-03	708.01	1.6067E-03	2.7799E-03
699.02	6.0176E-04	1.3153E-03	709.03	1.6081E-03	2.7787E-03
700.03	6.1356E-04	1.3232E-03	710.01	1.5916E-03	2.7743E-03
701.01	5.8006E-04	1.3207E-03	711.02	1.5929E-03	2.7669E-03
702.02	5.9280E-04	1.3085E-03	712.03	1.5837E-03	2.7646E-03
703.03	5.7802E-04	1.2999E-03	713.00	1.5752E-03	2.7580E-03
704.01	5.9953E-04	1.2966E-03	714.03	1.5724E-03	2.7537E-03
705.02	5.8331E-04	1.2974E-03	715.02	1.5607E-03	2.7502E-03
706.01	5.9850E-04	1.2985E-03	716.02	1.5529E-03	2.7424E-03
707.01	5.7730E-04	1.3034E-03	717.01	1.5469E-03	2.7355E-03
708.01	5.7118E-04	1.2912E-03	718.00	1.5375E-03	2.7284E-03
709.04	5.8149E-04	1.2903E-03	719.03	1.5319E-03	2.7205E-03
710.00	5.6416E-04	1.2891E-03	720.01	1.5259E-03	2.7157E-03
711.02	5.6487E-04	1.2760E-03	721.01	1.5171E-03	2.7080E-03
712.03	5.7790E-04	1.2790E-03	722.04	1.5147E-03	2.7004E-03
713.02	5.5758E-04	1.2787E-03	723.02	1.5078E-03	2.6969E-03
714.04	5.6441E-04	1.2729E-03	724.02	1.4998E-03	2.6896E-03
715.02	5.5506E-04	1.2694E-03	725.03	1.4959E-03	2.6811E-03
716.01	5.5870E-04	1.2614E-03	726.01	1.4938E-03	2.6764E-03
717.03	5.6685E-04	1.2661E-03	727.04	1.4872E-03	2.6746E-03
718.03	5.5241E-04	1.2714E-03	728.01	1.4744E-03	2.6674E-03
719.02	5.3884E-04	1.2589E-03	729.02	1.4732E-03	2.6581E-03
720.04	5.5484E-04	1.2546E-03	730.03	1.4678E-03	2.6520E-03
721.01	5.4100E-04	1.2571E-03	731.02	1.4671E-03	2.6469E-03
722.03	5.3637E-04	1.2480E-03	732.03	1.4588E-03	2.6424E-03
723.02	5.3331E-04	1.2349E-03	733.03	1.4536E-03	2.6345E-03
724.03	5.5753E-04	1.2394E-03	734.03	1.4532E-03	2.6307E-03
725.02	5.3352E-04	1.2455E-03	735.02	1.4448E-03	2.6280E-03
726.02	5.2953E-04	1.2315E-03	736.01	1.4378E-03	2.6214E-03
727.00	5.3932E-04	1.2256E-03	737.02	1.4335E-03	2.6139E-03
728.03	5.4190E-04	1.2297E-03	738.02	1.4300E-03	2.6082E-03
729.02	5.3666E-04	1.2358E-03	739.01	1.4277E-03	2.6061E-03
730.03	5.1715E-04	1.2267E-03	740.03	1.4178E-03	2.6018E-03

731.01	5.3767E-04	1.2246E-03	741.03	1.4152E-03	2.5963E-03
732.02	5.1508E-04	1.2267E-03	742.02	1.4083E-03	2.5920E-03
733.02	5.2116E-04	1.2195E-03	743.04	1.4037E-03	2.5866E-03
734.02	5.1222E-04	1.2175E-03	744.03	1.3978E-03	2.5817E-03
735.02	5.0786E-04	1.2045E-03	745.02	1.3940E-03	2.5765E-03
736.03	5.2845E-04	1.2072E-03	746.03	1.3884E-03	2.5716E-03
737.02	5.0610E-04	1.2093E-03	747.01	1.3848E-03	2.5686E-03
738.02	5.1718E-04	1.2049E-03	748.02	1.3755E-03	2.5637E-03
739.02	5.0300E-04	1.2048E-03	749.03	1.3714E-03	2.5560E-03
740.04	5.0698E-04	1.2028E-03	750.03	1.3697E-03	2.5507E-03
741.00	4.9398E-04	1.1979E-03	751.02	1.3687E-03	2.5499E-03
742.01	5.0245E-04	1.1932E-03	752.03	1.3587E-03	2.5478E-03
743.03	4.9112E-04	1.1911E-03	753.01	1.3562E-03	2.5439E-03
744.00	4.9011E-04	1.1797E-03	754.02	1.3496E-03	2.5400E-03
745.03	5.0342E-04	1.1788E-03	755.03	1.3576E-03	2.5559E-03
746.00	4.9336E-04	1.1804E-03	756.01	1.2906E-03	2.5398E-03
747.02	4.9618E-04	1.1779E-03	757.03	1.3244E-03	2.5046E-03
748.03	4.8941E-04	1.1780E-03	758.03	1.3320E-03	2.5073E-03
749.02	4.8325E-04	1.1682E-03	759.01	1.3429E-03	2.5259E-03
750.00	4.9655E-04	1.1665E-03	760.02	1.2885E-03	2.5236E-03
751.03	4.8414E-04	1.1661E-03	761.02	1.2968E-03	2.4925E-03
752.04	4.9250E-04	1.1602E-03	762.04	1.3178E-03	2.4931E-03
753.01	4.9658E-04	1.1679E-03	763.00	1.3073E-03	2.5072E-03
754.04	4.7796E-04	1.1646E-03	764.02	1.2832E-03	2.5011E-03
755.02	4.9016E-04	1.1592E-03	765.03	1.2948E-03	2.5059E-03
756.02	4.8680E-04	1.1641E-03	766.02	1.2411E-03	2.4909E-03
757.03	4.8479E-04	1.1686E-03	766.99	1.2771E-03	2.4739E-03
758.02	4.6562E-04	1.1633E-03	768.05	1.2505E-03	2.4781E-03
759.03	4.7664E-04	1.1565E-03	769.02	1.2532E-03	2.4720E-03
760.02	4.7296E-04	1.1630E-03	769.99	1.2288E-03	2.4627E-03
761.02	4.5892E-04	1.1634E-03	771.04	1.2302E-03	2.4425E-03
762.02	4.4362E-04	1.1463E-03	772.02	1.2323E-03	2.4292E-03
763.03	4.6656E-04	1.1356E-03	773.00	1.2459E-03	2.4260E-03
764.00	4.7164E-04	1.1496E-03	774.03	1.2455E-03	2.4363E-03
765.03	4.4825E-04	1.1499E-03	775.01	1.2195E-03	2.4310E-03
766.02	4.5548E-04	1.1457E-03	776.01	1.2226E-03	2.4125E-03
767.02	4.3803E-04	1.1429E-03	777.04	1.2394E-03	2.4167E-03
768.02	4.4146E-04	1.1345E-03	778.01	1.2199E-03	2.4235E-03
769.03	4.3623E-04	1.1252E-03	779.02	1.2115E-03	2.4170E-03
770.01	4.5698E-04	1.1297E-03	780.04	1.1971E-03	2.4014E-03
771.02	4.3082E-04	1.1342E-03	781.01	1.2220E-03	2.4053E-03
772.01	4.3429E-04	1.1232E-03	782.01	1.1764E-03	2.3988E-03
773.01	4.3576E-04	1.1256E-03	783.02	1.2068E-03	2.3812E-03
774.04	4.1934E-04	1.1205E-03	784.04	1.2008E-03	2.3901E-03
775.02	4.1931E-04	1.1043E-03	785.01	1.1971E-03	2.3958E-03
776.04	4.3884E-04	1.1059E-03	786.04	1.1768E-03	2.3967E-03
777.01	4.1780E-04	1.1056E-03	787.03	1.1633E-03	2.3865E-03
778.04	4.3162E-04	1.0972E-03	788.01	1.1559E-03	2.3728E-03
779.02	4.2933E-04	1.1005E-03	789.03	1.1611E-03	2.3660E-03
780.04	4.2987E-04	1.1029E-03	790.02	1.1516E-03	2.3630E-03
781.02	4.1996E-04	1.1047E-03	791.02	1.1443E-03	2.3502E-03
782.01	4.1220E-04	1.0992E-03	792.03	1.1607E-03	2.3549E-03
783.04	4.0561E-04	1.0872E-03	793.02	1.1220E-03	2.3487E-03
784.02	4.1372E-04	1.0766E-03	794.02	1.1409E-03	2.3323E-03
785.03	4.2504E-04	1.0774E-03	795.03	1.1315E-03	2.3294E-03
786.03	4.2460E-04	1.0840E-03	796.02	1.1427E-03	2.3318E-03

787.02	4.1872E-04	1.0853E-03	797.00	1.1176E-03	2.3276E-03
788.01	4.1925E-04	1.0857E-03	798.03	1.1339E-03	2.3244E-03
789.05	4.1965E-04	1.0977E-03	799.02	1.1097E-03	2.3256E-03
790.01	3.8105E-04	1.0881E-03	800.00	1.1103E-03	2.3171E-03
791.01	3.9911E-04	1.0659E-03	801.03	1.1019E-03	2.3156E-03
792.02	4.1310E-04	1.0743E-03	802.02	1.0874E-03	2.3059E-03
793.03	3.9260E-04	1.0784E-03	803.01	1.0887E-03	2.2944E-03
794.01	3.9259E-04	1.0700E-03	804.02	1.0878E-03	2.2913E-03
795.03	3.8971E-04	1.0685E-03	805.03	1.0758E-03	2.2824E-03
796.02	3.7969E-04	1.0569E-03	806.03	1.0870E-03	2.2814E-03
797.02	4.0036E-04	1.0571E-03	807.02	1.0563E-03	2.2723E-03
798.02	3.7597E-04	1.0534E-03	808.02	1.0735E-03	2.2557E-03
799.02	4.0260E-04	1.0517E-03	809.02	1.0682E-03	2.2527E-03
800.02	3.8099E-04	1.0583E-03	810.03	1.0704E-03	2.2458E-03
801.01	3.8426E-04	1.0558E-03	811.03	1.0749E-03	2.2485E-03
802.04	3.6949E-04	1.0515E-03	812.02	1.0598E-03	2.2475E-03
803.03	3.7104E-04	1.0413E-03	813.00	1.0565E-03	2.2373E-03
804.01	3.7094E-04	1.0345E-03	814.05	1.0565E-03	2.2293E-03
805.04	3.7741E-04	1.0329E-03	815.01	1.0599E-03	2.2271E-03
806.02	3.6798E-04	1.0259E-03	816.02	1.0590E-03	2.2313E-03
807.01	3.8788E-04	1.0262E-03	817.00	1.0372E-03	2.2215E-03
808.03	3.7122E-04	1.0284E-03	818.04	1.0578E-03	2.2157E-03
809.04	3.8293E-04	1.0291E-03	819.01	1.0446E-03	2.2239E-03
810.01	3.6073E-04	1.0242E-03	820.05	1.0301E-03	2.2180E-03
811.02	3.8306E-04	1.0212E-03	821.03	1.0201E-03	2.2018E-03
812.04	3.6336E-04	1.0236E-03	822.00	1.0362E-03	2.1933E-03
813.04	3.7540E-04	1.0195E-03	823.00	1.0397E-03	2.2066E-03
814.04	3.6592E-04	1.0224E-03	824.04	1.0016E-03	2.1970E-03
815.01	3.6667E-04	1.0237E-03	825.03	1.0219E-03	2.1782E-03
816.02	3.4742E-04	1.0162E-03	826.02	1.0232E-03	2.1808E-03
817.00	3.6426E-04	1.0120E-03	827.01	1.0261E-03	2.1904E-03
818.04	3.4153E-04	1.0062E-03	828.03	9.9263E-04	2.1852E-03
819.02	3.6113E-04	9.9693E-04	829.02	1.0002E-03	2.1667E-03
820.01	3.5502E-04	9.9955E-04	830.03	1.0067E-03	2.1649E-03
821.03	3.5935E-04	9.9756E-04	831.02	1.0027E-03	2.1677E-03
822.03	3.6091E-04	1.0035E-03	832.02	9.9179E-04	2.1643E-03
823.01	3.4914E-04	1.0088E-03	833.03	9.8965E-04	2.1564E-03
824.02	3.2944E-04	9.9432E-04	834.00	9.9033E-04	2.1555E-03
825.01	3.4770E-04	9.8323E-04	835.01	9.7593E-04	2.1506E-03
826.01	3.4481E-04	9.8546E-04	836.02	9.6954E-04	2.1290E-03
827.02	3.4249E-04	9.8032E-04	837.04	1.0080E-03	2.1351E-03
828.05	3.5354E-04	9.8227E-04	838.02	9.7360E-04	2.1467E-03
829.01	3.4261E-04	9.8769E-04	839.04	9.7463E-04	2.1333E-03
830.02	3.3449E-04	9.8199E-04	840.01	9.7802E-04	2.1334E-03
831.01	3.3406E-04	9.7368E-04	841.02	9.7398E-04	2.1433E-03
832.03	3.3878E-04	9.7315E-04	842.01	9.4258E-04	2.1383E-03
833.03	3.2405E-04	9.6323E-04	843.01	9.3643E-04	2.1122E-03
834.01	3.4581E-04	9.5692E-04	844.03	9.6136E-04	2.1092E-03
835.03	3.4177E-04	9.6238E-04	845.03	9.3886E-04	2.1082E-03
836.03	3.4844E-04	9.6605E-04	846.03	9.5483E-04	2.1020E-03
837.03	3.4136E-04	9.7469E-04	847.01	9.4350E-04	2.1047E-03
838.02	3.2305E-04	9.7066E-04	848.03	9.4047E-04	2.0993E-03
839.02	3.2728E-04	9.6329E-04	849.01	9.3860E-04	2.0974E-03
840.01	3.2148E-04	9.6070E-04	850.03	9.3345E-04	2.0989E-03
841.03	3.1793E-04	9.5253E-04	851.03	9.1228E-04	2.0842E-03
842.01	3.2076E-04	9.4455E-04	852.03	9.3693E-04	2.0768E-03

843.03	3.2846E-04	9.4419E-04	853.01	9.2586E-04	2.0871E-03
844.02	3.2151E-04	9.4209E-04	854.01	9.1031E-04	2.0791E-03
845.03	3.3341E-04	9.4152E-04	855.05	9.1291E-04	2.0671E-03
846.03	3.2443E-04	9.4574E-04	856.03	9.1741E-04	2.0648E-03
847.02	3.2386E-04	9.4375E-04	857.01	9.1609E-04	2.0689E-03
848.03	3.2004E-04	9.4352E-04	858.03	9.0334E-04	2.0685E-03
849.04	3.1021E-04	9.3414E-04	859.04	8.9352E-04	2.0557E-03
850.03	3.2715E-04	9.2975E-04	860.04	9.0707E-04	2.0535E-03
851.03	3.2485E-04	9.4132E-04	861.00	8.9116E-04	2.0552E-03
852.02	3.0446E-04	9.3443E-04	862.03	8.8773E-04	2.0422E-03
853.03	3.2414E-04	9.3126E-04	863.03	9.0412E-04	2.0465E-03
854.02	3.0469E-04	9.3372E-04	864.01	8.7825E-04	2.0492E-03
855.02	3.0988E-04	9.2597E-04	865.02	8.8608E-04	2.0462E-03
856.03	3.0691E-04	9.2528E-04	866.03	8.6269E-04	2.0464E-03
857.03	3.0243E-04	9.1896E-04	867.03	8.4917E-04	2.0246E-03
858.03	3.0901E-04	9.1591E-04	868.04	8.6751E-04	2.0111E-03
859.03	3.0384E-04	9.1409E-04	869.01	8.7181E-04	2.0163E-03
860.03	3.1224E-04	9.1442E-04	870.04	8.6365E-04	2.0209E-03
861.03	3.0359E-04	9.1774E-04	871.03	8.4753E-04	2.0104E-03
862.03	2.9510E-04	9.0900E-04	872.02	8.6138E-04	2.0078E-03
863.04	3.0801E-04	9.0599E-04	873.02	8.3771E-04	2.0047E-03
864.05	2.9998E-04	9.0873E-04	874.05	8.4620E-04	1.9940E-03
865.00	2.9935E-04	9.0469E-04	875.03	8.3534E-04	1.9862E-03
866.01	3.0006E-04	9.0214E-04	876.01	8.5072E-04	1.9834E-03
867.02	3.0085E-04	9.0347E-04	877.01	8.3479E-04	1.9821E-03
868.02	2.9476E-04	9.0294E-04	878.03	8.4493E-04	1.9774E-03
869.01	2.9371E-04	9.0029E-04	879.03	8.3779E-04	1.9805E-03
870.02	2.8738E-04	8.9559E-04	880.01	8.3282E-04	1.9802E-03
871.05	2.9264E-04	8.9216E-04	881.04	8.1798E-04	1.9717E-03
872.00	2.8588E-04	8.9042E-04	882.04	8.2508E-04	1.9632E-03
873.02	2.9002E-04	8.8723E-04	883.01	8.2045E-04	1.9619E-03
874.02	2.8433E-04	8.8405E-04	884.03	8.1543E-04	1.9551E-03
875.04	2.8818E-04	8.8061E-04	885.03	8.2111E-04	1.9533E-03
876.03	2.8503E-04	8.7894E-04	886.03	8.1066E-04	1.9521E-03
877.01	2.8496E-04	8.7330E-04	887.01	8.1113E-04	1.9463E-03
878.03	2.9147E-04	8.7283E-04	888.02	8.0985E-04	1.9467E-03
879.03	2.8703E-04	8.7095E-04	889.05	7.9739E-04	1.9424E-03
880.02	2.9610E-04	8.7341E-04	890.01	7.9659E-04	1.9343E-03
881.02	2.8441E-04	8.7683E-04	891.01	7.9297E-04	1.9265E-03
882.02	2.8500E-04	8.7205E-04	892.04	7.9892E-04	1.9229E-03
883.04	2.8469E-04	8.7100E-04	893.02	7.9146E-04	1.9209E-03
884.02	2.8418E-04	8.7070E-04	894.04	7.9225E-04	1.9153E-03
885.00	2.8177E-04	8.7174E-04	895.00	7.8988E-04	1.9114E-03
886.03	2.7197E-04	8.6583E-04	896.03	7.9481E-04	1.9099E-03
887.04	2.8068E-04	8.6183E-04	897.02	7.9398E-04	1.9182E-03
888.04	2.7272E-04	8.5826E-04	898.03	7.6873E-04	1.9131E-03
889.01	2.8388E-04	8.5641E-04	899.03	7.7350E-04	1.8973E-03
890.05	2.7735E-04	8.5899E-04	900.01	7.8040E-04	1.8962E-03
891.04	2.7948E-04	8.5855E-04	901.04	7.7413E-04	1.8969E-03
892.01	2.7492E-04	8.6067E-04	902.02	7.7263E-04	1.8970E-03
893.02	2.6733E-04	8.5533E-04	903.01	7.5718E-04	1.8891E-03
894.03	2.7442E-04	8.5371E-04	904.05	7.6811E-04	1.8819E-03
895.04	2.6293E-04	8.5188E-04	905.02	7.6073E-04	1.8827E-03
896.03	2.6835E-04	8.4580E-04	906.03	7.5797E-04	1.8772E-03
897.03	2.6801E-04	8.4657E-04	907.01	7.5861E-04	1.8761E-03
898.03	2.6219E-04	8.4212E-04	908.02	7.4788E-04	1.8689E-03

899.04	2.7005E-04	8.4033E-04	909.03	7.5811E-04	1.8654E-03
900.03	2.6289E-04	8.3924E-04	910.02	7.4640E-04	1.8652E-03
901.02	2.6879E-04	8.3740E-04	911.03	7.4891E-04	1.8607E-03
902.05	2.6432E-04	8.3924E-04	912.02	7.4412E-04	1.8597E-03
903.03	2.6175E-04	8.3690E-04	913.02	7.4218E-04	1.8575E-03
904.02	2.5810E-04	8.3207E-04	914.05	7.3636E-04	1.8541E-03
905.02	2.6498E-04	8.3034E-04	915.01	7.3620E-04	1.8531E-03
906.03	2.6236E-04	8.3400E-04	916.04	7.2442E-04	1.8476E-03
907.06	2.5369E-04	8.3131E-04	917.03	7.2963E-04	1.8426E-03
908.04	2.5461E-04	8.2481E-04	918.01	7.2267E-04	1.8412E-03
909.00	2.5743E-04	8.2205E-04	919.02	7.3045E-04	1.8561E-03
910.05	2.5974E-04	8.2349E-04	919.04	7.1697E-04	1.8549E-03
911.02	2.5506E-04	8.2352E-04	920.01	7.1434E-04	1.8310E-03
912.00	2.5575E-04	8.2165E-04	921.02	7.0818E-04	1.8257E-03
913.02	2.5393E-04	8.2287E-04	922.03	7.1030E-04	1.8205E-03
914.03	2.4639E-04	8.1993E-04	923.03	7.0718E-04	1.8186E-03
915.01	2.4914E-04	8.1657E-04	924.03	7.0315E-04	1.8136E-03
916.04	2.4185E-04	8.1222E-04	925.02	7.0353E-04	1.8100E-03
916.99	2.4702E-04	8.0581E-04	926.04	6.9785E-04	1.8071E-03
918.03	2.5282E-04	8.0797E-04	927.03	6.9556E-04	1.8008E-03
919.04	2.4545E-04	8.1059E-04	928.04	6.9617E-04	1.7973E-03
920.03	2.4149E-04	8.0480E-04	929.02	6.9378E-04	1.7958E-03
921.02	2.4684E-04	8.0267E-04	930.04	6.8655E-04	1.7898E-03
922.00	2.4110E-04	8.0172E-04	931.04	6.9052E-04	1.7849E-03
923.03	2.4480E-04	7.9914E-04	932.03	6.8592E-04	1.7812E-03
924.04	2.4162E-04	7.9928E-04	933.03	6.8866E-04	1.7787E-03
925.00	2.3911E-04	7.9530E-04	934.02	6.8414E-04	1.7784E-03
926.02	2.4428E-04	7.9435E-04	935.03	6.7924E-04	1.7748E-03
927.03	2.4125E-04	7.9643E-04	936.01	6.7554E-04	1.7684E-03
928.03	2.3830E-04	7.9669E-04	937.03	6.7964E-04	1.7650E-03
929.03	2.3234E-04	7.9464E-04	938.02	6.7490E-04	1.7636E-03
930.00	2.3328E-04	7.9801E-04	939.03	6.7364E-04	1.7608E-03
931.01	1.9852E-04	7.7874E-04	940.02	6.6858E-04	1.7576E-03
932.04	2.3851E-04	7.5674E-04	941.02	6.6617E-04	1.7525E-03
934.01	2.5876E-04	7.7804E-04	942.03	6.6634E-04	1.7498E-03
935.04	2.4597E-04	7.9097E-04	943.04	6.6060E-04	1.7455E-03
936.02	2.3416E-04	7.9083E-04	944.03	6.6336E-04	1.7422E-03
937.03	2.2370E-04	7.7998E-04	945.02	6.5591E-04	1.7387E-03
938.00	2.3944E-04	7.8003E-04	946.03	6.5950E-04	1.7349E-03
939.03	2.1777E-04	7.7852E-04	947.02	6.5431E-04	1.7332E-03
940.02	2.2780E-04	7.6698E-04	948.03	6.5414E-04	1.7297E-03
940.99	2.3610E-04	7.7177E-04	949.02	6.5095E-04	1.7280E-03
942.03	2.2447E-04	7.7537E-04	950.03	6.4585E-04	1.7223E-03
943.02	2.2058E-04	7.6961E-04	951.02	6.4688E-04	1.7176E-03
944.01	2.2168E-04	7.6749E-04	952.05	6.4498E-04	1.7156E-03
945.02	2.1148E-04	7.6007E-04	953.03	6.4371E-04	1.7140E-03
946.03	2.2029E-04	7.5125E-04	954.00	6.3830E-04	1.7107E-03
947.01	2.2035E-04	7.4582E-04	955.01	6.3818E-04	1.7062E-03
948.04	2.3583E-04	7.4507E-04	956.02	6.3510E-04	1.7024E-03
949.02	2.3681E-04	7.5261E-04	957.04	6.3635E-04	1.7004E-03
950.02	2.3647E-04	7.6221E-04	958.01	6.3165E-04	1.6994E-03
951.02	2.1396E-04	7.5760E-04	959.03	6.2779E-04	1.6947E-03
952.03	2.2406E-04	7.4401E-04	960.04	6.2718E-04	1.6904E-03
953.03	2.3629E-04	7.4991E-04	961.03	6.2649E-04	1.6881E-03
954.03	2.2472E-04	7.5487E-04	962.01	6.2238E-04	1.6853E-03
955.01	2.2819E-04	7.5679E-04	963.02	6.2161E-04	1.6817E-03

956.01	2.1195E-04	7.5629E-04	964.02	6.1904E-04	1.6786E-03
957.03	2.1138E-04	7.4668E-04	965.02	6.1771E-04	1.6747E-03
958.05	2.1346E-04	7.4230E-04	966.01	6.1819E-04	1.6734E-03
959.03	2.1189E-04	7.3787E-04	967.05	6.1286E-04	1.6718E-03
960.03	2.1627E-04	7.3281E-04	968.01	6.0996E-04	1.6677E-03
961.00	2.2563E-04	7.3767E-04	969.04	6.0890E-04	1.6639E-03
962.05	2.1051E-04	7.3693E-04	970.00	6.0736E-04	1.6610E-03
963.02	2.2104E-04	7.3413E-04	971.03	6.0455E-04	1.6585E-03
964.02	2.1298E-04	7.3594E-04	971.99	6.0241E-04	1.6558E-03
965.02	2.1085E-04	7.2816E-04	973.04	5.9915E-04	1.6522E-03
966.03	2.2073E-04	7.2446E-04	974.06	5.9730E-04	1.6477E-03
967.05	2.2612E-04	7.3165E-04	975.02	5.9554E-04	1.6447E-03
968.03	2.2004E-04	7.3927E-04	975.99	5.9396E-04	1.6415E-03
969.03	2.0526E-04	7.3478E-04	977.02	5.9189E-04	1.6379E-03
970.03	2.1248E-04	7.2897E-04	978.01	5.9020E-04	1.6348E-03
971.05	2.0552E-04	7.2558E-04	979.04	5.8874E-04	1.6314E-03
972.01	2.1442E-04	7.2233E-04	980.04	5.8839E-04	1.6293E-03
973.00	2.1434E-04	7.2686E-04	981.02	5.8391E-04	1.6273E-03
974.03	2.0856E-04	7.2869E-04	982.00	5.8190E-04	1.6231E-03
975.04	2.0272E-04	7.2451E-04	983.04	5.7953E-04	1.6174E-03
976.06	2.0664E-04	7.2259E-04	984.02	5.8481E-04	1.6165E-03
977.04	1.9952E-04	7.2077E-04	985.02	5.7776E-04	1.6167E-03
978.02	2.0079E-04	7.1562E-04	986.04	5.7658E-04	1.6135E-03
979.02	2.0212E-04	7.1306E-04	987.03	5.7220E-04	1.6103E-03
980.04	2.0427E-04	7.1297E-04	988.03	5.7141E-04	1.6062E-03
981.04	2.0169E-04	7.1325E-04	989.02	5.6964E-04	1.6035E-03
982.04	1.9816E-04	7.1037E-04	990.01	5.6765E-04	1.6005E-03
983.05	1.9833E-04	7.0342E-04	991.03	5.6568E-04	1.5973E-03
984.01	2.0875E-04	7.0335E-04	992.03	5.6441E-04	1.5945E-03
985.01	2.0820E-04	7.1003E-04	993.06	5.6217E-04	1.5918E-03
986.05	2.0243E-04	7.1346E-04	994.01	5.5980E-04	1.5884E-03
987.05	1.9637E-04	7.1365E-04	995.00	5.5896E-04	1.5849E-03
988.02	1.8681E-04	7.0724E-04	996.02	5.5830E-04	1.5828E-03
989.05	1.9079E-04	6.9787E-04	997.07	5.5501E-04	1.5801E-03
990.02	1.9670E-04	6.9674E-04	998.04	5.5465E-04	1.5780E-03
991.01	1.9608E-04	6.9951E-04	999.03	5.5026E-04	1.5738E-03
992.03	1.9215E-04	6.9653E-04	1000.00	5.5168E-04	1.5713E-03
993.02	2.0025E-04	6.9814E-04	1001.01	5.4692E-04	1.5700E-03
994.04	1.8841E-04	6.9870E-04	1002.05	5.4346E-04	1.5647E-03
995.05	1.9126E-04	6.9295E-04	1003.04	5.4476E-04	1.5610E-03
996.03	1.9376E-04	6.9402E-04	1004.01	5.4267E-04	1.5594E-03
997.03	1.8822E-04	6.9495E-04	1005.02	5.3953E-04	1.5561E-03
998.03	1.8279E-04	6.8867E-04	1006.03	5.3802E-04	1.5527E-03
999.02	1.8949E-04	6.8548E-04	1007.02	5.3654E-04	1.5498E-03
1000.04	1.8486E-04	6.8327E-04	1008.04	5.3415E-04	1.5463E-03
1001.02	1.9129E-04	6.8094E-04	1009.04	5.3347E-04	1.5435E-03
1002.01	1.9201E-04	6.8474E-04	1010.01	5.3024E-04	1.5409E-03
1003.03	1.8389E-04	6.8290E-04	1011.03	5.2992E-04	1.5382E-03
1004.01	1.8909E-04	6.8047E-04	1012.04	5.2802E-04	1.5361E-03
1005.04	1.8493E-04	6.8136E-04	1013.03	5.2595E-04	1.5336E-03
1006.01	1.8323E-04	6.7941E-04	1014.03	5.2450E-04	1.5314E-03
1007.04	1.8022E-04	6.7636E-04	1015.02	5.2053E-04	1.5278E-03
1008.02	1.7691E-04	6.6691E-04	1016.03	5.1988E-04	1.5232E-03
1009.03	1.9314E-04	6.6393E-04	1017.02	5.2094E-04	1.5209E-03
1010.06	1.9498E-04	6.7359E-04	1018.02	5.1737E-04	1.5191E-03
1011.02	1.8428E-04	6.7514E-04	1019.04	5.1578E-04	1.5160E-03

1012.01	1.8781E-04	6.7366E-04	1020.02	5.1398E-04	1.5142E-03
1013.03	1.7956E-04	6.7218E-04	1021.02	5.1175E-04	1.5105E-03
1014.01	1.8119E-04	6.6698E-04	1022.03	5.1084E-04	1.5063E-03
1015.02	1.8156E-04	6.6341E-04	1023.02	5.0951E-04	1.5047E-03
1016.04	1.8939E-04	6.6587E-04	1024.03	5.0809E-04	1.5011E-03
1017.03	1.8094E-04	6.6915E-04	1025.04	5.0685E-04	1.4991E-03
1018.04	1.7885E-04	6.6721E-04	1026.01	5.0501E-04	1.4957E-03
1019.00	1.6952E-04	6.5835E-04	1027.03	5.0353E-04	1.4931E-03
1020.03	1.8809E-04	6.5645E-04	1028.04	5.0146E-04	1.4897E-03
1021.04	1.7604E-04	6.5815E-04	1029.02	4.9978E-04	1.4872E-03
1022.02	1.8929E-04	6.5811E-04	1030.00	4.9781E-04	1.4840E-03
1023.03	1.7997E-04	6.6508E-04	1031.04	4.9825E-04	1.4816E-03
1024.00	1.7244E-04	6.6213E-04	1032.02	4.9572E-04	1.4789E-03
1025.03	1.6973E-04	6.5543E-04	1033.01	4.9470E-04	1.4758E-03
1026.06	1.7352E-04	6.4873E-04	1034.01	4.9493E-04	1.4741E-03
1027.02	1.8059E-04	6.4833E-04	1035.04	4.9111E-04	1.4723E-03
1028.00	1.8006E-04	6.5288E-04	1036.03	4.8972E-04	1.4690E-03
1029.00	1.7440E-04	6.5325E-04	1037.03	4.8873E-04	1.4662E-03
1030.05	1.7359E-04	6.4908E-04	1038.02	4.8721E-04	1.4641E-03
1031.03	1.7840E-04	6.4937E-04	1039.03	4.8555E-04	1.4618E-03
1032.02	1.7582E-04	6.5441E-04	1040.02	4.8505E-04	1.4599E-03
1033.03	1.6271E-04	6.5044E-04	1041.02	4.8358E-04	1.4590E-03
1034.03	1.6735E-04	6.4200E-04	1042.03	4.7738E-04	1.4548E-03
1035.03	1.6985E-04	6.3965E-04	1043.00	4.7924E-04	1.4499E-03
1036.01	1.7248E-04	6.3980E-04	1044.05	4.7745E-04	1.4479E-03
1037.05	1.6995E-04	6.3729E-04	1045.06	4.7680E-04	1.4457E-03
1038.03	1.8094E-04	6.4207E-04	1046.02	4.7408E-04	1.4430E-03
1039.01	1.6425E-04	6.4408E-04	1046.99	4.7391E-04	1.4395E-03
1040.00	1.7294E-04	6.4291E-04	1048.06	4.7175E-04	1.4366E-03
1041.01	1.5672E-04	6.4017E-04	1049.02	4.7160E-04	1.4342E-03
1042.07	1.6934E-04	6.3543E-04	1050.01	4.6948E-04	1.4318E-03
1043.04	1.6039E-04	6.3566E-04	1051.02	4.6914E-04	1.4294E-03
1044.02	1.6741E-04	6.3389E-04	1052.04	4.6618E-04	1.4270E-03
1045.00	1.6023E-04	6.3395E-04	1053.01	4.6578E-04	1.4239E-03
1046.04	1.6305E-04	6.3184E-04	1054.03	4.6522E-04	1.4221E-03
1047.04	1.5813E-04	6.2918E-04	1055.01	4.6353E-04	1.4207E-03
1048.02	1.6598E-04	6.3055E-04	1056.03	4.6023E-04	1.4180E-03
1049.04	1.5096E-04	6.2855E-04	1057.02	4.5946E-04	1.4148E-03
1050.05	1.5515E-04	6.1618E-04	1058.03	4.5867E-04	1.4128E-03
1051.03	1.7183E-04	6.2081E-04	1059.05	4.5473E-04	1.4095E-03
1051.99	1.5670E-04	6.2452E-04	1060.02	4.5523E-04	1.4048E-03
1053.05	1.6464E-04	6.2350E-04	1061.02	4.5465E-04	1.4029E-03
1054.05	1.4975E-04	6.2007E-04	1062.03	4.5364E-04	1.4013E-03
1055.02	1.6281E-04	6.1451E-04	1063.03	4.5073E-04	1.3988E-03
1056.01	1.5903E-04	6.1699E-04	1064.00	4.5112E-04	1.3958E-03
1057.03	1.6034E-04	6.1685E-04	1065.03	4.4907E-04	1.3942E-03
1058.03	1.5592E-04	6.1537E-04	1066.02	4.4783E-04	1.3916E-03
1059.03	1.5790E-04	6.1368E-04	1067.05	4.4637E-04	1.3890E-03
1060.04	1.5744E-04	6.1267E-04	1068.03	4.4595E-04	1.3872E-03
1061.01	1.5864E-04	6.1178E-04	1069.03	4.4355E-04	1.3852E-03
1062.02	1.5811E-04	6.1151E-04	1070.02	4.4238E-04	1.3826E-03
1063.02	1.5890E-04	6.1285E-04	1071.01	4.3966E-04	1.3793E-03
1064.06	1.5047E-04	6.0755E-04	1072.04	4.4055E-04	1.3768E-03
1065.05	1.6581E-04	6.0875E-04	1073.06	4.3819E-04	1.3753E-03
1066.01	1.5363E-04	6.1432E-04	1074.01	4.3734E-04	1.3730E-03
1067.05	1.5225E-04	6.1012E-04	1075.01	4.3482E-04	1.3702E-03

1068.04	1.4912E-04	6.0533E-04	1076.03	4.3508E-04	1.3676E-03
1069.06	1.5693E-04	6.0476E-04	1077.02	4.3258E-04	1.3652E-03
1070.04	1.5081E-04	6.0590E-04	1078.01	4.3297E-04	1.3625E-03
1070.98	1.5423E-04	6.0669E-04	1079.08	4.3100E-04	1.3607E-03
1072.01	1.3973E-04	5.9970E-04	1080.02	4.2995E-04	1.3587E-03
1073.04	1.5912E-04	5.9501E-04	1081.01	4.2866E-04	1.3569E-03
1074.04	1.5391E-04	6.0354E-04	1082.03	4.2714E-04	1.3540E-03
1075.01	1.4379E-04	5.9841E-04	1083.03	4.2651E-04	1.3523E-03
1076.01	1.5482E-04	5.9474E-04	1083.98	4.2450E-04	1.3499E-03
1077.05	1.5284E-04	5.9951E-04	1085.04	4.2313E-04	1.3473E-03
1078.02	1.4963E-04	6.0098E-04	1086.04	4.2190E-04	1.3452E-03
1079.03	1.4435E-04	5.9875E-04	1087.00	4.2001E-04	1.3429E-03
1080.06	1.4334E-04	5.9508E-04	1088.05	4.1796E-04	1.3393E-03
1081.04	1.4473E-04	5.9407E-04	1088.99	4.2006E-04	1.3372E-03
1082.02	1.3924E-04	5.8998E-04	1090.02	4.1771E-04	1.3365E-03
1083.06	1.4617E-04	5.8619E-04	1091.08	4.1702E-04	1.3355E-03
1084.03	1.4709E-04	5.8969E-04	1092.02	4.1224E-04	1.3331E-03
1085.00	1.4070E-04	5.8828E-04	1093.00	4.1320E-04	1.3301E-03
1086.03	1.4344E-04	5.8362E-04	1094.05	4.1004E-04	1.3282E-03
1087.03	1.4721E-04	5.8561E-04	1095.02	4.0804E-04	1.3242E-03
1088.04	1.4213E-04	5.8815E-04	1096.01	4.0901E-04	1.3217E-03
1089.05	1.3461E-04	5.8154E-04	1097.05	4.0614E-04	1.3197E-03
1090.04	1.4651E-04	5.7978E-04	1098.00	4.0643E-04	1.3177E-03
1090.99	1.3863E-04	5.8177E-04	1099.04	4.0297E-04	1.3153E-03
1092.02	1.4141E-04	5.8055E-04	1100.01	4.0311E-04	1.3127E-03
1093.05	1.3266E-04	5.7626E-04	1101.02	4.0048E-04	1.3100E-03
1094.02	1.4126E-04	5.7046E-04	1102.01	4.0098E-04	1.3073E-03
1095.03	1.4525E-04	5.7379E-04	1103.04	3.9975E-04	1.3055E-03
1096.03	1.4254E-04	5.7761E-04	1104.05	3.9872E-04	1.3033E-03
1097.01	1.3535E-04	5.7526E-04	1104.99	3.9829E-04	1.3019E-03
1098.03	1.3826E-04	5.7096E-04	1106.05	3.9538E-04	1.3000E-03
1099.04	1.3849E-04	5.6998E-04	1107.00	3.9424E-04	1.2976E-03
1100.02	1.4001E-04	5.7012E-04	1108.01	3.9178E-04	1.2949E-03
1101.02	1.3557E-04	5.6771E-04	1109.05	3.9114E-04	1.2913E-03
1102.04	1.4291E-04	5.6876E-04	1110.04	3.9085E-04	1.2889E-03
1102.98	1.3090E-04	5.6702E-04	1111.01	3.8969E-04	1.2864E-03
1104.06	1.4167E-04	5.6292E-04	1112.01	3.8928E-04	1.2839E-03
1105.04	1.3789E-04	5.6335E-04	1113.02	3.8837E-04	1.2824E-03
1106.05	1.4668E-04	5.6734E-04	1114.01	3.8539E-04	1.2799E-03
1107.01	1.3222E-04	5.6897E-04	1115.05	3.8625E-04	1.2772E-03
1108.02	1.3622E-04	5.6260E-04	1116.02	3.8288E-04	1.2744E-03
1109.01	1.3686E-04	5.6314E-04	1117.05	3.8395E-04	1.2697E-03
1110.04	1.3636E-04	5.6414E-04	1118.03	3.8590E-04	1.2674E-03
1111.04	1.3279E-04	5.6378E-04	1119.00	3.8714E-04	1.2668E-03
1111.98	1.3079E-04	5.6100E-04	1120.05	3.8876E-04	1.2694E-03
1113.07	1.3341E-04	5.5948E-04	1121.02	3.8161E-04	1.2698E-03
1114.04	1.3173E-04	5.6007E-04	1122.03	3.7846E-04	1.2660E-03
1115.02	1.3032E-04	5.6057E-04	1123.04	3.7712E-04	1.2623E-03
1116.03	1.2351E-04	5.5698E-04	1124.03	3.7711E-04	1.2600E-03
1117.06	1.2788E-04	5.5248E-04	1125.01	3.7410E-04	1.2568E-03
1118.03	1.2632E-04	5.5214E-04	1126.06	3.7669E-04	1.2539E-03
1119.03	1.2378E-04	5.4758E-04	1127.01	3.7505E-04	1.2532E-03
1120.03	1.2881E-04	5.4402E-04	1128.03	3.7461E-04	1.2520E-03
1121.02	1.3145E-04	5.4539E-04	1129.00	3.7267E-04	1.2508E-03
1122.01	1.2878E-04	5.4459E-04	1130.04	3.6985E-04	1.2471E-03
1123.02	1.3340E-04	5.4376E-04	1131.03	3.7027E-04	1.2446E-03

1124.06	1.3414E-04	5.4813E-04	1132.02	3.6841E-04	1.2427E-03
1125.01	1.2633E-04	5.4775E-04	1133.01	3.6819E-04	1.2405E-03
1126.02	1.2867E-04	5.4529E-04	1134.06	3.6635E-04	1.2383E-03
1127.02	1.2286E-04	5.4227E-04	1135.01	3.6650E-04	1.2362E-03
1128.02	1.2853E-04	5.3869E-04	1136.05	3.6507E-04	1.2337E-03
1129.01	1.2906E-04	5.4076E-04	1137.01	3.6575E-04	1.2329E-03
1130.03	1.2477E-04	5.3858E-04	1138.01	3.6201E-04	1.2304E-03
1131.04	1.3037E-04	5.3748E-04	1139.05	3.6126E-04	1.2270E-03
1132.03	1.2545E-04	5.3625E-04	1140.02	3.6065E-04	1.2250E-03
1132.99	1.3335E-04	5.3710E-04	1141.03	3.5969E-04	1.2229E-03
1134.02	1.2483E-04	5.3811E-04	1142.04	3.5965E-04	1.2213E-03
1135.05	1.3011E-04	5.3736E-04	1143.00	3.5789E-04	1.2198E-03
1136.07	1.2411E-04	5.3829E-04	1144.07	3.5669E-04	1.2175E-03
1137.04	1.2367E-04	5.3499E-04	1145.00	3.5535E-04	1.2150E-03
1138.04	1.2582E-04	5.3682E-04	1146.02	3.5591E-04	1.2131E-03
1139.03	1.1953E-04	5.3608E-04	1147.05	3.5349E-04	1.2115E-03
1140.07	1.1947E-04	5.3126E-04	1148.02	3.5327E-04	1.2097E-03
1141.03	1.2296E-04	5.3110E-04	1149.05	3.5070E-04	1.2072E-03
1142.04	1.1729E-04	5.2970E-04	1150.02	3.5096E-04	1.2042E-03
1143.05	1.2058E-04	5.2626E-04	1151.05	3.5058E-04	1.2017E-03
1144.06	1.1772E-04	5.2249E-04	1152.04	3.4938E-04	1.1998E-03
1145.03	1.2712E-04	5.2212E-04	1153.02	3.4992E-04	1.1983E-03
1146.01	1.2194E-04	5.2364E-04	1154.04	3.4775E-04	1.1968E-03
1147.00	1.2818E-04	5.2634E-04	1155.04	3.4738E-04	1.1945E-03
1148.07	1.1337E-04	5.2294E-04	1156.02	3.4705E-04	1.1928E-03
1149.02	1.2600E-04	5.1831E-04	1157.06	3.4621E-04	1.1913E-03
1150.05	1.1880E-04	5.1725E-04	1158.03	3.4525E-04	1.1901E-03
1151.03	1.3185E-04	5.1772E-04	1159.04	3.4323E-04	1.1884E-03
1152.04	1.2325E-04	5.2188E-04	1160.01	3.4271E-04	1.1863E-03
1153.05	1.2548E-04	5.2025E-04	1161.02	3.4186E-04	1.1853E-03
1154.00	1.2427E-04	5.2083E-04	1162.03	3.3908E-04	1.1840E-03
1155.01	1.2417E-04	5.2170E-04	1163.01	3.3725E-04	1.1806E-03
1156.03	1.1857E-04	5.1973E-04	1164.05	3.3724E-04	1.1773E-03
1157.07	1.2234E-04	5.1645E-04	1165.01	3.3772E-04	1.1759E-03
1158.06	1.2352E-04	5.1709E-04	1166.00	3.3695E-04	1.1748E-03
1159.00	1.2430E-04	5.1909E-04	1167.05	3.3572E-04	1.1732E-03
1160.04	1.2023E-04	5.1791E-04	1168.02	3.3468E-04	1.1716E-03
1161.05	1.2962E-04	5.2466E-04	1169.05	3.3278E-04	1.1691E-03
1162.03	1.0739E-04	5.2602E-04	1170.02	3.3327E-04	1.1673E-03
1163.06	1.1223E-04	5.1639E-04	1171.00	3.3178E-04	1.1661E-03
1164.02	1.1227E-04	5.1671E-04	1172.03	3.3036E-04	1.1637E-03
1165.04	1.0577E-04	5.1123E-04	1173.01	3.3026E-04	1.1623E-03
1166.04	1.1479E-04	5.0726E-04	1174.06	3.2653E-04	1.1599E-03
1167.03	1.1292E-04	5.0767E-04	1175.04	3.2732E-04	1.1568E-03
1168.05	1.1640E-04	5.0687E-04	1176.03	3.2765E-04	1.1559E-03
1169.06	1.1867E-04	5.1213E-04	1177.03	3.2505E-04	1.1536E-03
1170.05	1.0646E-04	5.1159E-04	1178.02	3.2758E-04	1.1523E-03
1171.01	1.1016E-04	5.0728E-04	1179.04	3.2256E-04	1.1504E-03
1172.02	1.0509E-04	5.0496E-04	1180.02	3.2368E-04	1.1473E-03
1173.04	1.0600E-04	4.9857E-04	1181.01	3.2291E-04	1.1459E-03
1174.02	1.1051E-04	4.9461E-04	1182.02	3.2282E-04	1.1440E-03
1175.03	1.1724E-04	4.9571E-04	1183.04	3.2209E-04	1.1424E-03
1176.05	1.1795E-04	5.0047E-04	1184.04	3.2006E-04	1.1406E-03
1177.06	1.1428E-04	5.0359E-04	1185.02	3.1999E-04	1.1384E-03
1178.03	1.0659E-04	4.9972E-04	1186.04	3.1909E-04	1.1374E-03
1179.02	1.1264E-04	4.9402E-04	1187.00	3.1819E-04	1.1350E-03

1180.04	1.1807E-04	4.9821E-04	1188.04	3.1820E-04	1.1334E-03
1181.02	1.1027E-04	4.9934E-04	1189.02	3.1616E-04	1.1324E-03
1182.07	1.1651E-04	5.0295E-04	1190.04	3.1519E-04	1.1304E-03
1183.05	9.5905E-05	4.9752E-04	1191.02	3.1385E-04	1.1288E-03
1184.03	1.1236E-04	4.8893E-04	1192.03	3.1286E-04	1.1264E-03
1185.04	1.1288E-04	4.9591E-04	1193.06	3.1313E-04	1.1245E-03
1185.99	1.0445E-04	4.9500E-04	1194.02	3.1214E-04	1.1231E-03
1187.07	1.0604E-04	4.8999E-04	1195.06	3.1135E-04	1.1219E-03
1188.02	1.0482E-04	4.8440E-04	1196.02	3.0701E-04	1.1186E-03
1189.04	1.1970E-04	4.8708E-04	1197.04	3.1039E-04	1.1147E-03
1190.03	1.0839E-04	4.9211E-04	1198.01	3.1142E-04	1.1150E-03
1191.06	1.1054E-04	4.8862E-04	1199.03	3.0963E-04	1.1150E-03
1192.04	1.1225E-04	4.8941E-04	1200.04	3.0661E-04	1.1135E-03
1193.03	1.1269E-04	4.9271E-04	1201.00	3.0540E-04	1.1105E-03
1194.01	1.0743E-04	4.9468E-04	1202.08	3.0553E-04	1.1076E-03
1194.99	1.0570E-04	4.9622E-04	1203.00	3.0696E-04	1.1075E-03
1196.05	9.2359E-05	4.9098E-04	1204.03	3.0339E-04	1.1064E-03
1197.05	9.9070E-05	4.8416E-04	1205.00	3.0252E-04	1.1037E-03
1198.05	9.3763E-05	4.7846E-04	1206.05	3.0305E-04	1.1019E-03
1199.02	1.0814E-04	4.7730E-04	1207.00	3.0167E-04	1.1006E-03
1200.01	1.0064E-04	4.8032E-04	1208.02	3.0195E-04	1.1000E-03
1201.04	1.0506E-04	4.7957E-04	1209.06	2.9729E-04	1.0969E-03
1202.03	9.8643E-05	4.7847E-04	1210.04	3.0043E-04	1.0938E-03
1203.08	1.0186E-04	4.7380E-04	1211.03	2.9925E-04	1.0935E-03
1204.04	1.0655E-04	4.7593E-04	1212.03	2.9810E-04	1.0918E-03
1205.06	9.7963E-05	4.7268E-04	1213.04	2.9784E-04	1.0906E-03
1206.02	1.1186E-04	4.7126E-04	1213.99	2.9570E-04	1.0889E-03
1207.04	1.0958E-04	4.8078E-04	1215.08	2.9633E-04	1.0870E-03
1208.01	9.8572E-05	4.8076E-04	1216.04	2.9322E-04	1.0845E-03
1209.05	9.9018E-05	4.7521E-04	1217.04	2.9622E-04	1.0817E-03
1210.02	1.0085E-04	4.7451E-04	1218.02	2.9432E-04	1.0816E-03
1211.04	9.5754E-05	4.7236E-04	1219.04	2.9379E-04	1.0799E-03
1212.03	9.8288E-05	4.6744E-04	1220.03	2.9304E-04	1.0794E-03
1213.02	1.0234E-04	4.6613E-04	1221.05	2.8929E-04	1.0763E-03
1214.06	1.0627E-04	4.6892E-04	1222.01	2.9219E-04	1.0738E-03
1215.03	1.0436E-04	4.7483E-04	1223.02	2.9118E-04	1.0742E-03
1216.01	9.1622E-05	4.7100E-04	1224.06	2.8770E-04	1.0715E-03
1217.01	1.0041E-04	4.6516E-04	1225.02	2.9038E-04	1.0695E-03
1218.05	1.0253E-04	4.7031E-04	1226.01	2.8888E-04	1.0702E-03
1219.03	9.1892E-05	4.7039E-04	1227.01	2.8419E-04	1.0664E-03
1220.04	8.7315E-05	4.5695E-04	1228.03	2.8810E-04	1.0635E-03
1221.04	1.1164E-04	4.5865E-04	1229.03	2.8660E-04	1.0637E-03
1222.01	9.5488E-05	4.6654E-04	1230.03	2.8581E-04	1.0622E-03
1223.04	9.3583E-05	4.5781E-04	1231.05	2.8558E-04	1.0612E-03
1224.01	1.0375E-04	4.5652E-04	1232.04	2.8353E-04	1.0596E-03
1225.04	1.0208E-04	4.6286E-04	1232.99	2.8375E-04	1.0572E-03
1226.00	9.1416E-05	4.5749E-04	1234.07	2.8396E-04	1.0558E-03
1227.06	1.0723E-04	4.5443E-04	1235.03	2.8361E-04	1.0554E-03
1228.00	1.0368E-04	4.5938E-04	1236.04	2.8107E-04	1.0540E-03
1229.03	1.0774E-04	4.6598E-04	1237.01	2.8112E-04	1.0510E-03
1230.02	8.9431E-05	4.6425E-04	1238.05	2.8112E-04	1.0501E-03
1231.04	9.8993E-05	4.5702E-04	1239.06	2.7875E-04	1.0492E-03
1232.04	9.8074E-05	4.6005E-04	1240.04	2.7744E-04	1.0467E-03
1233.05	9.4297E-05	4.5904E-04	1241.00	2.7848E-04	1.0456E-03
1234.06	9.6932E-05	4.6020E-04	1242.03	2.7555E-04	1.0443E-03
1235.05	8.6564E-05	4.5659E-04	1243.05	2.7567E-04	1.0424E-03

1236.04	9.5436E-05	4.5310E-04	1244.00	2.7427E-04	1.0399E-03
1237.04	9.4187E-05	4.5615E-04	1245.06	2.7470E-04	1.0376E-03
1238.01	9.0458E-05	4.5613E-04	1246.01	2.7322E-04	1.0357E-03
1239.03	8.7382E-05	4.5217E-04	1247.04	2.7489E-04	1.0346E-03
1240.05	8.9738E-05	4.4987E-04	1248.01	2.7280E-04	1.0333E-03
1241.07	8.3897E-05	4.4419E-04	1249.05	2.7587E-04	1.0334E-03
1242.01	9.3842E-05	4.3858E-04	1250.02	2.7034E-04	1.0336E-03
1243.01	9.8686E-05	4.4021E-04	1251.04	2.6841E-04	1.0290E-03
1244.02	1.0268E-04	4.4565E-04	1252.00	2.7189E-04	1.0276E-03
1245.03	9.5070E-05	4.4679E-04	1253.06	2.7027E-04	1.0277E-03
1246.02	1.0002E-04	4.4537E-04	1254.04	2.6817E-04	1.0263E-03
1247.03	9.9955E-05	4.5028E-04	1255.04	2.6830E-04	1.0245E-03
1248.08	8.8838E-05	4.4635E-04	1255.99	2.6697E-04	1.0238E-03
1249.03	1.0131E-04	4.4403E-04	1257.02	2.6457E-04	1.0204E-03
1250.07	9.5577E-05	4.4737E-04	1258.05	2.6751E-04	1.0186E-03
1251.00	1.0165E-04	4.5154E-04	1259.08	2.6640E-04	1.0183E-03
1252.04	8.4870E-05	4.5291E-04	1260.05	2.6635E-04	1.0174E-03
1253.02	8.4677E-05	4.4344E-04	1261.04	2.6521E-04	1.0165E-03
1254.04	8.9581E-05	4.3923E-04	1262.02	2.6537E-04	1.0165E-03
1255.03	9.1577E-05	4.3821E-04	1263.03	2.6054E-04	1.0155E-03
1256.03	9.3990E-05	4.3855E-04	1264.03	2.6011E-04	1.0117E-03
1257.02	9.3765E-05	4.3865E-04	1265.07	2.6105E-04	1.0095E-03
1258.03	9.5389E-05	4.3746E-04	1266.01	2.6051E-04	1.0090E-03
1259.04	1.0058E-04	4.3941E-04	1267.05	2.5934E-04	1.0074E-03
1260.05	1.0194E-04	4.4655E-04	1268.04	2.5901E-04	1.0052E-03
1260.96	9.7184E-05	4.5484E-04	1269.06	2.6006E-04	1.0042E-03
1262.06	7.5955E-05	4.5050E-04	1269.99	2.5915E-04	1.0040E-03
1263.01	8.0419E-05	4.3945E-04	1271.02	2.5762E-04	1.0023E-03
1264.03	8.3214E-05	4.3865E-04	1272.01	2.5657E-04	1.0001E-03
1265.03	7.5752E-05	4.3260E-04	1273.08	2.5744E-04	9.9826E-04
1266.03	9.0086E-05	4.3163E-04	1274.04	2.5817E-04	9.9834E-04
1267.04	7.3645E-05	4.2747E-04	1275.03	2.5534E-04	9.9731E-04
1268.02	8.9972E-05	4.1589E-04	1276.01	2.5642E-04	9.9533E-04
1269.03	1.0501E-04	4.2342E-04	1277.07	2.5707E-04	9.9606E-04
1270.03	1.0130E-04	4.3346E-04	1278.03	2.5361E-04	9.9594E-04
1271.00	1.0404E-04	4.4482E-04	1279.05	2.5151E-04	9.9272E-04
1272.07	7.5513E-05	4.4605E-04	1280.03	2.5412E-04	9.9045E-04
1273.02	7.1408E-05	4.2546E-04	1281.04	2.5529E-04	9.9249E-04
1274.06	9.8337E-05	4.2445E-04	1282.02	2.4914E-04	9.9248E-04
1274.97	8.3391E-05	4.3003E-04	1283.05	2.4724E-04	9.8691E-04
1276.05	8.6972E-05	4.1882E-04	1284.00	2.5351E-04	9.8583E-04
1277.03	1.0467E-04	4.2112E-04	1285.05	2.4929E-04	9.8736E-04
1278.03	1.0525E-04	4.3713E-04	1286.02	2.4744E-04	9.8263E-04
1279.05	8.2942E-05	4.3383E-04	1287.06	2.5506E-04	9.8106E-04
1280.03	1.0932E-04	4.3959E-04	1288.03	2.5674E-04	9.8598E-04
1281.02	7.3852E-05	4.4632E-04	1289.07	2.5330E-04	9.8907E-04
1282.06	8.3494E-05	4.3834E-04	1290.04	2.5196E-04	9.9111E-04
1283.01	6.3239E-05	4.2839E-04	1290.98	2.4710E-04	9.9197E-04
1284.06	8.7683E-05	4.1582E-04	1292.07	2.4537E-04	9.9164E-04
1285.01	9.1928E-05	4.2094E-04	1293.05	2.4763E-04	9.9880E-04
1286.02	1.0349E-04	4.3587E-04			
1287.01	7.0207E-05	4.3577E-04			
1288.05	8.8223E-05	4.2524E-04			
1289.05	8.1562E-05	4.2837E-04			
1290.02	8.2288E-05	4.2399E-04			
1291.04	9.0001E-05	4.2393E-04			

1292.02	9.5850E-05	4.3524E-04
1293.05	7.7431E-05	4.4267E-04
1294.05	6.7110E-05	4.3380E-04
1295.04	6.9325E-05	4.2531E-04
1296.02	6.8375E-05	4.1480E-04
1297.05	8.9672E-05	4.1339E-04
1298.02	9.4447E-05	4.2707E-04
1299.03	8.5817E-05	4.4151E-04
1300.02	6.1714E-05	4.3801E-04

Bibliography

1. D. Attwood, *Soft X-Rays and Extreme Ultraviolet Radiation Principles and Applications* (Cambridge University Press, New York, 1999).
2. A. G. Michette, *Optical Systems for Soft X-Rays* (Plenum Press, New York, 1986).
3. E. Hetch, *Optics*, 3rd edition (Addison-Wesley, Reading, 1998).
4. J. H. Underwood, "X-Ray Optics," Amer. Sci. **66**, 467 (1978).
5. P. Kirkpatrick and A. V. Baez, "Formation of optical images by X-Rays," J. Opt. Soc. Amer. **38**, 766 (1984): P. Kirkpatrick, "The X-Ray Microscope," Sci. Am. **180**, 44 (1949).
6. J. A. R. Samson and D. L. Ederer, *Vacuum Ultraviolet Spectroscopy*, Vols. I and II (Academic Press, New York, 1998).
7. W. B. Peatman, *Gratings, Mirrors, and Slits: Beamline Design for Soft X-Ray Synchrotron Radiation Sources* (Gordon and Breach, Amsterdam, 1997).
8. H. Keoppe, Ph. D. thesis, Gissen, Hesse, Germany 1923.
9. W. Deubner, "Reflection of x-rays frm artificially prepared bodies of laminar structures,"Ann. Phys. **5**, 261 (1930).
10. J. W. M. Dumond and J. P. Youtz, "Selective x-ray diffraction from artificially stratified metal films deposited by evaporation," Phys. Rev. **48**, 703 (1935).

11. E. Spiller, "Low-loss reflection coatings using absorbing materials," Appl. Phys. Lett. **20**, 365 (1972); E. Spiller, "Reflective multilayer coatings for the far UV region," Appl. Opt. **15**, 2333 (1976); E. Spiller, *Soft X-Ray Optics* (SPIE Optical Engineering Press, Washington 1994).

12. R. P. Haelbich and C. Kunz, "Multilayer interference mirrors for the XUV range around 100 eV photon energy," Opt Commun. **17**, 287 (1976).

13. T. W. Barbee, Jr. and D. L. Keith, "Synthetic structures layered on the atomic scale," in *Workshop on X-Ray Instrumentation for Synchrotron Radiation Research*, H. Winick and G. Brown, Eds., Standford Synchrotron radiation Laboratory Report **7804** (1978); T. W. Barbee, Jr., "Sputtered layered synthetic microstructure (LSM) dispersion elements," in *Low Energy X-Ray Diagnostics*, D. T. Atwood and B. L. Henke, Eds., AIP Conf. Proc. **75**, 131 (1981).

14. Information on the EUVE mission and the observed spectral lines can be obtained at http://ssl.berkeley.edu/euve.

15. A. B. C. Walker, T. W. Barbee, R. B. Hoover, R. B. Hoover, and J. F. Lindblom, "Soft X-Ray Images of the Solar Corona with a Normal Incidence Cassegrain Multilayer Telescope," Science **241**, 1781; M. J. Allen, A. B. C. Walker, O. Oluseyi, R. B. Hoover, and T. W. Barbee, "Chromospheric and Coronal Structure of Polar Plumes," Solar Phys. **174**, 367 (1997).

16. Information on the SOHO mission is available at http://sohowww.nascom.nasa.gov.

17. Information on the TRACE mission is available at http://vestige.lmsal.com/TRACE/.

18. R. C. Jaeger, *Introduction to Microelectronic Fabrication*,Vol. 5 (Addison-Wesley, Massachusetts, 1993).

19. R. White, *How Computers Work* (Ziff-Davis, California, 1997).

20. C. Montcalm, S. Bajt, P. B. Mirkarimi, E. Spiller, F. J. Weber, and J. A. Folta, "Multilayer reflective coatings for extreme ultraviolet lithography," in *Emerging Lithographic Technologies II*, Y. Vladimirski, Ed., Proc. SPIE, **3331**, 42 (1998).

21. D. A. Tichenor, G. D. Kubiak, W. C. Replogle, L. E. Klebanoff, J. B. Wronosky, L. C. Hale, H. N. Chapman, J. S. Taylor, J. A. Folta, C. Montcalm, R. M. Hudyma, K. A. Goldberg, and P. Naulleau, "EUV Engineering Test Stand," Emerging Lithographic Technologies IV, E. A. Dobisz, Ed., Proc. SPIE, **3997**, 48 (2000).

22. C. Montcalm, B. T. Sullivan, M. Ranger, J. M. Slaughter, P. A. Kearny, and Charles M. Falco, and M. Chaker, "Mo/Y multilayer mirrors for the 8-12-nm wavelength region," Opt. Lett. **19**, 1173 (1994); C. Montcalm, P. A. Kearney, J. M. Slaughter, B. T. Sullivan, M. Chaker, H. Pépin, and C. M. Falco, "Survey of Ti-, B-, and Y-based soft x-ray-extreme-ultraviolet multilayer mirrors for the 2- to 12-nm wavelength region," Appl. Opt. **35**, 5134 (1996).

23. D. L. Smith, *Thin-Film Deposition Principles & Practice* (McGraw-Hill, New York, 1995).

24. B. D. Cullity, *Elements of x-ray diffraction*, 2nd edition (Addison-Wesley, Massachusetts, 1978).

25. B. L. Henke, J. Y. Uejid, H. T. Yamada, and R. T. Tackaberry, "Characterization of multilayer x-ray anlysers: model and measurements," Opt. Eng. **25**, 937 (1986).

26. J. D. Jackson, *Classical Electrodynamics*, 2nd edition (John Wiley and Sons, New York, 1975).

27. J. H. Underwood, E. M. Gullikson, M. Koike, P. J. Batson, P. E. Denham, K. D. Franck, R. E. Tackaberry, and W. F. Steele, "Calibration and standards beamline 6.3.2 at the Advanced Light Source," Rev. Sci. Instrum. **67**, 9 (1996); J. H. Underwood and E. M. Gullikson, "High-resolution, high-flux, user friendly VLS beamline at the ALS for the 50-1300 eV energy region," J. Electr. Spectr. Rel. Phenom. **92**, 265 (1998); E. M. Gullikson, S. Mrowka, B. B. Kaufmann, "Recent developments in the EUV reflectometry at the Advanced Light Source," in *Emerging Lithographic Technologies V*, E. A. Dobisz, eds., Proc. SPIE **4343**, 363 (2001).

28. R. C. Weast, M. J. Astle, *CRC Handbook of Chemistry and Physics*, 63rd edition (CRC Press, Florida, 1982); see also http://www.webelements.com.

29. C. R. Brundle, C. A. Evans, Jr., and S. Wilson, *Encyclopedia of Materials Characterization* (Manning Publications, Connecticut, 1992).

30. D. B. Williams and C. B. Carter, *Transmission Electron Microscopy* (Prenum Press, New York, 1996).

31. Current reflectance results of EUV/soft x-ray multilayers are available at http://www-cxro.lbl.gov/multilayer/survey.html.

32. C. Montcalm, B. T. Sullivan, S. Duuay, M. Ranger, W. Steffens, H. Pépin, and M. Chaker, "In situ reflectance measurements of soft-x-ray/extreme-ultraviolet Mo/Y multilayer mirrors," Opt. Lett. **20**, 1450 (1995); C. Montcalm, B. T. Sullivan, M. Ranger, and H. Pépin, "Ultrahigh vacuum deposition-reflectometer system for the

in situ investigation of Y/Mo extreme ultraviolet multilayer mirrors," J. Vac. Sct. Technol. A **15**, 3069 (1997).

33. J. F. O' Hanlon, *A User's Guide to Vacuum Technology*, 2nd edition (John Wiley & Sons, New York, 1989).

34. The atomic scattering factor tables have been made available on the World Wide Web by E. M. Gullikson at http://www-cxo.lbl.gov/optical_constants.

35. R. W. James, *The optical principles of the diffraction of x-rays* (Ox Bow Press, Connecticut, 1948).

36. B. L. Henke, E. M. Gullikson, and J. C. Davis, "X-ray interactions: Photo absorption, scattering, transmission, and reflection at E = 50-30,000 eV, Z = 1-92," Atomic Data and Nuclear Data Tables **54**, 181 (1993).

37. J. Berkowitz, *Photo absorption, Photoiornization, and Photoelectron Spectroscopy*, (Academic Press, New York, 1979).

38. D. L. Windt, W. C. Cash, Jr., M. Scott, P. Arendt, B. Newman, R. F. Fisher, and A. B. Swartzlander, "Optical constants for thin films of Ti, Zr, Nb, Mo, Ru, Rh, Pd, Ag, Hf, W. Re, Ir, Os, Pt, and Au from 24 Å to 1216 Å," Appl. Opt. **27**, 246 (1988); D. L. Windt, "XUV optical constants of single-crystal GaAs and sputtered C, Si, Cr_3C_2, Mo, and W," Appl. Opt. **30**, 15 (1991).

39. R. Soufli and E. M. Gulikson, "Absolute photoabsorption measurements of molybdenum in the range 60-930 eV for optical constant determination," Appl. Opt. **37**, 1713 (1998).

40. C. Tarrio, R. N. Watts, T. B. Lucatorto, J. M. Slaughter, and C. M. Falco, "Optical constants of in situ-deposited films of important extreme-ultraviolet multilayer mirror materials," Appl. Opt. **37**, 4100 (1998).

41. J. I. Larruquert and R. A. M. Keski-Kuha, "Reflectance measurements and optical constants in the extreme ultraviolet for thin films of ion-beam-deposited SiC, Mo, Mg_2Si, and InSb and of evaporated Cr," Appl. Opt. **39**, 2772 (2000).

42. L. Kissel and R. H. Pratt, "Corrections to Tabulated Anomalous-Scattering Factors," Acta Cryst. **46**, 170 (1990).

43. L. D. Landau and E. M. Liftshitz, *Electrodynamics of Continuous Media*, 2nd edition (Addison-Wesley, New York, 1960).

44. J. E. Marsden and M. J. Hoffman, *Basic Complex Analysis* (Freeman, New York, 1973).

45. F. Wooten, *Optical Properties of Solids*, (Academic Press, New York, 1972)

46. D. Y. Smith and E. Shiles, "Finites-energy f-sum rules for valence electrons," Phys. Rev. B. **17**, 4689 (1978); D. Y. Smith, in E. D. Palik (Ed.), *Handbook of Optical Constants of Solids*, (Academic Press, New York, 1985).

47. F. R. Powell and T. A. Johnson, “Filter windows for EUV lithography,” in *Emerging lithographic Technologies V*, E. A. Dobisz, eds., Proc. SPIE Vol. **4343** (2001).

48. J. H. Weaver, C. Krafka, D. W. Lynch, and E. E. Koch, in *Physic Daten-Optical properties of metals*, H. Behrens and G. Ebel, eds. (Fachinformationszentrum, Karlsruhe, Germany, 1981), Vol. 18-2.

49. D. W. Juenker, L. J. LeBlanc, and C. R. Martin, "Optical properties of some transition metals," J. Opt. Soc. Am. **58**, 164 (1968).

50. Y. G. Chen and B. X. Liu, "Amorphous films formed through a multilayer technique in an immiscible Y-Mo system and their structural relaxation," Appl. Phys. Lett. **68**, 3096 (1996); Y. G. Chen and B. X. Liu, "Amorphous films formed through a multilayer technique in an immisible Y-Mo system and their elastic properties," J. Appl. Phys. **30**, 510 (1997).

51. B. M. Clemens and T. C. Hufnagel, "Comment on "Amorphous films formed by solid-state reaction in an immiscible Y-Mo system and their structural relaxation," Appl. Phys. Lett. **69**, 19 (1996).

52. X. Gu and T. C. Hufnagel, "Effect of annealing on Y/Mo multilayers," J. Appl. Phys. **86**, 2459 (1999).

53. J. B. Kortright, S. Joksch, and E. Ziegler, "Stability of tungsten carbon and tungsten silicon multilayer x-ray mirrors under thermal annealing and x-radiation exposure," J. Appl. Phys. **69**, 168 (1991).

54. V. Dupuis, M. F. Ravet, C. Tete, M. Piecuch, Y. Lepetre, R. Rivoira, and e. Ziegler, "Thermal evolution of X/C multilayers (with X = W, Ni, or SiWSi): a systematic study," J. Appl. Phys. **68**, 5146 (1990).

55. H. L. Bai, E. Y. Jiang, and C. D. Wang, and R. Y. Tian, "Enhancement of the reflectivity of soft-x-ray Co/C multilayers at grazing incidence by thermal treatment," J. Physics-Condensed Matter **8**, 8763 (1996); "Improvement of the thermal stability of Co/C soft x-ray multilayers through doping with nitrogen," J. Phys. Condens. Matter **9**, L205 (1997).

56. T. W. Barbee, Jr., *X-Ray Microscopy* (Springer, Berlin, 1984).

57. D. G. Stearns, M. B. Stearns, Y. Cheng, J. H. Stith, and N. M. Ceglio, "Thermally induced structural modification of Mo-Si multilayers," J. Appl. Phys. **67**, 2417 (1990).

58. M. T. Wilson, technical paper available at http://www.puretechinc.com/tech_papers/tech_papers.htm.

59. D. L. Windt, "IMD: Software for modeling the optical properties of multilayer films," Computer in Physics **12**, 360 (1998). A copy of the software can be downloaded at http://cletus.phys.columbia.edu/~windt/imd/.

60. S. Bajt, D. G. Stearns, and P. A. Kearney, "Investigation of the amorphous-to-crystalline transition in Mo/Si multilayers," J. Appl. Phys. **90**, 1017 (2001).

61. T. B. Massalski, H. Okamoto, P. R. Subramanian, and L. Kacprzak, *Binary Alloy Phase Diagrams*, 2nd edition in Vol. 3.

62. F. R. de Boer, R. Boom, W. C. m. Mattens, A. R. Miedema, and A. K. Niessen, *Cohesion in Metals: transition Metal Alloys*, in Vol. 1 of Cohesion and Structure series (North Holland, New York, 1988).

63. M. E. Bruner, B. M. Haisch, W. A. Brown, L. W. Acton, and J. H. Underwood, "Soft x-ray images of the solar corona using normal incidence optics," J. Phys. (Paris) Suppl. **49**, 115 (1988).

64. J. F. Seely, M. P. Kowalski, W. R. Hunter, J. C. Rife, T. W. Barbee, G. E. Holland, C. N. Boyer, and C. M. Brown, "On-blaze operation of a Mo/Si multilayer-coated concave diffraction grating in the 136-142 Å wavelength and near normal incidence," Appl. Opt. **32**, 4890 (1993); J. F. Seely, R. G. Cruddace,

M. P. Kowalski, W. R. Hunter, T. W. Barbee, J. C. Rife, R. Ely, and K. G. Stilt, "Polarization and efficiency of a concave multilayer grating in the 135-250 Å region and in normal-incidence and Seya-Manioc mounts," Appl. Opt. **34**, 7347 (1995); J. F. Seely, M. P. Kowalski, W. R. Hunter, T. W. Barbee, R. G. Cruddace, and J. C. Rife, "Normal-incidence efficiencies in the 115-340 Å wavelength region of replicas of the Skylab 3600 line/mm grating with multilayer and gold coatings," Appl. Opt. **34**, 6453 (1995); J. F. Seely, M. P. Kowalski, R. G. Cruddace, K. F. Heidemann, U. Heizmann, U. Kleineberg, K. Osterried, D. Menke, J. C. Rife, and W. R. Hunter, "Multilayer-coated laminar grating with 16% normal-incidence efficiency in the 150-Å wavelength region," Appl. Opt. **36**, 8206 (1997).

65. C. Montcalm, S. Bajt, J. F. Seely, "MoRu/Be multilayer coated grating with 10.4% normal-incidence efficiency in the 11.4 nm wavelength region," Opt. Lett. **26**, 125 (2001).

66. J. F. Seely, C. Montcalm, S. Baker, and S. Bajt, "High-efficiency MoRu/Be multilayer coated gratings operating near normal incidence in the 11.1-12.0 nm wavelength range," Appl. Opt. **40**, 5565 (2001).

67. U. Feldman, P. Mandelbaum, J. F. Seely, G. A. Doschek, and H. Gursky, "The potential for plasma diagnostics from stellar extreme ultraviolet observation," Astrophys. J. Suppl. **81**, 387 (1992).

68. B. Sae-Lao and C. Montcalm, "Molybdenum-strontium multilayer mirrors for the 8-12 nm extreme ultraviolet wavelength region," Opt. Lett. **26**, 468 (2001).

69. B. Sae-Lao and C. Montcalm, “Normal-incidence multilayer mirrors for the 8-12 nm wavelength region”, Advanced Light Source Compendium of User Abstracts 1999, available at http://alspubs.lbl.gov/compendium/.

70. L. I. Goray, "Numerical analysis for relief gratings working in the soft x-ray and XUV region by the integral equation method," in *X-Ray and UV Detectors*, R. B. Hoover and M. W. Tate, eds., Proc. SPIE **2278**, 168 (1994); L. I. Goray and B. C. Chernov, "Comparison of rigorous methods for x-ray and XUV grating diffraction analysis," in *X-Ray and Extreme Ultraviolet Optics*, R. B. Hoover and A. B. C. Walker, eds., Proc. SPIE **2515**, 240 (1995).

71. L. I. Goray and J. F. Seely, "Efficiencies of Master, Replica, and Multilayer Gratings for the Soft X-Ray - EUV Range: Modeling Based on the Modified Integral Method and Comparisons to Measurements", Appl. Opt. **41**, 1434 (2002).

72. D. G. Stearns, “The scattering of X-rays from non-ideal multilayer structure,” J. Appl. Phys. **65**, 1989.

73. See carroll@uiuc.edu

74. D. G. Stearns, D. P. Gaines, D. W. Sweeney, and E. M. Gullikson, “Nonspecular x-ray scattering in a multilayer-coated imaging system,” J. Appl. Phys. **84**, 1003 (1998).